

**HYDRODYNAMICS OF TAYLOR FLOW
IN CAPILLARIES AND
MONOLITH REACTORS**

HYDRODYNAMICS OF TAYLOR FLOW

IN CAPILLARIES AND

MONOLITH REACTORS

PROEFSCHRIFT

ter verkrijging van de graad van doctor
aan de Technische Universiteit Delft
op gezag van de Rector Magnificus prof. dr. ir. J.T. Fokkema,
voorzitter van het College voor Promoties,
in het openbaar te verdedigen

op dinsdag 2 december 2003
te 10:30 uur

door

Michiel Thijs KREUTZER

scheikundig ingenieur
geboren te Haarlem

Dit proefschrift is goedgekeurd door de promotoren:

Prof. dr. J.A. Moulijn

Prof. dr. F. Kapteijn

Samenstelling promotiecommissie:

Rector Magnificus

voorzitter

prof. dr. J.A. Moulijn

Technische Universiteit Delft, promotor

prof. dr. F. Kapteijn

Technische Universiteit Delft, promotor

prof. dr. ir. C. Kleijn

Technische Universiteit Delft

prof. dr. A. Renken

Ecole Polytechnique Fédérale de Lausanne

prof. dr. R. Krishna

Universiteit van Amsterdam

prof. dr. M. Winterbottom

University of Birmingham

dr. J.J. Heiszwolf

Air Products and Chemicals, Inc

Published and distributed by: DUP Science

DUP Science is an imprint of

Delft University Press

P.O. Box 98

2600 MG Delft

Telephone: +31 15 27 85 678

Telefax: +31 15 27 85 706

E-mail: info@library.tudelft.nl

ISBN 90-407-2443-1

Keywords: Chemical Engineering / Reactors / Hydrodynamics / Monoliths / Multiphase Flow.

©2003 by M.T. Kreutzer

All rights reserved. No part of the material protected by this copyright notice may be reproduced or utilised in any form or by any means, electronic or mechanical, including photocopying, recording or any information storage and retrieval system, without written permission of the publisher: Delft University Press

Printed in the Netherlands

Voor
Erik en Ietje

CONTENTS

I	INTRODUCTION	1
§ I.1	Advantages of structured reactors	1
§ I.2	Monoliths	2
§ I.3	Taylor flow	4
§ I.4	Outline and scope of this thesis	6
II	PRESSURE DROP	11
§ II.1	Introduction	11
§ II.2	Hydrodynamics of bubbles in capillaries	13
§ II.3	Numerical approach	17
§ II.4	Numerical results	20
§ II.5	Experimental	28
§ II.6	Results	31
§ II.7	Discussion	35
§ II.8	Conclusions	37
III	LIQUID–SOLID TRANSPORT PHENOMENA	43
§ III.1	Introduction	43
§ III.2	Model development	44
§ III.3	Formulation	47
§ III.4	Results	48
§ III.5	Literature data	60
§ III.6	Industrial relevance	62
§ III.7	Conclusions	64
IV	RESIDENCE TIME DISTRIBUTION	69
§ IV.1	Introduction	69
§ IV.2	Theory	71
§ IV.3	Experimental	86
§ IV.4	Results	91
§ IV.5	Discussion	94
§ IV.6	Conclusions	97

CONTENTS

V	GAS COMPONENT MASS TRANSFER	103
	§ V.1 Introduction	103
	§ V.2 Numerical Analysis	108
	§ V.3 Experimental	114
	§ V.4 Results and discussion	118
	§ V.5 Conclusions	123
VI	SCALING ASPECTS	129
	§ VI.1 Introduction	129
	§ VI.2 Strategy Development	130
	§ VI.3 Experimental	131
	§ VI.4 Results	134
	§ VI.5 Discussion	137
	§ VI.6 Stability	141
	§ VI.7 Monoliths as Gas-Liquid Contactors	142
	§ VI.8 Monoliths for three-phase reactions	147
	§ VI.9 Conclusions	149
VII	REACTOR DESIGN	155
	§ VII.1 Introduction	155
	§ VII.2 Monolith loop reactor	156
	§ VII.3 Kinetics	158
	§ VII.4 Reactor Model	160
	§ VII.5 Results	165
	§ VII.6 Discussion	170
	§ VII.7 Conclusions	171
VIII	CONCLUSIONS AND EPILOGUE	177
	§ VIII.1 Introduction	177
	§ VIII.2 Single Channel Investigations	178
	§ VIII.3 Reactor Scale Investigations	179
	§ VIII.4 Open questions	182
	SAMENVATTING	185
	PUBLICATIONS AND PRESENTATIONS	193
	DANKWOORD	196
	CURRICULUM VITAE	198

CHAPTER I

INTRODUCTION

§ I.1 ADVANTAGES OF STRUCTURED REACTORS

Reactions involving a gas, liquid and solid are found in many industrial processes. Usually, the solid is a heterogeneous catalyst, and the gas and liquid phases are the reactants. Because three phases are involved, the design of such reactors is complex and involves phenomena such as mass and heat transfer between the phases, intraparticle diffusion, backmixing, maldistribution and energy input. Three-phase reactors can be classified in two groups: (1) fixed-bed reactors, where the solid phase is stationary and the gas and liquid flow through the solid bed and (2) slurry reactors, where the solid catalyst – typically a fine powder – is flowing along with the gas and liquid phase, which are mixed either by the rising bubbles alone (bubble column reactor) or assisted by mechanical agitation (stirred slurry reactor).

In fixed-bed systems, the solid catalyst is usually randomly dumped into a vessel, and the exact geometry of the space available for the fluids to flow through is ill-defined and varies from place to place within the reactor. In slurry reactors, the flow of bubbles, suspended catalyst and the liquid, relative to one another, is highly chaotic. In fact, chaos theory has proven itself as a reliable tool to characterise the latter systems (van den Bleek *et al.*, 2002). The fact that the behavior of the flow at any given point in time and space is not well known in either reactor makes the theoretical analysis of these three-phase reactors from a first principles fluid mechanical study cumbersome if not impossible.

A more significant disadvantage of the variations of the hydrodynamics of the phases surrounding the catalyst is that it is difficult to tailor those same hydrodynamics to the chemical task of the reactor. This disadvantage can be overcome by structuring the catalyst. Here, the term *structuring* is used to indicate that the form of the catalyst in a more or less repeating regular arrangement of some building block of well defined geometry.

As an example, consider the mass transfer to or in the catalyst. In heterogeneous catalysis, it may be favourable to have small catalyst particles to ensure efficient use of the catalyst. In a fixed-bed reactor it becomes impossible to force the fluids through

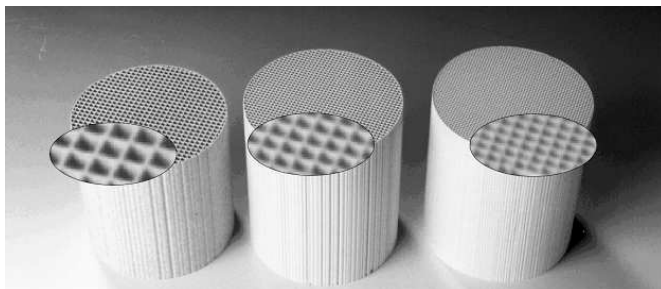


Figure 1.1: Three monoliths of cell density 200 cps, 400 cps and 600 cps. The blocks depicted here have a diameter of 10 cm.

the bed if the particles become too small, because the pressure drop, governed by the hydrodynamic diameter of the space between the particles, is directly coupled to the size of the particles. As a result, one has to resort to slurry reactors if the chemistry and mass transfer limitations of the process dictates the use of very small particles.

On the other hand, if the catalyst is structured, the chemical engineer can *design* the geometry of the catalyst, decoupling the characteristic length of the catalyst and the hydrodynamic diameter, and thus – in principle – decoupling pressure drop and mass transport.

The optimal geometry of a structured reactor is dictated by the nature of the process. For instance, for three-phase reactors that would benefit from counter-current flow, but do not require high mass transfer rates, a different structure would be designed that is favourable for counter-current flow. Examples of such structures are the internally finned monolith reactor (Lebens, 1999) and the three levels of porosity reactor (van Hasselt, 1999). A good review of the available literature on structured reactors and catalysts is given in Moulijn & Cybulski (1998).

§1.2 MONOLITHS

It may be argued that one of the most important contributions of catalysis to society in the last decades is the development of the automobile exhaust catalytic converter. In 1970, the state of California approved legislation that called for a 90 % reduction in pollutants from cars. A small catalytic reactor, now found in every car sold, allowed this massive reduction in pollution. Although the chemistry of the three-way catalytic converter is an interesting subject in itself, the point worth mentioning here is the fact that the catalytic car converter is a structured reactor, and the structure is called a *monolith*.

In the early stages of development, the automotive catalytic reactor was a fixed-bed gas-solid reactor. Although this system met the design criteria in terms of reduction of pollutants, vigorous shaking of the system (not uncommon in cars) caused attrition

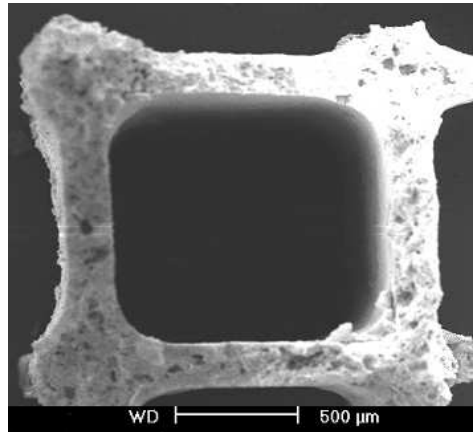


Figure 1.2: SEM picture of a coated monolith channel, showing the rounding of an initially square monolith channel by the coating process.

of the particles and the pressure drop over this reactor was high. One needs only to recall that a *turbocharger* can enhance the performance of a car engine by exploiting the excess pressure of the gasses leaving the engine to realize that the loss of engine performance due to the pressure drop in the exhaust reactor was a significant hurdle that needed a solution.

Monoliths – the word is derived from the Greek *monos* and *lithos*, suggesting the structure is made up of one brick or stone – are ceramic structures of parallel straight channels. The diameter of each channel is typically on the order of one millimeter, and the thickness of the walls is typically one-tenth of that, *i.e.* 100 μm . The open structure without bends hardly obstructs the flow, and with small channels a high surface area of the catalyst is obtained to ensure fast mass transfer. On the walls of the inert channels, a thin layer of catalytically active material is deposited to obtain a so called *egg-shell* catalyst, although it is also possible to prepare monoliths that have active material throughout the wall. The application of monoliths solved the problem of pressure drop in the automotive exhaust converter, and monoliths are now also used in other applications of gas cleaning where low pressure drop and dust tolerance is essential, for instance in deNO_x reactors that remove nitrous oxides from power plant emissions.

The size of the channels is usually indicated by the number of channels per square inch (cpsi) of frontal area of the structure. In Fig. 1.1, three typical monolith structures are shown. The cross sectional shape of most bare monolith channels is square. Coating a catalytically active layer on the walls makes the square channel become more rounded (Fig. 1.2). Coating usually involves a liquid solution of catalyst support that collects in the corners due to capillary forces during drying. For an overview of the

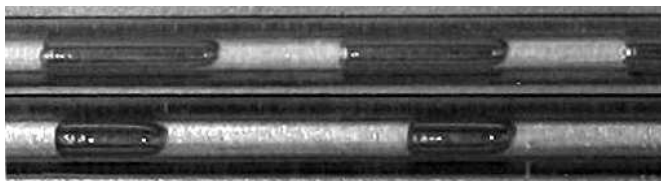


Figure 1.3: Two snapshots of the Taylor flow pattern of gas and liquid inside a capillary

preparation of monolith catalysts, see the reviews by Nijhuis *et al.* (2001) and Vergunst *et al.* (2001).

§ 1.3 TAYLOR FLOW

The use of monoliths in three-phase applications started later than the gas-only application and is still limited. One commercial process, the production of hydrogen peroxide in the anthraquinone process (Berglin & Herrman, 1984) is currently conducted using monoliths. However, several companies are investigating monoliths, *e.g.* Air Products and Chemicals, Inc have several patents, one involving dinitrotoluene hydrogenation (Machado *et al.*, 1999).

Whether monoliths are viable alternatives to the more common three-phase reactors depends on whether the geometry of the catalyst structure is beneficial to the chemical process. Immediately, one possible advantage can be seen: the walls of the monoliths are thin, and the active layer can be even thinner. As diffusion inside the catalyst is orders of magnitude lower for liquids than for gasses, concentration gradients due to slow diffusion, relative to reaction, can easily be overcome by using thin-walled monoliths. However, the same holds more or less for other fixed-bed reactors. In fact, the manufacture of catalysts of any shape for which only the outer part is active is a frequently used and well understood technique to overcome intraparticle diffusion limitations in fixed-bed reactors.

The more interesting question is whether the hydrodynamic behaviour of the gas and liquid flowing through the monolith channels has features that are beneficial to the reactor design. Two-phase flow through capillary channels is considerably different from two-phase flow through larger channels. As only small bubbles can be present in the channels, surface tension forces play a more dominant role. A reasonable definition of the term *capillary* might be obtained by requiring the dominance of surface tension forces. This indicates that the maximum size of a capillary should be based on the properties of the fluids that flow through it. In relation to multiphase flow, such a definition of a capillary might be that a (Taylor) bubble has zero rise velocity in a liquid filled sealed capillary (see *e.g.* Bretherton, 1961), but other definitions are possible. For low to moderate velocities the flow is laminar, and the predominant flow pattern is a



Figure 1.4: Streamlines in Taylor flow, revealing the circulation pattern in the liquid slug and the film layer between the bubble and the wall. Details of the numerical simulation are given in Chapter II.

slug flow pattern called Taylor flow, in reference to G.I. Taylor's classical paper (Taylor, 1960). Note that the name Taylor flow is encountered most commonly in chemical engineering literature dealing with monoliths, and a number of different names for the same flow pattern are commonly found, *e.g.* bubble–train flow, slug flow, intermittent flow. The Taylor flow pattern is the flow pattern that is observed at velocities of less than about 1 m/s. For a more thorough discussion of the various flow patterns in capillaries, see Triplett *et al.* (1999) and Fukano & Kariyasaki (1993).

In Taylor flow, the gas bubbles are too large to retain a spherical shape, and are stretched to fit inside the channel, see Fig. 1.3. Surface tension pushes the bubble towards the channel wall, and only a thin film of liquid remains between the bubble and the wall. The liquid is effectively sealed between the bubbles, and cannot escape the slug that it forms. This prevents bubble coalescence, and also leads to a recirculating flow pattern inside the liquid slug, see Fig. 1.4.

APPLICATIONS OF TAYLOR FLOW

The surface tension dominated flow of elongated bubbles has been recognised as a useful flow pattern for various applications outside of chemical reactor engineering. Perhaps the simplest and oldest one is the use of a bubble as a flowmeter (Fairbrother & Stubbs, 1935). Because the bubble extends over almost the entire cross-sectional area of the channel, the velocity of the bubble is nearly equal to the velocity of the liquid upstream and downstream of the channel, and by visual observation the velocity of the bubble can easily be measured. Other applications exploit the enhanced mass or heat transfer due to circulation, *e.g.* the improvement of microfiltration by adding gas bubbles to the capillary channels. The experimentally observed enhancement of microfiltration efficiency is also attributed to the removal of filter cake by the pressure pulsing caused by the passing of the bubbles and slugs (Cui *et al.*, 2003). Some have argued that circulation in the plasma separating red blood cells in microvascular flow enhances oxygen uptake and release, but the evidence for such convective enhancement is incomplete (Bos *et al.*, 1996).

Finally, the liquid slugs are practically sealed between two bubbles. This feature of Taylor flow was used to make so-called continuous flow analysers. In these machines, the samples that must be analysed are injected into the channel, separated by bubbles. Downstream, the samples are actually analysed, usually by spectroscopic means. Since

the bubbles prevent mixing of the samples, long capillary tubes with multiple analysis sections can be used with minimal mixing of consecutive samples. Also, many samples can be analysed at high speed, and continuous flow analysers were frequently used in for instance routine tests in hospitals (van Eerd & Kreutzer, 1987).

§ I.4 OUTLINE AND SCOPE OF THIS THESIS

The purpose of this thesis is to investigate the hydrodynamic behavior of Taylor flow, with the application to chemical reactor engineering in mind. Not only is the geometric structure of the monolith catalyst very regular, the flow pattern also has a well defined geometry. This makes the investigation of a monolith reactor from first principle fluid mechanics possible. This thesis starts with a fundamental investigation of a single circular capillary channel, and gradually changes focus to monolithic structures.

At the start of this thesis project, several studies of multi-phase flow in monoliths were already available. One of the earliest studies, (Satterfield & Özel, 1977) considered the pressure drop, and found that the type of gas/liquid distributor used significantly impacts the observed pressure drop. Monoliths can be seen as an array of capillary channels, and if the feed is evenly distributed over the channels, a model based on a single channel can be used to describe the entire reactor. Inside the monolith, there is no convective transport from channel to channel, so scale effects inside monoliths are absent, and the entire problem of scale-up is reduced to finding a proper distributor. Finding such a distributor, and demonstrating that monoliths can be operated as scale-independent reactors, was one of the goals of this work.

The monolith reactors studied in this thesis are down-flow reactors. At the university of Alabama, the group of R. Cerro reported several attempts to use monoliths as up-flow reactors (Crynes *et al.*, 1995; Thulasidas *et al.*, 1995). In the feed section of upflow monoliths, the gas phase is typically the dispersed phase and the liquid is the continuous phase. It was shown by de Tezanos Pinto *et al.* (1997) that it is difficult to let bubbles enter a capillary. In fact, it has been shown that up-flow in monoliths is very unstable (Reinecke & Mewes, 1999).

Chapter II deals with pressure drop of Taylor flow. Although the straight channels in monoliths have an insignificant resistance to flow, detailed knowledge of the pressure drop allows the characterisation of important features of the flow pattern. The pressure drop is investigated both numerically and experimentally, and is presented first because it gives valuable insight into the hydrodynamics.

Chapter III is a numerical study of the liquid-to-solid mass transfer in capillary channels. Although the enhancement of this mass transfer step by addition of a gas phase in capillaries has been long understood, the numerical study provides essential quantitative information.

Chapter IV is about the residence time distribution in monolith columns. There are numerous investigations in the open literature of the residence time distribution in

single channel capillaries, revealing that the presence of bubbles significantly reduces backmixing in capillary channels. An investigation of the behavior of an array of capillary channels operated in downflow, however, is still missing. The experimental technique of RTD is used to determine the extent of maldistribution in monoliths, and is used to select a gas–liquid distributor that minimizes maldistribution, allowing the use of a single channel model for an entire monolith column.

Chapter V treats the mass transfer characteristics of a process that is limited by the transfer of gas from the bubble to the catalyst. This situation, which is of considerable practical relevance to the application of monoliths, is studied numerically for a single round capillary and the numerical results are used to formulate an engineering model for the mass transfer. Although this chapter builds in part on the results of chapter III, the results show that the mass transfer steps in a gas–component limited system cannot be directly related to liquid–component limited systems.

Chapter VI is concerned with scale effects. The results of the preceding four chapters are discussed, and the extent to which a single channel model may be used to describe a monolith reactor is discussed. Further, the monolith reactor is compared to other three-phase reactors, again based on the results of the preceding chapters, to demonstrate the areas where the transport phenomena of two–phase flow in capillaries offer significant advantages over other types of three–phase reactors.

Chapter VII offers a design study for the hydrogenation of 2,4-dinitrotoluene that clearly benefits from the advantages of using monoliths.

Chapter VIII finally offers some concluding remarks on the results and highlights several aspects that still need future research.

BIBLIOGRAPHY

- BERGLIN, C. T. & HERRMAN, W. 1984 A method in the production of hydrogen peroxide. *European Patent* 102 934 A2.
- VAN DEN BLEEK, C. M., COPPENS, M.-O. & SCHOUTEN, J. C. 2002 Application of chaos analysis to multiphase reactors. *Chemical Engineering Science* 57 (22–23), 4763–4778.
- BOS, C., HOOFD, L. & OOSTENDORP, T. 1996 Reconsidering the effect of local plasma convection in a classical model of oxygen transport in capillaries. *Microvascular Research* 51, 39–50.
- BRETHERTON, F. P. 1961 The motion of long bubbles in tubes. *Journal of Fluid Mechanics* 10, 166–188.
- CRYNES, L. L., CERRO, R. L. & ABRAHAM, M. A. 1995 Monolith froth reactor: Development of a novel three-phase catalytic system. *A.I.Ch.E. Journal* 41 (2), 337–345.
- CUI, Z. F., CHANG, S. & FANE, A. G. 2003 The use of gas bubbling to enhance membrane processes – a review. *Journal of Membrane Science* 221, 1–35.
- VAN EERD, J. P. F. M. & KREUTZER, E. K. J. 1987 *Klinische chemie voor analisten*, , vol. 2.

- Utrecht/Antwerpen: Bohn, Scheltema en Holkema.
- FAIRBROTHER, F. & STUBBES, A. E. 1935 The bubble-tube method of measurement. *Journal of the Chemical Society* 1, 527–529.
- FUKANO, T. & KARIYASAKI, A. 1993 Characteristics of gas-liquid two-phase flow in a capillary tube. *Nuclear Engineering and Design* 141, 59–68.
- VAN HASSELT, B. 1999 *The Three-Levels-Of-Porosity-Reactor*. Ph. D. Thesis, Delft University of Technology.
- LEBENS, P. J. M. 1999 *Development and design of a monolith reactor for gas-liquid countercurrent operation*. Ph. D. Thesis, Delft University of Technology.
- MACHADO, R. M., PARRILLO, D. J., BOEHME, R. P. & BROEKHUIS, R. R. 1999 Use of a monolith catalyst for the hydrogenation of dinitrotoluene to toluenediamine. *United States Patent* US 6005143.
- MOULIJN, J. A. & CYBULSKI, A., ed. 1998 *Structured catalysts and reactors*. Marcel Dekker.
- NIJHUIS, T. A., BEERS, A. E. W., VERGUST, T., HOEK, I., KAPTEIJN, F. & MOULIJN, J. A. 2001 Preparation of monolithic catalysts. *Catalysis Reviews—Science and Engineering* 43 (4), 345–380.
- REINECKE, N. & MEWES, D. 1999 Oscillatory transient two-phase flows in single channels with reference to monolithic catalyst supports. *International Journal of Multiphase Flow* 25 (6-7), 1373–1393.
- SATTERFIELD, C. N. & ÖZEL, F. 1977 Some characteristics of two-phase flow in monolithic catalyst structures. *Industrial and Engineering Chemistry Fundamentals* 16, 61–67.
- TAYLOR, G. I. 1960 Deposition of a viscous fluid on the wall of a tube. *Journal of Fluid Mechanics* 10, 161–165.
- DE TEZANOS PINTO, M., ABRAHAM, M. A. & CERRO, R. L. 1997 How do bubbles enter a capillary? *Chemical Engineering Science* 52 (11), 1685–1700.
- THULASIDAS, T. C., CERRO, R. L. & ABRAHAM, M. A. 1995 the monolith froth reactor: Residence time modelling and analysis. *Chemical Engineering Research and Design* 73, 314–319.
- TRIPLETT, K. A., GHIAASIAAN, S. M., ABDEL-KHALIK, S. I. & SADOWSKI, D. L. 1999 Gas-liquid two-phase flow in microchannels, part i: two-phase flow patterns. *International Journal of Multiphase Flow* 25, 377–394.
- VERGUNST, T., LINDERS, M., KAPTEIJN, F. & MOULIJN, J. 2001 Carbon-based monolithic structures. *Catalysis Reviews—Science and Engineering* 43 (3), 291–314.

CHAPTER II

PRESSURE DROP OF TAYLOR FLOW IN CAPILLARIES

§ II.1 INTRODUCTION

Pressure drop is an important parameter to consider in designing fixed-bed reactors. Apart from fluid properties, the most relevant parameters are the superficial velocities of the fluids flowing through the reactor, the size and shape of the solids that constitute the bed, and the void fraction, *i.e.* the fraction of the reactor volume that is not occupied by the packing and thus is available for the fluids to flow through.

The most common type of fixed bed reactor is a vessel that is randomly filled with solid particles. Here, the term random is used to indicate that no attempt is made to position the particles with respect to one another in a regular, predefined manner. For single phase flow in random packings, the pressure drop can be described by the Ergun equation (Ergun, 1952). The Ergun equation is based on the assumption that the irregular packing can be modelled as an array of tubes, where the tube diameter and wall thickness of those tubes are chosen such that they resemble the space between the particles and the particle size, respectively. In the Ergun approximation, the frictional pressure drop is the sum of a laminar contribution and a turbulent contribution. For the laminar contribution, the friction factor is inversely proportional to the Reynolds number and consequently vanishes for high Reynolds numbers. The friction factor in the turbulent contribution is independent of the Reynolds number, and is a constant that reflects the surface roughness of the particles. The fact that the actual path through the reactor is tortuous is taken into account by replacing the true proportionality constants for tubes by empirical values.

For two-phase flow in randomly packed reactors, an approach similar to that proposed by Lockhart & Martinelli (1949) is most frequently used. First, the pressure drop is calculated assuming either the gas or liquid alone is flowing. Subsequently, the pressure drop of the two-phase system is calculated from an empirical, usually nonlinear correlation based on the two single-phase results.

Thus, for randomly packed reactors the correlations for pressure drop are highly empirical. If the packing of the reactor is not random, but rather a well-defined solid structure of regular, repeating elements, the purely empirical correlations might be re-

placed by more accurate ones for a single such element, and a first principles description of the fluid mechanics in one element might be used to fully characterize the hydrodynamic behaviour of the reactor. Of course, the use of a single element to describe the entire reactor assumes perfect fluid distribution over all elements.

The monolith reactor packings described in this thesis are not random, and in this chapter the pressure drop of two-phase flow in capillary channels is described. As the channels in monoliths are of capillary dimensions, the flow inside monoliths is laminar, and we do not consider turbulent contributions. Here, the pressure drop in single capillary channels, rather than in a monolith block, is described. In a single channel, distribution effects over the monolith cross section are absent, which makes the experimental investigation of the fundamental features of the pressure drop feasible.

The characteristics of single phase pressure drop in channels are well known, and we might content ourselves by using a Lockhart-Martinelli approach for two-phase flow. Indeed, the original work of Lockhart & Martinelli was in part based on experimental data in capillaries. In channels, the Lockhart-Martinelli approach has the advantage of predicting the behaviour for a wide range of fluid superficial velocities. Most of the experimental data, however, is obtained in larger channels, in which interfacial forces are less dominant. As Lockhart-Martinelli correlations are empirical, extrapolation to small channels is not recommended. An alternative method for correlating two-phase pressure drop is a homogeneous model. In this approach, the two fluids are treated as a single phase with an apparent viscosity and density that is based on a given combination of the liquid and gas properties. Chen *et al.* (2002) collected 11 sets of literature data for two-phase pressure drop in small diameter tubes, and found that neither the standard Lockhart-Martinelli models, nor the standard homogeneous models accurately predicted the data. Based on the experimental datasets, a correction was proposed to the homogeneous model. This correction factor is purely based on regression and included 6 dimensionless parameters. The average difference between the experimental data and the fitted correlation was 19 %, and for the experimental data obtained in small capillaries the difference between the model and the measurements was even higher.

Both the homogeneous model and the Lockhart-Martinelli model use little information about the two-phase flow pattern. The advantage is that no specific knowledge of the flow pattern is required to predict the pressure drop, and the –related and obvious– disadvantage is that no information about the flow pattern can be obtained from experimental pressure drop data. In other words, such correlations are useful for design purposes if only the pressure drop is required, but their additional value is limited.

The objective in this chapter is to develop a pressure drop model that is based on quantifiable features of the flow pattern, so experimental pressure drop data can be used to characterize the flow pattern. This limits the approach to a single flow regime. In capillaries, liquid slugs form regardless of the liquid flow-rate, provided the velocities are low enough to ensure laminar flow and the feed ratio of gas and liquid is suffi-

ciently close to unity. Upon entering into the channel, bubbles with a diameter larger than that of channel are elongated and due to interfacial forces only a thin film of liquid between the channel wall and the bubble remains. The resulting flow pattern of elongated bubbles, separated by liquid slugs, is referred to as Taylor flow (after Taylor, 1960). Note that in the literature a number of alternative terms can be found, *e.g.* slug flow, plug flow, bubble flow, intermittent flow, bubble train flow and elongated bubble flow.

In Taylor flow, the information that is specific to the flow pattern is the amount of bubbles per unit length of channel, *i.e.* the bubble frequency. The average bubble and slug length may be obtained from the bubble frequency in a straightforward manner. In Taylor flow, the slugs are sealed between the bubbles, preventing coalescence. Indeed, the length of a slug formed at the entrance of the channel remains constant over the entire length of the channel. The same holds for the bubble length, and the two-phase Taylor flow pattern in a capillary is fully characterised and determined by the bubble frequency, the liquid superficial velocity and the gas superficial velocity. The objective can thus be reformulated as: the development of a pressure drop model for Taylor flow in capillaries that allows the bubble frequency to be determined from experimental pressure drop data.

The outline of this chapter is as follows. Firstly, fundamental insight into the fluid mechanics of a bubble pushed through a capillary is reviewed. The amount of literature on this subject is vast, but most of the theory is limited to conditions where inertial forces may be ignored and comparison of first principles theory to experimental pressure drop data is practically absent. Moreover, in Taylor flow interfacial forces are dominant, and trace impurities are known to cause significant deviations from theory based on pure liquids. Secondly, a numerical study is presented that provides insight into the frictional pressure drop characteristics of a bubble pushed through a capillary where inertial forces are taken into account. Thirdly, an experimental study of pressure drop in Taylor flow is presented that relates the pressure drop to the slug frequency.

§ II.2 HYDRODYNAMICS OF BUBBLES IN CAPILLARIES

The flow of a long bubble through a capillary is a classical problem in fluid mechanics. It is often referred to as Bretherton's problem, in reference to his classical paper (Bretherton, 1961). Historically, bubbles in capillaries were often used as tracer bubbles to determine the velocity of the liquid in the capillary. Fairbrother & Stubbes (1935) noted that a wetting film is left between the bubble and the wall. From a continuity argument, this means that the bubble travels faster than the surrounding liquid. This excess bubble velocity has to be corrected for if the bubble velocity is used to measure the liquid velocity. At low velocities inertial effects may be ignored, and by dimensional analysis one finds that the excess bubble velocity is determined by the ratio of viscous and interfacial stresses. For a liquid of viscosity μ moving through a

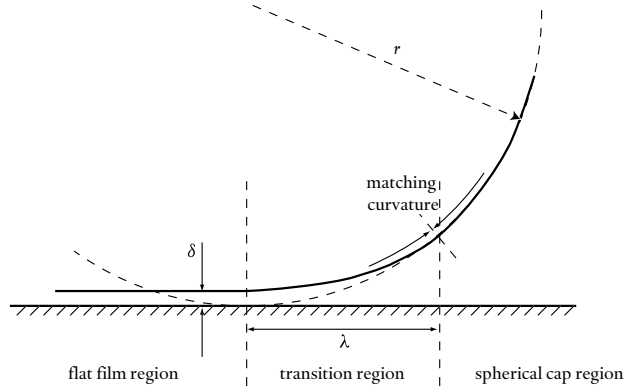


Figure 2.1: Schematic representation of the transition region between the flat film and the spherical front of the bubble (after Bretherton, 1961).

tube with a velocity u , this ratio is given by the Capillary number $Ca = \mu u / \gamma$, where γ is the surface tension. The data of Fairbrother & Stubbs showed that the thickness of the deposited film was proportional to $Ca^{1/2}$ for air bubbles displacing water with Capillary numbers of $7.5 \times 10^{-5} < Ca < 0.01$.

Bretherton (1961) pioneered the use of a lubrication analysis for the transitional region where the film is formed, *i.e.* between the spherical front of the bubble and the flat film far behind the front (Fig 2.1). The term ‘lubracting approximations’ comes from the description of ball bearings, in which metal to metal contact is prevented by means of an intervening layer of fluid. The approximations are that (1) the height of the fluid film is small compared to the length and (2) the pressure in the film is independent of the radial coordinate and (3) the axial gradients of velocity ($\partial u / \partial z$, $\partial^2 u / \partial z^2$) may be ignored with respect to the radial gradients ($\partial u / \partial r$, $\partial^2 u / \partial r^2$). Using these approximations, the Navier–Stokes equations reduce to the Reynolds equation (Reynolds, 1886).

The full analysis of Bretherton is lengthy, and here only a condensed scaling analysis from Aussilous & Quéré (2000) is given. The front of the bubble may be regarded as spherical with radius r , so the Laplace pressure difference across the gas–liquid interface is given by $\Delta p = 2\gamma / r$, provided the film thickness is small ($\delta \ll r$). In the region of constant film thickness, the curvature in the axial direction vanishes, and the Laplace pressure difference is given by $\Delta p = \gamma / r$. A balance of the viscous force and the pressure gradient in the transitional region yields

$$\frac{\mu u}{\delta^2} \sim \frac{1}{\lambda} \frac{\gamma}{r} \quad (2.1)$$

where λ is the length of the transitional region between the spherical and flat interface. The length λ is unknown, but we can estimate it by requiring that the Laplace pressure

is continuous at the interface or, in other words, that the curvature of the spherical part matches the curvature at the end of the transition region.

$$-\frac{\gamma}{r} - \frac{\gamma\delta}{\lambda^2} \sim -\frac{2\gamma}{r} \quad (2.2)$$

or $\lambda = \sqrt{\delta r}$, which yields upon substitution into Eq. 2.1 the now classical scaling rule $\delta/r \sim Ca^{2/3}$. In the limit of small Ca the film is thin compared to the channel radius, and the more rigorous analysis of the full Navier–Stokes equations in the transition region at the front and the back of the bubble by Bretherton results in $\delta/d = 0.66Ca^{2/3}$.

Bretherton measured the film thickness by monitoring the decrease in volume of a single liquid slug that propagated through an empty tube. As the slug deposited a film behind it, but no film is present in the empty tube in front of the slug, the film thickness could be calculated from the decrease in volume. Remarkably, the $Ca^{2/3}$ scaling law was confirmed for higher Capillary numbers using benzene and aniline as liquids, but for Ca lower than 10^{-3} , the film thickness was substantially larger than the theory predicted. Failure of the lubrication and matching method to predict the film thickness at low Ca raised doubt about the validity of the theory, as it was based on the assumption of low Ca . The method developed by Bretherton also gave an expression for the pressure drop over the bubble. In fact, the excess bubble velocity, film thickness and pressure drop are all related, and failure to predict the film thickness implies that the theory also does not predict the pressure drop accurately. Bretherton offered several possible explanations for the difference between theoretical and measured values, including surface roughness, interface instability and adsorbed impurities.

Nearly 30 years later, Ratulowski & Chang (1990) showed that the Marangoni effect of trace impurities is capable of explaining the discrepancy between the experimental data and Bretherton's theory. In regions of low surfactant concentration, the interface is mobile and a no–shear boundary is present at the gas–liquid interface. At regions of high surfactant concentration, the interface becomes rigid – Bretherton used the term "hardening of the surface" – and a no–slip boundary condition is more appropriate to describe the gas liquid interface. This effect is well known for bubbles in an open pool of water, where the drag increases dramatically with the presence of impurities, resulting in a significant reduction of the rise velocity. Bretherton had already shown that by using a no–slip boundary condition at the interface for a new lubrication analysis, both the pressure drop over the bubble and the film thickness increase by a factor $4^{2/3}$. This increase may be regarded as the upper limit for Marangoni effects, and indeed most of the experimental data is bounded by the upper and lower limit of surfactant effects. The true behavior of the interface is far more complex than the description using the limiting asymptote of surfactant effects. Surfactants are swept to the back of the bubble in the film regions and to the stagnation points in the end regions. The concentration of trace impurities is governed by the thermodynamic equilibrium of adsorption at the interface, the convection and diffusion of the trace impurities in the liquid and finally the gradient of surface tension with respect to the surfactant concen-

tration determines the extent of the effect of the impurities on flow behaviour. The full analysis of the problem by Ratulowski & Chang was able to describe the experimental data with reasonable assumptions for the values of thermodynamic equilibrium and the change of surface tension with concentration.

The theory of Bretherton has been confirmed by numerous numerical studies, in which, of course, ideal circumstances without impurities can easily be modelled. Shen & Udell (1985) used a finite element method to calculate the liquid velocity for a given interface. After convergence the position of the interface was updated iteratively. Only for the initial iterations, underrelaxation of the interface update was necessary to obtain a stable solution. In the limit of $Ca \rightarrow 0$, good agreement with Bretherton's lubrication approximation was found for both pressure drop and film thickness. A similar approach using finite difference discretization of the governing equations was used by Reinelt (1987), again confirming Bretherton's theory. Edvinsson & Irandoust (1996) used a *false transient* method in which the gas-liquid interface and the liquid velocity were calculated in each iteration. The grid surrounding the bubble was constructed using spines that allowed deformation of the grid. The usual translation of the coordinate system such that the bubble has zero axial velocity was dropped. This resulted in a net drift velocity of the bubble, from which the translational velocity of the coordinate system could be adjusted. With several repeats of this procedure the translational velocity was determined for up to four or five significant digits, and the transient simulation could run until the interface was stable. The finite-element simulations of Edvinsson & Irandoust confirmed the Bretherton analysis for low Ca . In the calculated bubble shapes, ripples were present at the back of the bubble. Ratulowski & Chang (1989) solved the lubrication equations without assuming a region of constant film thickness. The approach resulted in an expression for the wavelength of the interfacial ripples on the interface. For $Ca < 0.005$, the agreement between their analysis and the numerical results of Edvinsson & Irandoust is very good. The effect of inertia was first included by Edvinsson & Irandoust. They found that the rear spherical caps were flattened and the amplitude of the ripples increased as the Reynolds number increased. Also, the film thickness was reported to increase slightly with increasing inertial effects, although no attempt was made to quantify this effect. Giavedoni & Saita (1997, 1999) improved the numerical approach involving flexible grids by updating the velocity boundary conditions in each iteration to keep the bubble in place. A similar approach was used for the similar planar case by Heil (2001), who reported noticeable changes in film thickness and pressure drop when inertia was taken into account for Reynolds numbers up to 280. In most of the experimental studies reported in the literature, the Capillary number is varied by increasing the liquid viscosity, so the Reynolds number is always low. The only experimental data at high Reynolds numbers were recently reported by Aussilous & Qu ere (2000), who measured film thickness at high velocities using low viscosity liquids. A noticeable increase in film thickness was found and explained using a simple scaling analysis.

§ II.3 NUMERICAL APPROACH

The model problem studied in this work is a bubble moving in a round capillary of diameter d . The problem is considered to be two dimensional and axisymmetric. The gas-phase is not considered, *i.e.* the gas-phase has negligible viscosity and density, compared to the liquid phase, and the gas-side velocity field is not solved. We assume that the liquid flow is laminar. For single-phase flow in a tube, the transition to turbulence occurs around $Re = 2300$, and here we have limited the Reynolds number to 900. We assume the viscosity μ , density ρ and the surface tension γ are constant in the entire region.

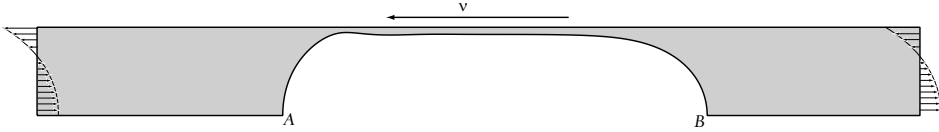


Figure 2.2: Schematic representation of the computational problem.

The region considered is a single bubble between two regions of liquid moving at an average velocity U , equal to the sum of the gas and liquid superficial velocity. Far away from the bubble, the liquid velocity is assumed to be developed into the parabolic Hagen–Poiseuille profile.

GOVERNING EQUATIONS

The equations of momentum conservation and continuity are given by

$$Re(u^* \cdot \nabla)u^* = -\nabla p^* + \nabla^2 u^* + BoCa^{-1}g^* \quad (2.3)$$

$$\nabla u^* = 0 \quad (2.4)$$

Eqs. 2.3 and 2.4 are already in their dimensionless form. Denoting dimensionless quantities by an asterisk, and using dimensionless coordinates $z^* = z/d$, $r^* = r/d$ and scaling the velocity with the average liquid velocity, $u^* = u/U$, the Reynolds number becomes $Re = (\rho U d / \mu)$, the Bond number becomes $Bo = \rho g d^2 / \gamma$ and the Capillary number becomes $Ca = \mu U / \gamma$. In Eq. 2.3, g^* is a unit vector in the direction of gravity. Finally, The pressure is scaled on the viscous scale, $p^* = p(\mu U / d)^{-1}$.

The effect of gravity in Bretherton’s problem is very limited. Hazel & Heil (2002) studied the impact of gravity on the film thickness and pressure drop and found only a small difference for $Bo = \pm 0.43$ (the sign of the Bond number indicates upflow or downflow). Edvinsson & Irandoust (1996) performed several calculations for $Re = 200$ and $-2 < Fr < 2$. The effect of gravity on the film thickness was significant for

$Ca > 0.01$. The dimensionless group $BoCa^{-1}$ can be rewritten as $ReFr^{-1}$. This indicates that even if inertia is taken into account, the effect of gravity becomes noticeable only if the Bond number is significantly larger than unity. In this study, the effect of gravity was not taken into account which limits the applicability of the results to absolute Bond numbers lower than unity.

The region is described in a reference frame in which the wall is moving at a constant velocity v . As mentioned in the introduction, the bubble moves faster than the average velocity of the liquid, so the translational velocity is part of the solution and cannot be specified beforehand. In this work, we closely follow the approach of Edvinsson & Irandoust (1996): from approximate initial guesses for the bubble shape and translational velocity, a transient simulation is carried out. During the simulation, the bubble starts to move and obtains an average axial velocity that is used to adjust the translational velocity of the reference frame.

The boundary conditions for the simulations are constant velocity at the wall

$$u_z^* = -v; \quad u_r^* = 0 \quad (2.5)$$

The parabolic Hagen–Poiseuille profile at the “inlet” and “outlet” becomes

$$u_z^* = 2 - 8r^{*2} - v; \quad u_r = 0 \quad (2.6)$$

Liquid volume conservation is automatically ensured by the fact that the parabolic profile is imposed on either side of the region.

Axial symmetry defines the velocity at the axis

$$\frac{\partial u_z^*}{\partial r^*} = 0; \quad u_r = 0 \quad (2.7)$$

For incompressible flow, we may choose a reference pressure anywhere in the region, and conveniently we set the pressure in the gas bubble to zero. The pressure at the liquid side of the gas interface then depends on the interface curvature by

$$p = \frac{2}{Ca} \kappa^* \quad (2.8)$$

in which $\kappa^* = \kappa/d$ is the local gaussian mean curvature of the interface. The angle of the interface with the axis was explicitly specified as $\pi/2$. Further, at the gas–liquid interface the gradient of the tangential velocity with respect to the normal of the interface is given by

$$\frac{\partial u_t}{\partial n} = \nabla \gamma \quad (2.9)$$

In the absence of surface tension gradients, the right hand side of Eq. 2.9 is zero and gives a no–shear boundary condition at the interface.



Figure 2.3: Example mesh. Top: initial mesh, bottom: converged mesh.

FINITE-ELEMENT FORMULATION

The commercial finite element package FIDAP was used to solve the fluid dynamics problem described above. The region of interest was meshed with two types of elements. Far away from the interface, fixed elements were used, while close to the interface the grid nodes were free to move along lines called spines. Fig 2.3 shows an initial mesh and the mesh of a converged case, to illustrate the mesh movement. A detail of the mesh in the flexible region is given in Fig. 2.4. Only nine-point quadratic elements were used. To obtain an estimate of the flow to start the transient calculation, the film thickness was estimated using Bretherton's law to generate a grid. The free surface was initially modelled as a no-shear boundary, and a steady state simulation provided the starting estimate of the flow field. This steady-state simulation typically converged in less than ten Newton-Rhaphson iterations. After the steady state simulation, the free surface boundary conditions were specified, and the flexible grid nodes were allowed to move. The system of equations, which now includes the position of the free surface nodes, was solved with the Newton-Rhaphson coupled solver, and a trapezoid implicit time integration was used until a reasonable estimate of the velocity could be made by averaging the velocity of the two nodes of the gas-liquid interface on the axis (located at A and B in Fig 2.2). The bubble velocity was subsequently subtracted from v , and the time integration was continued. In most simulations, 15 updates were used to achieve convergence. In the course of these simulations, the bubble displacement in laboratory coordinates was 5×10^3 channel diameters, and the residual dimensionless velocity of the bubble was less than 10^{-5} .

The simulation was started from the same initial estimate for Reynolds numbers up to 200. For higher Reynolds numbers, the simulations did not converge because the standard Galerkin finite element methods become unstable when the convective terms (characterised by the Reynolds number based on the characteristic element length) becomes more dominant. This can be overcome to some extent by using smaller elements, but this approach fails when the interface moves over a considerable distance. With decreasing element size, the spines also lie closer together, and mesh destruction becomes more likely (Fig. 2.4).

An alternative to a finer mesh is replacing the standard Galerkin scheme with a scheme that is more stable. Many different schemes are available and they all have in

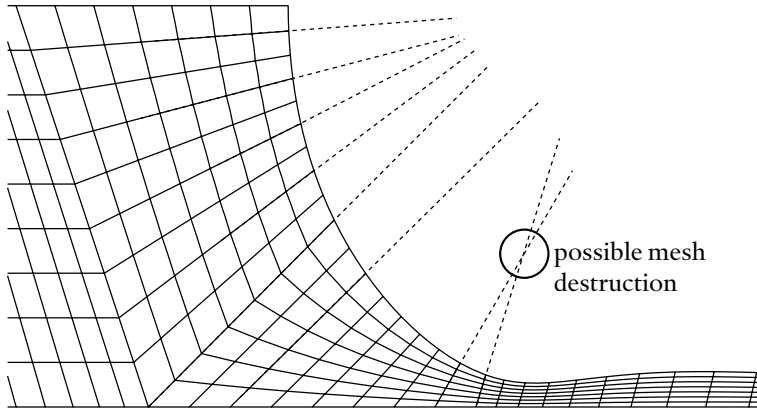


Figure 2.4: Detail of the mesh in the flexible region. The dotted lines indicate the spines, *i.e.* the allowed direction of node movement. The intersecting spines, marked by the circle, indicate possible mesh destruction if the interface movement is large.

common that they employ differing amounts of numerical diffusion. The diffusion has the effect of weighting the convection operators towards the upwind regions. *Upwinding* schemes can be broadly classified in two classes: low order and high order. First order schemes are first-order accurate, are unconditionally stable but introduce a high amount of numerical diffusion. Higher order schemes are at least second-order accurate, introduce less numerical diffusion, but are not as stable. In this work, a hybrid upwinding scheme was used that blends a first-order scheme with a higher-order scheme. The blending factor is computed dynamically in the course of the computations. For a given degree of freedom, the calculated blending factor is based on the local variations of that degree of freedom. Hybrid schemes have the advantage of only introducing high amounts of numerical diffusion in regions where it is necessary for stability. Of course, the extra computations make it more expensive computationally than non-hybrid schemes. For more details on the calculation of the blending factor, see FIDAP (1998)

For the simulations of $Re > 200$, the converged solution for $Re = 200$, *ceteris paribus*, was used as a starting estimate. As the initial estimate for these simulations was closer to the converged form of the bubble, fewer repeats of the bubble-velocity update were necessary.

§ II.4 NUMERICAL RESULTS

The majority of the calculations was performed using a grid with 3395 nodes, and several representative calculations were performed with a grid of 6255 nodes to check

PRESSURE DROP

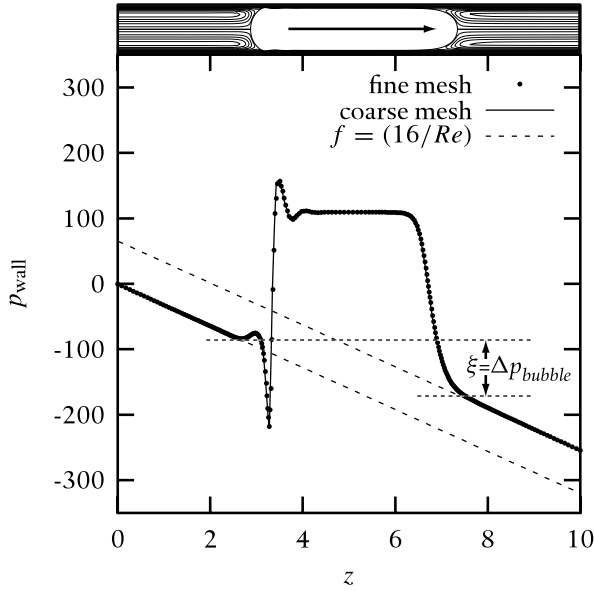


Figure 2.5: Wall pressure in the axial direction for $Ca=0.01$, $Re=100$, $\beta_L=0.65$, $L^*=10$. The markers are computed values using a grid of 6255 nodes, and the line represents the computed values on a grid of 3395 elements. The dotted line has $(\partial p^*/\partial z^*) = -32$, which corresponds to developed laminar flow in a tube. On top, the bubble shape and the liquid streamlines for this case are shown, and the direction of flow is indicated.

the gridsize dependence. As an example, Fig. 2.5 shows the pressure at the wall for both grids for a representative case. No significant change in the pressure at the wall is observed upon doubling the amount of elements. For the fine grid, the total pressure drop over the region was 1.3 percent higher than for the coarse grid.

For fully developed Hagen-Poiseuille flow of a single phase in a tube, the pressure drop is given by

$$\frac{\Delta p}{L} = \frac{16}{Re} \left(\frac{1}{2} \rho U^2 \right) \frac{4}{d} \quad \text{or} \quad \frac{\partial p^*}{\partial z^*} = -32 \quad (2.10)$$

Far away from the bubble, the pressure drop per length is constant and has a value that is consistent with Hagen–Poiseuille flow. In the region of constant film thickness, the shear of the gas is negligible, and Fig. 2.5 shows that the pressure at the wall is constant. The pressure drop over the entire bubble, however, is not zero, and the pressure difference over the frontal transition region is higher than the pressure drop over the rear transition region. The large oscillation at the rear of the bubble is caused by the presence of an inundation on the gas–liquid interface.

The total pressure drop over the entire computational domain can be decomposed into the frictional pressure drop of the liquid slug and the pressure drop over the bubble

$$\Delta p^* = -32L_{\text{slug}}^* + \Delta p_{\text{bubble}}^*(Re, Ca) \quad (2.11)$$

where $\Delta p_{\text{bubble}}^*$ describes the effects near the bubble, and is a function of Re and Ca . Note that in Eq. 2.11, the term $\Delta p_{\text{bubble}}^*$ now includes all the effects on the pressure of the bubble on the flow, including the effect of circulation in the slug and interfacial contributions. Because the frictional pressure drop is dominated by the slug region, we can model the effects of the bubble as part of the pressure drop in the slug to obtain

$$\Delta p^* = -32[1 + \xi(Re, Ca, L_{\text{slug}}^*)]L_{\text{slug}}^* \quad (2.12)$$

Now the function ξ describes how the pressure drop is affected by the presence of bubbles. The parameter L_{slug}^* now appears in the functional form of ξ , because with increasing slug length, the relative contribution of ξ to the overall friction in the slug decreases. In fact, for infinitely long slugs, the effects of bubbles vanish.

$$\lim_{L_{\text{slug}}^* \rightarrow \infty} \Delta p^* = -32L_{\text{slug}}^* \quad (2.13)$$

For a train of bubbles in a capillary, the dimensional pressure drop is then given by the pressure drop over the slugs alone

$$\frac{\Delta p}{L} = \beta_L f_{\text{slug}} \left(\frac{1}{2} \rho U^2 \right) \frac{4}{d} \quad (2.14)$$

where β_L , the dynamic hold-up of liquid in the channel, is the fraction of channel length occupied by the slugs. Here, the slug friction factor is given by

$$f_{\text{slug}} = \frac{16}{Re} \left[1 + \xi(Re, Ca, L_{\text{slug}}^*) \right] \quad (2.15)$$

In other words, an accurate model for pressure drop must include the bubble length—perhaps in the form of the bubble frequency—as a parameter. If the contribution of the end effects is significant, it also explains why Lockhart-Martinelli models or homogeneous models fail to predict the two-phase pressure drop accurately, even if interfacial effects are accounted for in a dimensionless correlation.

Experimentally, a wide range of slug lengths can be created in a given setup. The slug length is mainly determined by the geometry of the inlet of the channel, because once a volume of liquid is trapped between two bubbles, it cannot escape the slug it forms between the two sealing bubbles or either side. As a result, different slug lengths (or bubble frequencies) will be found in different set-ups, and this probably explains the spread in experimental data for capillary tubes in correlations based on homogeneous or two-phase multiplier (Lockhart-Martinelli) models.

The remainder of this chapter explores the function ξ , starting with the finite-element results.

PRESSURE DROP

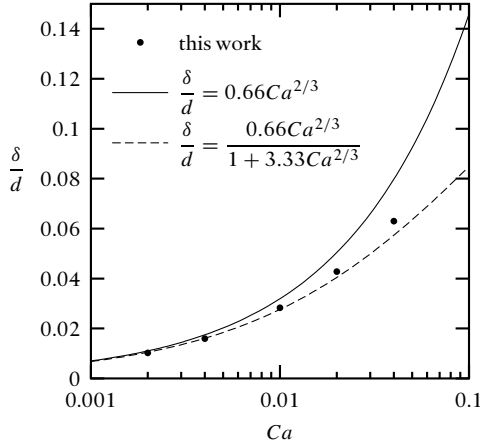


Figure 2.6: Film thickness at the middle of the bubble from simulations with $Re = 1$ (symbols). Bretherton's result is shown as a solid line, and the modified correlation from Aussilous & Quéré is plotted as a dashed line.

NEGLIGIBLE INERTIA

Most of the theoretical and experimental results reported in the open literature are obtained under conditions where inertia may be ignored ($Re < 10$). As a result only the numerical results for low Reynolds numbers can be compared to these experimental data and theory. Further, the classical Bretherton law for film thickness is only valid at low Ca . For higher Ca , the assumption that the film thickness is low compared to the channel radius is no longer valid. Aussilous & Quéré (2000) corrected the scaling analysis by replacing r by $r - \delta$ in Eqs. 2.1 and 2.2, which yields

$$\frac{\delta}{r} \sim \frac{Ca^{2/3}}{1 + Ca^{2/3}} \quad (2.16)$$

and used the experimental data of Taylor (1960) to find $\delta/d = 0.66Ca^{2/3}/(1 + 3.33Ca^{2/3})$. Note that the value of 0.66 is also obtained by Bretherton, so the equation reduces to Bretherton's law for low Ca . The factor 3.33 does not follow from the scaling analysis and is a purely empirical correction based on the experimental data. Fig. 2.6 shows the effect of the Capillary number on the film thickness at low Reynolds numbers. At low Ca , the agreement with Bretherton's results is good, while for $Ca > 0.01$, the film thickness is better described by the correlation proposed by Aussilous & Quéré. Bretherton's analysis also provided an expression for the pressure drop over a bubble by using a matching method for the rear transition region similar to the matching method for the front of the bubble.

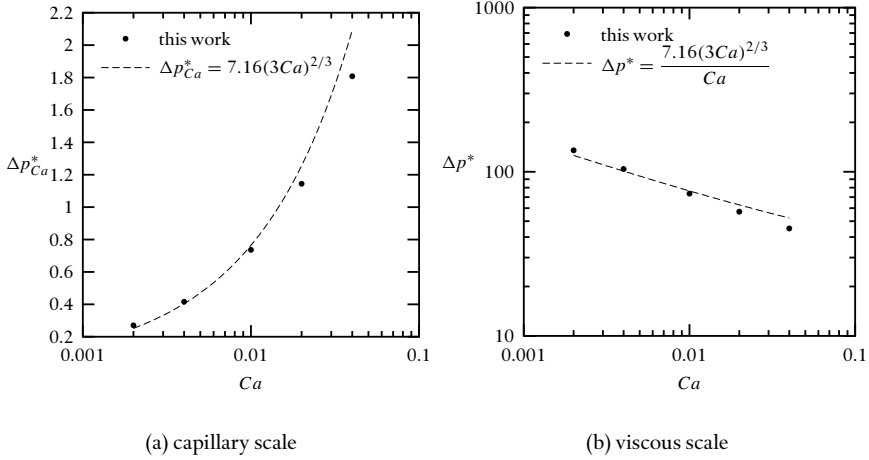


Figure 2.7: Pressure drop over the entire gas–liquid interface for simulations for $Re = 1$ (symbols). The theoretical result of Bretherton is plotted as a dashed line.

$$\Delta p = 7.16(3Ca)^{2/3} \left(\frac{\gamma}{d} \right) \quad (2.17)$$

The bubble pressure drop is plotted in Fig. 2.7(a) for $Re = 1$, and the agreement is good. Note that in Fig. 2.7(a), the pressure is dimensionalized on a capillary scale $p_{Ca}^* = p(\gamma/d)^{-1}$. At low Capillary numbers, the numerical result is slightly higher than the value predicted by Bretherton, which is best shown by plotting the bubble pressure drop on a viscous scale, see Fig. 2.7(b). As the capillary number increases, the effect of interfacial forces decreases with respect to viscous forces. As a result, the contribution of the interfacial forces to the pressure drop, *relative to the pressure drop in the slug* becomes smaller with increasing Ca .

Fig. 2.7(b) shows that the pressure drop over the bubble ranges from 130 at $Ca = 0.002$ to 50 at $Ca = 0.04$. Comparison with the Hagen–Poiseuille pressure drop of 32 per channel diameter reveals that the excess pressure drop is roughly equivalent to 3 or 4 channel diameters of developed flow. If the liquid slugs in Taylor flow are short, the presence of the bubbles has a measureable effect. For slugs that are five channel diameters long, the apparent friction factor is roughly fifty percent larger because of the bubbles. If the slugs are fifty channel diameters long, the apparent friction factor is increased only by five percent, and the bubble pressure drop can probably be ignored.

It should be noted that Bretherton based the Capillary number on the bubble velocity, while in our simulations, the Capillary number is based on the average liquid velocity. In Fig. 2.7(b), this difference was corrected for using the excess velocity. At high Ca , the correlation of Bretherton predicts a higher pressure drop than the simu-

PRESSURE DROP

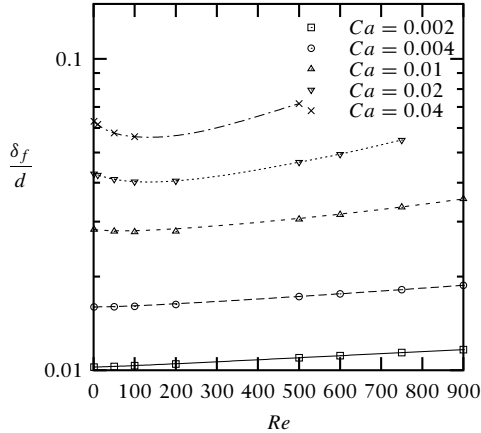


Figure 2.8: Film thickness at the middle of the bubble versus the Reynolds number for simulations at different Ca .

lations. Hazel & Heil (2002) found a similar deviation for the pressure drop over the nose of the bubble. Further, we do not expect agreement of the bubble pressure drop with Bretherton at high Ca , as the lubrication analysis is only valid for vanishing Ca .

EFFECT OF INERTIA

While the simulations for low Reynolds numbers could be compared to theory and empirical correlations based on literature data, this is not the case for conditions where inertia cannot be ignored. Fig. 2.8 shows the effect of inertia on the film thickness. The decrease in film thickness up to Reynolds numbers of about 100, followed by an increase for higher Reynolds numbers is in agreement with the numerical results of Giavedoni & Saita (1997, 1999) for low Re , the numerical results of Heil (2001) for the similar 2D planar case for Re up to 280 and the experimentally observed film thickening at high Re by Aussilous & Qu ere (2000). Aussilous & Qu ere included inertia in the scaling analysis, replacing Eq. 2.16 by

$$\frac{\delta}{r} \sim \frac{Ca^{2/3}}{1 + Ca^{2/3} - We} \quad (2.18)$$

thus accounting for the film thickening at high Reynolds numbers. The behaviour at low Reynolds numbers, however, has only been reported in the aforementioned numerical studies, and this effect has still not been explained.

Increasing the Reynolds number also changes the shape of the bubbles. Especially at higher Capillary numbers the interfacial forces are not high enough to maintain the hemispherical shape of the caps. With increasing Re , the nose of the bubble is elongated and the rear of the bubble is flatted, see Fig. 2.9.

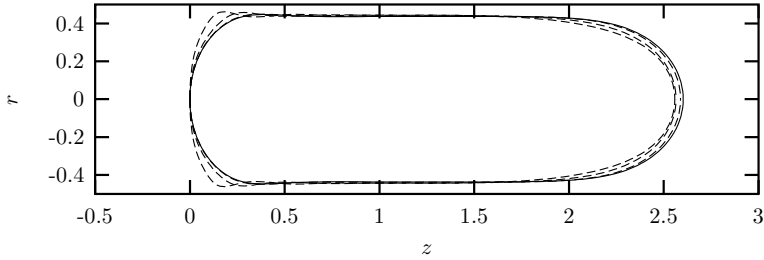


Figure 2.9: Shape of the gas–liquid interface for $Re = 1, 10, 100, 200$ at $Ca = 0.04$

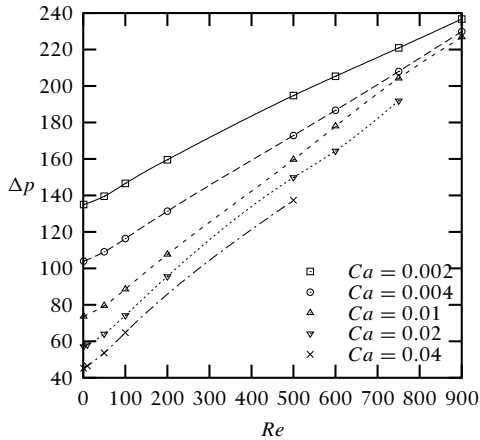


Figure 2.10: Pressure drop over the bubble versus Reynolds number for simulations at different Ca

Heil reported an increase in pressure drop in the transition region of the front of the bubble with increasing Re . In Fig. 2.10, the impact of inertia on the pressure drop over the bubble is plotted. Clearly, the pressure drop increases with increasing Reynolds number. The effect is slightly stronger for high Capillary numbers. At the bubble interface, the axial component of the velocity is zero in the moving reference frame, and develops into a parabolic profile far away from the bubble. This development of the flow pattern is similar to developing flow in a tube, and as a result, the pressure drop in the slug also increases due to the flow development.

In Fig. 2.11, the pressure drop over the entire region is plotted versus the Reynolds number. If we ignore the effect of the bubble and flow development on the flow in the slug ($\xi = 0$), the dimensionless pressure drop is estimated by a simple expression for Hagen–Poiseuille flow in the slug, *i.e.*, $\Delta p^* = 32L_{\text{slug}}^*$, where L_{slug}^* is the dimensionless length of the liquid slug. In Fig. 2.11, the deviation from this simple approximation

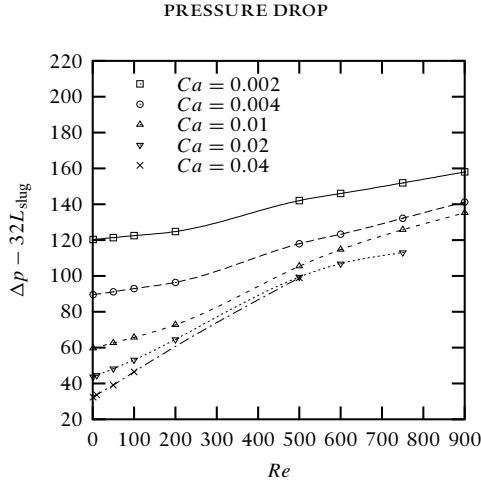


Figure 2.11: Pressure drop from the inlet to the outlet of the computational domain versus Reynolds number for several Ca . The contribution of fully developed flow in the slug has been subtracted, where the length of the slug is defined as the region without any gas in the cross section

is plotted. The same trend as for the bubble pressure drop is observed: (1) increasing the Capillary number decreases the pressure drop, (2) increasing the Reynolds number increases the pressure drop and (3) with increasing Ca , the effect of inertia increases.

The effect of inertia for the entire domain is smaller than for the bubble. At $Ca = 0.002$, the bubble pressure drop increases by 100 from $Re = 0$ to $Re = 900$, while the pressure drop over the entire domain only increases by 40. Thus, comparing Fig. 2.10 and Fig. 2.11, we observe that at low Reynolds number, the extra pressure drop caused by the bubble is almost equal to the difference in interfacial pressure from tip to tip. For high Reynolds numbers, the dramatic increase in pressure drop at the interface is not observed for the entire region.

Inertial effects are most important when flow changes direction. Fig. 2.12 shows the pressure distribution and streamlines at the rear of the bubble. At low Reynolds number, the interfacial pressure increases monotonically from the flat film to the tip of the bubble. Further, all the lines of constant pressure that originate at the bubble interface extend to the channel wall, which indicates that the entire interfacial pressure adds to the overall pressure drop. For higher Re , the centrifugal force of the recirculating liquid results in an increase in pressure near the tip of the bubble, where the streamlines are highly curved. In fact, a minimum in the interfacial pressure is observed, and only this pressure effect extends into the slug. The zone of high pressure close to the tip of the bubble does not extend to the channel wall, and as a result does not contribute to the overall pressure drop. This effect has been reported by Heil (2001) for 2D planar flow at the front of the bubble. In this work, the effect was found to be much more pronounced near the rear of the bubbles, which is consistent with the fact that at the rear,

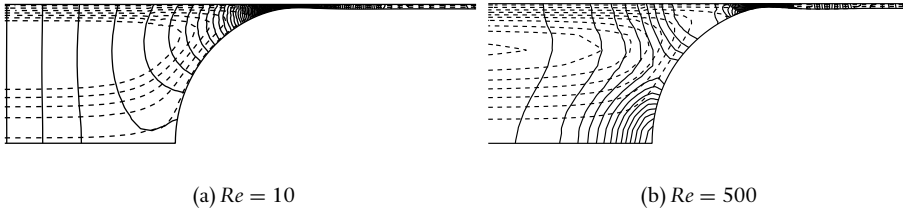


Figure 2.12: Contours of pressure (solid lines) and stream function (dashed lines) for $Ca = 0.004$.

the bubble shape is more deformed by inertial effects. Fig. 2.12 clearly shows that the pressure effect of inertia near the bubble tip is local, and this explains the lower effect of inertia on the pressure drop over the entire domain.

§ II.5 EXPERIMENTAL

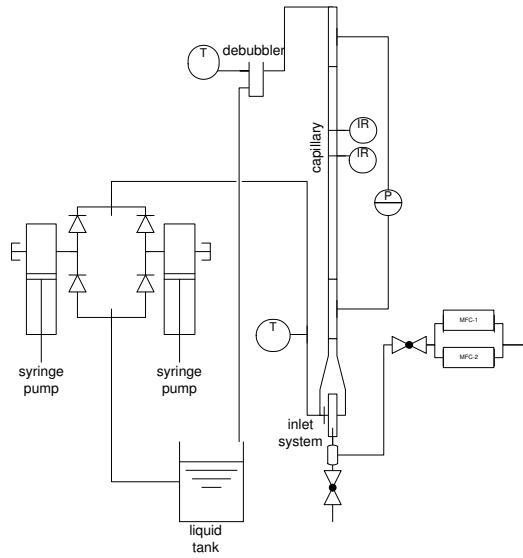
The numerical results reported here provide valuable insight into the pressure drop behavior of a Taylor bubble under conditions where inertia is relevant. However, numerical studies such as the one above fail to predict the film thickness that is found experimentally, probably due to the effects of surfactants. (note that the results above have been compared to other numerical studies). For pressure drop, no experimental data are available, even for the case of negligible inertia, and the rest of this chapter presents an experimental study of pressure drop in Taylor flow.

The vertical two-phase up-flow pressure drop was measured in a capillary of 2.3 mm internal diameter. The setup is depicted schematically in figure 2.13(a). A special inlet device, of which a cross section is drawn in figure 2.13(b), was used for feeding the gas and liquid into the capillary.

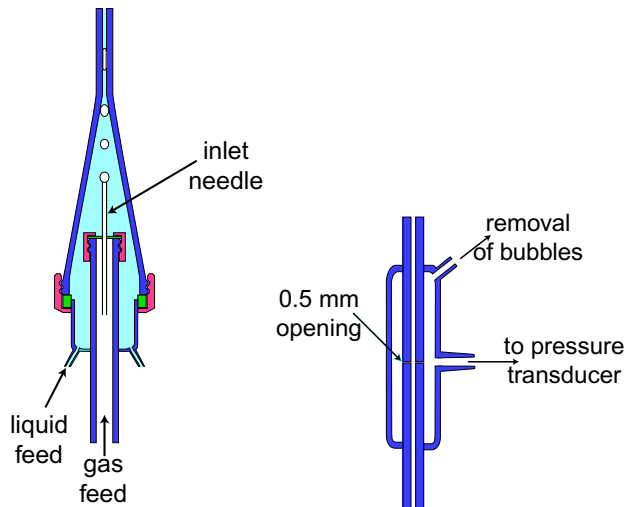
The liquid entered the system through two inlets at the bottom of the device. The internal diameter of the device was 35 mm at the bottom and slowly decreased over a length of 100 mm to the diameter of the capillary channel. The gas was injected through a flat tip hypodermic needle into the liquid approximately 50 mm below the inlet of capillary. By using different sized needles – three different ones were used in this study – the size of the bubbles leaving the needle could be adjusted. As the superficial velocity of the liquid is still very low at the tip of the needle, the impact of the liquid velocity on the size of the bubble was found to be moderate.

The liquid was continuously pumped through the channel by two ISCO 500D syringe pumps at 0-200 mL/min. A system of check valves allowed one pump to be refilled while the other was delivering liquid to the channel. The gas was delivered at 0-200 mL/min by two digital Brooks 5850S mass flow controllers. From the inlet up-

PRESSURE DROP



(a) overview



(b) inlet section

(c) pressure tap

Figure 2.13: The experimental setup.

wards, the channel consisted of a pressure tap segment, a segment of straight channel and a second pressure tap. Each segment had a tapered end on top that was polished such that it fitted seamlessly into the widening bottom of the next segment, so a perfectly aligned, seamless channel was formed. In the pressure tap elements, a slit of less than 0.5 mm connected the capillary to a larger chamber in which the pressure was measured via liquid filled lines using a Druck LPX 7000-XYZ differential pressure sensor, see Fig. 2.13(c). In the middle of the capillary channel, an infrared sensor was mounted that allowed the measurement of bubble and slug lengths and bubble velocity (for details, see Wolffenbuttel *et al.*, 2002). The infrared sensor has the benefit over conductivity methods of being able to efficiently detect liquids other than water.

The proper operation of the system was verified by doing liquid-only pressure drop measurements. The friction factor obtained from these experiments was within 5% of the Hagen-Poiseuille value of $16/Re$. It is well known that up-flow Taylor flow is unstable (Reinecke & Mewes, 1999). As a result, the compressible volume before the needle must be minimized. However, during startup of the system, liquid leaked through the needle causing an irregular gas flow into the needle. This dramatically broadened the spread in slug lengths, and could be resolved only by mounting a small liquid catcher just below the inlet system. As a result of installing this liquid catcher, the time required to achieve steady state flow was increased: it took up to 3 minutes before the pressure drop, bubble length and slug length were stable.

Once steady state was achieved, the bubble and slug lengths were measured for 30-60 seconds, and subsequently 100-200 recordings of pressure drop, temperature (inlet and outlet), gas velocity and liquid velocity were made. Experiments were performed using three different liquids: water, decane and tetradecane. The temperature difference between the inlet and the outlet was below 1 K for all experiments. The liquid properties were calculated from handbook correlations at the average temperature. The relevant physical properties of the liquids at 293 K are given in table 2.1. *Ceteris paribus*, the Capillary number in air/water, air/decane and air/tetradecane relate to each other as roughly 1:3:7, whereas the Reynolds numbers relate roughly as 1:0.8:0.3.

Table 2.1: Physical properties for the liquids used at 293 K.

liquid	ρ_L (kg/m ³)	μ_L (mPa · s)	γ (N/m)
water	996	1.01	0.073
decane	730	0.924	0.024
tetradecane	762	2.32	0.026

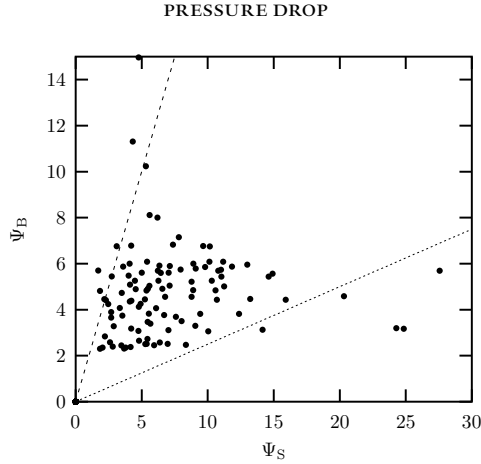


Figure 2.14: Experimental slug aspect ratio Ψ_S versus bubble aspect ratio Ψ_B .

§ II.6 RESULTS

BUBBLE AND SLUG LENGTHS

Using the inlet section described above, it was possible to vary the bubble and slug lengths over a wide range, see Fig. 2.14, where an overview of the experimental range is given. The smallest and largest needle created bubbles of approx. 5 and 15 mm in length inside the channel respectively, leading to aspect ratios Ψ_B of 2 to 7. If the liquid velocity was too low or too high, the bubbles started to coalesce before entering the channel. Roughly, stable slug and bubble sizes were found when $0.25 < u_{Ls}/u_{Gs} < 2$.

As mentioned in the introduction, the ratio of bubble to slug velocity is close to unity. As a result, the dynamic liquid hold-up β_L , based on the ratio of average slug length and bubble length, is expected to be close to the hold-up ϵ_L , based on the ratio of superficial velocities.

$$\beta_L = \frac{L_S}{L_S + L_B}, \quad \epsilon_L = \frac{u_{Ls}}{u_{Ls} + u_{Gs}} \quad (2.19)$$

In Fig. 2.15, β_L is plotted versus ϵ_L . The agreement is good, and we conclude that the experimental determination of the bubble and slug length is satisfactory.

BUBBLE VELOCITY

The measured bubble velocity u_B is plotted against the sum of gas and liquid superficial velocity, u_{TP} , in Fig. 2.16. The excess velocity of the bubbles is a function of the thickness of the liquid film. The calculations presented before showed that the film

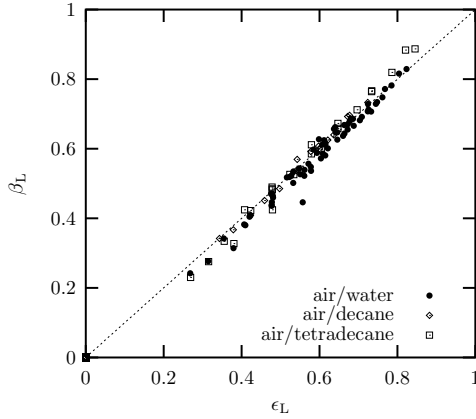


Figure 2.15: Comparison of hold-up based superficial velocities, ϵ_L , to hold-up based on bubble and slug length, β_L .

thickness is mainly determined by the Capillary number. For increasing Ca , the film thickness and the excess velocity increases.

The data show that the excess velocity indeed increased with velocity. Also, the excess velocity at the same velocities was lowest for water, and highest for tetradecane. The experimental data, however, do not agree with a correlation based on the Capillary number alone. However, the trend in the data show that indeed the excess velocity increases with increasing Capillary number Ca .

PRESSURE DROP

In Fig. 2.17, the friction factor, calculated from experiments by

$$f_{\text{obs}} = \frac{\left(\frac{\Delta p}{L}\right)_{\text{(tot)}} - \beta_L \rho g L}{\left(\frac{1}{2} \rho_L u_{\text{TP}}^2\right) \left(\frac{4}{d_c}\right) \beta_L} \quad (2.20)$$

multiplied with the Reynolds number is plotted versus the dimensionless slug length $\Psi_S = L_{\text{slug}}/d$. The experimental data clearly show that for each liquid, the friction factor is a function of slug length. Moreover, the results suggest that the slug length alone is sufficient to describe the experimental results for a given liquid, and no effect of the velocity is observed. This is surprising, because the numerical results suggest that Re and Ca have a strong impact on the slug friction factor, and both Ca and Re are linear functions of velocity. The experiments were conducted for a wide range of

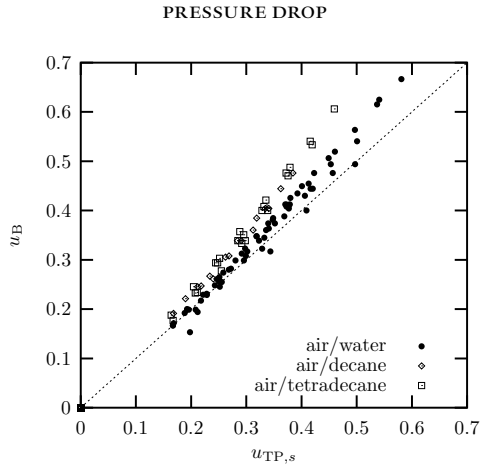


Figure 2.16: Comparison of bubble velocity u_B , measured using the infrared sensors, to the sum of gas and liquid superficial velocities, $u_{TP,s}$.

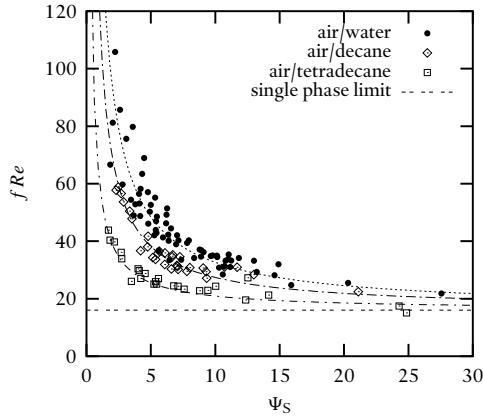


Figure 2.17: $(f Re)$ as a function of dimensionless slug length. channel diameter $d_c = 2.3$ mm

velocities, so the data for a given liquid were obtained for a wide range of both Ca and Re .

On the other hand, the observed dependence of pressure drop on the slug length is different for the different fluids. For water, which has the highest surface tension, the pressure drop is affected the most, while the data for the organic liquids show a less pronounced effect. Moreover, tetradecane, which is more viscous than decane, shows the smallest increase from the single phase limit $f = 16/Re$.

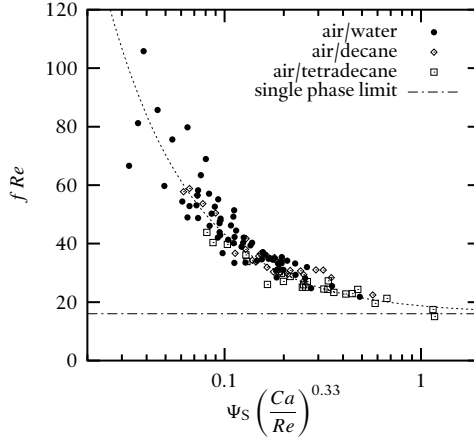


Figure 2.18: Final pressure drop correlation, $(f Re)$ as a function of the dimensionless group $\Psi_S(Ca/Re)^{0.33}$. channel diameter $d_c = 2.3$ mm

The fact that the friction factor is independent of velocity, but does vary with liquid properties can be modelled by using the ratio of the capillary number and the Reynolds number as a parameter. This dimensionless group, $Ca/Re = \mu^2/\rho d\gamma$, is independent of velocity. In other words, the excess pressure caused by the bubble ξ is likely to have the following functional form:

$$\xi = a \left(\frac{1}{\Psi_S} \left(\frac{Re}{Ca} \right)^b \right) \quad (2.21)$$

In Eq. 2.21, we have assumed that the pressure effects of the presence of bubbles are local at the slug ends. In other words, the slug is assumed to have a region of constant pressure drop far away from the bubbles, and the additional pressure drop caused by the bubbles can be included as an additional term that is inversely proportional to the slug length. Now, only the parameters a and b have to be determined by nonlinear regression, an expression was found that satisfactorily described all the data, see Fig. 2.18.

$$f = \frac{16}{Re} \left[1 + 0.17 \frac{1}{\Psi_S} \left(\frac{Re}{Ca} \right)^{0.33} \right] \quad (2.22)$$

From Bretherton's equation for the pressure drop, Eq. 2.17, we find that the dimensional pressure drop over a bubble scales with $\gamma^{0.33}$, as is the case for our correlation.

PRESSURE DROP

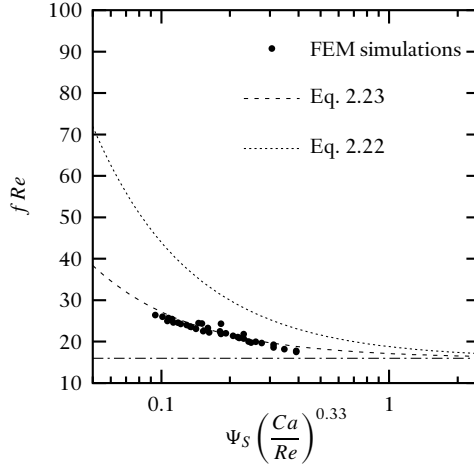


Figure 2.19: Numerical frictional pressure drop plotted using the same dimensionless groups as used for the experimental data. $100 < Re < 900$, $0.002 < Ca < 0.04$, $8 < L/d < 12$. The lines are based on Eq. 2.22 and on Eq. 2.23 with the proportionality constant changed to reflect the absence of impurities in the simulations.

§ II.7 DISCUSSION

The experimental results agree qualitatively with the numerical findings. On a viscous scale, the pressure drop increases with increasing Reynolds number and decreases with increasing Capillary number. The increase in pressure drop, however, is larger than found in the finite–element calculations. In Fig. 2.19, the same dimensionless plot as used for the experimental data is made for the numerical data. Apparently, the numerical data can be correlated using the same dimensionless group, which supports the experimental finding that the excess friction in the slug can be described by the parameter Ca/Re . A correlation that agrees with the numerical data can be constructed by replacing the constant 0.17 in Eq. 2.22 by 0.07, so there is a systematic difference of a factor of 2.5.

$$f = \frac{16}{Re} \left[1 + 0.07 \frac{1}{\Psi_S} \left(\frac{Re}{Ca} \right)^{0.33} \right] \quad (2.23)$$

This large difference cannot be attributed to experimental error. The liquid and gas feed rates were measured accurately and agree with the bubble velocity, which was measured independently. The liquid slug length was determined from the bubble velocity and the signal of the infrared probes. The measured values agree with visual observation. Further, the agreement of the dynamic holdup with the liquid feed fraction

also suggests that the slug length measurement is accurate. The accuracy of the pressure drop sensor was confirmed by single phase measurements. Also, for long slugs the deviation from single phase flow must vanish, and the experimental data indeed asymptotically approach $f = 16/Re$ as the slug length increases. Apart from the slug length and velocity, only the liquid properties are needed in Eq. 2.22. The liquid viscosity and density were not measured. The temperature of the liquid was measured both upstream and downstream of the channel, and the difference between the two was always within 1K. The average of these two temperature measurements was used to calculate the viscosity and density from handbook correlations.

The finite–element calculations were performed assuming clean liquids. More specifically, the right hand side of Eq. 2.9, $\nabla\gamma$, was set to zero, implying that the surface tension is constant in the entire region. Gradients in surface tension are caused by gradients in temperature or impurity concentration at the gas–liquid interface. In the experimental set–up, no attempt was made to work in ultra–pure conditions, and impurities were likely to be present. Possible sources for impurities are (1) the bulk liquids themselves, (2) lubricants in the gas feed (3) dissolved weakeners from the tubing. Moreover, after switching from organic liquids to water and vice versa, traces of liquid are likely to be left behind in the syringe pumps, even after rinsing several times.

Thus, since measurement error cannot account for the difference between the measured and calculated pressure drops, the likely cause of the difference are Marangoni effects. If the no–shear boundary condition at the gas–liquid interface is replaced by a no–slip boundary condition, Ratulowski & Chang (1990) showed that the Bretherton solution can be used with the transformation $Ca \rightarrow \frac{1}{4}Ca$. The pressure drop over the bubble in the lubrication analysis of Bretherton, Eq. 2.17, then transforms as $\Delta p \rightarrow 4^{2/3}\Delta p$. The factor $4^{2/3}$ is practically equal to the factor 2.5 which describes the difference between the experimental and numerical data. On the other hand, the analysis by Ratulowski & Chang did not include inertia, and the extension of the transformation to high Reynolds numbers should be applied with care.

If the entire gas–liquid interface is best described by a no–slip boundary condition, the pressure drop becomes dependent on the bubble length. In the experiments, the bubble length was varied independently of the slug length, see Fig 2.14, and no dependence on the bubble length was observed experimentally. Stebe & Barthes-Biesel (1995) reported several measurements in aqueous systems with elevated concentrations of the surfactant sodium dodecyl benzene sulphonate, where the pressure drop was indeed found to first increase with increasing bubble length, and later reach an asymptotic value significantly in excess of the clean surface theory. Park (1992) presented a model for the Marangoni effects on the front and the back of the bubble, which resulted in a critical bubble lengths below which the pressure drop over the bubble depends on the slug length.

In this study, surfactants were not added in high concentrations, and the Marangoni effects do not result in the bubble length dependence. This suggests that the surfactant concentration gradients are highest in the transition region, near the stagnation points

on the interface. Therefore, simply replacing the no-shear boundary condition by a no-slip boundary condition in the formulation of the fluid mechanical problem would not be sufficient to describe the moderate Marangoni effects for the conditions of the experiments reported here. Rather, the convection-diffusion equation for trace impurities should be included, combined with a function that describes the dependence of surface tension on surfactant concentration and a thermodynamic equilibrium model for surface adsorption. The extent to which such a numerical analysis would be useful depends on how accurately the additional parameters for the materials in the experiments are known.

The excess pressure drop is highest for water. As this system is most sensitive to Marangoni effects, it is also plausible to interpret the differences for the different liquids in Fig. 2.17 in terms of the difference in impact of Marangoni effects. However, this does not explain the difference between tetradecane and decane. Moreover, the numerical data suggest the same functional form for the excess pressure drop.

For application to monoliths, the experimental correlation is preferred because in a chemical reactor, ultra-pure liquids are not expected. The liquids used in this study, water and organic liquids without elevated concentrations of surfactants, are similar to those found in monolith applications. On the other hand, provided the liquids used in this single channel study are sufficiently close to those used in a monolith, pressure drop measurements can be used to obtain an estimate of the slug lengths found in monolith reactors.

§ II.8 CONCLUSIONS

In this chapter, the pressure drop of a train of bubbles in a capillary channels has been investigated. By using a finite-element description of a single bubble between liquid slugs, the problem was investigated numerically. The results for low Reynolds numbers agreed well with the classical lubrication analysis. Increasing the Reynolds number allowed the investigation of the behaviour of low viscosity liquids at high velocities. A significant increase in pressure drop was found as inertia becomes more important. Experimentally, the pressure drop was studied in a capillary using different liquids in a setup that allowed the independent variation of bubble and slug length.

An important observation is that apart from viscous, inertial and interfacial forces, the geometry of the bubble train flow has to be taken into account. More precisely, the aspect ratio of the slugs that separate the bubbles has a profound impact on the friction factor. This can be interpreted physically by realizing that in the middle of the slug, the flow profile across the channel resembles Hagen-Poiseuille flow, while at the ends of the slug, the flow pattern is significantly altered by the presence of the bubbles. Further, for each slug a Laplace pressure term must be included to account for the pressure drop caused by the bubble.

The influence of the slug length can easily be transformed into a dependence on the bubble frequency. Thus, more bubbles per unit channel length will result in a higher pressure drop. The theoretical foundations of the importance of the slug length – including quantitative estimates – were already laid out forty years ago. Most of the experimental data in the open literature, however, are still reported without bubble frequencies and the current engineering models do not take these effects into account. As a result, these engineering models fail to predict the pressure drop accurately in capillaries.

Although the numerical and experimental data show the same trends, the experimental data deviates systematically from the simulations. This deviation can be explained by Marangoni effects, that are not taken into account in the simulations, but are likely to be present in the experiments.

NOTATION

d	diameter, m
f	friction factor, –
g	gravitational constant, m/s^2
L	length, m
n	normal to the gas-liquid interface, –
p	pressure, Pa
r	radius, m
u ,	velocity, m/s
U	sum of gas and liquid superficial velocity, m/s

Greek letters

β	dynamic holdup, –
γ	surface tension, N/m
δ	film thickness, m
ϵ	holdup, –
κ	curvature, –
λ	length transition region, m
μ	viscosity, Pa s
ν	wall velocity, –
ρ	density, kg/m^3
ξ	excess pressure term, –

Dimensionless groups

Bo	Bond number ($=\rho g d^2/\gamma$), –
Ca	Capillary number ($=\mu u/\gamma$), –
Fr	Froude number ($=u^2/gd$), –

Re Reynolds number ($=\rho Ud/\mu$), –
 Ψ aspect ratio (L/d), –

Subscripts

B bubble
 c channel
 Ca capillary–scale
 G gas
 L liquid
 s superficial
 S slug
 t tangential
 TP two–phase

BIBLIOGRAPHY

- AUSSELOUS, P. & QUÉRE, D. 2000 Quick deposition of a fluid on the wall of a tube. *Physics of Fluids* 12 (10), 2367–2371.
- BREHERTON, F. P. 1961 The motion of long bubbles in tubes. *Journal of Fluid Mechanics* 10, 166–188.
- CHEN, I. Y., YANG, K.-S. & WANG, C.-C. 2002 An empirical correlation for two-phase frictional performance in small diameter tubes. *International Journal of Heat and Mass Transfer* 45 (17), 3667–3671.
- EDVINSSON, R. K. & IRANDOUST, S. 1996 Finite-element analysis of Taylor flow. *A.I.Ch.E. Journal* 42 (7), 1815–1823.
- ERGUN, S. 1952 Fluid flow through packed columns. *Chemical Engineering Progress* 48, 89sq.
- FAIRBROTHER, F. & STUBBES, A. E. 1935 The bubble-tube method of measurement. *Journal of the Chemical Society* 1, 527–529.
- FIDAP 1998 *FIDAP 8 Theory manual*. Fluent, Inc., Lebanon, USA.
- GIAVEDONI, M. D. & SAITA, F. A. 1997 The axisymmetric and plane case of a gas phase steadily displacing a Newtonian liquid – A simultaneous solution to the governing equations. *Physics of Fluids* 9 (8), 2420–2428.
- GIAVEDONI, M. D. & SAITA, F. A. 1999 The rear meniscus of a long bubble steadily displacing a Newtonian liquid in a capillary tube. *Physics of Fluids* 11 (4), 786–794.
- HAZEL, A. L. & HEIL, M. 2002 The steady propagation of a semi-infinite bubble into a tube of elliptical or rectangular cross–section. *Journal of Fluid Mechanics* 470, 91–114.
- HEIL, M. 2001 Finite Reynolds number effects in the Bretherton problem. *Physics of Fluids* 13 (9), 2517–2521.

- LOCKHART, R. W. & MARTINELLI, R. G. 1949 Proposed correlations for isothermal two-phase two-component flow in pipes. *Chemical Engineering Progress* 45 (1), 39–48.
- PARK, C. W. 1992 Influence of soluble surfactants on the motion of a finite bubble in a capillary tube. *Physics of Fluids A* 4 (11), 2335–2346.
- RATULOWSKI, J. & CHANG, H.-C. 1989 Transport of bubbles in capillaries. *Physics of Fluids A* 1 (10), 1642–1655.
- RATULOWSKI, J. & CHANG, H.-C. 1990 Marangoni effects of trace impurities on the motion of long gas bubbles in capillaries. *Journal of Fluid Mechanics* 210, 303–328.
- REINECKE, N. & MEWES, D. 1999 Oscillatory transient two-phase flows in single channels with reference to monolithic catalyst supports. *International Journal of Multiphase Flow* 25 (6-7), 1373–1393.
- REINELT, D. A. 1987 The rate at which a long bubble rises in a vertical tube. *Journal of Fluid Mechanics* 175, 557–565.
- REYNOLDS, O. 1886 On the theory of lubrication and its application to Mr. Beauchamp tower's experiments, including an experimental determination of the viscosity of olive oil. *Philosophical Transactions of the Royal Society of London* 177, 190 sqq.
- SHEN, E. I. & UDELL, K. S. 1985 A finite element study of low Reynolds number two-phase flow in cylindrical tubes. *Journal of Applied Mechanics* 52 (June 1985), 253–256.
- STEBE, K. J. & BARTHES-BIESEL, D. 1995 Marangoni effects of adsorption–desorption controlled surfactants on the leading end of an infinitely long bubble in a capillary. *Journal of Fluid Mechanics* 286, 25–48.
- TAYLOR, G. I. 1960 Deposition of a viscous fluid on the wall of a tube. *Journal of Fluid Mechanics* 10, 161–165.
- WOLFFENBUTTEL, B. M. A., NIJHUIS, T. A., STANKIEWICZ, A. & MOULIJN, J. A. 2002 Novel method for non-intrusive measurement of velocity and slug length in two- and three-phase slug flow in capillaries. *Measurement Science and Technology* 13 (10), 1540–1544.

CHAPTER III

LIQUID–SOLID TRANSPORT PHENOMENA

§ III.1 INTRODUCTION

In multi-phase chemical reactors, the transfer of matter and heat to or from the solid catalyst from the surrounding liquid is an important design parameter. The two main mechanisms for transport are molecular transport, or diffusion, and transport by flow in the liquid, or convection.

In agitated tank reactors, the catalyst particles move with the flow: relative to the particle the fluid may be regarded as stagnant, and the transport phenomena are dominated by diffusion. For a given composition of the liquid surrounding the catalyst, the diffusion coefficient is hardly a function of pressure or temperature, and the only way to enhance mass transfer is to increase the specific area of the catalyst by using small particles.

In packed-bed reactors, the catalyst is fixed with respect to the surroundings, and constant refreshment of the liquid near the catalyst by the flow in the reactor enhances the transport. Relevant parameters are the void fraction of the bed, the geometry of the catalyst used, and the flow rate of the fluids. The enhancement of transport of heat and matter by convection occurs at the expense of increasing pressure drop. Due to the random nature of the packing in most packed bed reactors, the pressure drop is relatively high, and reduction of particle size prohibits the enhancement of liquid-to-solid transfer.

This is a classical trade-off in chemical reactor engineering. Hydrodynamic behaviour and mass transfer are highly coupled. For turbulent systems, where exchange of matter, heat and momentum is dominated by convective exchange in the turbulent eddies, this coupling has been formalised as the Chilton-Colburn analogy (Colburn, 1933), which is well established for turbulent systems.

To overcome the coupling, the reactor must be operated in laminar flow to avoid the deadlock caused by turbulence. The geometry must be optimised to minimise pressure drop and maximise mass and heat transfer. The requirement of low pressure drop dictates that the path for the fluids be as straight as possible, hardly obstructing the flow.

Consequently, the monolith reactor is promising in this respect, as the small parallel channels fulfill both requirements.

One of the interesting features of Taylor flow is the enhancement of radial transfer of matter or heat in the slugs between the bubbles. In homogeneous laminar flow through a tube, the streamlines of the flow are parallel, and the only mechanism of radial transport is diffusion. In Taylor flow, circulation of the liquid in the slugs causes convective transport from the middle of the tube to the wall, increasing the radial transport.

The enhancement of liquid-to-wall transfer in Taylor flow has received considerable attention, and experimental data on liquid-to-wall transfer are abundant for a wide range of conditions. A dimensionless correlation is, however, still missing.

In this chapter, a numerical study of the liquid-to-wall transfer inside the liquid slug of Taylor flow is presented. The results are compared to literature data, and a simple engineering correlation, based on physically meaningful parameters is presented.

§ III.2 MODEL DEVELOPMENT

Heat and mass transfer coefficients can be calculated from the convection-diffusion equation in the domain of interest, provided the flow field and the boundary conditions are known. Analytical solutions for the flow field are often only available for very simple geometries or for limiting cases, *e.g.* Stokes flow or inviscid flow. As a result, analytical solutions for heat or mass transfer are even less abundant, and usually one has to resort to numerical methods to obtain the solution. For forced convection in ducts, a good overview of the available literature up to 1976 is available in Shah & London (1978). Mass and heat transfer are analogous, and the convection-diffusion equation has the same form. For heat transfer the equation is

$$\frac{\partial T}{\partial t} + (\mathbf{u} \cdot \nabla T) = \alpha \nabla^2 T \quad (3.1)$$

in which \mathbf{u} is the velocity vector, T is temperature and α is the thermal diffusivity. For mass transfer, the convection-diffusion equation has the form

$$\frac{\partial c}{\partial t} + (\mathbf{u} \cdot \nabla c) = D \nabla^2 c \quad (3.2)$$

in which D is the species diffusivity and c is the concentration. In the remainder of this chapter, we will discuss heat transfer, except when explicitly stated otherwise.

In this section, the single-phase case of forced convection in cylindrical tubes is first described in some detail, before the segmented gas-liquid flow in a tube is considered. In single-phase flow, a distinction is made between developing flow and developed flow. Laminar flow is considered as *hydrodynamically developed* if the velocity distribution is independent of the axial distance, and *thermally developed* if the dimensionless temperature distribution is independent of the axial distance. For a tube of

diameter d , the length required for development can be estimated by $(L/d) = 0.056Re$ for the flow field (Hornbeck, 1964), and $(L/d) = 0.03RePr$ for the temperature profile (Shah & London, 1978). For developed flow and a given constant wall temperature T_w , the Nusselt number is given by

$$Nu = \frac{hd}{k} = 3.658 \quad (3.3)$$

where h is the heat transfer coefficient and k is the thermal conductivity.

Close to the entrance of a tube, the flow field and temperature profile are developing. The relative rate of development of the velocity distribution and the temperature distribution depends on the Prandtl number Pr , which is defined as the ratio of momentum diffusivity to thermal diffusivity of the fluid. Likewise, the Schmidt number Sc is defined as the ratio of momentum diffusivity to mass diffusivity:

$$Pr = \mu c_p / k = \nu / \alpha \quad Sc = \mu / \rho D = \nu / D \quad (3.4)$$

Both dimensionless numbers are solely fluid properties. For liquids other than metals, both are larger than unity, indicating that for liquids, the mass and heat transfer entry lengths are longer than the hydrodynamical entrance lengths. In the thermally developing region, the Nusselt number is a function of axial distance. The problem of developing flow heat transfer in laminar flow was first investigated by Graetz (1883, 1885), and later independently by Nusselt (1910). For hydrodynamically developed flow and uniform temperature at $z = 0$, the local Nusselt number is given by

$$Nu_{\text{local}} = \frac{2}{9^{1/3} \Gamma(\frac{4}{3})} \left(\frac{z/d}{RePr} \right)^{-1/3} \quad (3.5)$$

The term local is used here to indicate that it is based on the heat flux, wall temperature and mixing–cup fluid temperature at a given cross section of the duct, *i.e.*

$$Nu_{\text{local}} = \frac{q'' d}{k(T_w - T_m)} \quad T_m = \frac{\int_A u T dA}{\int_A u dA} \quad (3.6)$$

where T_m is the cup–mixing temperature in the cross-section A of the duct. Frequently, the inlet and outlet temperature is measured instead of the local heat flux, and the mean (flow length averaged) Nusselt number can be calculated from the logarithmic mean temperature difference $(\Delta T)_{\text{lm}}$

$$Nu_{\text{mean}} = \frac{q''_{\text{mean}} d}{k(\Delta T)_{\text{lm}}} = \frac{1}{L} \int_0^L Nu_{\text{local}} dz \quad (3.7)$$

From integrating Eq. 3.5 one obtains the mean Nusselt number

$$Nu = \frac{3}{9^{1/3} \Gamma(\frac{4}{3})} \left(\frac{L/d}{RePr} \right)^{-1/3} \approx 1.615 \left(\frac{L/d}{RePr} \right)^{-1/3} \quad (3.8)$$

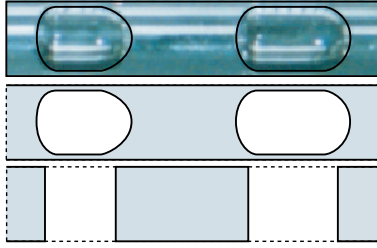


Figure 3.1: Simplification of the geometry studied

Eq. 3.8 has been obtained by various analytical and numerical methods, and has been validated by numerous experiments (for an overview, see the monograph by Shah & London, 1978). The dimensionless group $(L/dRePr)$ is called the Graetz number Gz . Note that in the open literature, the dimensionless groups $(L/dRePr)$, $c(L/dRePr)$, $(dRePr/L)$, and $c(dRePr/L)$, where c is an arbitrary constant, are all designated as the Graetz number. The criterion for the thermal entrance region may be written as $Gz = 0.03$, where $Nu = 3.40$. So, Eq. 3.8 is valid for small Gz only. The Nusselt number increases with decreasing Gz , and in the entrance region, the heat transfer is significantly higher than the asymptotic limit for the developed temperature profile. Also note that Eq. 3.8 is valid for thermal development only, which corresponds to single-phase heat transfer in heated section after a so-called calming section in which the velocity profile is allowed to develop.

Now consider the segmented flow of liquid and gas in a capillary channel. The geometry of a unit cell, *i.e.* a bubble and a slug, is complex and the shape of the bubbles and the thickness of the lubricating film between the bubble and the wall depend on the liquid and gas properties and the velocity of the unit cell. The principal features of the flow can, however, be studied by ignoring the thin film, and simplifying the gas-liquid interface to flat ends, see Fig. 3.1.

The resulting geometry is a cylinder, moving through the channel with a velocity equal to that of the bubbles. A reference frame moving with the slug is obtained by fixing the cylinder in space and moving the the wall of the cylinder with a uniform velocity u_{wall} , equal in magnitude to the slug velocity, but in opposite direction. The slug is confined by the two ends and the cylinder wall, and circulates. Duda & Vrentas (1971*b*) found a infinite-series analytical solution for closed-streamline axisymmetric flow in this cylinder in the limit of vanishing Reynolds number, *i.e.* so-called Stokes flow. Analytical solutions were obtained for both no-slip and no-drag boundary conditions at the ends of the cylinder. The former applies to solid spheres separating the slugs, while the latter corresponds to gas separating the slugs. Note that the applicability of the no-shear boundary condition is subject to the assumption of negligible Marangoni effects, see chapter II of this thesis. In a second paper (Duda & Vrentas, 1971*a*), the corresponding transient heat transfer problem was solved for the first case (no-slip at

the ends) using a formal Fourier series technique. The transient solution may be interpreted as the time–dependent behaviour of a slug as it flows at a constant velocity through the tube, *i.e.* the time may be regarded as the the length of the channel that the slug has travelled through. The method allowed the calculation of time dependent Nusselt numbers up to $(L/d) = 2.5$ for Peclet numbers ($Pe = u_{\text{wall}}d/\alpha$) of up to 400. Extension to higher (L/d) was prohibited as the eigenvalues of the solution were too close together as the aspect ratio was increased. For a developed temperature profile, they reported that the Nusselt number was approximately 2.5 times higher than the analogous single–phase developed value.

§ III.3 FORMULATION

Consider the closed-streamline laminar, developed flow in a cylinder of aspect ratio (L/d) , where the wall of the cylinder is moving at a uniform constant velocity. The motion of the fluid in the liquid is governed by the steady–state continuity equation

$$\nabla \cdot \rho \mathbf{u} = 0 \quad (3.9)$$

and the steady–state incompressible momentum balance (Navier–Stokes equation)

$$\rho(\mathbf{u} \cdot \nabla)\mathbf{u} = -\nabla p + \mu \nabla^2 \mathbf{u} + \rho g \quad (3.10)$$

The transient temperature distribution is calculated from Eq. 3.1, into which the steady state flow profile \mathbf{u} is substituted. In the absence of gravitational effects, one may assume that the flow is axisymmetrical, and only the 2–D case has to be solved in the region between the axis and the wall. Dimensionless equations can be introduced by choosing as references the tube radius R , the wall velocity u_{wall} , the initial temperature T_0 and the wall temperature T_{wall} :

$$t^* = \frac{tu_{\text{wall}}}{R} \quad p^* = \frac{p}{\rho u_{\text{wall}}^2} \quad U = \frac{u}{u_{\text{wall}}} \quad T^* = \frac{T - T_0}{T_{\text{wall}} - T_0} \quad (3.11\text{a–d})$$

$$Re = \frac{\rho u_{\text{wall}} R}{\mu} \quad Pe = \frac{\rho c_p u_{\text{wall}} R}{k} \quad (3.12\text{a–b})$$

in which * denotes a dimensionless quantity. The resulting dimensionless equations are:

$$\nabla U = 0 \quad (3.13)$$

$$(U \cdot \nabla)U = -\nabla p^* + \frac{1}{Re} \nabla^2 U \quad (3.14)$$

$$\frac{\partial T^*}{\partial t^*} + (U \cdot \nabla T^*) = \frac{1}{Pe} \nabla^2 T^* \quad (3.15)$$

The boundary conditions are no-slip at the wall, axial symmetry at the axis and no-drag at the ends.

$$U_z = 1, \quad U_r = 0, \quad \text{at the wall} \quad (3.16)$$

$$\frac{\partial U_z}{\partial r} = 0, \quad U_r = 0, \quad \text{at the axis} \quad (3.17)$$

$$\frac{\partial U_r}{\partial z} = 0, \quad \text{at the ends} \quad (3.18)$$

Initially, all the fluid inside the cavity has a uniform temperature $T^* = 0$, and for $t > 0$, the moving cylinder wall has a fixed temperature $T^* = 1$, and the evolution of the amount of heat transferred through the wall is monitored in time.

$$T = 0, \quad \text{in the fluid, } t = 0 \quad (3.19)$$

$$T = 1, \quad \text{at the wall, } t > 0 \quad (3.20)$$

$$\frac{\partial T}{\partial r} = 0, \quad \text{at the axis, } t > 0 \quad (3.21)$$

$$\frac{\partial T}{\partial z} = 0, \quad \text{at the ends, } t > 0 \quad (3.22)$$

§ III.4 RESULTS

The analytical solution presented by Duda & Vrentas (1971*a*) shows that the Nusselt number in the cylindrical cavity has the following dependencies:

$$Nu = Nu(t^*, \Psi, Pr, Re) \quad (3.23)$$

in which Ψ represents the aspect ratio (L/d) of the cylinder. For liquids, the Prandtl number Pr is larger than unity, e.g. 1-10 for water and 5-50 for light organic liquids. For the analogous mass transfer case, the Prandtl number is replaced by the Schmidt number Sc , which for liquids is typically larger than 300. For a capillary tube with a diameter of 1 mm, the slug velocities of interest are between 0.01 and 0.5 m/s. For water, this implies that the Reynolds number lies between 10 and 500. The relevant range of aspect ratio Ψ is harder to predict a priori, but for the application to monolith slug flow, the upper limit may be estimated as $\Psi = 10$ (see chapter VI for experiment slug aspect ratios in monoliths). The lower limit is considered to be 0.5. For a similar case of heat transfer in a cylindrical cavity, Duda & Vrentas (1971*a*) reported that the heat transfer was dominated by convection for Peclet numbers larger than 400. As this chapter focusses on the mass transfer behaviour of segmented gas-liquid flow, the criterion $Pe = ReSc > 400$ will always be met, and Eq. 3.23 may be replaced by

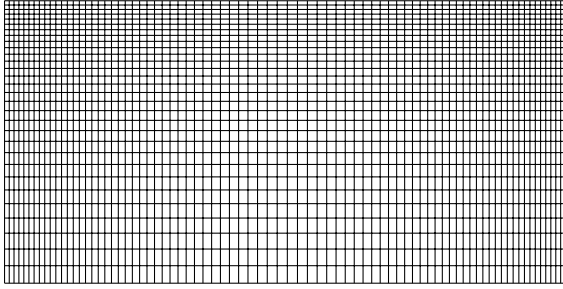


Figure 3.2: A 30×80 example of a grid as used in the calculations. The upper boundary is the moving wall, the lower boundary is the channel axis. The left and right boundaries are the flat ends of the cylinder. The length to diameter ratio is unity here.

$$Nu = Nu(t^*, \Psi, Pe) \quad (3.24)$$

FLOW

The axisymmetric steady–state flow problem (Eqs. 3.9–3.18) and the transient heat transfer problem (Eqs. 3.1, 3.19–3.22) were solved in rectangular grids of different aspect ratios with the finite element computational fluid dynamics solver FIDAP.

An example of the grid used in the calculations is shown in Fig. 3.2. The grid is refined near the ends and near the wall, as the expected temperature gradients are highest at the wall. The initial value for the flow problem was zero velocity in the entire domain, and from the initial values, the solution was iterated until the convergence criteria for the continuity and momentum equations were met. The limiting criterion for convergence was the residual of the continuity equation, which was reduced by 7 orders of magnitude until the solution was considered complete. In Fig. 3.3 the streamlines are plotted for $\Psi = 1$ and $\Psi = 2$ at $Re = 100$. In the limit of very low Reynolds number, the Navier–Stokes equations may be modified to yield the slow form of the vorticity diffusion equation, and introduction of the stream function ψ

$$u_r = -\frac{1}{r} \frac{\partial \psi}{\partial r} \quad u_z = \frac{1}{r} \frac{\partial \psi}{\partial z} \quad (3.25)$$

leads to a fourth order differential equation for the scalar stream function. For the cylindrical cavity discussed here, Duda & Vrentas (1971*b*) found an infinite series solution of the stream function in cylindrical cavity flow for several boundary conditions. For no–drag at the ends, the stream function is given by

$$c_m = \frac{\Psi [1 - (-1)^m]}{m\pi} \quad (3.26)$$

$$a_m = \frac{I_0\left(\frac{m\pi}{\Psi}\right) I_2\left(\frac{m\pi}{\Psi}\right) - I_1^2\left(\frac{m\pi}{\Psi}\right)}{I_2^2\left(\frac{m\pi}{\Psi}\right)} \quad (3.27)$$

$$F_m(r) = \frac{r I_1\left(\frac{m\pi r}{\Psi}\right) I_2\left(\frac{m\pi}{\Psi}\right) - r^2 I_1\left(\frac{m\pi}{\Psi}\right) I_2\left(\frac{m\pi r}{\Psi}\right)}{I_2^2\left(\frac{m\pi}{\Psi}\right)} \quad (3.28)$$

$$\psi(r, z) = \sum_{m=1}^{\infty} \frac{c_m}{a_m} F_m(r) \sin\left(\frac{m\pi z}{\Psi}\right) \quad (3.29)$$

In Fig. 3.4, the analytical solution is plotted with the numerical solution. The numerical solution for $Re = 8$ practically overlaps with the analytical Stokes–flow solution. At $Re = 128$, only a small deviation is caused by inertial effects. Fig 3.3 (b) illustrates that for longer cylinders with an aspect ratio larger than unity, the streamlines are nearly parallel at a distance of more than $0.5 d$ from the ends. In this region of parallel streamlines the velocity profile equals the parabolic Hagen–Pouseuille profile, corrected for the translation of the reference frame. For Hagen–Pouseuille flow, the distance from the axis where the velocity equals the average velocity is $r/r_{\text{tube}} = 1/\sqrt{2} \approx 0.707$. In the moving reference frame, this distance corresponds to zero axial velocity. For the streamlines depicted in Fig. 3.3 (b), the vortex centre is located at $r/r_{\text{tube}} \approx 0.709$, in good agreement with the theoretical Hagen–Pouseuille value. Due to the no-drag boundary conditions at the ends of the cylinder, no secondary vortices were found, and all the principal features of the flow are illustrated by Fig. 3.3.

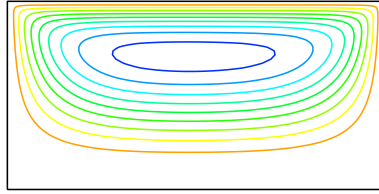
HEAT-TRANSFER

The solution of the velocity field was incorporated in the transient thermal convection–diffusion equation to determine the heat transfer characteristics. During the transient simulation, the volume–averaged mean temperature T_{mean}^* in the slug was monitored. When the simulation has proceeded to time t^* , the distance travelled by the slug in the tube is given by $t^* = L_{\text{tube}}/r$, and we can define a Graetz number by

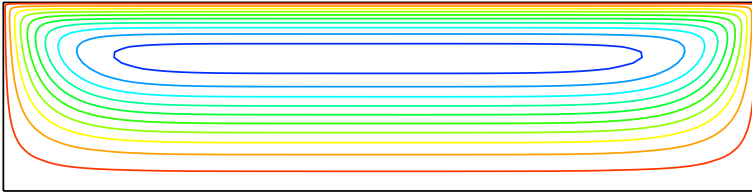
$$Gz = \frac{t^*}{Pe} = \frac{L_{\text{tube}}/r}{RePr} \quad (3.30)$$

The length averaged Nusselt number is given by

$$\frac{Nu}{2} = Nu_R = \frac{Pe}{t^*} \ln[1 - T_{\text{mean}}^*] \quad (3.31)$$

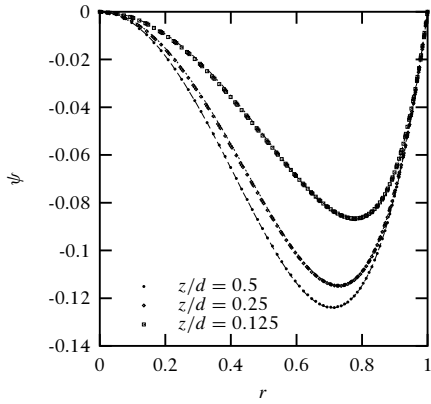


(a)

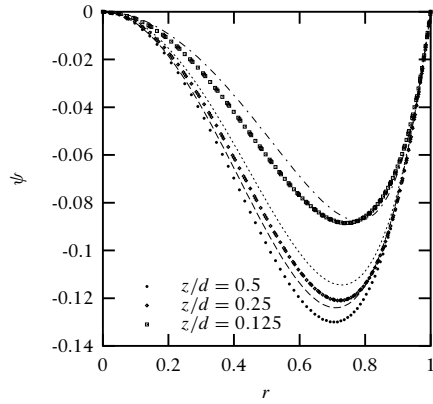


(b)

Figure 3.3: Lines of constant stream function. (a) $(L/d) = 1, Re = 8$, (b) $(L/d) = 2, Re = 8$



(a) $Re = 8$



(b) $Re = 128$

Figure 3.4: Comparison of the numerical solution (markers) with the analytical solution of Duda & Vrentas (1971b) (lines). Stream function at three cross sections of the cavity for $(L/d) = 1$.

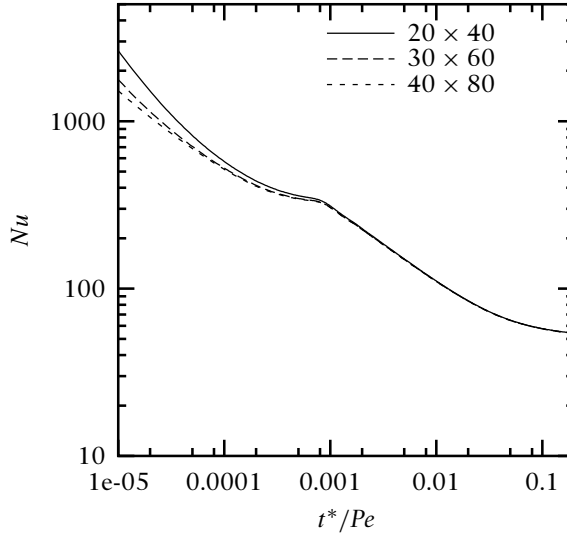


Figure 3.5: Development of the Nusselt number during the transient heat-transfer calculation. Various grid sizes, $(L/d) = 1$, $Re = 8$, $Pr = 1024$

in which Nu_R is the Nusselt number, based on tube radius, rather than tube diameter.

The local Nusselt number is calculated by:

$$\frac{Nu_{loc}}{2} = \frac{Pe}{1 - T^*} \frac{\partial T^*(1)}{\partial r} \quad (3.32)$$

In Fig. 3.5, the Nusselt number is plotted versus the Graetz number for $Pe = 8192$ for three grid sizes. The Nusselt number drops monotonously with increasing Graetz number, as is the case for single phase flow. At very early times, the Nusselt number drops rapidly. Here the circulating liquid that comes in contact with the moving wall still has the initial temperature. The heat penetrates only the first element in the computational grid, and as a result the solution depends very much on the size of these elements. The temperature profile for the very early times is given in Fig. 3.6a–b.

For times $2 < t^* < 8$, the decline is less rapid. This is caused by the fact that in this range, the first full circulation of the fluid is completed, and the average temperature of

Table 3.1: Grid dependence of the Nusselt number for $\Psi = 1$, $Re = 8$, $Pr = 1024$.

Grid	Δ_0	$t^*/Pe = 0.001$	$t^*/Pe = 0.01$	$t^*/Pe = 0.1$	$t^*/Pe = 0.2$
20×40	0.03301	311.58	111.03	57.68	54.14
30×60	0.01734	305.84	110.44	57.52	53.98
40×80	0.01012	305.02	110.36	57.50	53.98

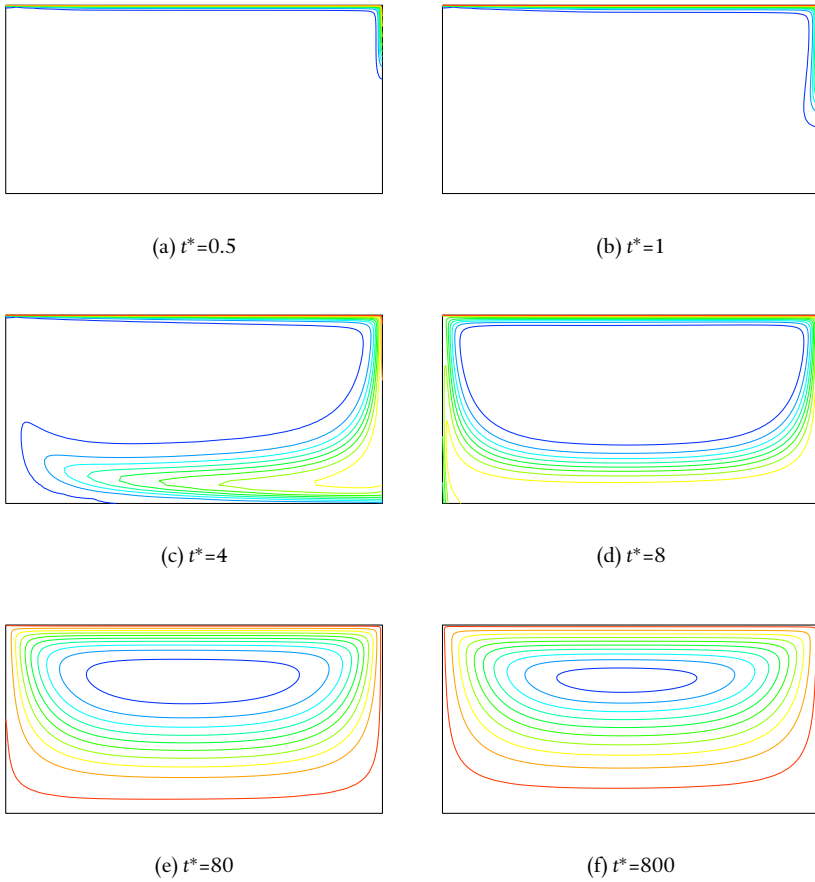


Figure 3.6: Development of the temperature profile, $(L/d) = 1$, $Re = 8$, $Pr = 1024$

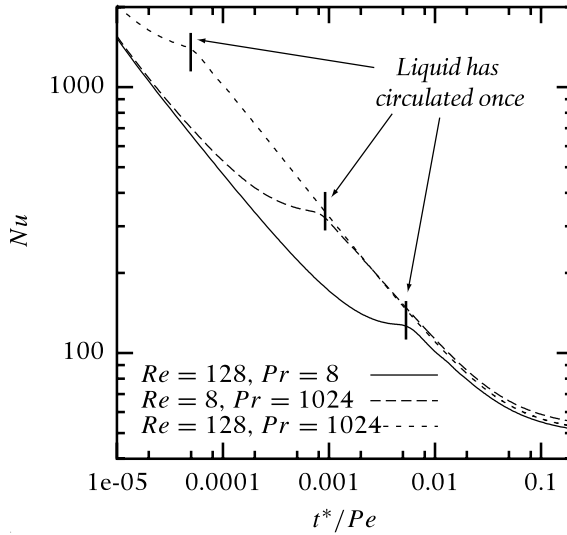


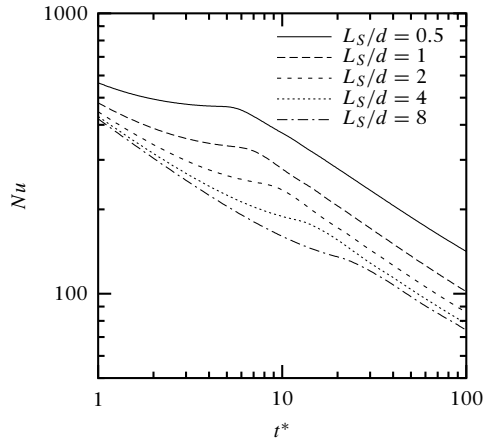
Figure 3.7: Development of the Nusselt number during the transient heat-transfer calculation for various Peclet numbers ($L/d = 1$, grid is 40×80).

the slug rises, while the transfer of heat is not yet affected by the recirculated liquid, see Fig. 3.6c.

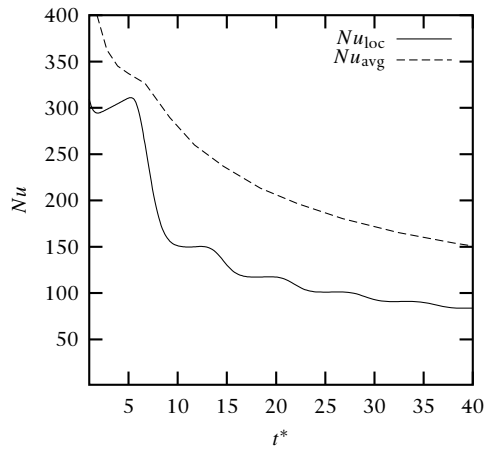
For times $t^* > 8$, the contour lines of temperature are closed, and the Nusselt number drops steadily with increasing Graetz number until the profile is fully developed. In this region, the heat penetration extends over multiple grid elements, and the solution becomes less grid dependent. In table 3.1, the Nusselt number is listed for three grid sizes. For each grid, the radial length of the elements next to the moving wall, Δ_0 , is also listed. The listed results show that for $t^* > 8$, the Nusselt number converges rapidly with increasing grid size: for the finest grid the Nusselt number is accurate to three digits.

In Fig. 3.7, the impact of the Peclet number on the developing Nusselt number is shown. For the Peclet numbers considered here ($Pe \gg 400$), the Nusselt number is a function of t^*/Pe alone, provided the liquid has circulated at least once.

The time required for the temperature profile to develop is longer if the slug aspect ratio Ψ increases. In Fig. 3.8(a), the developing Nusselt number is plotted versus the dimensionless time for various slug aspect ratios. As the slug aspect ratio increases, the time for a full circulation of the liquid also increases. For example, for $\Psi = 8$ the circulation is complete at $t^* = 30$. The effect of circulation is most profound in the first circulation. While for the length-averaged Nusselt number, the effect of circulation can only be seen for the first circulation, for the local Nusselt number a periodic behaviour is observed for several circulations. In Fig. 3.8(b), the length-averaged Nus-



(a)



(b)

Figure 3.8: Development of the Nusselt number. (a) Time required for circulation of the liquid for various aspect ratios. (b) In the length-averaged Nusselt number, the impact of the first circulation of liquid is visible. The local Nusselt number shows the impact of subsequent circulations. In (b), $\Psi = 1$, $Pe = 8192$ in (a) and (b).

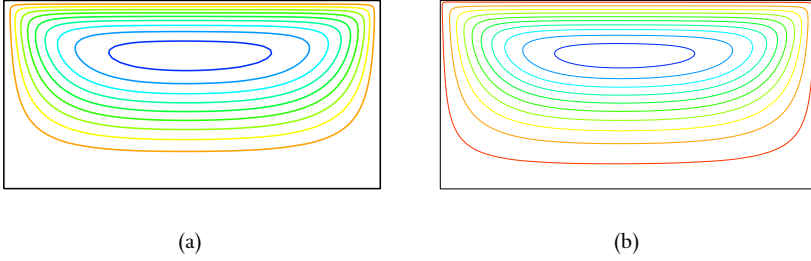


Figure 3.9: Streamlines of the developed velocity (a) and contours of temperature for the developed temperature. $(L/d) = 2, Re = 8, Pr = 1024, t^* = 800$

selt number and the local Nusselt number are plotted together for $\Psi = 1$, where the circulation time is 8, and the decline of the local Nusselt number shows increasing and decreasing decline with a period of 8.

Eventually, the temperature profile becomes fully developed. In thermally developed flow, the temperature inside the slug keeps approaching the wall temperature, but a constant temperature field is obtained if we scale the temperature with the wall temperature and the lowest temperature in the liquid T_{\min} , i.e. $T^{**} = (T - T_{\min}) / (T_{\text{wall}} - T_{\min})$.

In Fig. 3.9 the developed temperature and velocity are plotted next to each other. The temperature gradients perpendicular to the streamlines are much larger than the gradients along the streamlines. At very high Peclet numbers convection is dominant, and the temperature gradients along a streamline tend to zero. At infinite Pe , the temperature will become constant along a streamline, and the isotherms of the temperature field will coincide with the streamlines. Then the solution of the stream function (Eqs. 3.26–3.29) can be used directly to estimate the Nusselt number for fully developed flow by calculating

$$\lim_{\substack{Pe \rightarrow \infty \\ Re = 0}} \frac{Nu_{\infty}}{2} = \frac{\frac{1}{\Psi} \int_0^{\Psi} \frac{\partial \psi(1, z)}{\partial r} dz}{1 - \frac{1}{\Psi} \int_0^{\Psi} \int_0^1 r \psi(r, z) dr dz} \quad (3.33)$$

For the numerator of Eq. 3.33, we obtain

$$\frac{1}{\Psi} \int_0^{\Psi} \frac{\partial \psi(1, z)}{\partial r} dz = \sum_{m=1}^{\infty} \frac{2[-1 + (-1)^m](\cos(m\pi) - 1)}{m^2 \pi^2} = 1 \quad (3.34)$$

and for the denominator we have

$$\frac{1}{\Psi} \int_0^\Psi \int_0^1 r \psi(r, z) dr dz = \sum_{m=1}^{\infty} \frac{P_m}{Q_m} \quad (3.35)$$

in which P_m and Q_m are given by

$$\begin{aligned} P_m = 2\Psi^2 \left[m^2 \pi^2 I_0^2 \left(\frac{m\pi}{\Psi} \right) - 4I_1 \left(\frac{m\pi}{\Psi} \right)^2 \Psi^2 - m^2 \pi^2 I_1^2 \left(\frac{m\pi}{\Psi} \right) - \right. \\ \left. (-1)^m m^2 \pi^2 I_0^2 \left(\frac{m\pi}{\Psi} \right) - 4(-1)^m \Psi^2 I_1^2 \left(\frac{m\pi}{\Psi} \right) + \right. \\ \left. (-1)^m m^2 \pi^2 I_1^2 \left(\frac{m\pi}{\Psi} \right) \right] (\cos(m\pi) - 1) \end{aligned} \quad (3.36)$$

$$Q_m = m^5 \pi^5 \left[-m\pi I_0^2 \left(\frac{m\pi}{\Psi} \right) + 2\Psi I_0 \left(\frac{m\pi}{\Psi} \right) I_1 \left(\frac{m\pi}{\Psi} \right) + m\pi I_1^2 \left(\frac{m\pi}{\Psi} \right) \right] \quad (3.37)$$

The similarity of the stream function and the temperature is further illustrated by Fig. 3.10(a), where the stream function is plotted together with the temperature field at $t^* = 0.2$ for the same conditions as in Fig. 3.3(a) and Fig. 3.6(f), *i.e.* $Pe = 8192$, $t^* = 0.2$. Although the agreement is less than perfect, it should be noted that in the simulation the Peclet number is not infinite, which explains why the two variables do not completely overlap. Also, for the calculation of the temperature field upwinding was used, while this was not necessary for the velocity. Finally, the assumption that the temperature is constant along a streamline holds only for short slugs, and as the circulation time increases, the deviation from Eq. 3.33 will be larger.

In Fig. 3.10(b), the developed Nusselt number is plotted as a function of the aspect ratio. The analytical estimate agrees well with the finite element simulation for $\Psi = 0.5$, while for longer slugs, the difference between the analytical estimate and the CFD result is 20 percent.

The Nusselt numbers for developed segmented flow provide useful insight into the enhancement of heat or mass transfer in segmented gas-liquid flow. For long slugs, the asymptotic Nusselt number is about 40, which is more than an order of magnitude higher than the single phase limit of 3.658. This increase is caused by two effects. Recall the definition of the local Nusselt number

$$\frac{Nu_{loc}}{2} = \frac{Pe}{1 - T_{mean}^*} \frac{\partial T^*(1)}{\partial r}$$

Firstly, the gradient of the temperature field near the wall is larger. From Fig. 3.10(a), it is clear that the minimum of the temperature field coincides with the minimum of the stream function, which is located at $r/r_{tube} = 1/\sqrt{2}$. If convective transport dominates, the lowest temperature is found in the vortex centre in recirculating flow, (see Fig. 3.6), whereas in single-phase Hagen–Poiseuille flow the minimal temperature is found at the axis of the tube. As a result, the radial distance over which

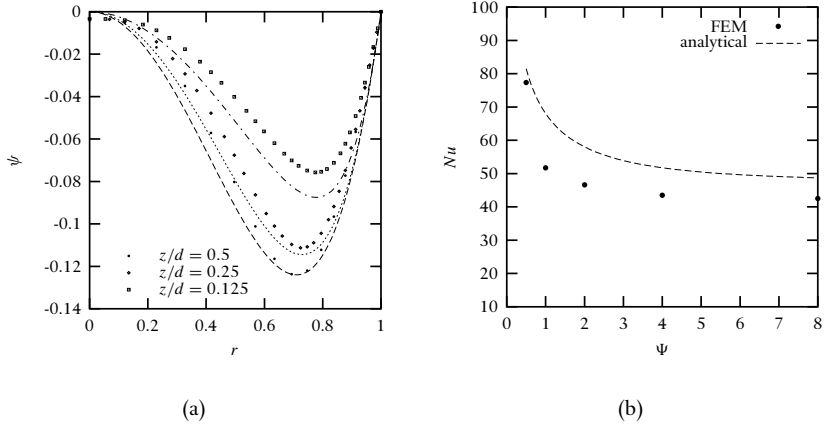


Figure 3.10: Comparison of the stream function and the temperature (a) Stream function (lines) and temperature (points) at three radial cross sections for $\Psi = 1$, $Pe = 8192$, $t^* = 0.2$. (b) Comparison of the developed Nusselt number from Eq. 3.33 (line) with the numerically obtained Nu_{loc} at $Pe = 8192$, $t^* = 0.2$.

the maximum temperature difference is found is reduced by a factor 3.3, and in a first approximation the dimensionless temperature gradient at the wall is increased by the same amount.

Secondly, the circulation reduces the amount of axial dispersion. In single phase flow, the temperature difference is defined using the mass-flow averaged temperature, or *mixing-cup* temperature. Conceptually, the mixing-cup temperature is the temperature that would be obtained by collecting all the fluid flowing through a cross section of the tube and mixing it in an adiabatic container. In single phase flow, the contribution of the fast flowing fluid near the axis of the channel to the mixing-cup temperature is larger than the slow flowing liquid near the wall, and the temperature difference $(1 - T_{mean}^*)$ is higher than the conceptually equivalent mixing-cup temperature difference in slug flow, which is given by the volume-averaged temperature difference.

ENGINEERING CORRELATION

For design purposes, the computed heat transfer characteristics of a cylindrical cavity should be presented in a simplified equation form. From Fig. 3.7, it is clear that the length averaged Nusselt number scales with t^*/Pe to the power $-1/2$ before it approaches its asymptotic value, which suggests the functional form of an engineering equation has the form $Nu^2 = a^2 + b/Gz$, such that a describes the developed behaviour and b the developing behaviour. By regression, the following correlation was obtained

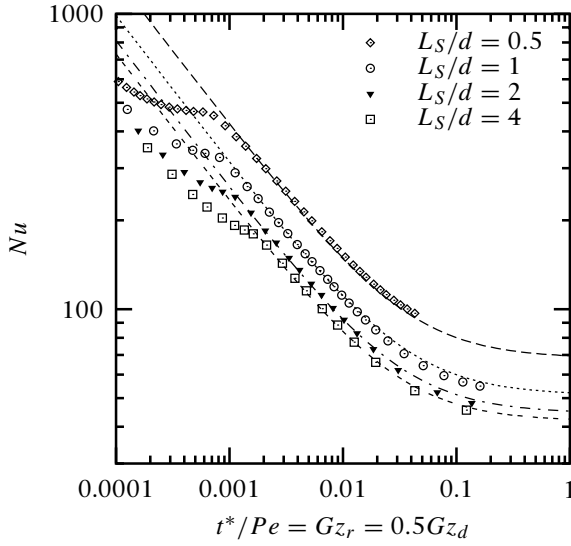


Figure 3.11: The Nusselt-Graetz correlation for $0.5 < \Psi < 4$. The lines are computed from Eq. 3.39c.

$$a(\Psi) = 40 (1 + 0.28\Psi^{-4/3}) \quad (3.39a)$$

$$b(\Psi) = 90 + 104\Psi^{-4/3} \quad (3.39b)$$

$$Nu = \sqrt{[a(\Psi)]^2 + \frac{b(\Psi)}{Gz}} \quad (3.39c)$$

A graphical comparison of the correlation and the finite element calculations is shown in Fig. 3.11.

Eq. 3.39c predicts the heat transfer in segmented gas-liquid flow in capillaries, provided the simplified geometry may be used to describe the flow. The most severe simplification introduced by using a cylindrical cavity is the fact that in segmented gas-liquid flow, the circulating liquid is not in direct contact with the wall. In reality, the circulating liquid is separated from the wall by a thin lubricating film. The thickness of this film may be estimated by

$$\delta = \frac{0.66Ca^{2/3}}{1 + 3.335Ca^{2/3}} \quad (3.40)$$

in which δ is the dimensionless thickness of the film d_{film}/d and Ca is the capillary number, $Ca = \mu u/\gamma$, where u is the slug velocity and γ is the surface tension.

If the capillary number is small, the film is thin and the resistance to heat or mass transfer is negligible. At a certain capillary number, the film is so thick that it becomes

the dominant resistance to transfer to the wall and the cylindrical cavity flow no longer adequately describes the behaviour of segmented gas-liquid flow.

The temperature profile in the film depends on film thickness, the bubble length and the slug length. If the bubble is long enough, the wall temperature penetrates fully into the film, and the film temperature is practically equal to the wall temperature. On the other hand, for a long slug the temperature profile in the film will develop into a straight line, and film theory can be used to estimate the Nusselt number for the film

$$Nu_{\text{film}} = \delta^{-1} \quad (3.41)$$

For shorter slugs, the film resistance will not develop into 3.41. The periodic change of boundary condition at the side of the film opposite of the wall – no flux when the bubble passes by, and exchange of heat when the slug passes by – can be accounted for numerically by changing the geometry under investigation, but a simple resistance-in-series approach using Eqs. 3.39c and 3.41 is not recommended for short slugs and bubbles. For instance, in the very first part of the tube, heat has to penetrate through the film layer before the heat mixes into the circulating zone, which will move the inflection points of the Nu vs. Gz curves in Fig. 3.8 to higher $Gz (= t^*/Pe)$. In any case, the presence of the film will lower the overall flux of heat, and the simplification of the geometry in this study must be realised when comparing to experimental data.

§ III.5 LITERATURE DATA

In this section, experimental data from literature sources are compared with the numerical results. Although an overwhelming amount of literature data on heat or mass transfer in two-phase flow is available, in most cases detailed information about the flow pattern is not presented. Moreover, the data available for slug flow are usually reported without the slug frequency or bubble and slug length.

Oliver & YOUNGH-HOON (1968*b*) measured heat transfer in two-phase flow in capillaries using very viscous liquids. Although the slug and bubble length were varied in a controlled way, the use of viscous liquids results in high capillary numbers, and the circulating part of the slug is separated from the wall by a relatively thick film layer. Moreover, some of the liquids were also very non-newtonian, and for these liquids a recirculating zone was absent (Oliver & YOUNGH-HOON, 1968*a*). As a result, the flow is significantly different from the simplified geometry used here. Their experimental Nusselt numbers are significantly lower than those predicted by Eq. 3.39c, and this difference can be attributed to the film resistance.

HATZIANTONIOU & ANDERSSON (1982) measured the dissolution of benzoic acid in 0.17 m tubes with diameters of 2.350 and 3.094 mm. Melted benzoic acid was poured into the glass tube, where it was allowed to cool. The thickness of the solid coating was adjusted by a well-centred steel rod inside the tube. Experiments were performed for different slug lengths. BERČIČ & PINTAR (1997) prepared tubes with a benzoic acid

coating in a manner similar to that described by Hatziantoniou & Andersson (1982). During the experiments the gas and liquid slug lengths were controlled and adjusted by changing the time interval for dosing gas or liquid by two independently driven peristaltic pumps. Berčić & Pintar used tubes that were between 25 and 35 cm long, but did not mention the exact length of the tubes. The experiments by Berčić & Pintar and Hatziantoniou & Andersson were performed using long slugs and short tubes. In fact, a significant fraction of their data was measured under conditions where the liquid inside the slug could only circulate one or two times. As can be seen from Fig 3.11, the correlation proposed in this work overpredicts the Nusselt number for short contact times. Comparison of the experimental data with Eq. 3.39c showed that this was indeed the case.

Horvath *et al.* (1973) measured the hydrolysis of N-benzoyl-arginine ethyl-ester in a 1.2 m tube coated with the immobilised enzyme Trypsin. The intrinsic rate of this reaction is so high that the wall concentration of the reactant at the wall is essentially zero under the experimental conditions used. A special device was used to introduce bubbles into the liquid, that made it possible to obtain liquid slugs of high uniformity. From the conversion, the rate of transfer to the wall was calculated, and plotted against Reynolds number and slug length. The Schmidt number for all experiments was $Sc = 1700$. The experimental data are reported as Nu versus Ψ with Re as a parameter and Nu versus Re with the aspect ratio Ψ as a parameter. As the study deals with mass transfer, the use of the Sherwood number instead of the Nusselt number would have been more appropriate, so the appropriate substitutions have been made. The Sherwood numbers were corrected for the fact that they were calculated based on the total area in the tube, *i.e.* including the parts of the tube that were occupied by gas bubbles. The following equation was used to calculate the Sherwood number from the conversion:

$$X = 1 - \exp\left(-4Sh \frac{\pi dL}{4W}\right) \quad (3.42)$$

in which W is the sum of the gas and liquid volumetric flow rates. This equation can be rewritten to obtain

$$k_{LS} \left(\frac{4}{d}\right) = \frac{u_{LS} + u_{Gs}}{L} \ln\left(\frac{c_{\text{exit}} - c_{\text{wall}}}{c_{\text{inlet}} - c_{\text{wall}}}\right) \quad (3.43)$$

The left hand side of Eq. 3.43 is the mass transfer group $k_{LS}a$, and is based on the total tube area. The slug area is related to the tube area by the ratio of the liquid and total flow rates, or the liquid hold-up ϵ_L . The mass transfer coefficient based on the liquid can be obtained by

$$k_{LS} \left(\frac{4}{d}\right) = \left(\frac{k_{LS}}{\epsilon_L}\right) \left(\frac{4\epsilon_L}{d}\right) \quad (3.44)$$

in other words, by dividing the mass transfer coefficient by the liquid hold-up. The Sherwood numbers from Horvath *et al.* (1973) were corrected using Eq. 3.44 to ob-

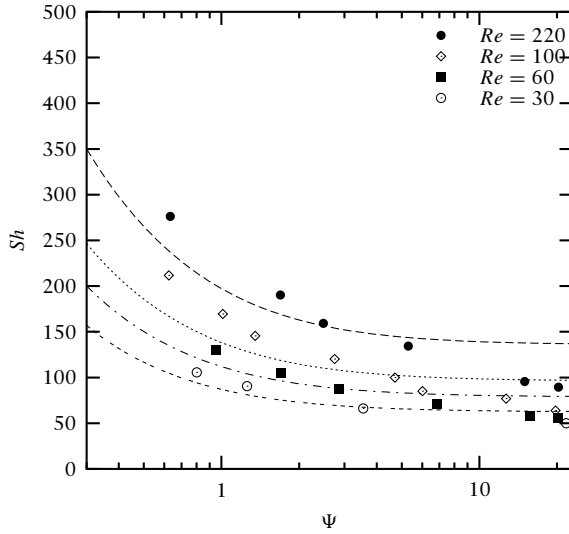


Figure 3.12: Sherwood number plotted against the slug aspect ratio. Experimental data from Horvath *et al.* (1973), lines based on Eq. 3.39c.

tain the Sherwood number based on slug area to allow comparison with the numerical results.

In Fig. 3.12, the experimental data are compared with the results of this work. The agreement of the cylindrical cavity calculations is very good for low Reynolds numbers. Note that at low Reynolds numbers, the capillary number is also low. For higher Re , the impact of the film resistance increases. For $Re = 220$, the Nusselt number based on Eq. 3.41 is $Nu_{\text{film}} = 120$ if the surface tension were equal to that of pure water. As the liquid used was a solution, the surface tension was probably lower. For long slugs, the Nusselt number approaches a value of 100. For short slugs at $Re = 220$, good agreement with the model is found.

§ III.6 INDUSTRIAL RELEVANCE

For liquid–phase mass transfer, the Schmidt number is typically much larger than unity, so the mass transfer by convection is much faster than the mass transfer by diffusion. The results presented in this chapter show that the mass transfer of a liquid–phase component to the wall of a channel in segmented gas–liquid flow in a capillary (Taylor flow) is an order of magnitude faster than the mass transfer in single phase flow through a capillary. In Fig. 3.13, the Nusselt or Sherwood number is plotted as a function of the Graetz number, illustrating that this order of magnitude improvement is

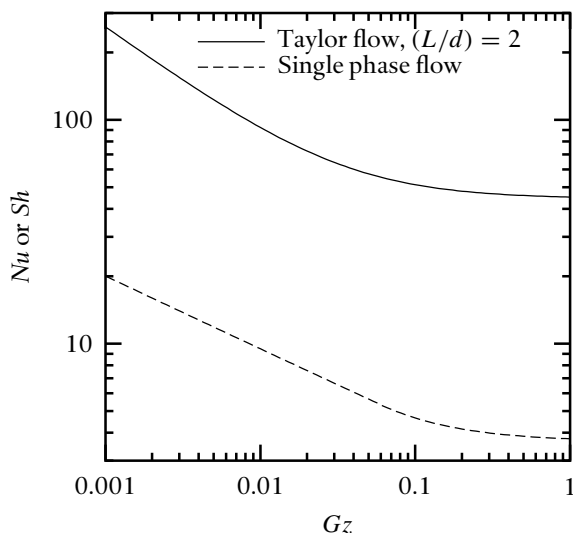


Figure 3.13: Mass transfer in circular channels for Taylor flow and single phase flow.

also found in the developing region. This tremendous improvement can be explained by realising that the circulation in the slugs continuously transports liquid phase components to the wall. In single phase flow, this convective contribution is absent. When the results of this chapter are combined with the pressure drop correlations from chapter II of this thesis, it is apparent that the improvement of the mass transfer behaviour does not lead to a similar increase in pressure drop. Recalling the correlation for the friction factor in Taylor flow,

$$f = \frac{16}{Re} \left[1 + 0.17 \frac{1}{\Psi} \left(\frac{Re}{Ca} \right)^{0.33} \right] \quad (3.45)$$

the increase in frictional pressure drop with respect to single-phase flow in liquid slugs ranges from a factor 3 for an aspect ratio $\Psi = 2$ to a factor 1.5 at $\Psi = 8$ for typical organic liquids. Note that both the friction factor in Eq. 3.45 and the Nusselt number in Eq. 3.39c are based on the volume of the slugs alone: the volume of the tube occupied by the bubbles have neither mass transfer nor pressure drop. If the entire tube length is considered, both the Sherwood and the friction factor must be multiplied by the liquid hold-up.

When the specific process needs imposed by the intended application require fast liquid-solid mass transfer in three-phase applications, the general reactor engineering practice been to use turbulent contactors. In turbulent systems with small solid particles, the mass transfer of liquid-phase components can be high, but the price for this high mass transfer is high energy input: both the momentum balance and the com-

ponent mass balance are dominated by chaotic exchange in turbulent eddies, and the Chilton-Colburn analogy applies. In monoliths, which are operated in a laminar Taylor flow regime, such coupling of energy requirement and mass transfer is absent. The Taylor flow pattern in monoliths causes a convective enhancement of the mass transfer which brings the liquid-phase components to the solid in an ordered, deterministic way. This accurately describes the benefit of using monoliths: the convection wastes no energy bringing the liquid-phase components to the wall, which makes the laminar flow pattern in Taylor flow an excellent way of contacting a liquid and a solid, even if the gas-phase is inert.

The results of this work are not only beneficial for the description of mass transfer in monoliths. The heat transfer to polymer melts in extruders, for instance, is an example of closed-streamline cavity flow of great industrial relevance (for a recent numerical study, see Syrjälä, 1999). The circulating flow of the melt between two flights of an extruder screw, the screw root and the barrel is similar to the flow problem discussed in this work. Recently, considerable efforts have been made to explain the observed increase in filtration efficiency in micro-filtration by adding gas to the liquid that needs to be purified (Laborie *et al.*, 1998, 1999). In micro-filtration, liquid flows through a bundle of capillary tubes with permeable walls. The observed increase in filtration efficiency can be caused by removal of filter cake by the passing bubbles, or by enhancement of bulk diffusion due to the slug flow pattern, as described in this work.

§ III.7 CONCLUSIONS

The numerical work performed in this study shows that principal features of the mass and heat transfer in segmented-liquid flow can be described by the following correlation of Nusselt with the Graetz number and slug aspect ratio, provided that the dominant mechanism of transfer is convective and the liquid has circulated at least once inside the slug.

$$a(\Psi) = 40 (1 + 0.28\Psi^{-4/3}) \quad (3.46a)$$

$$b(\Psi) = 90 + 104\Psi^{-4/3} \quad (3.46b)$$

$$Nu = \sqrt{[a(\Psi)]^2 + \frac{b(\Psi)}{Gz}} \quad (3.46c)$$

The transition to convection-dominated flow occurs around $10^2 < Pe < 10^3$ (Duda & Vrentas, 1971a). With respect to the application of the results of this work to mass transfer in monolith reactors, the product $ReSc$ will always be higher than 10^3 in monoliths. It should be realised that this correlation is only valid if the mass transfer resistance of the lubrication film separating the liquid slugs from the wall may be ignored.

The mass or heat transfer in Taylor flow is at least an order of magnitude higher than the single phase equivalent. This indicates that the circulating flow pattern is very effective in promoting radial mass and heat transfer. This result shows that monoliths are not only an attractive alternative for gas–liquid–solid reactions, but also for liquid–solid reactions where high mass transfer at low pressure drop is required.

The mass transfer rate predicted by this correlation was compared to experimental values obtained in Taylor flow. For experimental data were the thickness of the lubricating film was small and the length of the channel was long enough to ensure that the liquid inside the slug had circulated several times, good agreement of the numerical work presented in this chapter and the literature data was found.

NOTATION

a	specific area, m^{-1}
a, b	fitting parameters in Eq. 3.39c, –
c	concentration, mol/m^3
c_p	fluid specific heat at constant pressure, J/kgK
d	diameter, m
D	diffusivity, m^2/s
f	friction factor, –
g	gravitational constant, m/s^2
h	heat transfer coefficient, $\text{W}/\text{m}^2\text{K}$
k	thermal conductivity, W/mK
k_{LS}	liquid–solid mass transfer coefficient, m/s
L	length, m
p	pressure, Pa
Pr	Prandtl number ($\mu c_p/k$), –
q''	wall heat flux, W/m^2
r	radial coordinate, m
R	channel radius, m
t	time, s
T	temperature, K
T_{av}	volume–averaged temperature, K
u, \mathbf{u}	velocity, m/s
W	sum of gas and liquid flowrate, m^3/s ,
X	conversion, –
z	axial coordinate, m

Greek letters

α	fluid thermal diffusivity, $k/\rho c_p$, m^2/s
β	dynamic holdup, –

δ	dimensionless film thickness, –
Δ_0	radial length of elements next to wall, –
ϵ	holdup, –
μ	viscosity, Pa s
ρ	density, kg/m ³
ψ	stream function, m ³ /s
Ψ	aspect ratio (L/d), –

Dimensionless numbers

Ca	Capillary number ($\mu u/\gamma$), –
Gz	Graetz number ($L/dRePr$ or $L/dReSc$), –
Nu	Nusselt number (hd/k), –
Pe	Peclet number ($RePr$ or $ReSc$), –
Re	Reynolds number ($\rho u d/\mu$), –
Sc	Schmidt number ($\mu/\rho D$), –
Sh	Sherwood number (kd/D), –

Subscripts

G	gas
L	liquid
lm	logarithmic mean
loc	local
s	superficial

BIBLIOGRAPHY

- BERČIČ, G. & PINTAR, A. 1997 The role of gas bubbles and liquid slug lengths on mass transport in the Taylor flow through capillaries. *Chemical Engineering Science* 52 (21/22), 3709–3719.
- COLBURN, A. P. 1933 A method of correlating forced convection heat transfer data and a comparison with fluid friction. *Transactions of the A.I.Ch.E.* 29, 174–210.
- DUDA, J. L. & VRENTAS, J. S. 1971a Heat transfer in a cylindrical cavity. *Journal of Fluid Mechanics* 45, 261–279.
- DUDA, J. L. & VRENTAS, J. S. 1971b Steady flow in the region of closed streamlines in a cylindrical cavity. *Journal of Fluid Mechanics* 45, 247–260.
- GRAETZ, L. 1883 Über die Wärmeleitungsfähigkeit von Flüssigkeiten (on the thermal conductivity of liquids) part 1. *Annalen der Physik und Chemie* 18, 79–94.
- GRAETZ, L. 1885 Über die Wärmeleitungsfähigkeit von Flüssigkeiten (on the thermal conductivity of liquids) part 2. *Annalen der Physik und Chemie* 25, 337–357.
- HATZIANTONIOU, V. & ANDERSSON, B. 1982 Solid-liquid mass transfer in segmented

- gas-liquid flow through a capillary. *Industrial and Engineering Chemistry Fundamentals* 21 (4), 451–456.
- HORNBECK, R. W. 1964 Laminar flow in the entrance region of a pipe. *Applied Scientific Research, Section A* 13, 224–232.
- HORVATH, C., SOLOMON, B. A. & ENGASSER, H.-M. 1973 Measurement of radial transport in slug flow using enzyme tubes. *Industrial and Engineering Chemistry Fundamentals* 12 (4), 431–439.
- LABORIE, S., CABASSUD, C., DURAND-BOURLIER, L. & LAINÉ, J. M. 1998 Fouling control by air sparging inside hollow fibre membranes- effects on energy consumption. *Desalination* 118, 189–196.
- LABORIE, S., CABASSUD, C., DURAND-BOURLIER, L. & LAINÉ, J. M. 1999 Characterisation of gas-liquid two-phase flow inside capillaries. *Chemical Engineering Science* 54, 5723–5735.
- NUSSELT, W. 1910 Die Abhängigkeit der Wärmeübergangszahl von der Rohrlänge (the dependence of the heat-transfer coefficient on the tube length). *Verein Deutscher Ingenieure Zeitschrift* 54, 1154–1158.
- OLIVER, D. R. & YOUNGH-HOON, A. 1968a Two-phase non-Newtonian flow - part I: Pressure drop and hold-up. *Transactions of the Institution of Chemical Engineers* 46, T106–T115.
- OLIVER, D. R. & YOUNGH-HOON, A. 1968b Two-phase non-Newtonian flow - part II: Heat transfer. *Transactions of the Institution of Chemical Engineers* 46, T116–T122.
- SHAH, R. K. & LONDON, A. L. 1978 *Laminar flow forced convection in ducts*, *Advances in Heat Transfer*, vol. Supplement 1. New York: Academic Press.
- SYRJÄLÄ, S. 1999 On the analysis of fluid flow and heat transfer in the melt conveying section of a single screw extruder. *Numerical Heat Transfer, Part A* 35, 25–47.

CHAPTER IV

RESIDENCE TIME DISTRIBUTION

§ IV.1 INTRODUCTION

The performance of a chemical reactor is to a large extent determined by the degree of mixing in the reactor. On a small scale, mixing enhances transport phenomena, so especially when multiple phases are involved, a high degree of local mixing is beneficial. On the other hand, mixing on a large scale is certainly not always desired. The rate of most chemical reactions increases with increasing reactant concentrations. The term *backmixing* is used to describe mixing of fluid elements that have long been in the reactor with fluid elements that have just entered the reactor. Backmixing usually lowers the average concentration of reactants in the reactor, and as a result, the average rate of reaction typically goes down. Also, some processes have a distinct optimal residence time of the fluids in the reactor. Especially for multiple complex reactions in one vessel the fraction of reactants that is converted to useful products can have an optimal residence time. If part of the fluid stays longer or shorter in the reactor, the useful fraction is lower. In such processes, backmixing leads to a larger distribution of residence times of individual molecules in the reactor, and this is to be prevented. So, in short, the large-scale mixing characteristics of a reactor can have a negative impact on both the conversion and selectivity in the reactor.

The concept of residence time distribution is a powerful method to analyse the effect of backmixing in a chemical reactor. Its main power is the experimental simplicity: introducing a tracer pulse into a reactor and monitoring when the tracer leaves the reactor results in an exit concentration–time curve, which is called the residence time distribution (RTD). Note that the experimental technique only measures concentrations *outside* the reactor, and does not fully describe the mixing behaviour *inside* the reactor; many different flow fields inside a reactor can result in the same RTD. However, the RTD curve gives enough information – exact for first order kinetics, and approximately for more complex kinetics, – to predict how a chemical conversion will behave in the reactor. The combination of experimental simplicity and wealth of information resulted in the preference of RTD over more complex hydrodynamic descriptions in

chemical engineering practice from the moment the concept was proposed by Danckwerts (1956).

With respect to local mixing and backmixing, Taylor flow has some interesting features. First, when a chemical reaction occurs on the wall of the capillary, the recirculation inside the liquid slug enhances the radial mass transfer to the film. This film is very thin, so very high mass transfer rates can be achieved, as was described in chapter III of this thesis. Second, the degree of backmixing, even compared to homogeneous laminar flow, is diminished by the presence of the bubbles, which effectively seal packets of liquid between them. In fact, the only mechanism for transfer of matter from one slug to the next is by diffusion from the slug to the film, and subsequent diffusion from the film to the next slug. The combination of enhanced radial mass transfer (local mixing) and suppressed backmixing makes Taylor flow an ideal hydrodynamic regime for gas-liquid-solid reactions. In fact, if one tries to envision small mixers moving without contact with one another in plug flow through a reactor, one is destined to arrive at something that is at least very similar to Taylor flow. Although the extent of backmixing in a single channel is probably minimal, the same does not necessarily hold for a monolith column. If the distribution of gas and liquid into the monolith channels is not perfect, the velocity of the slugs and bubbles can vary from channel to channel. The extent of this distribution can – in principle – be detected by comparing the residence time distribution (RTD) of Taylor flow in a single channel with the RTD of a monolith block.

The aim of this chapter is (1) to describe the residence time distribution of Taylor flow inside capillary channels, (2) to determine the residence time distribution in monoliths, operated in cocurrent down-flow, (3) to investigate the extent of velocity distribution and (4) to optimise the distributor design to minimise effects of scaling up from a single capillary to a capillary bundle.

DESCRIPTION OF PREVIOUS WORK

The low axial dispersion in Taylor flow has been studied extensively in single capillary channels. In continuous flow analysers, samples are separated by bubbles which prevent mixing of samples. This was of great importance in the automation of clinical diagnosis (van Eerd & Kreutzer, 1987). For these analysers, Thiers *et al.* (1971) studied the inter-slug mass transfer in a capillary. Using sufficiently long liquid slugs, the reasonable assumption was made that the film and the slug have sufficient time to mix, and the dispersion in their apparatus could be modelled using a tanks-in-series model, connected by the film between the slugs. Their experimental data allowed the calculation of the ratio of slug volume to slug-to-slug flow rate, resulting in a reasonable correlation for film thickness as a function of bubble velocity.

For short liquid slugs, full mixing between slug and film can no longer be assumed. Horvath *et al.* (1973) and Berčić & Pintar (1997) demonstrated experimentally that for shorter slugs, the rate of mass transfer is a function of the length of the slug and the

slug velocity. This is in agreement with solutions of the convection-diffusion equation inside the liquid slug, which is a mild function of slug length. Also, the contact time of the film and the slug may be too short to reach equilibrium between the film and the slug. (see chapter III of this thesis for the experimental data for Horvath *et al.* and a discussion of the mass transfer behaviour)

As a consequence, for short liquid slugs the film region and the liquid slugs have to be described as separate regions with mass transfer between them. Pedersen & Horvath (1981) have studied the axial dispersion in Taylor flow at 0.7 cm/s for slugs with a length to diameter ratio $\Psi_S = 10$. In a reference frame moving with the slugs, each liquid slug was modelled as a volume, exchanging matter with the film, which was modelled by a tanks-in-series model. The experimental data could be described by using a mass transfer coefficient between 10^{-3} and 10^{-2} cm/s.

Thulasidas *et al.* (1995b) investigated residence time distribution of cocurrent up-flow in capillaries and monoliths. The stagnant liquid film becomes a falling film when the orientation of the capillary is changed from horizontal to vertical. In a single channel at bubble velocities of 0.03 m/s, the impact of the falling film was small in circular capillaries, and a model comparable to the one by Thiers *et al.* (1971) could be used to describe the experimental data. In square capillaries the falling film is thick in the corners, and in the corners the the velocity in the falling film is substantially higher. In upflow the falling film flows downward and the slugs move upward. As a result, for up-flow with square channels the spread of the response peak was an order of magnitude higher than predicted. For higher slug velocities, the effect of gravity on the film was less pronounced, and the square capillaries behaved more like circular capillaries.

In a subsequent paper (Thulasidas *et al.*, 1999), an infinite series solution was used for radial diffusion, and the gravity driven flow in the film was taken into account. The improved mathematical model described the experimental data accurately. The results of a single capillary were compared to the results for a bundle of square capillaries simulating a monolith. The results showed that in up-flow, the monolith was almost completely back-mixed, and the single channel data did not agree at all with the monolith data. Recently, Mantle *et al.* (2002) have visualised up-flow in monoliths at low superficial velocities using MRI tomography . In most of the channels, the flow was indeed upward, but a wide range of velocities was found. Further, in a significant number of channels, the direction of flow was downward, resulting in recirculation over the monolith block. This recirculation behaviour, combined with the spread in velocities, explains the large extent of back-mixing observed by Thulasidas *et al.* (1999).

§ IV.2 THEORY

Residence time distributions are usually represented by E -curves. The function E is the exit age distribution function for fluids leaving the reactor. It may be obtained directly by injecting (in a very short time) an amount of tracer at $t = 0$ into the reactor,

and recording the tracer concentration C versus time. The exit concentration is then normalised in two ways. First, the area under the curve is normalised to unity:

$$E_t(t) = \frac{C(t)}{\int_0^{\infty} C(t)dt} \quad (4.1)$$

In principle, the integral in the denominator yields the amount of tracer injected, and it can be used to set up a mass balance to check that all of the tracer has indeed left the system (only once). From the $E_t(t)$ curve (where the subscript t denotes that the E -curve is not dimensionless with respect to time) the mean residence time τ can be obtained by calculating the first moment

$$\tau = \int_0^{\infty} tE_t(t)dt \quad (4.2)$$

The mean residence time is used to define a dimensionless time $\theta = t/\tau$, and the $E_t(t)$ curve is made completely dimensionless by using θ .

$$(E(t/\tau)) = E(\theta) = \tau E_t(\tau\theta) \quad (4.3)$$

SINGLE CAPILLARIES

From the nature of Taylor flow and the results of previous work, we conclude that the residence time distribution in Taylor flow can be described by a two-zone model (*Piston Exchange model*). The liquid film can be modelled as a stagnant layer, provided that the gravity effects may be ignored. For upflow the velocity in the gravity driven film is downward, and for upflow the impact of this velocity is likely to be more severe than for downflow, where the film and the slugs flow in the same direction.

In this work, we have used a continuum approach to the description of flow in a channel, rather than a discrete tanks-in-series model. Heiszwolf *et al.* (2001) showed that the typical length of a Taylor flow unit cell (*i.e.* a bubble and a slug) is about 5 mm. Therefore, per meter column length typically 200 slugs will be found, and the tanks-in-series may safely be collapsed to differential equations in the axial direction. The liquid film is modelled as a stagnant zone, and the slugs are modelled as a plug flow zone with no axial dispersion. This leads to the following set of partial differential equations for the channel:

$$\frac{\partial C_{\text{dyn}}}{\partial t} = -u_{\text{dyn}} \frac{\partial C_{\text{dyn}}}{\partial z} - \frac{k_{\text{SFA}}}{\phi} (C_{\text{dyn}} - C_{\text{st}}) \quad (4.4)$$

$$\frac{\partial C_{\text{st}}}{\partial t} = \frac{k_{\text{SFA}}}{1 - \phi} (C_{\text{dyn}} - C_{\text{st}}) \quad (4.5)$$

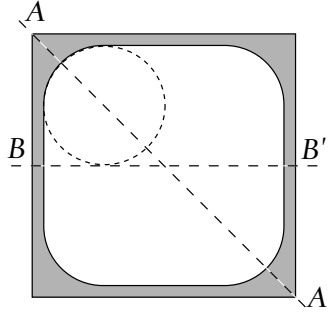


Figure 4.1: The shape of the liquid film for $Ca < 0.04$.

Eq. 4.4 describes the evolution of the liquid phase concentration in the dynamic phase, *i.e.* the slugs. The first term on the right hand side is the convective term, where C_{dyn} is the concentration in the slugs, and u_{dyn} is the velocity of the slugs in laboratory coordinates. The second term describes the exchange of matter with the film. Here C_{st} is the concentration in the static phase, *i.e.* in the film, and k_{SFA} is the mass transfer group, expressed per unit channel volume. The parameter ϕ is the fraction of liquid that is in the dynamic phase. Eq. 4.5 describes the evolution of the film concentration, which is coupled to Eq. 4.4 by the exchange of matter.

In order to use Eqs. 4.4–4.5 for Taylor flow, correlations are needed for ϕ and k_{SFA} .

DYNAMIC LIQUID FRACTION

In chapter II, the thickness of the film between the bubble and the wall is described in detail. For round channels, theoretical considerations using lubrication analysis lead to Bretherton's scaling law (Bretherton, 1961).

$$\frac{\delta}{d_{\text{ch}}} \sim Ca^{\frac{2}{3}} \quad Ca = \frac{u\mu_L}{\gamma} \quad (4.6)$$

in which the Capillary number is the ratio of viscous to interfacial forces. Strictly, the Capillary number is based on the actual velocity of the bubble. However, only a small error is introduced by replacing the bubble velocity by the sum of the gas and liquid superficial velocity. For round channels, various improvements on the work of Bretherton have been published, which include inertial and Marangoni effects. However, the cross section of bare monolith channels is square, and coated monoliths have a cross section that is square with rounded corners. The effect of the shape of the channels is much more important than inertial effects, and in a first approximation the shape of the film may be based on the Capillary number alone.

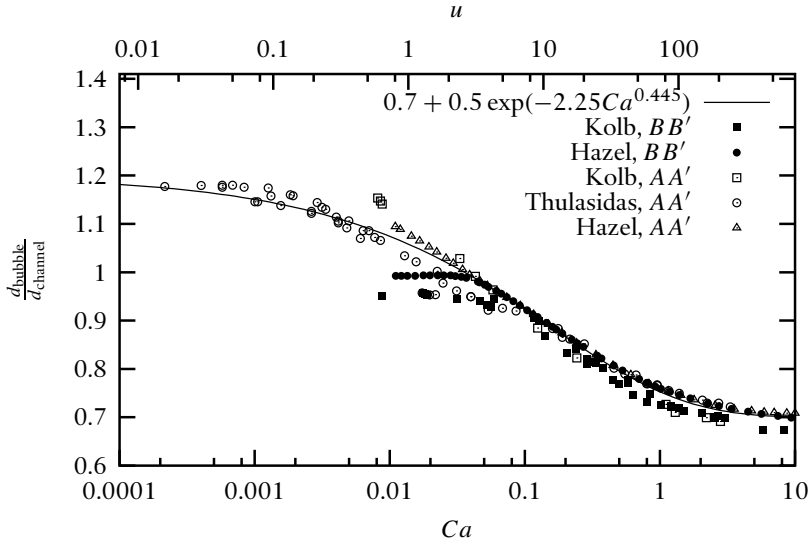


Figure 4.2: Bubble diameter versus Ca in square capillaries. Experimental data from Thulasidas *et al.* (1995a) and Kolb & Cerro (1991), numerical data from Hazel & Heil (2002). On the top axis, the velocity of the bubble is plotted, assuming water-like properties $\mu_L = 10^{-3}$ Pa s and $\gamma = 0.073$ N m $^{-1}$.

For square channels, Kolb & Cerro (1991) measured the shape of the liquid film for different capillary numbers in the directions AA' and BB' (see Fig. 4.1). Note that the channel diameter is defined in the direction BB' , so in the direction AA' the maximum bubble size is $\sqrt{2}$.

Thulasidas *et al.* (1995a) measured the film thickness in the direction AA' using optical methods for a wide range of capillary numbers. Hazel & Heil (2002) computed the shape of bubbles in square capillaries using a finite–element free surface formulation, similar to chapter II of this thesis.

In Fig. 4.2, the experimental data (Kolb & Cerro, 1991; Thulasidas *et al.*, 1995a) and numerical data (Hazel & Heil, 2002) are plotted against the capillary number. The data presented in Fig. 4.2 are for horizontal flow. In square capillaries, the influence of gravity on the film thickness is more pronounced than in circular capillaries: for upflow smaller bubble radii are reported, and the reverse effect was observed experimentally and numerically for downflow. For the diagonal (AA') direction, the agreement between all the data is good. For $Ca \rightarrow 0$, the dimensionless bubble diameter approaches 1.2. If the film would vanish at low capillary numbers, the asymptote would be $\sqrt{2}$. In other words, even at low velocities the film does not vanish in the corners. Note that the upper limit is based on the data of Thulasidas *et al.* alone. For $Ca \rightarrow \infty$, the dimensionless bubble diameter approaches a value of 0.7. For $Ca > 0.04$, the bubble diameter in

RESIDENCE TIME DISTRIBUTION

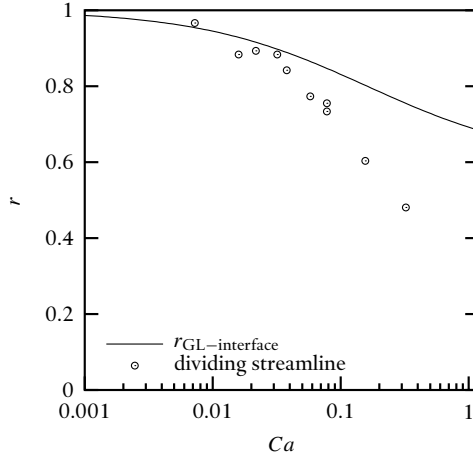


Figure 4.3: Comparison of the film thickness between the wall and a bubble or a slug. In stead of the thickness of the film, the distance r/r_{channel} from the axis is plotted. The solid line represents the thickness of the film when a bubble passes by. The line is calculated from the low-inertia correlation of Aussilous & Qu ere (2000), which is based on experimental data. The markers are measurements of the radial distance from the axis of the streamline dividing the circulating region of the slug from the film region (Thulasidas *et al.*, 1997).

both directions is the same and the bubble is axisymmetric, while for $Ca < 0.04$ the bubble diameter in the BB' direction is virtually independent of Ca .

Using the asymptotic values of 1.2 and 0.7, the dimensionless bubble diameter in the diagonal direction was correlated against the Capillary number as

$$\frac{d_{b,\text{square}}}{d_{\text{channel}}} = 0.7 + 0.5 \exp(-2.25Ca^{0.445}) \quad (4.7)$$

which is also plotted in Fig. 4.2. For monoliths, the region of interest is $Ca < 0.04$. Here the bubble diameter in the direction BB' is close to the width of the channel. From the data of Hazel & Heil, a value of $d_{\text{bubble}}/d_{\text{channel}} = 0.99$ is obtained, while the experimental data of Kolb & Cerro is somewhat lower, $d_{\text{bubble}}/d_{\text{channel}} \approx 0.95$.

Note that the film is also present between the slug and the wall. Thulasidas *et al.* (1997) measured the location of the streamline dividing the circulating liquid in the slug from the film. For circular capillaries, the location of the dividing streamline is plotted in Fig. 4.3 together with the bubble diameter based on the low-inertia film thickness correlation of Aussilous & Qu ere (2000):

$$\frac{r_{\text{GL-interface}}}{r_{\text{channel}}} = 1 - \left(\frac{1.334Ca^{2/3}}{1 + 3.334Ca^{2/3}} \right) \quad (4.8)$$

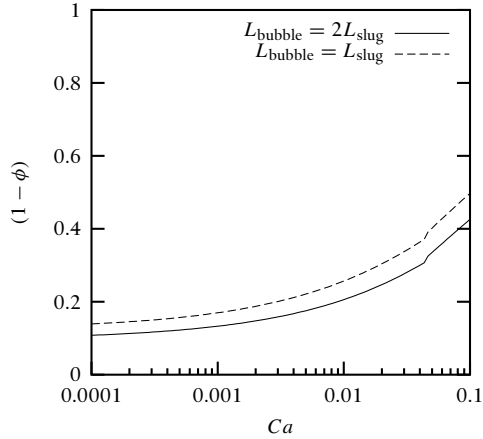


Figure 4.4: Static liquid fraction $(1 - \phi)$ as a function of Capillary number Ca .

For circular capillaries at low Ca , the film thickness between the slug and the wall is comparable to the film thickness between the bubble and the wall, while for $Ca > 0.05$, the film between the slug and the wall becomes thicker. For $Ca > 0.5$, the circulating region completely vanishes. Without circulating region, the flow is called *complete bypass flow*, and the criterion $Ca > 0.5$ was already found by Taylor (1960).

For square capillaries, Kolb & Cerro (1991) calculated streamlines in downflow Taylor flow. The plotted streamlines in the directions AA' and BB' indicate that for $Ca < 0.04$, the shape of the film is the same for the bubble and the slug.

For monoliths, the region of interest is $Ca < 0.05$, and we assume here that the film thickness is the same for the slug and the bubble. The fraction of liquid in the film is also a function of the ratio of bubble to slug length. Ignoring the velocity in the film due to gravity, we can equate this ratio to the ratio of total gas and liquid flow:

$$\frac{L_S}{L_S + L_B} \approx \frac{\phi_L}{\phi_L + \phi_G} \quad (4.9)$$

In chapter II, the validity of this approximation has been found acceptable for round channels. The correlations of Thulasidas *et al.* (1995a) and Eq. 4.9, were used to calculate the static liquid fraction $(1 - \phi)$ for two slug lengths, see Fig. 4.4.

MASS TRANSFER

The slug to wall mass transfer for a reacting system with negligible film resistance has been described in detail in chapter III of this thesis. The mass transfer to the film is likely to be similar to reacting mass transfer to the wall. However, at the moment of introduction of a tracer into the tube, the film concentration is in equilibrium with the

tracer concentration in the slug, so the initial condition for residence time distribution experiments is different from reacting mass transfer experiments. The high Sherwood number for the developing region of the channel is therefore not likely to represent the behaviour in a tracer experiment. The engineering correlation that was developed in chapter III reads:

$$a(\Psi_S) = 40 \left(1 + 0.28\Psi_S^{-4/3} \right) \quad (4.10a)$$

$$b(\Psi_S) = 90 + 104\Psi_S^{-4/3} \quad (4.10b)$$

$$Sh = \sqrt{[a(\Psi_S)]^2 + \frac{b(\Psi_S)}{Gz}} \quad (4.10c)$$

where Ψ_S is the slug length to diameter ratio. Here $a(\Psi_S)$ represents the developed Sherwood number (in the limit $Gz \rightarrow \infty$, $Sh = a(\Psi_S)$), which may be regarded as the lower limit for tracer experiments.

SINGLE CHANNEL LITERATURE DATA

Thulasidas *et al.* (1999) measured the residence time distribution of Taylor flow in a round single capillary with a diameter of 2 mm. The tracer was a KCl solution, of which the concentration in each slug was measured at the inlet and outlet of the tube using a conductivity meter. The length of the tube between inlet and outlet measurement was 57 cm.

Fig 4.5 shows one of the experimental curves. The data reported by Thulasidas *et al.* were in a dimensional form based on the tracer injection concentration, and their curve was made dimensionless here using the E -curve to determine the average residence time and dividing by the area under the curve. The highest concentration was found at $\theta \approx 0.9$. In the PE model, the highest concentration corresponds to the slug that was injected with tracer at the inlet. This indicates that roughly 10 % of the liquid is stagnant. Eq. 4.8 predicts a stagnant fraction of 0.05, which is 50 % lower than the experimental value. It is well known that at low Ca , correlations such as Eq. 4.8 underpredict the film thickness if impurities are present (for details, see chapter II and the experimental data of Bretherton (1961)).

For KCl the diffusion coefficient in water is $2.1 \times 10^{-9} \text{ m}^2/\text{s}$ (Cussler, 1997), and the mass transfer parameter k_{SFA} is calculated from the Sherwood correlation Eq. 4.10c as

$$k_{SFA} = \frac{ShD}{d} \frac{4\epsilon_L}{d} \quad (4.11)$$

The developed value for k_{SFA} is 0.02 s^{-1} , while the developing value equals 0.045 s^{-1} . The higher the mass transfer group, the smaller the amount of tracer that passes through the channel without exchanging with the film. The amount of tracer that does not exchange with the film shows up in the E -curve as a sharp peak, where the width of the peak is only determined by the width of the tracer injection curve. The amount of

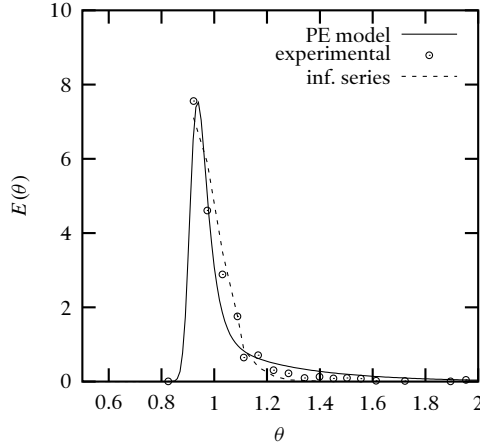


Figure 4.5: Dimensionless E -curve for a single channel. Markers: experimental data of Thulasidas *et al.* (1999). Full line: two-zone piston-exchange model. Dashed line: infinite series solution of the convection-diffusion equation for each slug, as calculated by Thulasidas *et al.*. $u_{\text{bubble}} = 2.0 \text{ cm/s}$, $Ca = 2.84 \times 10^{-4}$, $L_{\text{bubble}} = 2.6 \text{ cm}$, $L_{\text{slug}} = 0.83 \text{ cm}$.

tracer that is transferred to the film is slowly released to subsequent slugs, and appears in the E -curve as a long tail. So, increasing the mass transfer group increases the area under the tail of the E -curve. In Fig. 4.5, the E -curve for the two-zone model is plotted with parameters $k_{\text{SFA}} = 0.02 \text{ s}^{-1}$ and $\phi = 0.9$. The curve was calculated by numerically integrating Eqs. 4.4 and 4.5. Instead of a Dirac pulse, the experimental concentration versus time curve of the inlet was used. The calculated curve predicts a slightly larger tail than was found experimentally. This indicates that the mass transfer between the film and the slugs should be modelled with the developed Sherwood number instead of the developing one, which is larger and thus results in an even larger area under the tail. Finally, the model curve that was found by Thulasidas is also plotted in Fig. 4.5. This curve is based on a model that describes Taylor flow as discrete plugs, but for each slug and for the film infinite series solutions were used to model the radial diffusion processes. This model under-predicts the tailing, which might be caused by modelling the slug-film exchange as a pure diffusional process without enhancement by convection. On the other hand, the model of Thulasidas *et al.* describes the curve before the tailing better than the two-zone model, which is likely related to the more appropriate discrete features of their model. Note that for the experiment in Fig. 4.5, 16 slugs are between the inlet and the outlet, so collapsing the discrete tanks in series to differential equations in the axial direction is probably less appropriate for this particular experiment.

MONOLITH COLUMN

Before treating the monolith, first consider the hypothetical case of a multi-tubular reactor with thousands of channels in perfect plug flow, but where the residence times in the individual channels are normally distributed. The response to a Dirac inlet pulse of the fluid of all the channels collected at the exit is a Gaussian curve, provided the axial dispersion is not too large. Next, consider a similar tubular reactor, but now there is axial dispersion in each channel, and the residence time in all the channels is equal. The response curve of this reactor would also be a Gaussian curve.

From these hypothetical cases, it is clear that a single impulse response measurement in a monolith cannot distinguish axial dispersion inside the channels from a normal distribution of channel velocities, as was pointed out by Levenspiel & Fitzgerald (1983), who called the latter situation the Gaussian-convective model. The velocity distribution over the channels can be taken into account by adding an axial dispersion term to the dynamic zone of the single channel model. As a result, the Piston Dispersion Exchange model for the residence time distribution is obtained, which is widely used for packed bed columns (*e.g.* Iliuta *et al.*, 1996; Stegeman *et al.*, 1996).

$$\frac{\partial C_{\text{dyn}}}{\partial t} = D_{\text{ax}} \frac{\partial^2 C_{\text{dyn}}}{\partial z^2} - u_{\text{dyn}} \frac{\partial C_{\text{dyn}}}{\partial z} - \frac{k_{\text{SFA}}}{\phi} (C_{\text{dyn}} - C_{\text{st}}) \quad (4.12)$$

$$\frac{\partial C_{\text{st}}}{\partial t} = \frac{k_{\text{SFA}}}{1 - \phi} (C_{\text{dyn}} - C_{\text{st}}) \quad (4.13)$$

Introducing the following dimensionless parameters,

$$\theta = \frac{t u_{\text{dyn}} \phi}{L} \quad x = \frac{z}{L} \quad (4.14a)$$

$$Pe = \frac{u_{\text{dyn}} L}{D_{\text{ax}}} \quad N = \frac{k_{\text{SFA}} L}{u_{\text{dyn}} \phi} \quad (4.14b)$$

we obtain the dimensionless form of Eqs. 4.12–4.13:

$$\frac{\partial C_{\text{dyn}}}{\partial \theta} = \frac{1}{\phi Pe} \frac{\partial^2 C_{\text{dyn}}}{\partial x^2} - \frac{\partial C_{\text{dyn}}}{\partial x} - \frac{N}{\phi} (C_{\text{dyn}} - C_{\text{st}}) \quad (4.15)$$

$$\frac{\partial C_{\text{st}}}{\partial \theta} = \frac{N}{1 - \phi} (C_{\text{dyn}} - C_{\text{st}}) \quad (4.16)$$

The boundary and initial conditions that lead to the solution for the residence time distribution of Eqs. 4.15–4.16 are

$$C_{\text{dyn}} = 0, \quad C_{\text{st}} = 0 \quad \text{at} \quad t = 0 \quad (4.17a)$$

$$C_{\text{dyn}} = \delta(0) \quad \text{at} \quad x = 0 \quad (4.17b)$$

$$\frac{\partial C_{\text{dyn}}}{\partial x} = 0 \quad \text{at} \quad x = 1 \quad (4.17c)$$

Using axial dispersion to model maldistribution in a monolith column is efficient from a modelling point of view: the behaviour of the column is still described by a single channel model, which alleviates the engineer from calculating the Piston-Exchange curves for many channels and recombining them. The significant reduction in computational cost associated with using a single channel model is especially useful when the solution to the partial differential equations must be computed many times in a parameter estimation routine.

In Table 4.1, the variance for the various models introduced so far are given (Shah, 1979). It is apparent, that the contributions to the variance of the axial dispersion and the exchange with the static liquid are almost independent: only the exchange term is multiplied by a factor $(Pe^{-1} + 1)$. This suggests that applying dispersion to account for maldistribution is valid, provided the Peclet number is large enough.

Solutions to Eqs. 4.15–4.17c were calculated numerically using the DSS/2 routines (Schiesser, 1991) for the discretisation of the differential equations and LSODES (Hindmarsh, 1983) for the integration of the resulting ODE's. The same code was used to calculate the E -curves for the single channel models, where the Peclet number was set to 4000. If we set Pe to ∞ , a Dirac pulse has to propagate through the system. Setting Pe to a high finite value adds a tiny amount of dispersion to an otherwise pure convective equation, which stabilises the solution.

The most rigorous test of the multichannel PDE model was obtained from calculating the PE-model E -curves for 50 channels, combining those curves and comparing to a PDE curve. Using a normally distributed random number generator for each of the channels would require a very large number of channels to get reproducible results.

Table 4.1: variance of the E -curves for the various models for closed–open boundary conditions (Shah, 1979)

Axial Dispersion	$\sigma_{\theta}^2 = \frac{2}{Pe} + \frac{3}{Pe^2}$
PE model	$\sigma_{\theta}^2 = \frac{2(1 - \phi)^2}{N}$
PDE model	$\sigma_{\theta}^2 = \frac{2}{Pe} + \frac{3}{Pe^2} + \frac{2(1 - \phi)^2}{N} \left(\frac{1}{Pe} + 1 \right)$

RESIDENCE TIME DISTRIBUTION

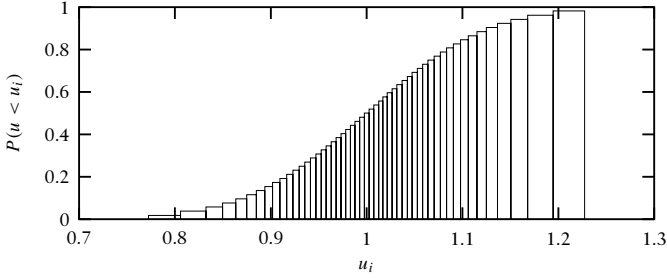


Figure 4.6: Using the cumulative normal distribution function to define velocities in individual channels: The fraction of channels having a lower velocity than channel i versus the velocity in channels i .

Here, we adopted a different approach, see Fig. 4.6. The cumulative distribution function gives a value between 0 and 1, that represents the fraction of samples from a distributed variable having a lower value. We divide this range – the vertical axis in Fig. 4.6 – into equal intervals, one for each channel. Taking the inverse of the cumulative distribution function from the midpoints of those intervals defined the velocity in each channel. The normal distributions were made dimensionless by dividing by the average velocity for all the channels.

The resulting E -curves must be combined on the same time scale. Using a subscript i to denote values for individual channels and no subscript for average values, we obtain

$$\theta_i = \frac{\tau_i}{\tau} \theta \quad (E(\theta))_i = \frac{\tau_i}{\tau} E_i(\theta_i) \quad (4.18)$$

Since each of the channels has a different velocity, the parameters of the PE-model change as well. The mass transfer parameter has to be multiplied by τ_i/τ . Only a small error is introduced if we do not change the static fraction with changing velocity, see Fig. 4.4, which shows that ϕ is not a strong function of velocity. For each of the channels, the value of Pe is kept at 4000.

A typical E -curve for the PE-model, the PDE-model, and the combination of the 50 channels is shown in Fig. 4.7. Here the relative standard deviation of the velocities in the 50 channels was 0.1, (*i.e.* $\sigma/u_{\text{dyn}} = 0.1$). The effect of maldistribution has a significant effect on the initial breakthrough time and the height of the peak. The effect on the tail of the curve is not as pronounced. This can be interpreted physically by realizing that the behavior of the film is practically independent of velocity. As the shape of the tail is mainly determined by the behaviour of the film, it follows that the tail of the E -curve is not very dependent on the velocity distribution. On the other hand, the shape of the early part of the E -curve is determined by the fast moving liquid inside the slugs, where the impact of velocity distribution is maximal.

Figure 4.7 indicates that the PDE model may indeed be used to model a maldistributed large number of channels, provided the velocities are normally distributed and

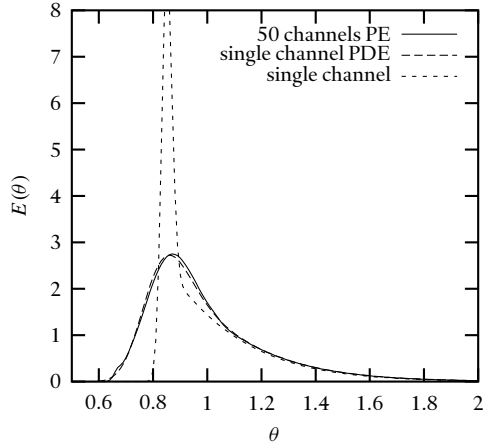


Figure 4.7: E -curves for a single channel (PE model), the combination of 50 channels (PE model) with a normal distribution of velocities and for a single channel with axial dispersion added (PDE model). For all single (PE) channels, $\phi=0.85$, $N=1.0$, $Pe=4000$. For the 50 channels, the dimensionless standard deviation σ of the velocities was 0.10. For the PDE model, $Pe = 195$, $\phi=0.85$, $N=1.0$.

the spread in distribution is not too large. These conditions are identical to the conditions for which a single channel with axial dispersion may be described by a Gaussian curve, which was the underlying concept for using the PDE model. For $Pe < 100$, the $E(\theta)$ curve of the axial dispersion model is no longer symmetric, and the maximum of the E -curve shifts from $\theta = \phi$ to lower values. In Fig. 4.8(a), suitable PDE curves are plotted together with the 50 channel curves for different extents of velocity maldistribution. Clearly, the use of the PDE model becomes less suitable if severe velocity maldistribution is present, because the maximum of the peak for the PDE model is significantly lower than the value of $\theta \approx \phi$ obtained for the maldistributed channels.

For axial dispersion in a channel without a stagnant zone, the standard deviation of the $E(\theta)$ curve is given by (Levenspiel, 1999):

$$\sigma_{\theta} = \sqrt{\frac{2}{Pe} - \frac{3}{Pe^2}} \quad (4.19)$$

Fig. 4.8(a) shows that the standard deviation of the velocities of all channels is related to the Peclet number in Eq. 4.19. In other words, the Peclet number that is obtained from fitting experimental E -curves to the PDE model will provide the distributions of velocities over the monolith cross section. The calculations shown in the figures were calculated for $N = 1$ alone. Several calculations for $N = 0.5$ revealed that independent of the mass transfer parameter:

RESIDENCE TIME DISTRIBUTION

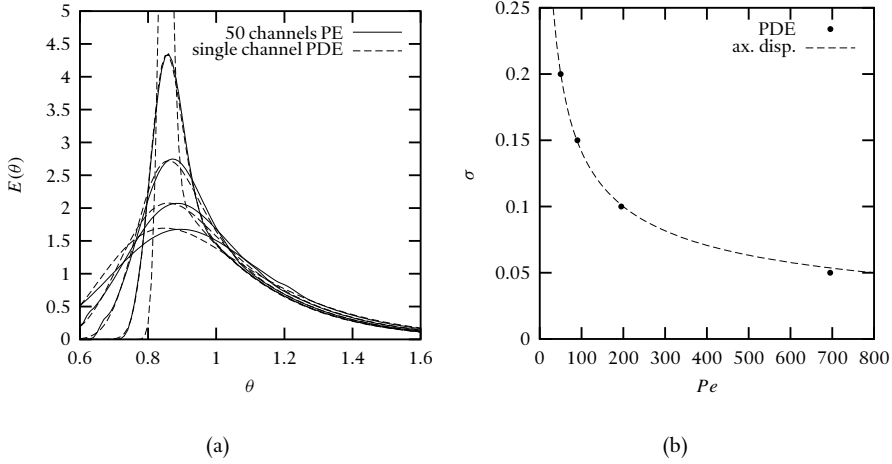


Figure 4.8: (a) Comparison of the E -curves from combining 50 channels and the E -curve from the PDE model. For all curves, $\phi = 0.85$ and $N = 1.0$. The velocity standard deviations were 0.05, 0.10, 0.15 and 0.20. (b) The velocity standard deviation versus the Peclet numbers used in the PDE model. The symbols refer to the values used in (a). The line is the standard deviation of $E(\theta)$ -curve for the axial dispersion model (without stagnant zone), Eq. 4.19.

- The (mal-)distribution of velocities in channels that individually behave according to the piston-exchange model, can be accurately model as a *false* axial dispersion in one channel.
- The Peclet number Pe corresponding to the axial dispersion can be used in Eq. 4.19 to obtain the standard deviation of the channel velocities.
- For $Pe < 100$, the maximum in the E -curve of the PDE model is too early.

EFFECT OF HOLD-UP DISTRIBUTION

Up to now, we have quietly assumed that the liquid holdup is the same in all channels, independent of the velocity inside the channels. The holdup in a channel is given by the ratio of liquid flowrate to total flowrate (Eq. 4.9), so the assumption of constant holdup implies

$$u_{Gs} = c_1 u_{Ls} + c_2 \quad (4.20)$$

in which the constant $c_2 = 0$ and c_1 is positive. This is unrealistic, because an increase in liquid flowrate through a channel will more likely cause a decrease in gas flowrate, which suggests that in Eq. 4.20, the constant c_1 should be negative. The equation

that describes all possible combinations of gas and liquid superficial flowrates inside a channel, of which Eq. 4.20 is a simple linear example, can be found by realising that the pressure drop over all the channels is the same. In other words, Eq. 4.20 is an isobar. The pressure drop over a channel has a frictional contribution and a gravitational contribution. For constant fluid properties and slug length, the group $F = 16[1 + 0.17\Psi_S^{-1}(Re/Ca)^{0.33}]$ is constant and the total pressure drop over a channel can be calculated with the pressure drop model of chapter II:

$$\begin{aligned} \frac{\Delta p}{L} &= -\frac{F\mu}{\rho(u_{L_s} + u_{G_s})d_{ch}} \frac{1}{2} \rho(u_{L_s} + u_{G_s})^2 \frac{4}{d_{ch}} \frac{u_{L_s}}{u_{L_s} + u_{G_s}} + \rho g \frac{u_{L_s}}{u_{L_s} + u_{G_s}} \\ &= -\frac{2Fu_{L_s}}{d_{ch}^2} + \rho g \frac{u_{L_s}}{u_{L_s} + u_{G_s}} \end{aligned} \quad (4.21)$$

At zero pressure drop, this reduces to

$$u_{G_s} = -u_{L_s} + \frac{\rho g d_{ch}^2}{2F\mu} \quad (4.22)$$

which shows that an increase in liquid velocity causes a decrease in gas velocity. The actual shape of isobars in monoliths is more complicated. The assumption that the slug aspect ratio Ψ_S is constant does not hold, and such isobars will be discussed in chapter VI, and here we consider only linear isobars. Only when the extent of distributions is not too large, a linearisation of the isobar is allowed.

If the constant c_1 is equal to -1, such as for zero pressure drop at constant slug length, then the total superficial velocity ($u_{L_s} + u_{G_s}$) in all the channels is the same, and the Peclet number that will be found from the RTD experiment will be infinite, reflecting that all the tracer that is introduced at $t=0$ leaves the reactor at the same time. If the constant c_1 is larger or smaller than -1, a distribution of u_{L_s} will lead to a distribution of both u_{TP} and ϵ_L . Channels with a higher holdup will contribute more to the E -curve. Provided the distribution of u_{L_s} and an isobar is given, the E -curve can be calculated in the following manner. Let $f(u_{L_s})$ be a distribution of liquid superficial velocities with mean $\langle u_{L_s} \rangle$, such that

$$\int_0^\infty f(u_{L_s}) du_{L_s} = 1 \quad \langle u_{L_s} \rangle = \mu_1(u_{L_s}) = \int_0^\infty u_{L_s} f(u_{L_s}) du_{L_s} \quad (4.23)$$

Now the distribution of gas superficial velocity may be calculated from

$$f(u_{G_s}) du_{G_s} = f(u_{L_s}) \frac{du_{L_s}}{|du_{G_s}|} du_{G_s} \quad (4.24)$$

where the derivative is calculated using the isobar (e.g. Eq. 4.20). The residence time that corresponds to a given u_{L_s} , assuming an isobar of the form Eq. 4.20, is equal to

RESIDENCE TIME DISTRIBUTION

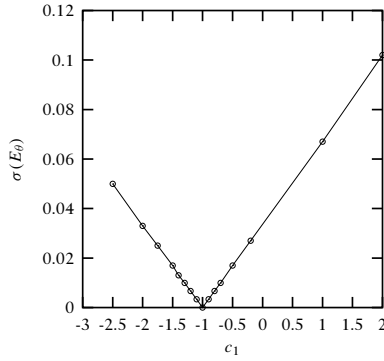


Figure 4.9: The standard deviation of the E -curve, calculated from a Gaussian distribution of u_{L_s} ($\mu = 0.075$ m/s, $\sigma = 0.005$ m/s) for various proportionality constants in a linear isobar (Eq. 4.20 with $c_2 = 0.075(1 - c_1)$ m/s or $u_{TP} = 0.15$ m/s).

$$t(u_{L_s}) = \frac{L}{u_{TP}} = \frac{L}{(c_1 + 1)u_{L_s} + c_2} \quad (4.25)$$

and by substitution of Eq. 4.20 the change in residence time with the change in u_{L_s} is given by

$$\frac{dt}{du_{L_s}} = \frac{L(c_1 + 1)}{[(c_1 + 1)u_{L_s} + c_2]^2} \quad (4.26)$$

The normalised amount of liquid that leaves the reactor in a time dt is given by the total velocity u_{TP} times the holdup, or $u_{TP}\epsilon_L = u_{L_s}$, times the fraction of channels having that total velocity:

$$Edt = \frac{u_{L_s}f(u_{L_s})du_{L_s}}{\langle u_{L_s} \rangle} \quad (4.27)$$

from which the E -curve is obtained by dividing by dt .

$$E(u_{L_s}) = \frac{u_{L_s}f(u_{L_s})[(c_1 + 1)u_{L_s} + c_2]^2}{L(c_1 + 1)\langle u_{L_s} \rangle} \quad (4.28)$$

and a plot of $E(u_{L_s})$ versus $t(u_{L_s})$ gives the E -curve. Using this approach to take a distribution of holdup into account for a linear isobar, it is clear that the standard deviation of the E -curve disappears as c_1 approaches -1. In Fig. 4.9, the standard deviation of the E -curve is plotted for several values of c_1 , which shows that the width of the E -curve is proportional to $|c_1 + 1|$, while for $c_1=1$, $\sigma(E_\theta)=\sigma(u_{L_s})/\mu_1(u_{L_s})$. Note that for a linear isobar, a Gaussian E -curve is obtained. For non-linear isobars, this is not necessarily the case.

The fact that the pressure drop in Taylor flow results in a negative constant c_1 shows that a given (dimensionless) distribution of u_{LS} results in a smaller (dimensionless) distribution of residence times. The isobar for constant slug aspect ratio Ψ_S and zero pressure drop shows that if a distributor sprays droplets on a monolith block, these droplets move through the channels as slugs at a constant velocity and the length of the bubbles between these slugs is determined by the interval between subsequent droplets that enter the channel. In other words, the pressure drop behaviour of Taylor flow “corrects” to some extent the maldistribution of liquid flowrates in the channels caused by an imperfect distributor.

To conclude the model development, we add a word of caution regarding the terminology used in this chapter. The word *dispersion* is used exclusively to describe a contribution to the E -curve that can be described by a second order derivative of the concentration in the axial direction, and the dimensionless number Pe is used exclusively to describe the proportionality constant for that contribution. Frequently, however, the Peclet number is directly calculated from the E -curve by taking the inverse of Eq. 4.19 as a measure for the width of the $E(\theta)$ curve, *i.e.* $(2/Pe) = \sigma_\theta^2$. In this chapter, the Bodenstein number Bo will be used for that purpose.

§ IV.3 EXPERIMENTAL

The residence time distribution measurements were performed using a coloured dye tracer. The experimental apparatus used in this work is shown in Fig. 4.10. A pump was used to recirculate water through the system. Most of the liquid was recirculated to the main liquid tank. Through a valve a part of the liquid was directed towards the monolith column. The liquid passed through a filter, and the liquid flow rate to the column was measured using one of two liquid flow meters (Digi-flow). Gas was fed into the monolith column from a digital mass flow controller (Brooks).

A small tube of known volume was filled with a concentrated tracer solution, and injected into the main liquid feed line by opening valves before and after the small tube. The injected tracer is passed through a static mixer to ensure complete mixing with the main liquid. Such complete mixing is essential if the measured inlet concentration curve is to be used for a mass balance, because otherwise a spectroscopic measurement of concentration does not give the mixing-cup concentration. Directly downstream of this mixer, the concentration of the liquid feed to the column was measured using a transmission flow cell.

The monolith column consisted of a distributor section at the top, and one, two or four 50 cm sections of a single monolith block. The cylindrical monolith blocks (diameter 4.3 cm) had a channel density of 400 cells per square inch (cpsi). The monoliths were coated with resin to prevent leakage. The monolith sections were connected in such a way, that the space between subsequent monolith blocks was less than 5 mm.

RESIDENCE TIME DISTRIBUTION

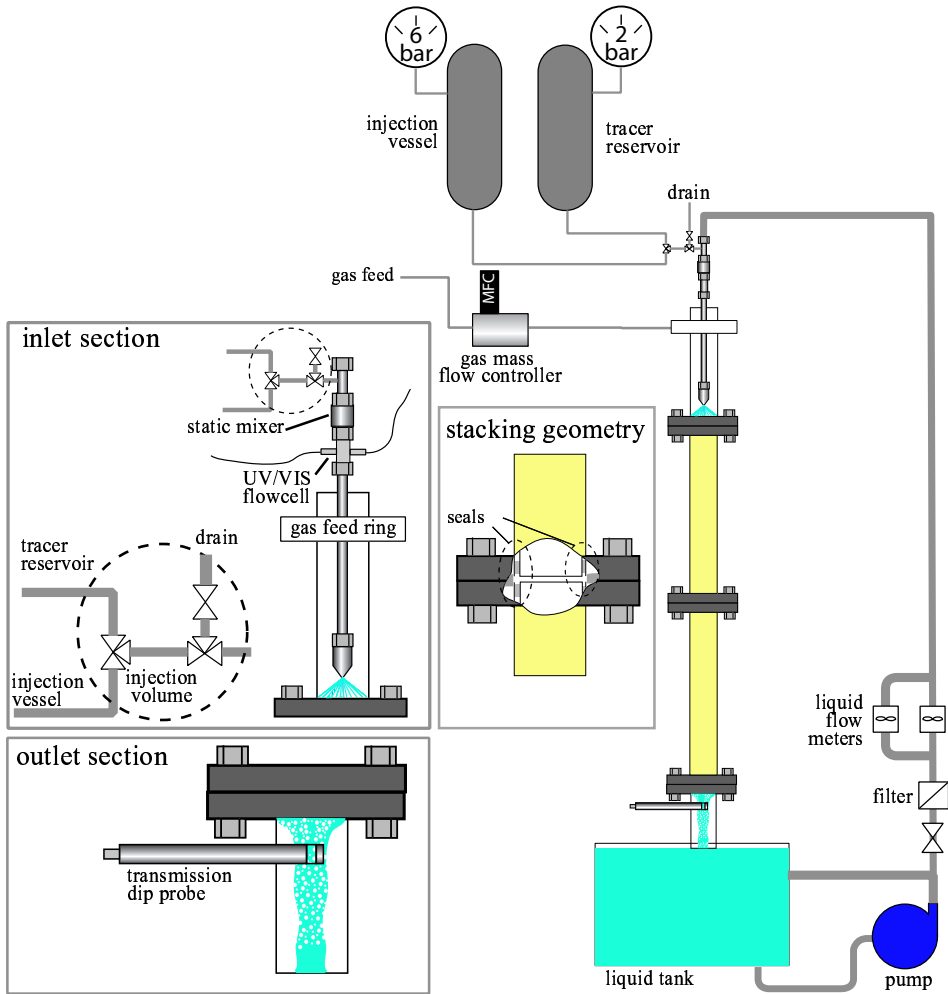


Figure 4.10: The setup used in the experiments.

Two types of distributors were used: a nozzle (Spraying systems) with even distribution characteristics and a static mixer distributor (see Fig. 4.11). The nozzle was positioned in such a way, that the spray hitting the monolith just touched the column wall. In the static mixer inlet section, the tube diameter was reduced at the top, and in the reduced part, 3 SMV-4 static mixer elements (Koch) were mounted. The reduced diameter increased the linear velocity of the gas and liquid, resulting in a better gas-liquid dispersion. Downstream of the SMV-4 elements, the tube diameter was grad-

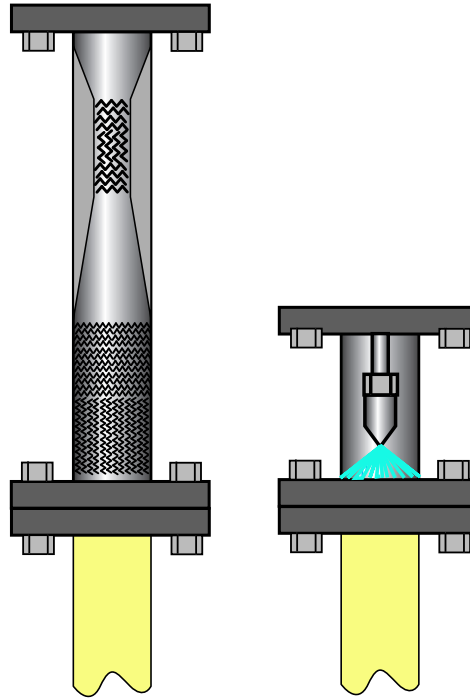


Figure 4.11: The distributors used in the experiments. left: static mixer, right: nozzle

ually increased to 4.3 mm, where two SMV-2 static mixer elements were mounted. 5 mm below these elements, the first monolith section was mounted.

Below the monoliths, a transmission dip probe (Ocean optics) was mounted to record the tracer concentration leaving the monolith.

MEASUREMENT TECHNIQUE

Both the inlet pulse at the top of the column and the response curve at the bottom of the column were measured by spectroscopy in the visual range. The inlet pulse was easy to measure, and a standard transmission flow cell was used. The flow cell was calibrated by running solutions of known dye concentration through the flow cell. Fig. 4.12 shows the recorded spectra for several tracer concentrations. A straight line was obtained for the concentration versus the absorbance using the Lambert-Beer law:

$$A = \alpha(\lambda) b C = -\log \left(\frac{I - I_{\text{dark}}}{I_{\text{ref}} - I_{\text{dark}}} \right) \quad (4.29)$$

RESIDENCE TIME DISTRIBUTION

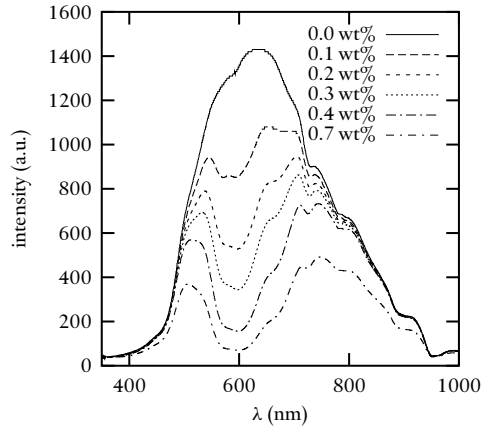


Figure 4.12: The spectra for different concentrations of tracer. The maximum absorption occurred at 600 nm. In the RTD experiments, the tracer concentration was always lower than 0.2 wt%.

where A is the absorbance, b is the path length, c is the concentration, α is the wavelength dependent absorption coefficient, I is the intensity at concentration c , I_{ref} is the intensity of pure water, and I_{dark} is the intensity with the light source turned off.

The outlet pulse was impossible to measure using a flow cell directly under the monolith, because the gas-liquid flow out of the column was a froth, and bubbles inside that froth deflected the light away from the receiving fibre. At first, a gas-liquid separator was used to remove the bubbles, and the liquid flow out of the separator was analysed with a standard flow cell. However, the minimal volume of the separator was about equal to the monolith volume, and the response curve was dominated by this back-mixed separator tank. It is possible to deconvolute the contribution of the separator out of the response curve, but this required an excessive amount of filtering and curve smoothing.

The solution to this problem was found by using a transmission dip probe (Ocean Optics). In this probe, part of the liquid leaving the monolith flows through a small cell of adjustable optical path length. On one side of this cell, six fibres emit light, and one fibre collects the light. On the other side of the cell a concave mirror is situated. It was found that in this probe, the light from at least two fibres made it to the collecting fibre, and the light from the other four fibres either reflected away by passing through a bubble, or also reached the collecting fibre.

The probe was tested in a bubble column, filled with liquid of a known tracer concentration. A gas sparger was placed below the probe, such that bubbles passed through the cell, which was confirmed by visual observation. The spectrum of the probe was recorded with an integration time of 100 ms. Analysis of the spectra showed that although the absolute values of the intensity at different wavelengths varied, the ra-

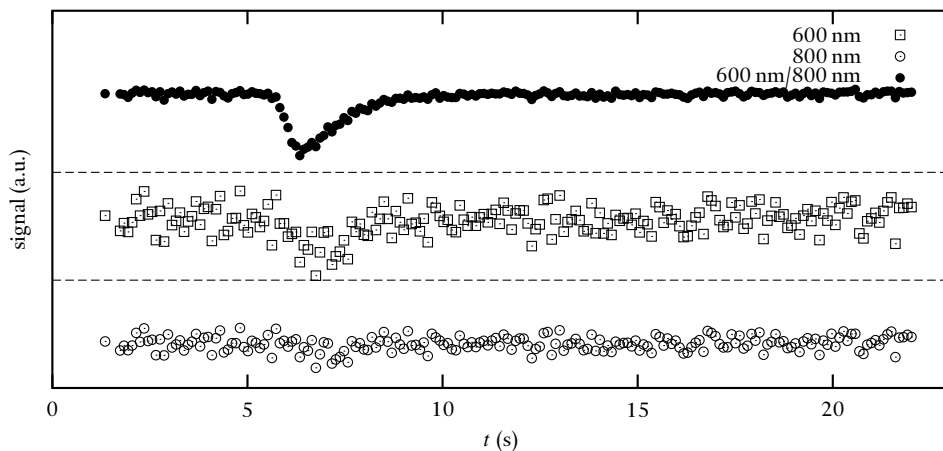


Figure 4.13: Illustration of the use of the dip probe at two different wavelengths, experimental data collected by mounting the dip probe under the monolith.

ratio of the intensity at two different wavelengths was constant for a given concentration. Thus, the absolute height of the spectrum varied with time, but the shape of the spectrum did not vary with time. The best results were obtained by choosing a wavelength near the maximum absorption by the colour dye (600 nm), and a wavelength practically unaltered by the dye (800 nm). The intensity ratios were processed in the same way as Eq. 4.29, with the intensities replaced by the intensity ratios. A straight line was obtained in a plot of the absorbance versus concentration with $R^2 = 0.998$.

The probe was mounted 3 cm below the monolith in the centre of the column tube. As depicted schematically in Fig. 4.10, the liquid leaving the monolith contracts, so the liquid passing through the dipprobe does not come from the centre of the monolith alone. A sample set of raw data recorded by the spectrometer is shown in Fig. 4.13, which shows that the recorded intensities at 600 nm and 800 nm appears to be extremely contaminated with noise, but the calculated intensity ratio shows a relatively clean pulse response.

During all calibration experiments the signal was recorded several hundreds of times and from these long series the average value and standard deviation were calculated. Calculation of the error propagation based on these standard deviations revealed that the amount of noise from the spectrometer in the calculated concentration was approximately constant over the range of concentrations measured.

RESIDENCE TIME DISTRIBUTION

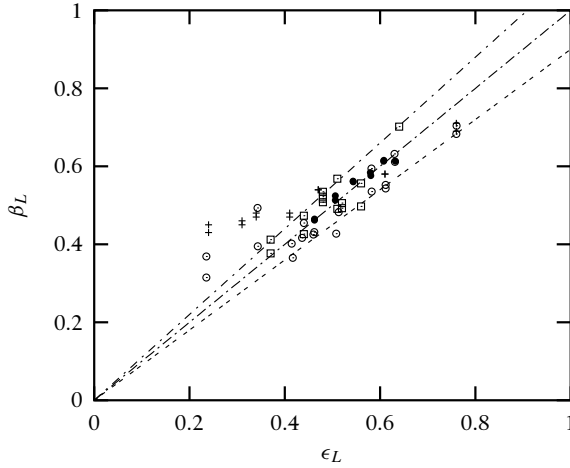


Figure 4.14: Comparison of liquid holdup, calculated from the first moment of the E -curve, with the holdup based on superficial velocities. The lines indicate parity and $\pm 10\%$

§ IV.4 RESULTS

The reproducibility of the setup was found to be very good, and essentially the recorded responses at the inlet and the outlet were identical for several runs. The amount of tracer was calculated by integrating the concentration in time, and the difference between the inlet and outlet was within 10%, with an average error of 4%. The impact of the spread in the inlet pulse was calculated by comparing the variance of the outlet curve from the inlet curve. For a given vessel, the variance at the outlet can be calculated from the inlet variance by

$$\sigma_{\text{vessel}}^2 = \sigma_{\text{out}}^2 - \sigma_{\text{in}}^2 \quad (4.30)$$

The variance of the inlet signal was found to be less than 2% of the variance of the outlet signal. Apart from the monolith, liquid flows through the inlet tube, the nozzle, the top spray and the froth below the monolith. It is safe to assume that the flow is plug flow in these parts. This means that the only deconvolution that is required to process the outlet curve is the subtraction of the total residence time outside the monolith from the outlet curve, which can be easily estimated from the liquid flow rate.

The $c(t)$ -curves were transformed into $E(\theta)$ curves by dividing by the integral of the $c(t)$ -curve and calculating the first moment of the $E_t(t)$ curve to obtain τ . The dynamic liquid holdup in the monolith can be calculated from

$$\beta_L = \frac{\phi_L \tau}{V} \quad (4.31)$$

Table 4.2: Experimental conditions for the Figs. 4.16, and the estimated parameters for those experiments. The values between brackets indicate the 95 % confidence interval.

Fig	L	u_{Ls}	u_{Gs}	Pe	ϕ	N
a	2	0.15	0.04	296 (± 27)	0.90 (± 0.018)	0.96 (± 0.07)
b	2	0.15	0.14	178 (± 9)	0.96 (± 0.013)	0.54 (± 0.04)
c	1	0.15	0.04	199 (± 14)	0.77 (± 0.012)	1.56 (± 0.05)
d	1	0.12	0.14	67 (± 3)	0.84 (± 0.016)	0.38 (± 0.03)
e	1	0.14	0.15	110 (± 5)	0.84 (± 0.011)	0.29 (± 0.03)
f	0.5	0.11	0.15	59 (± 7)	0.86 (± 0.06)	1.2 (± 0.14)

where V is the open volume of the monolith and τ is the residence time from the E -curve. Fig. 4.14 shows a comparison of the dynamic holdup β_L with the holdup based on superficial velocities, $\epsilon_L = u_{Ls}/(u_{Ls}+u_{Gs})$. The residence time based on the E -curves was within 10 % of the theoretical value, except for several measurements at low liquid holdup.

The experimental data were fitted to the numerical PDE-model. The noise in the signal was constant for all concentrations, so the objective function in the minimisation routines was the sum of squared residuals, and no weighing factors were included. From the initial guess, first the more robust simplex method (Nelder & Mead, 1965) was used to find the approximate minimum. Subsequently, the Levenberg-Marquardt

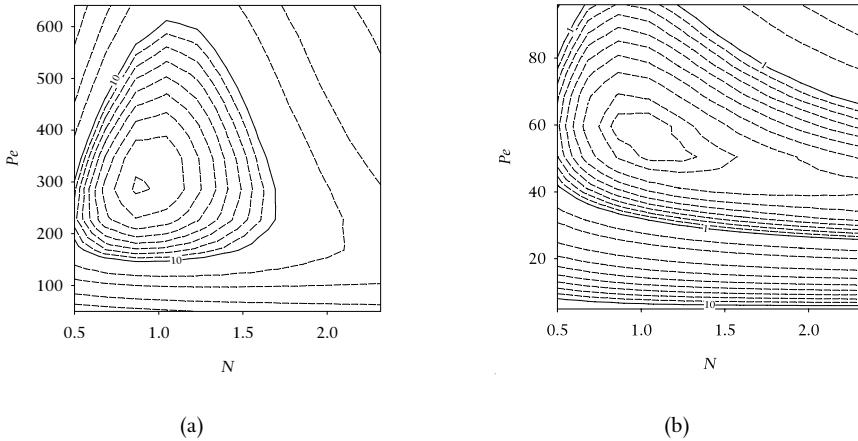


Figure 4.15: Contour plots of the objective function in the fitting procedure. The plots show the sum of squared residuals against N and Pe for the best fit of ϕ . (a) corresponds to Fig 4.16(a), (b) corresponds to Fig 4.16(f)

RESIDENCE TIME DISTRIBUTION

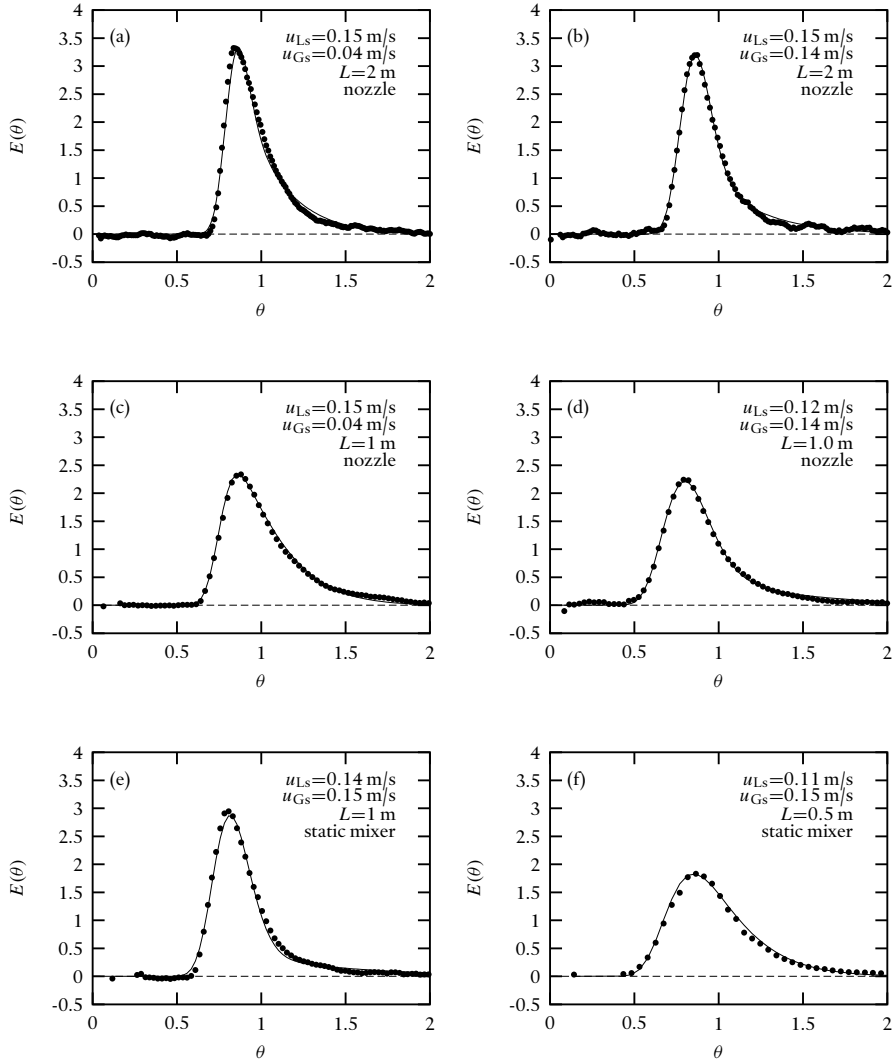


Figure 4.16: Experimental E -curves (markers) and fitted PDE curves (lines) Nozzle distributor, except for (e) and (f), where the static mixer was used. (See table 4.2 for the fitted PDE parameters)

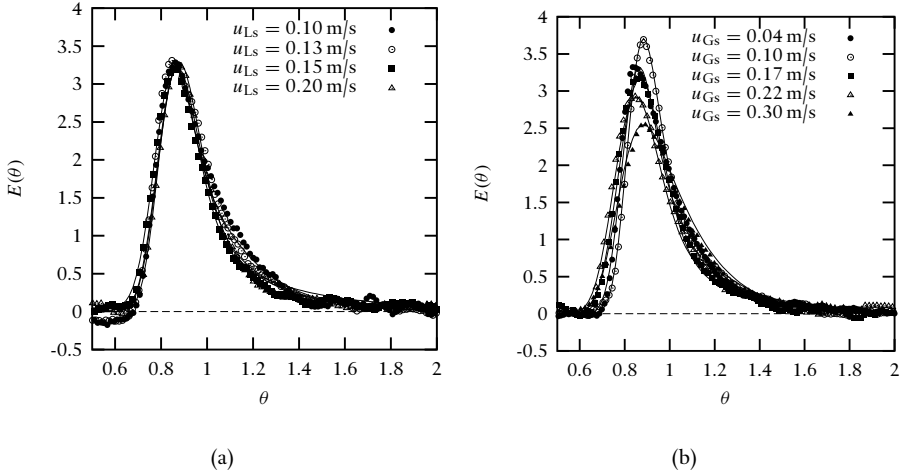


Figure 4.17: Impact of the liquid and gas superficial velocity on the shape of the E -curves. (a) u_{Ls} varied at $u_{Gs} \approx 0.15$ m/s. (b) u_{Gs} varied at $u_{Ls} \approx 0.15$ m/s. $L_{col} = 2$ m, nozzle distributor.

method (Levenberg, 1944; Marquardt, 1963) was used to enhance the rate of convergence to find the exact minimum. Fig. 4.15 shows contour plots of the sum of squared residuals.

Six experimental curves are shown in Fig. 4.16, and the flow rates, column length and fitted parameters for those curves are given in Table 4.2. In all but a few cases, the PDE model fitted very nicely to the experimental curves, which indicates that for monoliths, using a PE-model for a single capillary and describing maldistribution by axial dispersion captures the main features of the flow. The influence of the liquid velocity on the $E(\theta)$ curves was small, see Fig. 4.17(a). Increasing the gas velocity lowered the maximum of the E -curve slightly. Figs. 4.17(b) shows the effect of a more than sixfold increase in gas velocity. Especially for gas flowrates above 0.2 m/s, the peak becomes broader. Increasing the column length resulted in narrower $E(\theta)$ curves. In Fig. 4.16, comparing curves (a) with (c) and (b) with (d) shows the difference between 2 meter and 1 meter of column length. Finally, using the static mixer leads to narrower E -curves than using the nozzle. This is illustrated by Figs. 4.16(d-e).

§ IV.5 DISCUSSION

In all cases, asymmetric curves typical for PDE-models were found. This indicates that the back-mixing problems, encountered in upflow (Thulasidas *et al.*, 1999) are not present when monoliths are operated down-flow. The agreement of the liquid holdup,

based on the first moment of the E -curve and the holdup based on no-slip slug flow in Fig. 4.14 indicates that velocity and holdup maldistributions are not severe, provided the liquid holdup is not too low. As an extreme scenario, consider what happens when some of the channels are without liquid: the gas velocity in these channels will be very high, since the pressure drop in those channels must be the same as in the channels with liquid flowing. As a result, the presence of gas-only channels will result in lower total velocities in the channels with two-phase flow, and a higher holdup of liquid is observed. Note that this is an extreme scenario: it is not necessary that channels are completely without liquid. If the isobar is a non-linear function for which (du_{Gs}/du_{Ls}) increases with decreasing holdup (*i.e.* for which the total velocity u_{TP} increases with decreasing holdup), the same effect happens.

Although the individual curves could all be fitted to the PDE model, a large scatter was found when the fitted parameters were correlated against velocity of hold-up. Stegeman *et al.* (1996) showed that the parameters Pe and N are very sensitive towards deviations in the first moment of the E -curve τ , which may explain the scatter. Further, the PDE model assumes that the maldistributions result in a Gaussian contribution to the E -curve. If the the isobar of possible combinations of u_{Ls} and u_{Gs} is linear and the distribution of u_{Ls} (or u_{Gs}) is Gaussian, this is indeed the case. If the isobar is not linear, or if the distribution of u_{Ls} is not Gaussian, the resulting E -curve deviates from a Gaussian shape, and some of the long tail is wrongly attributed to tracer exchange with the stagnant liquid.

The average value of the static fraction was $1 - \phi \approx 0.15$, which is slightly lower than the static fraction estimates based on film thickness correlations (see Fig. 4.4). These correlations were derived from data of horizontal flow, and there is agreement in the literature that the film fraction in downflow is lower.

The Peclet numbers obtained from fitting showed that for the two meter column, $Pe \approx 200$, while for the one meter and 0.5 meter column values of 100 and 50, respectively were found.

The parameter N was also roughly proportional to the column length. The data for the one meter column showed much more scatter. The contour plot in Fig. 4.15(b) shows that the uncertainty in the mass transfer group is larger for short columns. Comparing Figs. 4.16 (e) and (f) shows that for the 1 meter column (e), a distinct tail can be clearly seen, while for the 0.5 meter column (f), the tail is buried in the peak broadening of the main peak. The mass transfer group k_{SFA} was approximately 0.3 s^{-1} . This is in agreement with the mass transfer model, provided the diffusion coefficient of the tracer is $3 \times 10^{-9} \text{ m}^2/\text{s}$.

Levenspiel & Fitzgerald (1983) warned that for a system that is dominated by a dispersion mechanism, *i.e.* a stochastic velocity distribution, the variance of the dimensional E_t -curve σ_t^2 grows linearly with length ($\sigma_t^2 \propto L$) whereas for a Gaussian-convective system (deterministic velocity fluctuations), the variance is proportional to \sqrt{L} . In our experiments, the peak broadening that is characterised by the Peclet number is stochastic, because $Pe \propto L$ implies that the variance of the E -curve is proportional to

the length, *i.e.* $\sigma_t^2 \propto L$ and $\sigma_\theta^2 \propto L^{-1}$. In the single channel data, the broadening of the peak is absent, and only the long tail is present. This suggests that the hydrodynamic behaviour inside the channels is not causing the length dependent behaviour, and the more plausible explanation is velocity maldistribution. The monoliths in our setup are not stacked directly on top of each other, but rather there is a small space between them, see Fig. 4.10. If the velocity in each block has the same distribution, then redistribution in the open space between the blocks would result in a more narrow distribution. This redistribution is a stochastic process, which is in agreement with the observed length dependence of the Peclet number.

Several experiments performed in a one meter column with six stacked monoliths showed less dispersion than the column with only two blocks: the average Pe increased from 100 to 160, which confirms the assumption that redistribution between blocks leads to more plug flow behaviour. However, the increase in Pe is clearly not only dependent on the number of stackings. Reinecke & Mewes (1999) showed that in monoliths, oscillatory transients in the velocity may also be present. In the single channel study described in chapter II of this thesis, it was indeed observed that it takes a long time for Taylor flow in a single channel to stabilise. For multiple channels, such oscillations are likely to be more severe, and such random (stochastic) velocity fluctuations may also lead to a broadening of the peak that obeys the scaling $\sigma_\theta^2 \propto L^{-1}$ that was found experimentally.

From the proposed model, we can estimate the amount of maldistribution in monoliths from the RTD data. For a single monolith block, the standard deviation is approximately 0.20 for the nozzle distributor and 0.15 for the static mixer. Three redistributions between the stacked monolith blocks reduces this to 0.10. Note that the standard deviation only corresponds to the standard deviation of u_{TP} if the holdup in the channels is constant. If at constant pressure drop an increase in liquid flowrate is accompanied by a decrease in gas flowrate, the standard deviation of u_{TP} is larger than the standard deviation of the E -curve. Although an accurate model for the pressure drop was presented in chapter II of this thesis, it is not possible to predict the shape of the isobar without an estimate of the slug length. In chapter VI, some isobars are discussed for a column in which the slug length was measured.

We can define a Bodenstein number for the E -curve, based on the moments of the curve alone, *i.e.*

$$\frac{2}{Bo} = \frac{\sigma^2}{\tau^2} = \sigma_\theta^2 \quad (4.32)$$

Comparing the thus obtained Bo with σ_θ^2 from the PDE model (see table 4.1) shows that $Bo \approx 2/\sigma_\theta^2$. On average, the Bodenstein number was about 30 per meter column length if the nozzle was used as a distributor. With the static mixer as a distributor, $Bo \approx 40L$. Typically, in order to calculate the conversion in a reactor, a reactor can be considered as plug flow if the Bodenstein number is larger than 100. Therefore, down-flow monoliths can be regarded as plug flow, except for short columns.

While the $Bo > 100$ criterion holds for single reactions, the effect of residence time distribution on product distribution when multiple reactions are involved can be more severe. As was stated in the introduction, many different flow patterns may result in the same residence time distribution. This follows from the fact that the RTD is based on measurements outside the reactor alone. For the calculation of the conversion and selectivity of multiple reactions in a monolith column, the information that is obtained from E -curves may not be enough. For the additional information on how fluid elements of different age encounter one another in the reactor – the earliness of mixing – two extremes may be identified: (1) complete segregation: fluid elements of the same residence time mix only when they leave the reactor and (2) maximum mixedness: fluid elements of different residence times mix as soon as they enter the reactor.

For monoliths, it is immediately clear which model to choose. There is no convective transport from channel to channel, so for a single block the segregation model is the obvious choice. If several blocks are stacked on top of each other, it may be necessary to use a PDE-model-in-series (with mixing in between), in which the Peclet number for each section is chosen in such a way that for the entire ensemble the tracer curve is recovered.

The work presented in this chapter is concerned with the residence time distribution of the liquid phase alone. However, only little speculation is required to propose a model for the gas phase. In Taylor flow, the bubbles do not coalesce, and in a single channel the gas phase will be in perfect plug flow. The distribution of gas phase superficial velocities may be deduced from the isobar and the distribution of the liquid phase superficial velocities. So, for the gas phase this results in an axial dispersion parameter alone.

§ IV.6 CONCLUSIONS

The residence time distribution of monolith catalyst carriers was found to be close to that of plug flow, if the monolith is operated in the Taylor flow regime in co-current down-flow. The RTD of Taylor flow in single capillary channels is well understood, and a two-zone pure convective-exchange model was formulated that is plausible when compared to literature data. The maldistribution of velocity over the monolith channels was modelled by adding dispersion to the single channel model. This approach was tested and found to be a valid approximation. The variance of the E -curve depends on the distribution of holdup and total linear velocity in the channels, and the relative contribution of both can be found provided the pressure drop behaviour in the individual channels is known.

Experiments were performed to measure the RTD in monoliths. The data allow the following conclusions:

- Monolith RTD behaviour can be interpreted using a PDE model.

- The effect of maldistributions over the channels leads to a dispersion-like contribution to the E -curve with a variance in the order of 0.2 for a single block.
- The extent of maldistribution depends on the distributor used.
- A static mixer system is a better distributor than a nozzle.
- Stacking monolith blocks leads to redistribution, which in turn reduces the observed amount of backmixing and maldistribution.
- The holdup calculated based on no-slip slug flow agrees with the experimental hold-up, except for low hold-up, where the presence of gas-only channels leads to an increase in average holdup in the channels.
- The measured fraction of liquid in the film agrees well with a calculation, based on experimental film thickness correlations for square capillaries.
- The measured slug-to-film mass transfer agrees with a solution of the convective-diffusion equation for the slug, provided that the tracer in the slug is in equilibrium with the film at the entrance of the reactor.

NOTATION

a	interfacial area per unit channel volume, m^{-1}
A	absorbance, -
b	path length, m
c_1, c_2	constants in linear isobar equations
C	concentration, kg/kg
C_{dyn}	dynamic phase concentration, -
C_{st}	static phase concentration, -
D	diffusion coefficient, m^2/s
D_{ax}	axial dispersion coefficient, m^2/s
d	diameter, m
E_t	residence time distribution, s^{-1}
E	residence time distribution, -
f	distribution function, -
I	intensity, counts/s
I_{dark}	intensity without light source
I_{ref}	intensity without tracer
k_{SF}	film to slug mass transfer coefficient, m/s
L	column length, m
L_B	bubble length, m

RESIDENCE TIME DISTRIBUTION

L_S	slug length, m
t	time, s
u	velocity, m/s
u_{dyn}	velocity dynamic phase, m/s
u_{G_S}	superficial gas velocity, m/s
u_{L_S}	superficial liquid velocity, m/s
V	monolith volume, m ³
z	axial coordinate, m

Greek letters

α	absorption coefficient
β_L	dynamic holdup, m ³ /m ³
γ	surface tension, N/m
δ	film thickness, m
$\delta()$	dirac pulse (Eq. 4.17b)
ϵ_L	liquid holdup, m ³ /m ³
λ	wavelength, m
μ_L	liquid viscosity, Pa s
μ_1	first moment
σ	standard deviation, s ⁻¹ or -
θ	dimensionless time
τ	mean residence time from E -curve, s
ϕ_L	liquid flow rate, m ³ /s
ϕ_G	gas flow rate, m ³ /s
ρ	density, kg/m ³
σ	surface tension, N/m

Dimensionless numbers

Bo	Bodenstein number, based on E -curve moments. ($= \sigma^2/2\tau^2$)
Ca	capillary number ($= \mu_L u/\sigma$)
F	Taylor flow friction group ($= 16[1 + 0.17\Psi_S^{-1}(Re/Ca)^{1/3}]$)
Gz	(mass) Graetz number ($= L/dReSc$)
N	mass transfer group ($= k_{SF}L/u$)
Pe	Peclet number ($= uL/D_{ax}$)
Re	Reynolds number ($= \rho u d/\mu$)
Sh	Sherwood number ($= kd/D$)
x	dimensionless length
θ	dimensionless time
ϕ	dynamic liquid fraction
Ψ_S	slug aspect ratio, m/m

BIBLIOGRAPHY

- AUSILOUS, P. & QUÉRE, D. 2000 Quick deposition of a fluid on the wall of a tube. *Physics of Fluids* 12 (10), 2367–2371.
- BERČIČ, G. & PINTAR, A. 1997 The role of gas bubbles and liquid slug lengths on mass transport in the Taylor flow through capillaries. *Chemical Engineering Science* 52 (21/22), 3709–3719.
- BREHERTON, F. P. 1961 The motion of long bubbles in tubes. *Journal of Fluid Mechanics* 10, 166–188.
- CUSSLER, E. L. 1997 *Diffusion, Mass Transfer in Liquid Systems*, 2nd edn. Cambridge, United Kingdom: Cambridge University Press.
- DANCKWERTS, P. V. 1956 Continuous flow systems, distribution of residence times. *Chemical Engineering Science* 2 (1), 1–13.
- VAN EERD, J. P. F. M. & KREUTZER, E. K. J. 1987 *Klinische chemie voor analisten*, , vol. 2. Utrecht/Antwerpen: Bohn, Scheltema en Holkema.
- HAZEL, A. L. & HEIL, M. 2002 The steady propagation of a semi-infinite bubble into a tube of elliptical or rectangular cross-section. *Journal of Fluid Mechanics* 470, 91–114.
- HEISZWOLF, J., ENGELVAART, L., VAN DER EIJDEN, M., KREUTZER, M., KAPTEIJN, F. & MOULIJN, J. 2001 Hydrodynamic aspects of the monolith loop reactor. *Chemical Engineering Science* 56 (3), 805–812.
- HINDMARSH, A. C. 1983 ODEPACK, a systematized collection of ODE solvers. In *Scientific Computing, Applications of Mathematics and Computing to the Physical Sciences* (ed. R. S. Stepleman), *IMACS Transactions on Scientific Computation*, vol. 1, pp. 55–64. Amsterdam: Elsevier Science Ltd.
- HORVATH, C., SOLOMON, B. A. & ENGASSER, H.-M. 1973 Measurement of radial transport in slug flow using enzyme tubes. *Industrial and Engineering Chemistry Fundamentals* 12 (4), 431–439.
- ILIUTA, I., THYRION, F., MUNTEAN, O. & GIOT, M. 1996 Residence time distribution of the liquid in gas-liquid cocurrent upflow fixed-bed reactors. *Chemical Engineering Science* 51 (20), 4579–4593.
- KOLB, W. B. & CERRO, R. L. 1991 Coating the inside of a capillary of square cross-section. *Chemical Engineering Science* 46 (9), 2181–2195.
- LEVENBERG, K. 1944 A method for the solution of certain non-linear problems in least squares. *Quarterly Applied Mathematics* 2, 164–168.
- LEVENSPIEL, O. 1999 *Chemical Reaction Engineering*, 3rd edn. John Wiley and Sons, New York.
- LEVENSPIEL, O. & FITZGERALD, T. J. 1983 A warning on the misuse of the dispersion model. *Chemical Engineering Science* 38 (3), 489–491.
- MANTLE, M. D., SEDERMAN, A. J. & GLADDEN, L. F. 2002 Dynamic MRI visualization of two-phase flow in a ceramic monolith. *A.I.Ch.E. Journal* 48 (4), 909–912.
- MARQUARDT, D. W. 1963 An algorithm for least squares estimation of nonlinear pa-

- rameters. *Journal of the Society for Industrial and Applied Mathematics* 11, 431–441.
- NELDER, J. A. & MEAD, R. 1965 A simplex method for function minimization. *Computer Journal* 7, 308–313.
- PEDERSEN, H. & HORVATH, C. 1981 Axial dispersion in a segmented gas-liquid flow. *Industrial and Engineering Chemistry Fundamentals* 20, 181–186.
- REINECKE, N. & MEWES, D. 1999 Oscillatory transient two-phase flows in single channels with reference to monolithic catalyst supports. *International Journal of Multiphase Flow* 25 (6-7), 1373–1393.
- SCHIESSER, W. E. 1991 *The Numerical Method of Lines – Integration of Partial Differential Equations*. San Diego CA, USA: Academic Press.
- SHAH, Y. T. 1979 *Gas-liquid-solid reactor design*. New York: McGraw Hill.
- STEGEMAN, D., VAN ROOIJEN, F. E., KAMPERMANS, A. A., WEIJER, S. & WESTERTERP, K. R. 1996 Residence time distribution in the liquid phase in a cocurrent gas-liquid trickle bed reactor. *Industrial and Engineering Chemistry Research* 35 (2), 378–385.
- TAYLOR, G. I. 1960 Deposition of a viscous fluid on the wall of a tube. *Journal of Fluid Mechanics* 10, 161–165.
- THIERS, R. E., REED, A. H. & DELANDER, K. 1971 Origin of the lag phase of continuous-flow analysis curves. *Clinical Chemistry* 17 (1), 42–48.
- THULASIDAS, T. C., ABRAHAM, M. A. & CERRO, R. L. 1995a Bubble-train flow in capillaries of circular and square cross section. *Chemical Engineering Science* 50 (2), 183–199.
- THULASIDAS, T. C., ABRAHAM, M. A. & CERRO, R. L. 1997 Flow patterns in liquid slugs during bubble-train flow inside capillaries. *Chemical Engineering Science* 52 (17), 2947–2962.
- THULASIDAS, T. C., ABRAHAM, M. A. & CERRO, R. L. 1999 Dispersion during bubble-train flow in capillaries. *Chemical Engineering Science* 54 (1), 61–76.
- THULASIDAS, T. C., CERRO, R. L. & ABRAHAM, M. A. 1995b the monolith froth reactor: Residence time modelling and analysis. *Chemical Engineering Research and Design* 73, 314–319.

CHAPTER V

GAS COMPONENT MASS TRANSFER

§ V.1 INTRODUCTION

The term *intrinsic* kinetics is used for the rate of a catalysed reaction that is based on the actual conditions inside the catalysts. These conditions, mainly the temperature and concentrations of species involved, may be constant throughout the catalyst volume and may be essentially equal to the concentrations outside the catalyst. If this is the case, the measured kinetics can be interpreted as the intrinsic kinetics in terms of measured concentrations and temperature outside the catalyst. However, if heat or mass transfer rates are comparable to the rate of reactions, significant gradients in temperature and concentration develop, and the conditions measured outside the catalyst can only be interpreted as *observed* or *effective* kinetics. Inside the catalyst, diffusion of reactants is balanced by reaction, and the integral of the reaction rate over the catalyst volume is balanced by the transfer rate to the catalyst. Assuming the catalyst is in the liquid phase, the reaction is also balanced by the transfer rate from the gas phase to the liquid phase for the gas components. Analogous balances in terms of the heat of reaction and heat transfer may be written for the energy equation. In this chapter, only mass transfer limitations will be considered.

Whether the overall mass transfer rate of gas-phase reactants to the catalyst is relevant in the design of three-phase reactors is largely determined by the ratio of reaction rates on the one hand and mass transfer rates on the other hand. For slow reactions (or high mass transfer rates), the observed behaviour of the reactor is independent of the transport phenomena. For fast reactions (or low mass transfer rates), the observed kinetics are at least in part coupled to transport phenomena, and this coupling is referred to as (mass) transfer *limitations*. The effect of transport limitations is not limited to the rate of reaction or the observed conversion. The changes in concentration inside the catalyst may also have an impact towards the selectivity of the reaction, which is usually negative. If the undesired reaction is one that reduces the catalyst activity, the stability of the catalyst may also be reduced by transport limitations. For instance, such catalyst deactivation is frequently encountered for hydrogenation reactions, where the desired reaction of an unsaturated compound with hydrogen competes with the unde-

sired oligomerisation of the compound. In fact, this is a selectivity problem with hydrogen pressure as a control parameter. The presence of hydrogen inside the catalyst favours the first reaction, and a decrease in hydrogen concentration inside the catalyst by transport limitations leads to a relative increase in the oligomerisation reaction. For this reason alone, many hydrogenation reactions are carried out under high hydrogen pressure, especially if the process suffers from mass transfer limitations.

In chapter III of this thesis, the mass transfer of liquid phase components was studied and validated with literature data of a fully mass transfer limited liquid-solid reaction. Here the adjective *fully* indicates that the process is completely limited by mass transfer: in other words, molecules are converted immediately as they come into contact with the catalyst, and the concentration in(side) the catalyst is essentially zero. Under these conditions, the observed kinetics are completely determined by the mass transfer behaviour.

In three-phase reactors, the catalyst is usually in the liquid phase and for the gas phase components two mass transfer steps need to be considered: first from the gas phase to the liquid phase and subsequently from the liquid phase to the catalyst. In the simplest case, these mass transfer steps may be regarded as independent of one another, and a so-called “bulk” region of constant concentration of dissolved gas components in the liquid far from the gas or solid phase can be used to model the independent steps as resistances-in-series. This approach, in which the spatial variation of concentration is modelled by straight lines in the thin “films” near the gas and solid phase (Lewis, 1916; Whitman, 1923), is normally valid for (agitated) slurry reactors. In fixed-bed trickle reactors, the concept of a bulk phase is usually less valid because of the absence of a true bulk region of constant concentration: the “films” on the gas-liquid side and the liquid-solid side may overlap if the liquid layer covering the catalyst is thin. Moreover, in the case of incomplete wetting some of the outer surface of the catalyst may be exposed directly to the gas phase, and the entire concept of a liquid phase between the gas and solid no longer holds, let alone a bulk region of constant concentration.

The purpose of this chapter is to describe the overall mass transfer rate of gas components in the bubbles for a two-phase Taylor flow to the outer surface of the solid catalyst. Experimentally, the fast hydrogenation of α -methylstyrene is used to operate a monolith pilot reactor under mass transfer limited conditions and – in some experiments – fully mass transfer limited conditions. As in chapter III of this thesis, computational fluid dynamics will be used to solve the velocity field and the convection-diffusion equation in Taylor flow to obtain insight into the observed behaviour.

In Fig 5.1, three different mass transfer steps for the gas-component can be identified: (1) $k_{GS}a_{GS}$, the transfer from the bubble through the liquid film directly to the catalyst, (2) $k_{GL}a_{GL}$, the transfer from the caps of the gas bubble to the liquid slug and (3) $k_{LS}a_{LS}$, the transfer of dissolved gas from the liquid slug to the catalyst. In the simplest approximation, we ignore all possible overlap and interaction between these transfer steps. The last two steps can then be considered as resistances in series and are

GAS COMPONENT MASS TRANSFER

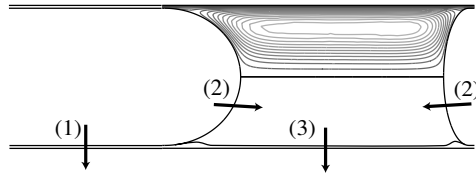


Figure 5.1: Mass Transfer of gas components in Taylor flow. The top part shows streamlines. The bottom part shows the mass transfer steps for the gas to the catalyst wall. (1) gas to solid through the liquid film; (2) gas to liquid through the caps of the bubble; (3) liquid to solid from the liquid slug through the stagnant layer to the catalyst wall.

in parallel with respect to the first step, and for the overall mass transfer the following expression can be used

$$k_{\text{ov}}a = k_{\text{GS}}a_{\text{GS}} + \left(\frac{1}{k_{\text{GL}}a_{\text{GL}}} + \frac{1}{k_{\text{LS}}a_{\text{LS}}} \right)^{-1} \quad (5.1)$$

Here, the specific areas are defined per unit channel volume: $a_{\text{LS}} = 4\epsilon_{\text{L}}/d$ is the specific area of channel walls in contact with the slugs, $a_{\text{GS}} = 4(1 - \epsilon_{\text{L}})/d$ is the specific area of the channel wall in contact with the thin film separating the bubbles from the wall and a_{GL} is the specific area of the spherical caps of bubbles.

DESCRIPTION OF PREVIOUS WORK

Although initial work focused mainly on monolith reactors as an alternative for trickle-bed reactors (*e.g.* Edvinsson & Cybulski (1995)), recent literature deals increasingly with processes normally carried out in slurry reactors (Heiszwolf *et al.*, 2001; Machado *et al.*, 1999). In fact, the only current large scale commercial application of monoliths, the hydrogenation of anthraquinone in hydrogen peroxide production (Berglin & Herrman, 1984), is traditionally performed in slurry reactors.

Perhaps because of the intended comparison with trickle-bed reactors, the first experimental studies of three-phase reactions in monoliths were performed at rather low superficial velocities. Mazzarino & Baldi (1987) performed the hydrogenation of α -methylstyrene in monoliths operated in single phase flow and two-phase cocurrent up and down flow. For the two-phase experiments, $0.5 < u_{\text{LS}} < 3.5$ mm/s and $1.0 < u_{\text{GS}} < 11$ mm/s. The observed reaction rates were comparable to those obtained in a packed reactor with 3 mm catalyst particles. For upflow, it was observed that the gas had passed through a limited number of channels, and the increase of observed reaction rate with an increase of gas flow rate was interpreted in terms of an increase in channels with two-phase flow. A similar effect was observed for downflow: increasing the liquid flow rate resulted in a larger number of channels with liquid. Nowadays, with the benefit of progressing knowledge of gas-liquid flow in monolith channels, it is doubtful whether

Taylor flow indeed occurred at such low linear velocities and their downflow results may be better interpreted as a falling film monolith reactor (Lebens, 1999).

Hatziantoniou *et al.* (1986) hydrogenated mixtures of nitrobenzene and nitrotoluene in a downflow monolithic Pd catalyst reactor at linear velocities above 5 cm/s. Their monolithic catalyst was made by alternating layers of corrugated and plane plates to obtain approximately triangular channels with a cross sectional area of 2 mm². This monolith carrier was covered with a washcoat of SiO₂, but the cross sectional shape of the coated channels was not reported. From their data, the pseudo-first order rate constant based on reactor volume $k_V = r_V / c_H^*$ could be estimated at 0.15 s⁻¹. Their attempts at modelling the mass transfer under the assumption that the experiments were performed under fully mass transfer limited conditions were largely unsuccessful, as was indicated by Hatziantoniou *et al.* themselves. Initially, the circulation in the slugs was assumed to effectively saturate the bulk liquid. Then, a model of film theory ($k_{GL} = D/\delta$) with an estimate of the film thickness δ in round channels significantly over-predicted the observed reaction rate. The film theory was replaced by penetration theory ($k_{GL} \sim 2\sqrt{D/\pi\tau}$), where the contact time τ was based on the total flow residence time times the gas holdup. The remaining mass transfer step were subsequently fitted to the experimental data. The outcome of this fitting procedure suggested that the mass transfer to the film between the bubble and the wall accounted for most of the observed reaction rate. The experimental finding that the observed reaction rate did not increase significantly with increasing gas holdup was attributed to the limited range of holdup in the experiments.

Smits *et al.* (1996) hydrogenated 1-octene and styrene in a 400 cpsi monolith reactor with washcoated square channels. The superficial velocities were in the range $0.04 < u_{TP} < 0.45$ m/s. The observed reaction rate first increased with increasing total velocity. Like Mazzarino & Baldi, Smits *et al.* interpreted this as an improvement of the distribution with increasing flowrate. A more interesting observation was that if the linear velocity u_{TP} was increased even further, the observed reaction rate dropped. This drop in observed reaction rate was also interpreted in terms of distribution effects: the maximum reaction rate corresponded roughly to the velocity at which gravity balances friction in the channels, and they postulated that this terminal velocity gives the best Taylor flow characteristics. Using estimates for the solubility of hydrogen, the maximum of the observed pseudo-first order rate constant for hydrogen was $k_V \approx 0.5$ s⁻¹.

Nijhuis *et al.* (2001) hydrogenated α -methylstyrene and benzaldehyde over monolithic Ni catalyst in the same pilot reactor as used in this study. The linear velocity varied between $0.1 < u_{TP} < 0.4$ m/s. Cell densities between 200 and 600 cpsi were used, and the observed pseudo-first order rate constants varied between 0.03 s⁻¹ for the 200 cpsi catalyst and 0.25 s⁻¹ for the 600 cpsi catalyst. The experimental finding of Hatziantoniou *et al.* (1986) that the holdup has little impact on the observed reaction rate was confirmed. The observed reaction rates were compared with a theoretical model (Moulijn & Cybulski, 1998). It was found that the model over-predicted the ex-

perimental results: for a typical case for 400 cpsi, the model predicted 0.75 s^{-1} , while the experimentally obtained observed reaction rate was only 0.14 s^{-1} . As a partial explanation for this difference, it was suggested that even washcoated monolith channels are not round, and that a model based on round channels will always under-predict the average thickness of the film between the bubble and the wall. Naturally, a thicker film poses a larger resistance to mass transfer.

The hydrogenation of benzaldehyde by Nijhuis *et al.* allowed a comparison of monoliths with conventional reactors for selective hydrogenations. The results indicate that the thin washcoat of catalytically active material has characteristics that are similar to the small catalyst particles used in commercial slurry reactors. The trickle-bed reactor, that was also considered in this study, suffered from severe reduction in selectivity due to the internal and external mass transfer limitations associated with the large catalyst particle size. Later, Nijhuis *et al.* (2003) modelled the hydrogenation of styrene in monoliths and trickle-bed reactors, and reported not only that the monolith reactor outperforms the trickle-bed in terms of productivity per unit reactor volume, but also demonstrated that the superior mass transfer characteristics of monolithic reactors results in less deactivation of the catalyst by gum-formation.

Finally, Broekhuis *et al.* (2001) conducted an unspecified nitro-aromatic hydrogenation in an internal circulation (Berty) autoclave, and measured a pseudo-first order rate constant for hydrogen of $k_V = 2.5 \text{ s}^{-1}$. No attempt was made to model this reaction, but it was shown that present models all under-predicted the observed reaction rate.

The observations from the open literature for fast hydrogenation reactions in monoliths, summarised above, indicate that a satisfactory model for the transfer for gas-phase components to the catalyst is still missing. Further, a progressively increasing trend can be observed in the reported pseudo-first order observed rate constants. The earliest work was performed under downflow conditions where Taylor flow may not have been established. The falling film flow in monoliths is not significantly different from trickling flow, and as a result no spectacular enhancements with respect to trickle-bed reactors was found. For upflow conditions, the observed reaction rates were consistently higher, but agreement is found that maldistribution effects are severe, especially at low flowrates. Klinghoffer *et al.* (1998) thoroughly studied the impact of distributor design for upflow monoliths, including perfect alignment of the channels with the holes of a perforated plate distributor, and indeed found that distribution is very problematic in upflow. This may be explained by the findings of de Tezanos Pinto *et al.* (1997), who demonstrated that entrance of bubbles into a capillary channel is hindered by the required deformation of the gas-liquid interface. For downflow operation, maldistribution effects were also consistently reported, especially at very low flowrates. In fact, only once a decrease in activity was reported with increasing velocity. In later papers, the superficial velocities were high enough for Taylor flow to establish and the observed reaction rates are much higher. However, the reported observed reaction rates differ substantially, which suggest that external mass transfer was

not fully limiting and the different intrinsic rates for the various reactions still played an important role.

§ V.2 NUMERICAL ANALYSIS

In order to obtain some insight into the characteristics of gas-component mass transfer, the computational fluid dynamics package Fluent5 was used to simulate mass transfer in a Taylor flow slug between two bubbles in round capillary channels. The film thickness between the bubbles and the wall was estimated using the correlation of Irandoust & Andersson (1989)

$$\frac{d_{\text{bubble}}}{d_{\text{channel}}} = 0.64 + 0.36 \exp(-3.08Ca^{0.54}) \quad (5.2)$$

In Taylor flow, the caps are not exactly hemispherical if inertial effects are important. For this reason, several simulations were performed using elongated front caps and flattened rear caps, and using realistic shapes for the caps, the change in mass transfer characteristics was less than 15%. For all simulations, first the velocity field was calculated from the continuity equation and the Navier–Stokes equations

$$\nabla \cdot \rho \mathbf{u} = 0 \quad (5.3)$$

$$\rho(\mathbf{u} \cdot \nabla)\mathbf{u} = -\nabla p + \mu \nabla^2 \mathbf{u} + \rho \mathbf{g} \quad (5.4)$$

Subsequently, the steady state convection–diffusion equation

$$(\mathbf{u} \cdot \nabla)c = D \nabla^2 c \quad (5.5)$$

was solved. The boundary conditions were no–slip at the wall, no–shear at the gas–liquid interface and symmetry on the channel axis for the velocity field and zero concentration at the wall, saturation concentration at the gas–liquid interface and symmetry at the channel axis. The simulations were performed in a translating reference frame fixing the bubbles in place.

$$u_z = -u_{TP}, u_r = 0, \quad \text{at the wall} \quad (5.6)$$

$$\frac{\partial u_z}{\partial r} = 0, \quad u_r = 0, \quad \text{at the axis} \quad (5.7)$$

$$\frac{\partial u_t}{\partial n} = 0, \quad \text{at the bubbles} \quad (5.8)$$

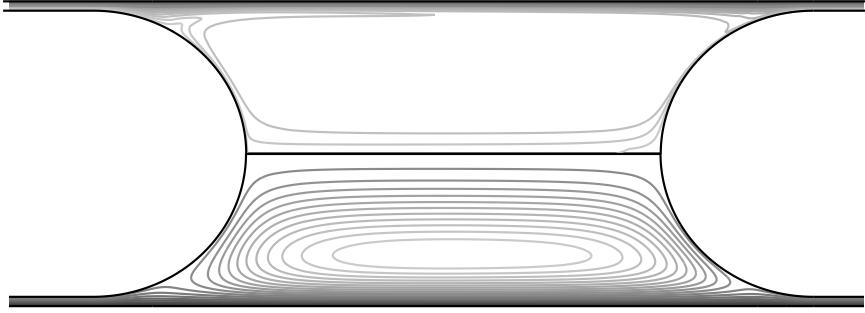


Figure 5.2: Concentration contours of 20 equally spaced intervals between 0 and c^* (top half) and streamlines (bottom half) for a simulation with $D=1.4 \times 10^{-8} \text{ m}^2/\text{s}$, $u_{\text{TP}}=0.4 \text{ m/s}$, $d_{\text{channel}}=1.0 \text{ mm}$, $L_{\text{slug}}+L_{\text{bubble}}=4d_{\text{channel}}$ and holdup $\epsilon_L=0.5$.

$$c = 0, \quad \text{at the wall} \quad (5.9)$$

$$\frac{\partial c}{\partial r} = 0, \quad \text{at the axis} \quad (5.10)$$

$$c = c^*, \quad \text{at the bubbles} \quad (5.11)$$

In Eq. 5.8, $(\partial u_t / \partial n)$ is the derivative of the tangential velocity u_t with respect to the normal n of the gas-liquid interface.

In the simulations the diffusion coefficient, linear velocity, bubble length and slug length were varied within the ranges given in table 5.1. A representative solution of both the velocity field and the concentration is shown in Fig. 5.2. The velocity field has all the important characteristics that were also found for the physically more realistic simulations reported in chapter II, where the shape of the gas liquid interface was part of the solution: in the liquid slug a circulation zone is separated from the wall by a thin film region. The contour lines of the concentration clearly show that the largest resistance to mass transfer in the slug is located in the thin film region. The majority

Table 5.1: Parameters for the simulations

parameter		value
channel diameter	d_{channel}	0.8–1.5 mm
diffusion coefficient	D	1.5×10^{-8} – $5.0 \times 10^{-8} \text{ m}^2/\text{s}$
slug length	L_{slug}	1.3–8.3 mm
bubble length	L_{bubble}	0.5–8.5 mm
linear velocity	u_{TP}	0.1–0.4 m/s
viscosity	μ_L	0.001 Pa s
density	ρ_L	1000 kg/m ³

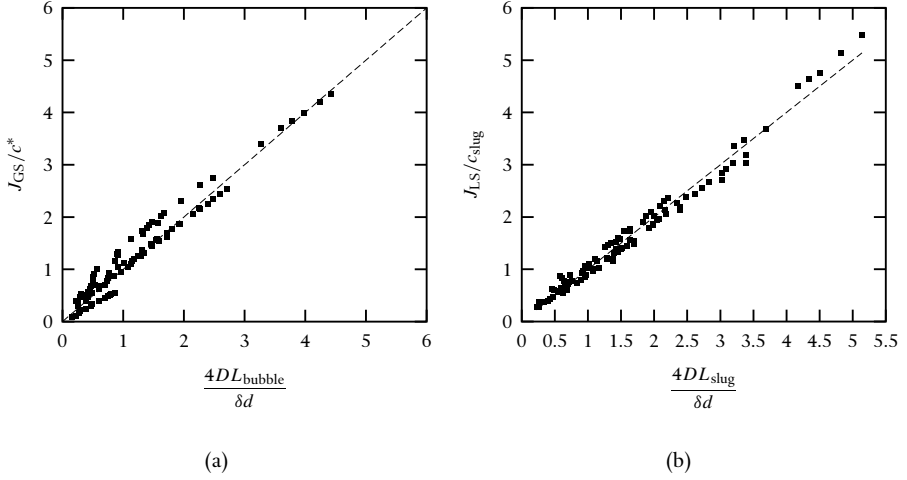


Figure 5.3: (a) Parity plot of the the mass transfer through the film based on film theory (a) Flux through the film for a bubble, Eq. 5.12, (a) Flux through the film for the slug, Eq. 5.13

of the circulation zone is characterised by a region of constant concentration. Near the caps the concentration is higher and the fluid elements of high concentration are transported by convection along the axis and the streamline that separates the circulation zone from the film layer. For all simulations, the wall-area averaged mass transfer rate to the wall was recorded separately for the slug and bubble region. The independence of grid density was checked by quadrupling the amount of nodes. For all simulations, this resulted in a change in fluxes of less than 5%. For the bubble region, the mass transfer could be accurately modelled using film theory, *i.e.*

$$J_{GS} = kA_{GS}(c^* - 0) = \frac{D}{\delta}L_{\text{bubble}}\pi d(c^* - 0) \quad (5.12)$$

For the slug region, the same approach could be used, replacing the saturation concentration by the volume-averaged concentration in the circulating zone

$$J_{LS} = kA_{LS}(c_{\text{slug}} - 0) = \frac{D}{\delta}L_{\text{slug}}\pi d(c_{\text{slug}} - 0) \quad (5.13)$$

So, the problem of formulating a mass transfer model can be reduced to the problem of formulating a model that predicts the average slug concentration. A very simple model for this concentration can be obtained by assuming that the flux out of the circulating zone is described by Eq. 5.13, and by assuming that penetration theory holds for the bubble caps, so we obtain for the flux into the slug

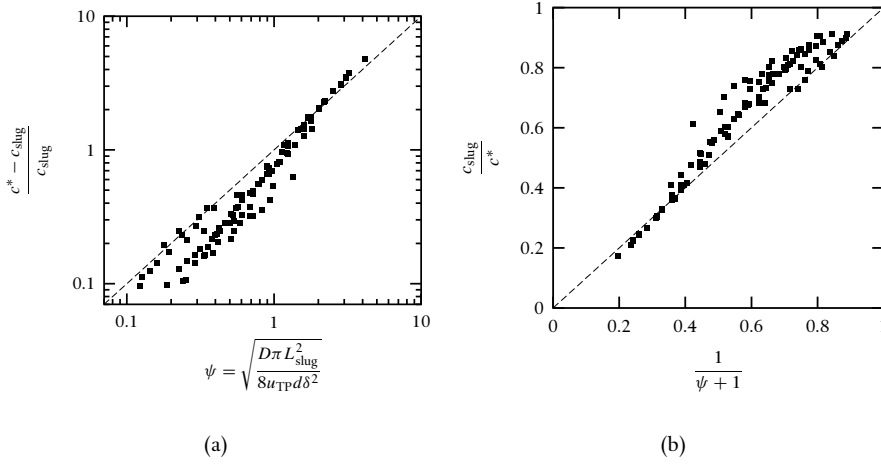


Figure 5.4: (a) Parity plot of the left hand side and right hand side of Eq. 5.15. (b) same plot, but now rewritten in term of the relative slug concentration.

$$J_{GL} = kA_{GL}(c^* - c_{slug}) \sim 2 \cdot 2 \sqrt{\frac{D}{\pi \tau}} \frac{1}{2} \pi d^2 (c^* - c_{slug}) \quad \tau \sim \frac{d}{2u_{TP}} \quad (5.14)$$

where τ is the contact time. Equating Eq. 5.13 and Eq. 5.14 and solving for concentration yields

$$\frac{L_{slug}}{\delta} \sqrt{\frac{D\pi}{8u_{TP}d}} \sim \frac{c^* - c_{slug}}{c_{slug}} \quad (5.15)$$

Fig. 5.4(a) shows a plot of the left hand side of this equation versus the right hand side. Although the agreement is not exact, it is clear that the dimensionless group obtained from this simple scaling analysis can be used as a single parameter that describes the slug concentration. Note that in this simple analysis, we have tacitly assumed a bulk region of constant concentration between the gas-to-liquid transfer near the caps and the liquid-to-wall transfer. In other words, we have ignored the direct convection from the cap to the film near the wall, which would result in a higher mass transfer. Also we have ignored the convection of high concentration fluid elements to that same cap, which would lower the gas liquid transfer. Apparently these two effects, which describe the mass transfer as a “caterpillar track” of fluid elements along a single streamline, almost cancel each other. The error made by estimating the slug concentration using Eq. 5.15 is largest when the predicted slug concentration is highest, see Fig. 5.4(b).

High slug concentrations correspond to (1) short slugs, (2) low diffusion coefficients or (3) high velocities, so we may interpret the cases of high slug concentrations as cases where convective mass transfer dominates conductive mass transfer. The “caterpillar track” effect is a convective contribution to mass transfer that, in terms of resistances, short-circuits the gas-to-liquid mass transfer and liquid-to-wall mass transfer. Therefore, this explains the breakdown of the simple model presented here that ignores this convective short-circuiting. On the other hand, the error made is acceptable: If the predicted slug concentration is $0.75c^*$, and the slug concentration from the full CFD solution is $0.85c^*$, the error in the mass transfer rate from the slug is 13%. Further, assuming equal bubble and slug length, the error in the total transfer rate to the wall is half of that, 7%.

One experimental finding reported in the literature can already be explained by the numerical study presented here: the impact of holdup is limited. If the conditions are such that the slug is completely saturated with the gas-phase component, and if the film thickness is the same for the slug and the bubble, the mass transfer is indeed completely independent of the holdup. The experimental evidence that the film thickness for the slug is comparable to the film thickness for the bubble was already presented in chapter IV (see Fig. 4.3 on page 75).

SQUARE CHANNELS

The results above were obtained for circular channels. As has been described in chapter II, reliable correlations for the film thickness in round channels are available. For square channels, the experimental or numerical data are much less abundant. In chapter IV, an overview of the two experimental data sets (Thulasidas *et al.*, 1995; Kolb & Cerro, 1991) and one numerical data set (Hazel & Heil, 2002) was presented. In table 5.2, the results are summarised: for the bubble diameter from corner to corner (AA'), the data from the three sources could be represented by a single correlation. For the bubble diameter from the middle of a wall to the facing middle of an opposite wall (BB'), the agreement is considerably less: the numerical work of Hazel & Heil predicts a film that is five times thinner than the experimental data of Kolb & Cerro.

So, the uncertainty in the film thickness is probably more important than the uncertainty in slug concentration. Also, for square capillaries, the film thickness is not constant along the perimeter. However, we can define an effective film thickness by solving the diffusion equation for a square capillary and a film characterised by round interfaces in the corners and flat interfaces in between, and integrating the flux along the perimeter of the channel. The results of this calculation are presented in Fig. 5.5 for the experimental data of Thulasidas *et al.* and the numerical data of Hazel & Heil (2002). Clearly, the uncertainty in effective film thickness based on literature data is too large to be used for design purposes. Moreover, the simulations for circular capillaries show that the (effective) film thickness is the most important parameter in the description of gas-component mass transfer.

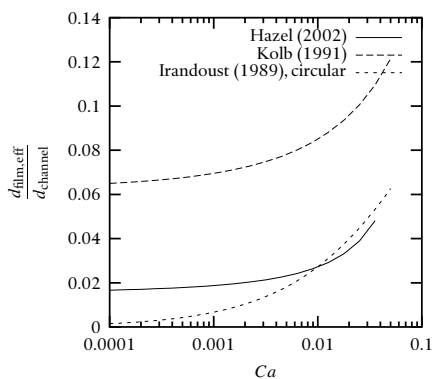


Figure 5.5: Effective film thickness in a square capillary. based on the correlations in table 5.2. The average value is based on the average value for the film thickness in the direction BB' (≈ 0.97). For comparison, the film thickness in round capillaries based on Irandoust & Andersson (1989) is also plotted to indicate that the film thickness is much more sensitive to Ca in round capillaries.

For washcoated monolith channels, the channels are neither round nor square. In the washcoating process, the channels are filled with a solution of the coating material and subsequently most of this solution is blown out. This leaves a small amount of material in the channels, that contracts towards the corners due to surface tension forces. For this cross sectional shape of the channels, no data on the film thickness has been reported. In Fig. 5.5, the correlation of Irandoust & Andersson (1989) is also plotted, and it goes without saying that if a high external mass transfer is desired, the coating process should be optimised to obtain round channels, as this gives the lowest film thickness. Further, the large variation of observed reaction rates in the literature may well be caused by a variation in the rounding of the catalysts.

Table 5.2: Bubble thickness in square capillaries. The directions AA' and BB' are illustrated in Fig. 4.2 on page 74.

Reference	direction	bubble diameter ($d_{\text{bubble}}/d_{\text{channel}}$)
Kolb & Cerro (1991)	AA'	
Thulasidas <i>et al.</i> (1995)	AA'	$\approx 0.7 + 0.5 \exp(-2.25Ca^{0.445})$
Hazel & Heil (2002)	AA'	
Kolb & Cerro (1991)	BB'	≈ 0.95
Hazel & Heil (2002)	BB'	≈ 0.99

Table 5.3: Physical properties for the hydrogenation of α -methylstyrene carried out in toluene at 100 °C. †: Vargaftik *et al.* (1999), ‡: Reid *et al.* (1987)

Name	Symbol	Value	Unit
liquid density†	ρ	790	kg/m ³
liquid viscosity†	η	$2.71 \cdot 10^{-4}$	Pa s
surface tension†	γ	0.0196	N/m
gas diffusivity‡	D_{H_2}	$3.5 \cdot 10^{-8}$	m ² /s

Provided the film thickness is known, we can estimate the mass transfer of gas components in monoliths with the following two simple equations. For the mass transfer from the bubble to the catalyst we use film theory

$$k_{GS}a_{GS} = \frac{D}{\delta} \frac{4(1 - \epsilon_L)}{d} \quad (5.16)$$

In this equation, the term $(1 - \epsilon_L)$ represents the volumetric fraction of the channel that is occupied by the bubbles. For the mass transfer from the slug to the catalyst the mass transfer group is represented by

$$k_{LS}a_{LS} = \frac{D}{\delta} \frac{4\epsilon_L}{d} \left(1 + \frac{L_{\text{slug}}}{\delta} \sqrt{\frac{D\pi}{8u_{TP}d}} \right)^{-1} \quad (5.17)$$

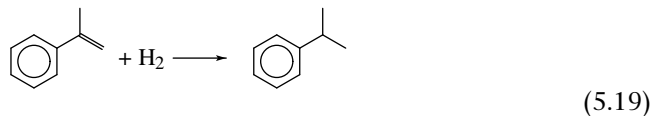
Finally, the overall mass transfer group is obtained by the sum of Eqs. 5.16 and 5.17.

$$k_{ov}a = k_{GS}a_{GS} + k_{LS}a_{LS} \quad (5.18)$$

Note that a correlation for the slug length and for the film thickness must be provided. For the rounded channels that are used in this work, such a correlation for the film thickness is at present not available.

§ V.3 EXPERIMENTAL

The hydrogenation of α -methylstyrene to cumene over a palladium on γ -alumina catalyst



is a well known model system used to determine three-phase reactor performance under mass transfer limited conditions (e.g. Cini & Harold (1991), Khadilkar *et al.* (1996) and Frank *et al.* (1999)), because of its high intrinsic reaction rates. The reaction is zero order in α -methylstyrene until the concentration becomes too low, indicating strong adsorption of α -methylstyrene on the catalyst. In general first order behaviour in hydrogen is observed, although this could be caused by mass transfer limitations; Germain *et al.* (1974) observed a reaction order of 0.64 when mass transfer resistances were eliminated. In general, 100% selectivity to cumene is observed.

CATALYST PREPARATION

Bare cordierite monoliths (diameter $d=0.01$ m, length $L=0.25$ m, cell densities of 200, 400 and 600 cells per square inch (cps)), were obtained from Corning Inc., NY. On the wall of the monoliths, first a washcoat of γ - Al_2O_3 was deposited. A mixture of 150 g alumina (Condea Puralox, SBA-200), 85 g of colloidal alumina (Alfa, 20% solids) and 150 g of demineralized water was ball-milled for 10 hours. During milling, the pH was kept constant at 3.5 by addition of nitric acid. The slurry obtained by milling had a viscosity of 20 mPa.s. Monoliths were dipped in the slurry for 2 minutes. Excess slurry was blown out and the monoliths were dried overnight under constant rotation. The final washcoat was obtained by calcination in air at 723 K for 4 hours. The amount of washcoat was measured by weight, and was typically 20 wt. % of the bare cordierite monolith. A typical washcoated sample is shown in Fig. 1.2 on page 3: the radius of the rounding in the corners is one fourth of the channel diameter.

5×10^{-4} moles of PdCl_2 was dissolved in 200 ml of acetone. 0.5 ml 2 N HCl was added to enhance the solubility. The solution was recycled over the monoliths to ion exchange with the solution for 24 hours, and the monoliths were dried at 393 K for 2 hours. The catalysts were calcined at 772 K for 4 hours and reduced at 393 K for 6 hours in hydrogen. The obtained palladium loading was 1.8 %, based on the washcoat weight.

SETUP

A pilot-scale reactor (diameter 0.01 m, length 2 m) was used in the hydrogenation experiments. The reactor is operated continuously for gas and batch-wise for liquid, see Fig. 5.6.

The reactor column has an internal diameter of 17 mm. Monoliths were stacked inside the column with 10 mm spacing between them using metal connecting parts. Teflon tape was used to seal the open space between these connectors and the monoliths to prevent by-pass of gas or liquid. The entire setup was well insulated and kept at operating temperature during the experiments. The pressure in the reactor was maintained by a pressure controller in the vent. The liquid flowrate in the reactor was set by a mass flow controller just behind the pump. The flowrates of nitrogen and hydrogen

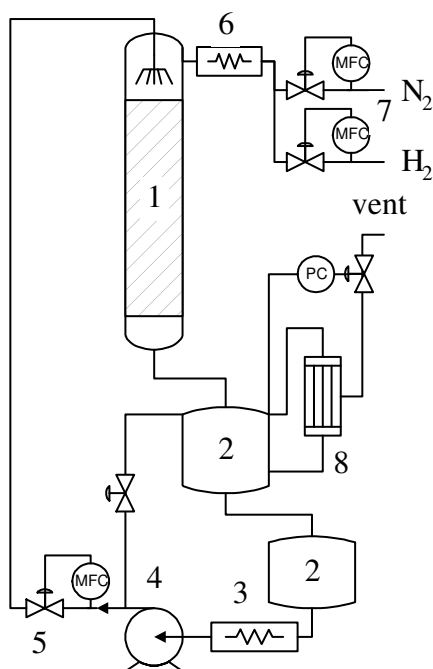


Figure 5.6: Schematic representation of the pilot scale monolith setup: (1) reactor; (2) liquid vessels; (3) liquid preheater; (4) liquid pump; (5) liquid mass flow controller; (6) gas preheater; (7) gas mass flow controllers; (8) condenser.

were set by mass flow controllers. In order to enhance the gas and liquid distribution, 8 bare monolith pieces of 1 cm long were stacked, rotated 45 degrees with respect to one another, see Fig. 5.7. In this way, each short channel is exposed to several channels of the next section, and redistribution occurs. The use of such short misaligned sections or slices has been successfully applied by Satterfield & Özel (1977) to enhance liquid distribution.

EXPERIMENTAL PROCEDURE

Prior to experiments, the catalyst was reduced in situ at 393 K for at least one hour. Since impurities have a large impact on the rate and deactivation behaviour of the system (El-Hisnawi *et al.*, 1982), the α -methylstyrene was passed over an adsorber bed to remove the polymerisation inhibitor p-tert-butylcatechol. Without this purification step, reproducible results could not be obtained and a strong catalyst deactivation was observed.

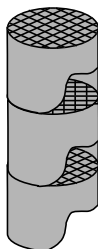


Figure 5.7: Distributor used under the nozzle in the monolith

The setup was allowed to reach steady state at the setpoint temperature and pressure and the run was started by setting the setpoints for the liquid and gas flowrate. Samples were taken from the reactor inlet at regular intervals. Typically, nine samples were taken per experiment, after which the set points were changed to new values. Experiments were performed until the liquid α -methylstyrene concentration dropped below 10 wt. %.

The liquid samples were analysed by gas chromatography to determine the liquid phase composition. Using UNIFAC, the gas phase composition was calculated to correct for the evaporated liquid phase components. The total weight loss during a run, caused by sampling and evaporation, was measured. The composition of the gas lost by evaporation was calculated using UNIFAC at the condenser temperature. From the liquid phase composition, corrected for the above mentioned influences, the amount of α -methylstyrene N_{aMS} in the setup was calculated. The observed rate per cubic meter of monolith $V_R = 0.25\pi d_M^2 L_M$ was calculated by

$$r_{v,\text{obs}} = \frac{dN_{\text{aMS}}}{dt} \frac{1}{V_R} \quad (5.20)$$

From the observed rate, the conversion of hydrogen per pass was calculated. All the mass transfer steps are proportional to the hydrogen pressure, which drops as the conversion of hydrogen increases. In order to calculate a rate constant, this drop in

Table 5.4: Experimental conditions

parameter	value
temperature	323 – 413 K
hydrogen pressure	10 bar
nitrogen pressure	10 bar
liquid superficial velocity	0.1–0.4 m/s
gas superficial velocity	0.1–0.4 m/s
liquid hold-up	0.25 – 0.75

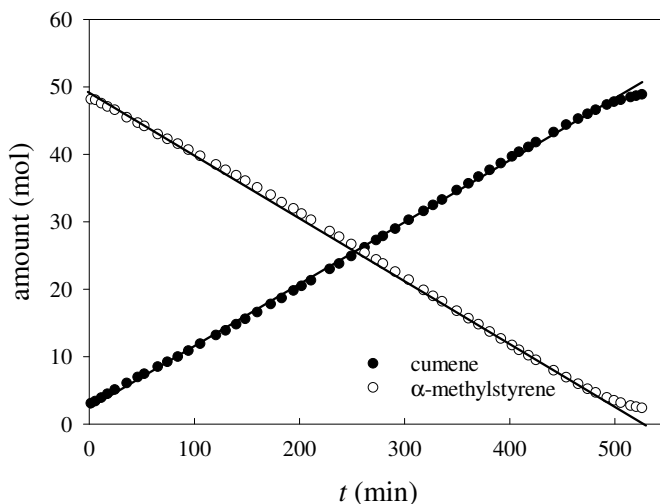


Figure 5.8: Determination of stability during a long run at constant operating conditions.

partial hydrogen pressure has to be corrected for. It can be shown that the rate constant is given by

$$k_{v,obs} = \frac{r_{v,obs}}{C_{H_2}^{sat}} \left(\frac{-\ln(1 - \xi_{H_2})}{\xi_{H_2}} \right) \quad (5.21)$$

where $\xi_{H_2} = (p_{H_2,in} - p_{H_2,out})/p_{H_2,in}$ is the conversion of hydrogen per pass, based on partial hydrogen pressure. If the system is fully limited by mass transfer, the rate constant $k_{v,obs}$ is equal to the mass transfer rate in a channel:

$$k_{v,obs} = k_{ov}a(1 - \epsilon_M) \quad (5.22)$$

in which ϵ_M is the solid volume of a monolith divided by the sum of the solid and void volume in a monolith, so $k_{ov}a$ is an overall mass transfer group per unit reactor volume.

§ V.4 RESULTS AND DISCUSSION

REPRODUCIBILITY

The stability of the catalyst was studied by performing a run for several hours. A plot of the fraction of α -methylstyrene vs. time for such a run can be seen in Fig. 5.8.

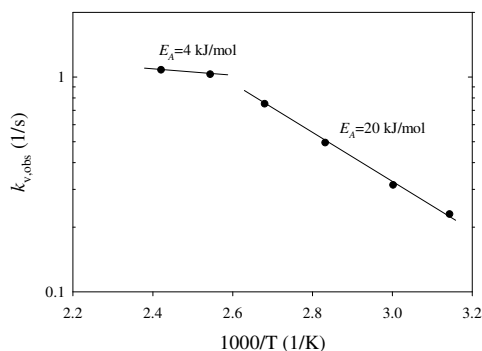


Figure 5.9: Arrhenius plot of the first order rate constant, based on reactor volume. Catalyst: 400 cpsi monolith 1.8 % Pd/ γ -Al₂O₃, $d = 0.01$ m, $L = 0.75$ m, $u_{Ls} = 0.15$ m/s, $u_{Gs} = 0.2$ m/s.

The straight line in Fig. 5.8 indicates that during an experiment, the catalyst does not deactivate. It also shows that for our experimental conditions, the order of the reaction in α -methylstyrene is zero. As external transfer processes obeying Fick's law are first order processes, the rate is not limited by mass transfer of α -methylstyrene. In subsequent runs, the operating conditions were varied, but the operating conditions at the beginning and the end of a run were always kept at the same value so that possible deactivation could be detected. Although the activity did not drop within one run, during shut-down, refilling and start-up of the reactor, deactivation was sometimes observed. This deactivation was minimised by retaining a high hydrogen pressure in the reactor during cooling down. As soon as deactivation of the catalyst was observed, it was replaced, and the data for the deactivated catalyst were ignored.

IMPACT OF TEMPERATURE

To verify that the experiments were performed in the externally mass transfer limited regime, measurements were performed for the same flow conditions at temperatures from 318 K to 413 K. If the reaction is only limited by internal diffusion, the observed activation energy would be half of the activation energy of the intrinsic kinetics. The intrinsic activation energy was determined by Germain *et al.* (1974) as 42 kJ/mol in a slurry reactor with sufficiently small particles ($d_p < 3\mu\text{m}$) at moderate temperatures. As soon as the reaction becomes externally mass transfer limited, the observed activation energy drops even further, approaching zero.

In Fig. 5.9, the observed reaction rate constants are plotted against the reciprocal of temperature, so the activation energy can be obtained from the slope in the plot. At lower temperatures, the activation energy was found to be 20 kJ/mol, so under those conditions, the reaction is internally mass transfer limited. At temperatures above 373

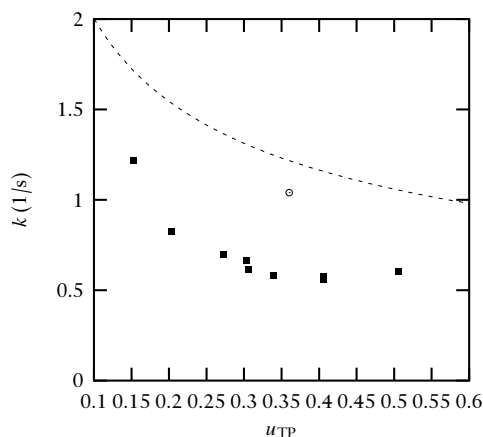


Figure 5.10: Observed rate in 400 cpsi monoliths as a function of two phase flowrate. The closed symbols refer to measurements at $T = 373$ K; Catalyst: 400 cpsi 1.8 % Pd/ γ - Al_2O_3 , $d = 0.01$ m, $L = 0.75$ m. The open symbol is taken from Fig. 5.9 at $T = 393$ K. The line is calculated from the model for external mass transfer in 400 cpsi monoliths with liquid hold-up $\epsilon_L = 0.5$.

K, the slope of the Arrhenius plot begins to bend, indicating that at those temperatures, the reaction becomes externally mass transfer limited. Based on these results, the reactions should be carried out at temperatures in excess of 413 K. However, at such temperatures, the evaporation of toluene from the reactor was significant, even though a condenser was used. Significant evaporation would make the analysis of the liquid samples inaccurate. Moreover, at high temperatures, the catalyst deactivates faster. As a compromise, further experiments were performed either at 373 K or at 393 K. As a consequence, depending on the conditions the observed rates will sometimes be lower than the maximum mass transfer rates predicted by the model. On the other hand, since the reaction is carried out close to mass transfer limitation, the observed rates will follow the trends predicted by the mass transfer model.

From the temperature dependence of the observed rate, we can also estimate the film thickness in our monolith. In the Eqs. 5.16–5.18, the slug length and the film thickness are unknown. Assuming that the slug length is approximately 3 times the channel diameter, we find that the film thickness is 1×10^{-4} m and that the slug is nearly saturated. The channels of the washcoated monolith had rounded corners with a radius of one quarter of the channel diameter, so the maximum bubble size in the diagonal direction of the channel is $(1/2 + 1/\sqrt{2})d \approx 1.2d$. The capillary number at the onset of full mass transfer limitation was $Ca = 4.8 \times 10^{-3}$. For this capillary number the correlations for square channel predict a bubble size that is close to $1.2d$, so the concept of a flat film and a thick rounded film in the corner does not hold anymore. Here, the round channel correlation of Irandoust & Andersson is used, multiplied by a factor to account

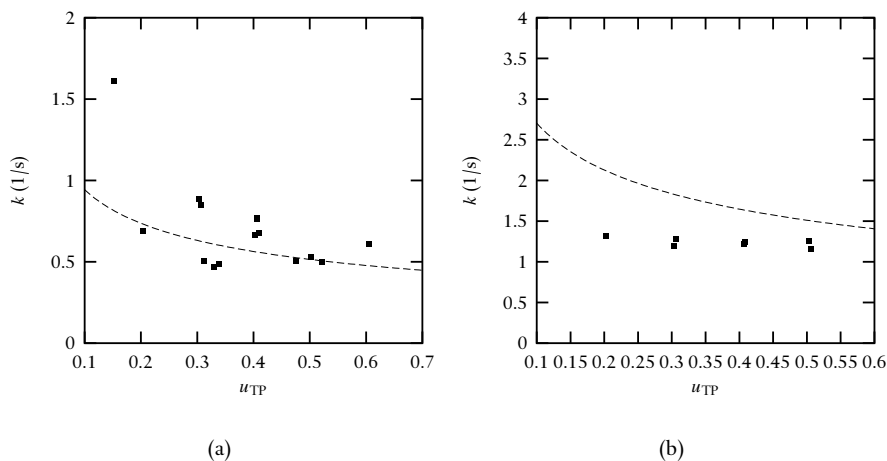


Figure 5.11: (a) Observed rate in 200 cpsi monoliths as a function of two phase flowrate. $T = 393$ K; Catalyst: 200 cpsi 1 % Pd/ γ -Al₂O₃, $d = 0.01$ m, $L = 0.75$ m. The line is calculated from the model for external mass transfer in 200 cpsi monoliths with liquid hold-up $\epsilon_L = 0.5$. (b) Observed rate in 600 cpsi monoliths as a function of two phase flowrate. $T = 393$ K Catalyst: 600 cpsi 1 % Pd/ γ -Al₂O₃, $d = 0.01$ m, $L = 0.5$ m. The line is calculated from the model for external mass transfer in 600 cpsi monoliths with liquid hold-up $\epsilon_L = 0.5$.

for the rounded corners. For $Ca = 4.8 \times 10^{-3}$, Eq. 5.2 predicts $\delta = 3.2 \times 10^{-5}$ m, so the correction factor is 3.

MASS TRANSFER MEASUREMENTS

The observed reaction rate constants as function of unit cell velocity are summarised in Figs 5.10, and 5.11. The lines in these figures are the right hand side of Eq. 5.22 in which $k_{ov}a$ is derived from the mass transfer model presented in this chapter, with the film thickness based on three times the film thickness predicted by Eq. 5.2 (Irlandoust & Andersson, 1989).

It should be noted that the lines were calculated for a liquid hold-up ϵ_L of 0.5, *i.e.* $u_{Ls} = u_{Gs}$, and the experimental points were obtained for $0.25 < \epsilon_L < 0.75$. Experimentally, little impact of hold-up was observed, which is in agreement with the fact that the slugs are nearly completely saturated. The model predicts very high mass transfer rates at low liquid velocities and high cell densities: for 600 cpsi $k_{ov}a$ equals 2.1 at $u_{TP} = 0.2$ m/s. If the velocity is increased from 0.2 to 0.6 m/s, the mass transfer parameter drops by 30% for all cell densities. For different cell densities at 0.4 m/s, $k_{ov}a$

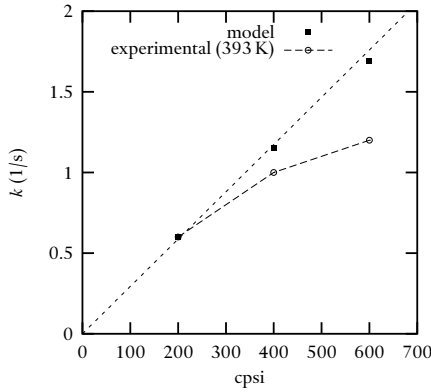


Figure 5.12: Observed rate constant k and predicted $k_{ov}a$ for different cell densities at 393 K and $u_{TP} = 0.35$ m/s

is 0.6, 1.15 and 1.69 for 200, 400 and 600 cps monoliths, respectively, which indicates that the mass transfer increases linearly with cell density (see Fig 5.12).

The data in Fig. 5.10 were obtained at 373 K. This is not in the fully mass transfer limited regime, which was determined from the data in Fig. 5.9 to begin at 393 K if $k_{ov}a = 1$ s⁻¹. For comparison, the observed rate at 393 K from Fig. 5.9 is also plotted. This point is just fully mass transfer limited, and is close to the value predicted by the model. Although the other measurements are not fully mass transfer limited, the observed rate constants will be significantly affected by the external mass transfer as predicted by this model. The model predicts that the mass transfer improves with decreasing flowrate due to the decrease in film thickness. The experimental data of the 200 and 400 cps monoliths confirm this prediction.

At 200 cps, the geometrical surface area $a = 4/d_c$ is lower, and the observed rates are lower than for 400 cps. The rates in Fig. 5.11(a) were measured at 393 K, while the predicted mass transfer parameter is below 1 s⁻¹. As a consequence, the reaction is assumed to be fully mass transfer limited, which is confirmed by the good agreement between experiment and model.

Fig. 5.11(b) shows the data for the higher cell density we have used, 600 cps. The model predicts a mass transfer parameter of 1.4 s⁻¹ and up. As a consequence, the reaction is not fully mass transfer limited, even at 393 K. Surprisingly, no increase of the observed rate constant is found at lower flowrates.

§ V.5 CONCLUSIONS

Monolith reactors are excellently suited for fast catalytic reactions that would suffer from mass transfer limitation if carried out in conventional reactors. In this chapter the fast hydrogenation of α -methylstyrene was used to investigate the mass transfer from the gas bubbles in Taylor flow to the catalyst. The experiments showed that the mass transfer group $k_{ov}a$ exceeds 1 s^{-1} in a 400 cpsi monolith with rounded corners. The mass transfer characteristics improved with increasing cell density and with decreasing velocity, because of a decrease in thickness of the film between the train of bubbles and slugs in Taylor flow.

A simple model was proposed for gas–component mass transfer in Taylor flow. In this model, the film near the wall is the largest resistance to mass transfer. This mass transfer step can adequately be described by film theory. The absorption at the bubble caps was described by penetration theory. The critical parameters in this model are:

- the effective thickness of the film between the bubble and the wall, which is hard to predict because the shape of a channel in a monolith is neither round nor square. The present correlations for the film thickness are not suitable for design purposes.
- the liquid slug length.
- the gas and liquid velocity.

The model was validated by a numerical analysis of the convection–diffusion in Taylor flow slug between two bubbles.

NOTATION

a	specific surface area, m^2/m^3
C	concentration, mol/m^3
d	diameter, m
D	diffusion coefficient, m^2/s
J	flux, $\text{mol}/\text{m}^2/\text{s}$
k	mass transfer coefficient, m/s
k_v	reaction rate constant, $1/\text{s}$
L	length, m
N	amount, mol
n	scaling factor
n	normal of the gas–liquid interface (Eq. 5.8)
Q	heat flux, W/m^2
r_v	observed reaction rate, $\text{mol}/\text{m}^3\text{s}$
T	temperature, K

u	superficial liquid velocity, m/s
u_{TP}	unit cell velocity ($= u_{L,s} + u_{G,s}$), m/s

Greek letters

ϵ_L	liquid holdup, m^3/m^3
δ	film thickness, m
λ	thermal conductivity, W/mK
η	viscosity, Pa s
ρ	density, kg/m^3
γ	surface tension, N/m
τ	contact time, s
Ψ	aspect ratio ($= L/d$)
ξ	conversion

Dimensionless numbers

Ca	Capillary number ($= \eta u / \gamma$)
Re	Reynolds number ($= \rho u d / \mu$)
Sc	Schmidt number ($= \eta / \rho D$)
Sh	Sherwood number ($= k_L d / D$)

subscripts

b	bubble
c	channel
GL	gas-liquid
GS	gas-solid
LS	liquid-solid
M	monolith
obs	observed
ov	overall
s	superficial
t	tangential
w	wall

BIBLIOGRAPHY

- BERGLIN, C. T. & HERRMAN, W. 1984 A method in the production of hydrogen peroxide. *European Patent* 102 934 A2.
- BROEKHUIS, R. R., MACHADO, R. M. & NORDQUIST, A. F. 2001 The ejector-driven monolith loop reactor — experiments and modelling. *Catalysis Today* 69, 93–97.
- CINI, P. & HAROLD, M. P. 1991 Experimental study of the tubular multiphase catalyst.

- A.I.Ch.E. Journal* 37 (7), 997–1008.
- EDVINSSON, R. K. & CYBULSKI, A. 1995 A comparison between the monolithic reactor and the trickle-bed reactor for liquid phase hydrogenations. *Catalysis Today* 24, 173–179.
- EL-HISNAWI, A. A., DUDUKOVIC, M. P. & MILLS, P. L. 1982 Trickle-bed reactors: Dynamic tracer tests, reaction studies and modelling of reactor performance. In *Chemical Reaction Engineering* (ed. J. Wei & C. Georgakis), *American Chemical Society Symposium Series* 196, pp. 421–440. American Chemical Society.
- FRANK, M. J. W., KUIPERS, J. A. M., VERSTEEG, G. F. & VAN SWAAIJ, W. P. M. 1999 The performance of structured packings in trickle-bed reactors. *Transactions of the Institution of Chemical Engineers* 77, 567–582.
- GERMAIN, A. H., LEFEBVRE, A. H. & L'HOMME, G. A. 1974 Experimental study of a catalytic trickle bed reactor. In *Chemical Reaction Engineering – II* (ed. H. Hulburt), *Advances in Chemistry Series*, vol. 133, chap. 13, pp. 164–180. American Chemical Society.
- HATZIANTONIOU, V., ANDERSSON, B. & SCHÖÖN, N.-H. 1986 Mass transfer and selectivity in liquid-phase hydrogenation of nitro compounds in a monolithic catalyst reactor with segmented gas-liquid flow. *Industrial and Engineering Chemistry Process Design and Development* 25 (4), 964–970.
- HAZEL, A. L. & HEIL, M. 2002 The steady propagation of a semi-infinite bubble into a tube of elliptical or rectangular cross-section. *Journal of Fluid Mechanics* 470, 91–114.
- HEISZWOLF, J., ENGELVAART, L., VAN DER EIJNDEN, M., KREUTZER, M., KAPTEIJN, F. & MOULIJN, J. 2001 Hydrodynamic aspects of the monolith loop reactor. *Chemical Engineering Science* 56 (3), 805–812.
- IRANDOUST, S. & ANDERSSON, B. 1989 Liquid film in Taylor flow through a capillary. *Industrial and Engineering Chemistry Research* 28, 1684.
- KHADILKAR, M., Y.WU, AL-DAHMAN, M., DUDUKOVIC, M. & COLAKYAN, M. 1996 Comparison of trickle-bed and upflow reactor performance at high pressure: Model prediction and experimental observation. *Chemical Engineering Science* 51 (10), 2139–2148.
- KLINGHOFFER, A. A., CERRO, R. L. & ABRAHAM, M. A. 1998 Influence of flow properties on the performance of the monolith froth reactor for catalytic wet oxidation of acetic acid. *Industrial and Engineering Chemistry Research* 37 (4), 1203–1210.
- KOLB, W. B. & CERRO, R. L. 1991 Coating the inside of a capillary of square cross-section. *Chemical Engineering Science* 46 (9), 2181–2195.
- LEBENS, P. J. M. 1999 *Development and design of a monolith reactor for gas-liquid countercurrent operation*. Ph. D. Thesis, Delft University of Technology.
- LEWIS, W. K. 1916 The principle of counter-current extraction. *Industrial Engineering and Chemistry* 8, 825–836.
- MACHADO, R. M., PARRILLO, D. J., BOEHME, R. P. & BROEKHUIS, R. R. 1999 Use of a monolith catalyst for the hydrogenation of dinitrotoluene to toluenediamine. *United*

- States Patent* US 6005143.
- MAZZARINO, I. & BALDI, G. 1987 Liquid phase hydrogenation on a monolith catalyst. In *Recent Trends in Chemical Reaction Engineering* (ed. B. Kulkarni, R. Mashelkar & M. Sharma), p. 181. New Dehli: Wiley Eastern Ltd.
- MOULIJN, J. A. & CYBULSKI, A., ed. 1998 *Structured catalysts and reactors*. Marcel Dekker.
- NIJHUIS, T. A., DAUTZENBERG, F. M. & MOULIJN, J. A. 2003 Modelling of monolithic and trickle-bed reactors for the hydrogenation of styrene. *Chemical Engineering Science* 58, 1113–1124.
- NIJHUIS, T. A., KREUTZER, M. T., ROMIJN, A. C. J., KAPTEIJN, F. & MOULIJN, J. A. 2001 Monolith catalysts as efficient three-phase reactors. *Chemical Engineering Science* 56 (3), 823–829.
- REID, R. R., PRAUSNITZ, J. M. & POLING, B. E. 1987 *The properties of gasses and liquids*, 4th edn. New York: McGraw-Hill.
- SATTERFIELD, C. N. & ÖZEL, F. 1977 Some characteristics of two-phase flow in monolithic catalyst structures. *Industrial and Engineering Chemistry Fundamentals* 16, 61–67.
- SMITS, H. A., STANKIEWICZ, A., GLASZ, W. C., FOGLE, T. H. A. & MOULIJN, J. A. 1996 Selective three-phase hydrogenation of unsaturated hydrocarbons in a monolithic reactor. *Chemical Engineering Science* 51 (11), 3019–3025.
- DE TEZANOS PINTO, M., ABRAHAM, M. A. & CERRO, R. L. 1997 How do bubbles enter a capillary? *Chemical Engineering Science* 52 (11), 1685–1700.
- THULASIDAS, T. C., ABRAHAM, M. A. & CERRO, R. L. 1995 Bubble-train flow in capillaries of circular and square cross section. *Chemical Engineering Science* 50 (2), 183–199.
- VARGAFTIK, N. B., VINOGRADOV, Y. K. & YARGIN, V. S. 1999 *Handbook of Physical Properties of Liquids and Gases, Pure Substances and Mixtures*. Begell House Inc., New York.
- WHITMAN, W. G. 1923 The two-film theory of absorption. *Chemical and Metallurgical Engineering* 29, 146–148.

CHAPTER VI

SCALING ASPECTS

§ VI.1 INTRODUCTION

One of the biggest challenges in chemical reactor design is *scale-up*, or the use of studies on a small scale to predict behaviour on a large scale. This requires understanding how all relevant phenomena depend on size, such as (1) the interaction of diffusion and reaction inside catalyst particles, (2) the transport phenomena on catalyst particle and reactor scale and (3) flow patterns of all the fluid phases involved.

The intra-particle phenomena are relatively well understood, and solutions of the diffusion-reaction equation inside particles have been generalised using the Thiele-modulus, and scale-up of the particle size is well established. Criteria to perform bench scale experiments without diffusional limitations to obtain the true kinetics are well developed and can be successfully applied, and – provided the intra-particle effective diffusion coefficient can be accurately predicted, such bench scale experiments may safely be extrapolated to larger particles (see *e.g.* Weisz & Prater, 1954; Berger *et al.*, 2001).

For the hydrodynamics and the related transport phenomena, such progress has not been made. In fixed-bed reactors, problems of maldistribution and wall effects cause significant deviations. For reactors with moving catalysts, such as stirred tank reactors and slurry bubble columns, the problems are even more severe, and changes in the flow pattern are not understood well enough to design large scale reactors without large scale studies. In bubble columns, large-scale circulation patterns appear that are very scale dependent and that are hard to predict from small scale studies. For instance, one company decided to use a multi-tubular reactor for a Fisher-Tropsch process instead of a – concededly preferable – bubble column for scale-up reasons alone (Krishna & Sie, 1994).

Monolith reactors should be relatively easy to scale up. There is no convective transport from channel to channel, so maldistribution cannot originate inside the monolith. In fact, the structure suggests that one can make a model for one channel, and multiply that by the number of channels to obtain the reactor model. Of course, maldistribution can occur at the entrance of the column and between monolith blocks, but (1) the origin of the maldistribution is very local, so a proper design of the distributor

and the spacing between the monolith blocks can solve this problem and (2) the distribution at the inlet of a monolith block continues unaltered through the entire monolith block. Provided the extent of maldistribution is not too severe, a single channel model can be used, in which case scale-up issues are essentially absent. In this thesis, the experimental work on monolith reactors was restricted to reactors of relatively small size: the diameter of the largest column used was 0.1 m. As a result, we cannot demonstrate that monolith reactors are scalable to a very large scale using a single channel model alone. However, the scaling from a single channel system to the thousands of channels of a monolith provides valuable information that can be used to scale to even larger reactors.

The purpose of this chapter is to propose a scale-up strategy based on cold-flow experiments alone, which are considerably cheaper and easier than hot flow (reactive) pilot scale experiments. Restricting ourselves to cold-flow studies implies we have to study what happens inside the particle, *i.e.* where the reaction takes place, in a different way. Several recycle reactors with vigorous stirring have been reported in the open literature (van de Riet *et al.*, 1998; Berger *et al.*, 2001) that allow the study of intra-particle phenomena using small monolith samples on a bench scale with good external transport properties. Such reactors can be used to study intra-particle phenomena on a bench scale, similar to the diluted bed methods used for conventional fixed-bed reactors (Berger *et al.*, 2002).

A central position in the scale-up analysis is the pressure drop behaviour. Whatever the distribution, the pressure drop over all the channels must be the same. Based only on the equality of the pressure drop in all the channels, Grolman *et al.* (1996) formulated stability criteria for Taylor flow in a down-flow monolith column. Their pressure drop model was a simplified version of the model used here, but the stability criteria they developed still hold and will be used here.

Pressure drop data can be used to obtain information about the slug length. Berčič & Pintar (1997) demonstrated experimentally that the gas to liquid mass transfer in Taylor flow is also a strong function of the slug length. In this chapter the scale-up strategy will be used to predict the gas to liquid mass transfer in a monolith column to validate the pressure drop based approach.

§ VI.2 STRATEGY DEVELOPMENT

In chapter II of this thesis, a model has been proposed for the pressure drop in single capillary channels. Aside from fluid properties and superficial velocities, the length of the liquid slugs separating the bubbles was the most important parameter. In the single channel setup, the liquid slug length was completely determined by the geometry of the inlet. Once a slug of a certain length is formed, it is sealed between two bubbles and its length does not change as it passes through the channel. Inside monolith channels, the

same holds and the length of the slugs will be determined by the fluid dynamics at the inlet.

In chapter IV of this thesis, we have demonstrated that for a pilot-scale monolith column ($d_M=0.043$ m) the standard deviation of the E -curve is $\sigma_\theta^2 \approx 0.2$ for a single monolith block and even less when multiple blocks are stacked on top of each other. Moreover, the RTD experiments could be used to design and test a distributor that minimises the observed maldistribution of velocities.

The scale-up strategy that is proposed here can be summarised as follows:

- For a given large scale monolith column, RTD measurements can be used to optimise the distributor with the standard deviation of the E -curve as criterion. Note that RTD experiments only provide the distribution of the E -curve, and the pressure drop behaviour is needed to interpret this in terms of distributions of gas and liquid superficial velocities.
- Subsequently, pressure drop measurements can be used to determine the slug length as a function of operating conditions. The slug length depends on the distributor design, and for a large scale distributor the characteristics may be different.
- The slug length is required to map the pressure drop versus gas and liquid superficial velocity. From such a map, conclusions can be drawn about the hold-up distribution and total velocity distribution.
- Finally, once the slug length is known, slug length dependent mass transfer steps can be predicted.

Apart from RTD experiments, which were performed in a different column, this procedure is followed for a cold-flow set-up describe below.

§ VI.3 EXPERIMENTAL

The experimental setup used for this chapter is depicted in Fig. 6.1. The liquid was pumped from the main liquid tank (G) using a centrifugal pump (K). A shower-head distributor (A) was used to spray the liquid on a 0.1 m monolith column (B). The gas flow rate could be set using two solenoid valves (D). The monolith column consisted of several single block sections (B,C) that could be connected using flanges, such that the space between the blocks was less than 5 mm. The outlet of the monolith block was open, *i.e.* at atmospheric pressure, and using a pressure sensor located above the shower-head, the pressure drop over the column could be measured. Gas-to-liquid mass transfer experiments were performed by measuring the oxygen concentration of the inlet and outlet stream using two oxygen sensors (E) in two well stirred tanks. For the outlet stream, only a small fraction of the total flow was sampled from the main

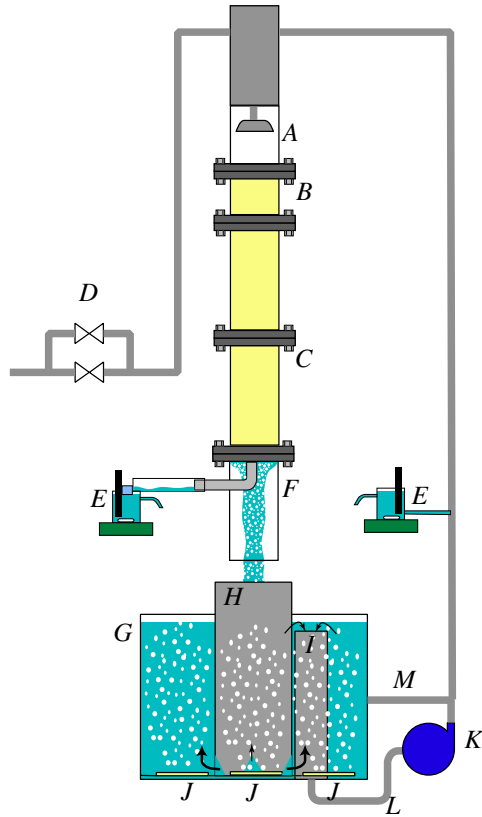


Figure 6.1: The setup used in the experiments.

stream using an elbow tube (F) that could be positioned at different radial positions under the column. During mass transfer experiments, oxygen was stripped out of the main liquid tank by bubbling nitrogen through spargers (J) at the bottom. Short-cutting of liquid was prevented using a down-comer (H) and a draft tube (I).

Special care was taken in the design of the outlet section, see Fig. 6.2, for two reasons: (1) the mass transfer from gas to liquid should be as small as possible and (2) the mass transfer should be as reproducible as possible, which requires a well defined liquid sampling method. A stainless steel bent tube (A) is mounted just under the monoliths. Part of the gas-liquid dispersed flow leaving the monoliths runs through the tube into a bigger diameter tube. The two-phase flow quickly separates into stratified flow, minimising the mass transfer after the monolith section. The liquid is collected in a stirred beaker with an overflow, where the dissolved gas sensor (D) is mounted. To prevent bubbles from reaching the sensor, and to minimise the mass transfer from the

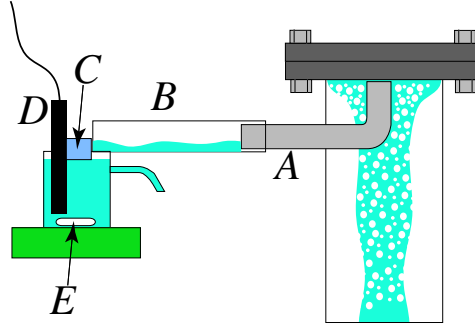


Figure 6.2: Experimental setup, detail of the outlet section.

air to the stirred tank, the beaker is covered with glass wool (C). De-mineralised water and air were used in all experiments.

From the pressure drop, the friction factor for the liquid slugs was calculated analogously to chapter II by

$$f_{\text{obs}} = \frac{\left(\frac{\Delta p}{L}\right)_{\text{(tot)}} - \rho_L g \beta_L}{\left(\frac{1}{2} \rho_L u_{\text{TP}}^2\right) \left(\frac{4}{d_{\text{ch}}}\right) \beta_L} \quad (6.1)$$

where Δp is the experimental pressure drop, L is the column length, β_L is the liquid holdup, ρ_L is the liquid density, u_{TP} is the sum of the liquid and gas superficial velocity, d_c is the channel diameter and g is the gravitational constant.

The gas-liquid mass transfer group $k_{\text{GL}} a_{\text{GL}}$ was calculated assuming plug flow by

$$k_{\text{GL}} a_{\text{GL}} = \frac{u_{\text{TP}}}{L} \ln \left(\frac{C_{\text{sat}} - C_{\text{in}}}{C_{\text{sat}} - C_{\text{out}}} \right) \quad (6.2)$$

where C_{sat} is the saturation concentration of oxygen and C_{in} and C_{out} are the inlet and outlet oxygen concentration, respectively. A major problem was that a significant amount of oxygen was transferred to the liquid in the shower-head section before entering the monolith column. The contribution of the distributor to the mass transfer was accounted for by first doing experiments using a 12 cm monolith column. Subsequently experiments were done in a longer column where the measured outlet concentration of the 12 cm section was used as the inlet concentration for the rest of the column. The electrodes that were used to measure the oxygen concentration were calibrated every three hours at the operating temperature. Frequent calibration was needed in order to measure the concentration with an accuracy of 1%. In all experiments, after the gas and liquid flow rates were set, the system was allowed to reach

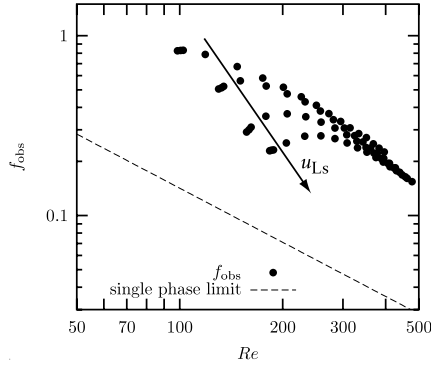


Figure 6.3: The slug friction factor versus the Reynolds number for a 200 cpsi monolith column. The different trends in the figure are for different superficial liquid velocities: the arrow indicates the direction of increasing liquid velocity.

steady state before either the pressure drop and the oxygen concentration were measured at least 50 times. In post-processing of the data, the average of the 50 measurements was used, and the standard deviation of the 50 measured points was used to verify steady state.

§ VI.4 RESULTS

The observed friction factor from measurements in a 0.26 m long column is plotted versus the Reynolds number together with the single phase limit $f = 14.2/Re$ for square channels (Shah & London, 1978) in Fig. 6.3. In the same setup as the one used in this work, Heiszwolf *et al.* (2001b) measured the slug length in the column using conductivity measurements from electrodes mounted on opposite sides of a channel. As only one pair of electrodes was used, the velocities could not be calculated from the cross correlation of the signal from two probes and the two phase superficial velocity was used to calculate the bubble and slug length from the conductivity data. The dimensionless slug length $\Psi_S (=L_{\text{slug}}/d_{\text{channel}})$ measured by the conductivity probe was correlated as a function of the liquid holdup β_L by

$$\Psi_S = \frac{\beta_L}{-0.00141 - 1.556\beta_L^2 \ln(\beta_L)} \quad (6.3)$$

Note that this fitted correlation has no clear physical basis (for the original data, see Heiszwolf *et al.* (2001b)). Also, it should be noted that these data were obtained using a different shower-head with about twice the number of jets than the one used in this study.

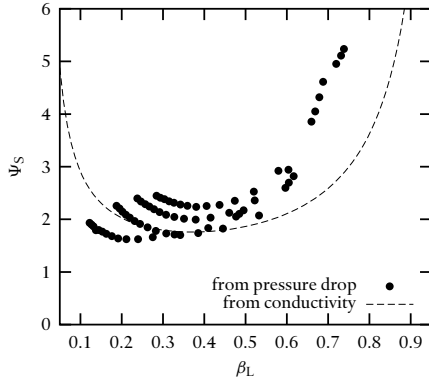


Figure 6.4: Dimensionless slug length Ψ_S for a 200 cpsi column as a function of the the holdup β_L from two different methods. The markers indicate Ψ_S calculated from pressure drop. The line represents the correlation Eq. 6.3 from Heiszwolf *et al.* (2001b)

The pressure drop correlation developed in chapter II can be used to estimate the slug length from the experimental friction factor. Because the channels of the monolith are square, we have replaced the single phase limit for round channels $f=16/Re$ with the single phase limit for square channels $f=14.2/Re$ to obtain

$$f = \frac{14.2}{Re} \left[1 + 0.17 \frac{1}{\Psi_S} \left(\frac{Re}{Ca} \right)^{0.33} \right] \quad (6.4)$$

In Fig. 6.4 the slug lengths obtained from the conductivity measurements, Eq. 6.3, is plotted versus the holdup together with the slug length calculated from the pressure drop model, Eq. 6.4. The conductivity correlation Eq. 6.3 has a minimum of $\Psi_S=2$ at $\beta_L=0.4$. The slug length from pressure drop also shows a minimum at similar holdup. Especially at higher liquid holdups, the slug length determined by pressure drop is somewhat higher than the slug length based on conductivity.

No single channel experiments for gas to liquid mass transfer were performed for this thesis, so experimental data from the open literature are used. Berčič & Pintar (1997) measured gas–liquid mass transfer in a single channel for a wide range of superficial gas and liquid velocity. Their experimental set-up allowed the independent variation of bubble and slug length. They correlated their data for a methane-water system as

$$k_L a = \frac{0.133 u_{TP}^{1.2}}{L_{slug}^{0.5}} \quad (6.5)$$

We have accounted for the difference in diffusivity for oxygen and methane by assuming that Eq. 6.5 scales with the square root of diffusivity, *i.e.* assuming that gas–

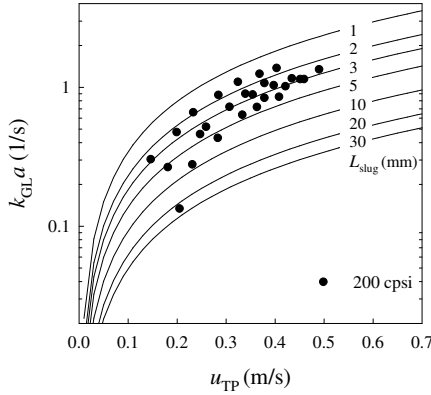


Figure 6.5: Gas-to-liquid mass transfer as a function of slug velocity u_{TP} for a 200 cpsi monolith. ($d_c = 1.56$ mm). The markers represent experimental data. The lines are computed from Eq. 6.5 using various values for the slug length, as indicated in the figure.

to-liquid mass transfer in Taylor flow is better described by a penetration theory model than by a film theory model. Interestingly, the mass transfer from Eq. 6.5 is a function of the slug length and is not a function of the bubble length. Intuitively, a penetration theory model with contact time calculated from the bubble length seems more logical for this case. In fact, Higbie (1935) first proposed the penetration theory using experimental data for *single* Taylor bubbles in capillaries in which the contact time was related to the bubble length. A possible explanation for the completely different behaviour of bubble-train Taylor flow may be offered by assuming that the lubricating film near the wall is completely saturated each time the bubble passes by. If that is the case, then the data of Berčić & Pintar describe (1) the partial depletion of the film between the wall and the slug and (2) the transfer of gas to the slug at the bubble caps. The specific interfacial area associated with film depletion is inversely proportional to the channel diameter, whereas the interfacial area associated with transfer from the caps is independent of channel diameter. Berčić & Pintar varied the channel diameter between 1.5 mm and 3.1 mm and found no impact of channel diameter, which suggests that film depletion only plays a minor role.

In Fig. 6.5, the experimental gas-liquid mass transfer data in a 200 cpsi monolith column are plotted together with several model lines from Eq. 6.5. There is significant scatter in the data. This is mainly caused by the severe error propagation of the uncertainty of concentration (1%) in the terms $(C_{sat} - C_{in,out})$: the experimentally determined C_{in} and C_{out} were close to C_{sat} due to the high gas-liquid gas transfer in the distributor section. In spite of the large scatter, comparison of the experimental data for the monolith with the single channel correlation reveals that the slug length is ap-

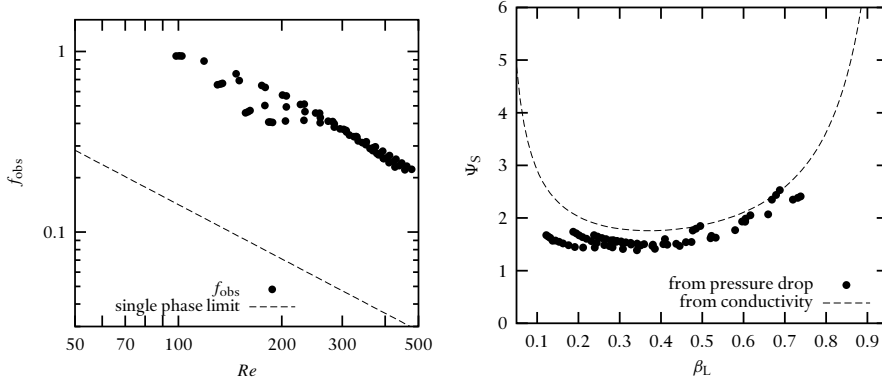


Figure 6.6: The effect of the distributor pressure drop. The measurements are the same as for Fig. 6.3 and 6.4, but now the pressure drop over the distributor is accounted for with $c_1=10$ in Eq. 6.6.

proximately 3 mm. Using the channel diameter $d_{ch}=1.56$ mm for 200 cpsi this becomes $\Psi_S=2$.

§ VI.5 DISCUSSION

The slug length derived from pressure drop is not in perfect agreement with the pressure drop obtained from the conductivity measurements. The pressure drop was measured above the distributor section, and the pressure drop of the gas phase in the shower-head section was estimated from the Bernoulli equation (White, 1998; Heiszwolf *et al.*, 2001a):

$$\Delta p_{dist} = c_1 \frac{A_{jet}}{A_M} \frac{1}{2} \rho_L u_{jet}^2 \quad (6.6)$$

where A_{jet} is the total cross sectional area of the jets, A_M is the open frontal area of the monolith and u_{jet} is the velocity of the liquid jets. For the pressure loss constant we have used $c_1=2.5$ in agreement with Heiszwolf *et al.* (2001a).

Fig. 6.3 shows that the friction factor for a given Re tends to drop with increasing $u_{L,S}$. As a result, the slug length determined by the friction factor depends on $u_{L,S}$ and the hold-up β_L .

By changing the value c_1 to 10, the observed effect of the liquid velocity on the friction factor (or slug length) could be removed and a better agreement between the slug lengths from the two different methods was obtained, see Fig 6.6. This suggests that $c_1=10$ is a better proportionality constant for the distributor used. The absolute pres-

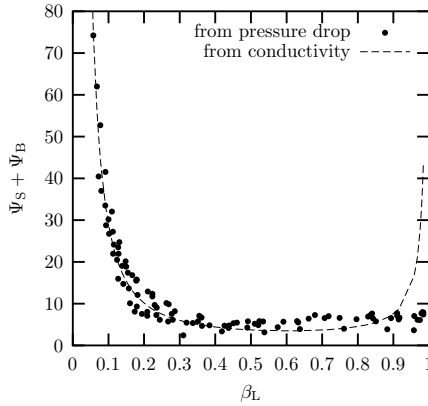


Figure 6.7: Dimensionless unit cell length (bubble length plus slug length divided by channel diameter) as a function of holdup. Data from van der Eijnden (1999).

sure drop in monoliths is low, so the impact of a small pressure drop over the distributor can be large if it is not properly accounted for.

As stated before, the conductivity measurements were performed with a slightly different shower-head by van der Eijnden (1999). During these experiments, pressure drop was also recorded. Fig. 6.7 shows the dimensionless length of the unit cell ($\Psi_S + \Psi_B$) calculated from these pressure drop measurements of van der Eijnden (1999), together with the conductivity results. As for this comparison the same distributor was used, the agreement is better, especially at low liquid holdup. On the other hand, the pressure drop method systematically over-predicts the unit cell length for $0.5 < \beta_L < 0.8$. In order to explain this, it is illustrative to make a contour plot of the pressure drop per unit length as a function of gas and liquid superficial velocity, see Fig. 6.8. This contour plot was generated using the pressure drop model, Eq. 6.4, and the slug length correlation, Eq. 6.3.

Note that the contour plot will be slightly different if the slug length from pressure drop measurements are used. So, we are faced with a chicken-and-egg problem: the pressure drop data are obtained from a maldistributed column, and we cannot use the resulting isobars to split the distribution of the E -curve into the distributions of gas and liquid superficial velocities. However, the relevant feature of the isobar is the slope du_{Gs}/du_{Ls} and not the actual pressure drop it represents, so the error introduced by using the maldistributed pressure drop data in processing an E -curve depend on how much this slope changes. For the data of van der Eijnden, the minimal slug length from both conductivity and pressure drop is found at $\beta_L \approx 0.4$, and increases for higher and lower holdup. The main difference is that for higher holdup, the slug length obtained from pressure drop is slightly higher.

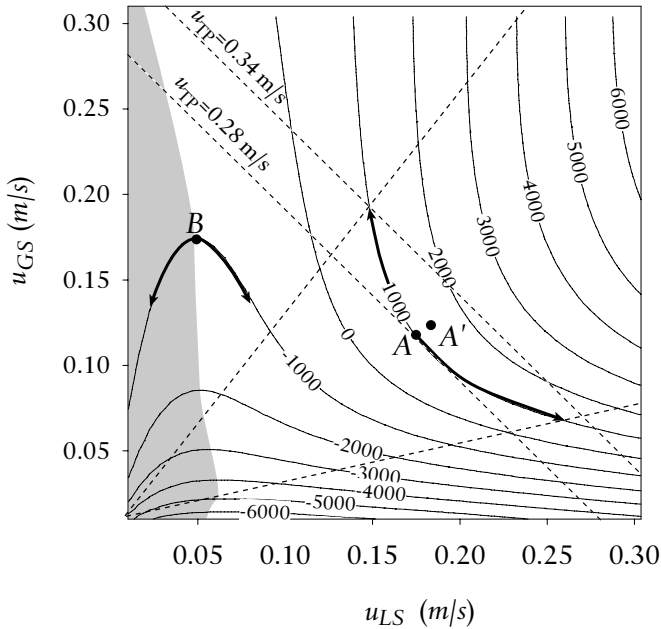


Figure 6.8: Contour lines of constant pressure drop per unit length versus gas and liquid superficial velocity. The lines were calculated for a 200 cpsi monolith using Eq. 6.4 for the friction factor and Eq. 6.3 for the slug length.

The conductivity measurements of van der Eijnden can be used to explain the error made by using maldistributed pressure drop data. Consider the contour line $(dp/dL)=1000$ Pa/m. In the absence of maldistribution, this pressure drop is obtained when operating the monolith at $u_{LS}\approx 0.17$ m/s, $u_{GS}\approx 0.11$ m/s (point A in Fig. 6.8). If maldistribution is present, this pressure drop is obtained in each channel for any combination of u_{LS} and u_{GS} on the contour line, since the pressure drop in all the channels must be the same. The question is: How large is the range of combinations? The range can be obtained from RTD experiments, provided the contour lines of equal pressure drop are known. Note that for the example of a distribution around point A, the isobar is not linear, and the analytical solution presented in chapter IV, based on a first-order Taylor expansion of the isobar around point A, cannot be used, and the ranges of velocity and hold-up must be calculated from the *E*-curve numerically. In the figure, four dotted lines show a possible outcome of processing an *E*-curve. Two lines of slope -1 indicate a range of total velocities between 0.28 m/s and 0.34 m/s. The two lines pointing away from the origin indicate a range in holdup. The arrows pointing away from point A indicate all possible combinations of gas and liquid velocities that may be obtained for these ranges. For most of these channels, the sum of gas and liquid superficial

velocity is higher than 0.28. Point A' shows an estimate of the average gas and liquid velocity for the maldistributed case. In other words, for the same pressure drop the total velocity in the maldistributed case (A') is higher than the velocity without maldistribution (A). Note that for point A' in the absence of maldistribution a pressure drop of $(dp/dL)=1300$ Pa/m would be obtained.

It follows from the same line of argument that for a given average gas and liquid velocity, maldistribution lowers the pressure drop. This has already been demonstrated experimentally by Satterfield & Özel (1977), who observed that better distributors increased the pressure drop. Of course, inspection of the friction factor equation, Eq. 6.4, reveals that the lower pressure drop for maldistributed flow translates into a larger slug length.

The argument followed above strongly depends on the curvature of the contour lines

$$\left. \frac{\partial^2 u_{Gs}}{\partial u_{Ls}^2} \right|_{\Delta p = \text{constant}}$$

which is largest for the lines of positive pressure drop in the region $u_{Ls} \approx 1.5u_{Gs}$ or $\beta_L \approx 0.6$. Note that this is exactly the region where the pressure drop over-predicted the slug length. For point B in Fig.6.8, the situation is reversed and consequently in this area the pressure drop method will under-predict the slug length.

In short, using the pressure drop to determine the slug length is a powerful tool provided that one considers the effect of distributor pressure drop and maldistribution. Because van der Eijnden determined the slug length by conductivity, we can explain the errors introduced by the method. Further, the distributor used in this chapter is not at all optimised. For the RTD experiments in chapter IV, a spray nozzle was used that was designed to evenly distribute liquid over a surface. The static-mixer distributor was designed with the application of monoliths in mind. It is for this reason that it is recommended to first optimise a distributor using RTD experiments, and later use the pressure drop data to further interpret the E -curve.

The ideal experimental tool to study the maldistribution of holdup and velocity in a large scale monolith would be a tomographic method that has the spatial resolution on a channel scale *and* is fast enough to capture individual bubbles and slugs. Recently Glad-den and co-workers have made considerable progress in applying MRI tomography to study monoliths (Mantle *et al.*, 2002). At present, however, the temporal resolution is limited to slowly moving bubbles. Also, MRI tomography is also limited to relatively small columns. Nevertheless, MRI tomography in combination with RTD and pressure drop measurements would be a powerful method to confirm the –experimentally much simpler– scale-up strategy proposed in this work by direct observation on a small scale.

SCALING ASPECTS

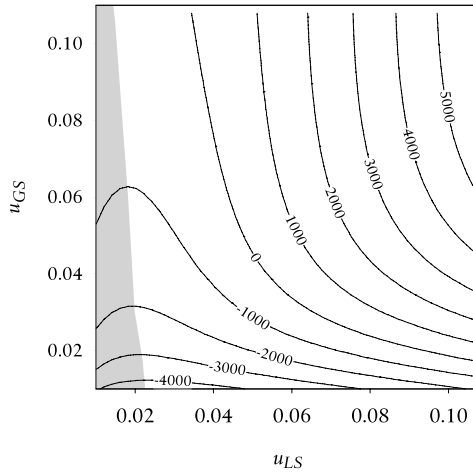


Figure 6.9: Contour lines of constant pressure drop per unit length versus gas and liquid superficial velocity. The lines were calculated for a 600 cpsi monolith using Eq. 6.4 for the friction factor and Eq. 6.3 for the slug length. Note that the range of velocities is lower than in Fig. 6.8.

§ VI.6 STABILITY

Grolman *et al.* (1996) performed a stability analysis based on the contour lines of pressure drop, such as Fig. 6.8. In short, the flow in a capillary bundle will be unstable if a decrease in velocity results in an increased resistance to flow, *i.e.* an increase in pressure drop. For the gas velocity, this is never the case for the monoliths used here. For the liquid velocity, the shaded region in Fig. 6.8 shows the region where a decrease in liquid velocity will lead to an increase in pressure drop.

Grolman *et al.* found a similar region, but their pressure drop model ignored the slug-length dependent effects on the friction factor. Using a friction factor $f=16/Re$, they found an unstable region for $u_{Ls} < 0.18$ m/s. Using the pressure drop model developed in chapter II, the unstable region reduces to $u_{Ls} < 0.05$ m/s. In other words, higher slug-length averaged friction factors reduce the extent of the unstable region. This indicates that in order to obtain the lowest stable operating velocities, a distributor should be used that generates small slugs. The increased contribution of friction to the overall pressure drop decreased the unstable region. Since increasing the cell density of a monolith also increases the contribution of friction to the pressure drop, monoliths of high cell density should be used if a high residence time (low velocity) is required. Fig. 6.9 shows a contour plot of constant pressure drop per unit length for a 600 cpsi monolith, in which the unstable region is reduced to $u_{Ls} < 0.02$ m/s.

One important characteristic of the unstable region is the low liquid holdup. In chapter IV, the residence time based on the $E(t)$ curves showed significant deviations

from the holding time based on superficial velocities (see Fig. 2.15). The analysis shown here suggests that this is caused by unstable operation at low liquid holdup. Again, the combination of RTD and pressure drop provides valuable information about the large-scale operation of monoliths.

§ VI.7 MONOLITHS AS GAS-LIQUID CONTACTORS

The findings of the work presented in this chapter indicate that monoliths can be scaled up reliably from a single channel to the thousands of channels in a monolith block. The mass transfer experiments showed that in the 0.1 m column used in this work, the slug length is approximately 3 mm. As these experiments were performed in monoliths with a channel diameter of 1.56 mm, the agreement with $\Psi_S \approx 2$ from the pressure drop measurements is striking. Despite the large scatter in the data, the gas-liquid mass transfer measurements may be regarded as yet another tool to determine the slug length, albeit a somewhat inaccurate one.

Although the experiments were useful in that respect alone, several other aspects of the gas-to-liquid mass transfer are worth mentioning here. When high gas-liquid mass transfer rates are required, one usually turns to vigorous stirring. Indeed, bench scale autoclaves that are designed to study kinetics of chemical reactions in the absence of gas-liquid mass transfer limitations typically have a stirrer engine that is larger than the autoclave itself. It is self evident that this approach is not very scalable: the energy required to achieve the same mass transfer characteristics on a large scale are enormous. As a result, the $k_{GL}a_{GL}$ values reported for large scale stirred tank reactors, $\mathcal{O}(0.1 \text{ s}^{-1})$, are typically an order of magnitude lower than the values reported for bench scale stirred tank reactors, $\mathcal{O}(1 \text{ s}^{-1})$.

While a careful study of the pressure drop in monoliths revealed a wealth of information, it may be reiterated here that the pressure drop in monolith reactors is low, *i.e.* the rough estimate $f \approx 20/Re$, reported by Heiszwolf *et al.* (2001a), is probably sufficient for designing the pumps and compressors for a monolith reactor, and the studying of the “fine print” in this work serves an entirely different purpose. A low pressure drop implies a low energy requirement, so the following question immediately presents itself: “Are monoliths scalable gas-liquid contactors with good mass transfer characteristics at low energy input and, if this is the case, why?”

For the sake of generality, we state here that most gas-liquid contactors where the liquid phase is the continuous phase are turbulent, at least for the liquid phase. Moreover, the difficulty in scaling-up turbulent gas-liquid contactors can in part be contributed to the difficulty of understanding the backmixing, flow behaviour of the large scale eddies, and gas-liquid interactions in the turbulent liquid phase of many of these reactors, such as stirred tank reactors, air-lift reactors and bubble columns.

In a turbulent flow field, the maximum stable bubble size is given by a balance of the (eddy) shear stresses ($\sim \tau$) and the surface tension stresses ($\sim \gamma/d$) that resist bubble

deformation. The ratio of these stresses gives a criterion for bubble break-up

$$We = \frac{\tau d}{\gamma} > We_{\text{crit}} \quad (6.8)$$

where We is a Weber number and We_{crit} is the critical Weber number for break up. Hinze (1955) postulated that bubble break-up is mainly caused by eddies of the same scale as the bubble scale. The mean square fluctuating velocity over a distance l in a turbulent fluid field where $l_p \ll l \ll l_k$ (l_p being the scale of the primary eddies and l_k being the (kolmogorov) scale of the smallest eddies) is given by Batchelor (1951) as a function of the power dissipated per unit volume (P/V) as

$$\overline{u_{(l)}^2} \propto \left(\frac{P}{V}\right)^{2/3} \left(\frac{l}{\rho_L}\right)^{2/3} \quad (6.9)$$

so using Hinze's postulate the shear stress τ caused by turbulence is

$$\tau \propto \rho_L \overline{u_{(l)}^2} \propto \rho_L \left(\frac{P}{V} \frac{d_b}{\rho_L}\right)^{2/3} \quad (6.10)$$

which can be used in the critical Weber number. Combining Eqs. 6.8 and 6.10 we have

$$d_b \propto \frac{\gamma^{2/5}}{(P/V)^{2/5} \rho_L^{1/5}} \quad (6.11)$$

This equation was derived by Hinze (1955) for the maximum bubble diameter, and experimental work on bubble size distributions revealed that only a different proportionality constant is needed to use Eq. 6.11 for the mean Sauter bubble diameter. The mean Sauter bubble diameter d_{SM} is related to the interfacial area for gas-liquid mass transfer by

$$a = \frac{6\epsilon_G}{d_{\text{SM}}} \quad (6.12)$$

in which ϵ_G is the gas hold-up. For the mass transfer coefficient k_L , Calderbank & Moo-Young (1961) used the experimental evidence that k_L is independent of the bubble size and that $k_L \propto D^{-2/3}$ to propose $Sh = Sc^{1/3} Re^{3/4}$, with Re based on Eq. 6.9 and d_b , which can be written as

$$k_L \propto \frac{[(P/V)\mu_L]/\rho_L^2)^{1/4}}{(\mu_L/\rho_L D)^{2/3}} \quad (6.13)$$

Combining Eqs. 6.11, 6.12 and 6.13, we obtain

$$k_L a \propto \left(\frac{P}{V}\right)^{0.65} \epsilon_G \quad (6.14)$$

where all the fluid properties are lumped into the proportionality constant. So, using turbulence theory we can relate the mass transfer group $k_L a$ to the power input per unit volume. The short analysis presented here is by no means exhaustive. For instance, the turbulence intensity is far from homogeneous throughout a vessel, the gas density is not considered while it should be (Wilkinson & van Dierendonck, 1990), and the presence of surfactants may prevent bubble coalescence, resulting in lower bubble sizes. Eq. 6.14 just shows that by adding more power per unit volume to a turbulent gas-liquid dispersion, the mass transfer group $k_L a$ increases, which is mainly caused by a reduction in bubble diameter. Further it shows that for gas-liquid mass transfer, the contactor should have a high gas hold-up. In fact, designing stirrers and spargers that generate a high hold-up is the bread and butter of gas-liquid contactor designers.

The power input by sparging per unit liquid volume can be estimated from the work done by the gas

$$\frac{P}{V} = \frac{(\Delta p)_{\text{gas}} \phi_{\text{gas}}}{V} = \frac{(\rho_L g H_0)(A u_{G_s})}{A H_0} = \rho_L g u_{G_s} \quad (6.15)$$

in which H_0 is the liquid level without sparging and A is the vessel diameter. The work done by a stirrer can be measured directly with a torque meter or estimated from literature correlations.

In Fig. 6.10, $k_L a$ values are shown versus power input per unit volume for several bubble columns and stirred tank reactors. Schlüter & Deckwer (1992) reported $k_L a$ values versus power input for stirred tank reactors of 0.072m^3 - 3m^3 . Linek *et al.* (1990) reported $k_L a$ values versus power input and correlated all their data with the single curve for $k_L a/u_{G_s}^{0.4}$ versus (P/V) . In Fig. 6.10, the data of Linek *et al.* are plotted for $u_{G_s} = 2.12\text{ mm/s}$ and $u_{G_s} = 4.24\text{ mm/s}$, and because here the change of hold-up with the change of superficial gas velocity is not accounted for the data appear as two separate curves in Fig. 6.10. Note that $k_L a$ and (P/V) for the turbulent systems are reported per unit liquid volume. Clearly, the exponent of the power input per unit volume agrees with the theoretical value, based on homogeneous isotropic turbulence, indicated by the lines with slope 0.65 in Fig. 6.10.

Monoliths are *laminar* gas-liquid contactors, of which the behaviour is not governed by turbulence theory, and this fact alone suggests that the mass transfer behaviour in terms of the power per unit volume will be different. In fact, only at the inlet of the monolith column energy is required to generate small bubbles. Once they are generated, the bubbles in the capillaries extend over almost the entire cross section of the capillary and bubble coalescence is prevented by the slugs that are sealed between the bubbles, and no energy is required to maintain the small bubbles.

The power required to operate a down flow monolith column is dominated by the static head of the liquid pumped to the top of the column if a low pressure drop distributor such as the static mixer configuration from chapter IV is used. Analogously to the equation for bubble columns, this liquid feed static head may be written as

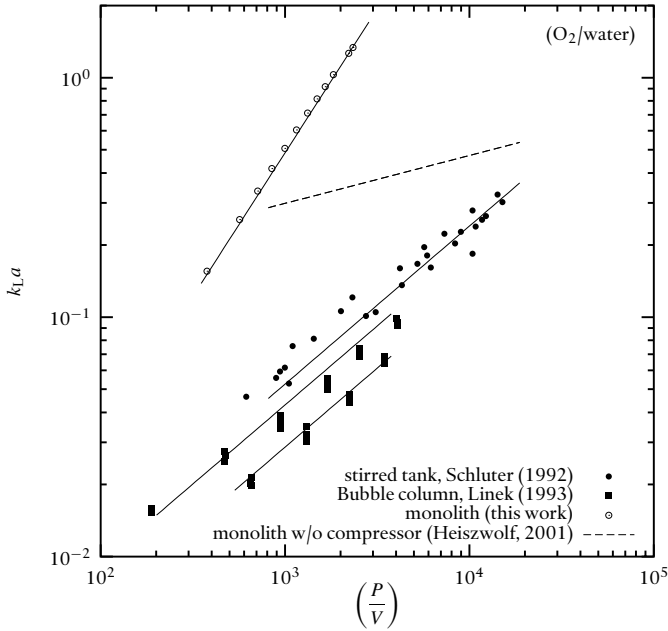


Figure 6.10: The mass transfer group $k_L a$ versus power input per unit volume for several turbulent contactors ($k_L a$ and (P/V) per unit liquid volume) and monoliths ($k_L a$ and (P/V) per unit channel volume) for oxygen transfer to water.

$$\frac{P}{\bar{V}} = \frac{(\Delta p)_{\text{liq., feed}} \phi_{\text{liq.}}}{V} = \frac{(\rho_L g H_0)(A u_{Ls})}{A H_0} = \rho_L g u_{Ls} \quad (6.16)$$

Here we assume that the feed pipe is large enough to ignore frictional losses. In addition to this term, we need the work required to force the gas and the liquid through the column, for which

$$\frac{P}{\bar{V}} = \frac{(\Delta p)_{\text{col}} \phi_{\text{liq.}}}{V} + \frac{(\Delta p)_{\text{col}} \phi_{\text{gas}}}{V} \quad (6.17)$$

Note that monoliths may be operated at zero pressure drop in the column, in which case these terms reduce to zero. Moreover, at zero pressure drop a compressor is not needed. However, because the column pressure drop is low, only a small compressor is needed to force additional gas through the column. Heiszwolf *et al.* (2001a) reported $k_L a$ versus power input for such a compressor-less configuration based on experimental data obtained with the shower head distributor. Their data are plotted in Fig. 6.10 using a dashed line and clearly show that the mass-transfer characteristics of monolith reactors are superior to (agitated) bubble column reactors. However, in a compressor-

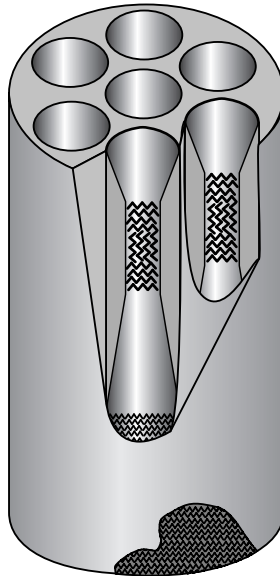


Figure 6.11: An impression of a scaled-up distributor, based on the design used for residence time distribution experiments.

less configuration, $k_L a$ hardly increases with increasing power input, because the gas hold-up decreases with increasing liquid superficial velocity, and as a result the slug length increases.

The mass transfer correlation obtained in single channels, Eq. 6.5, indicates that if the slug length is held constant, $k_L a$ scales with $(P/V)^{1.2}$. In Fig. 6.10, a second line for monoliths is plotted for a reactor in which a small compressor is added to keep the liquid hold-up at $\epsilon_L = 0.5$, assuming a lower pressure drop distributor is used, such as the static mixer described in chapter IV and a column length of one meter. For such a configuration the exponent of the power input is 1.2. Further, for such a configuration monoliths allow for at least an order of magnitude reduction in the power input required to obtain a given mass-transfer rate. We have only considered a 200 cpsi monolith, because the gas-liquid mass transfer is independent of the channel diameter. Using higher cell density monoliths for only gas-liquid contacting is therefore not recommended.

In addition to the better performance of the monoliths, the scalability of the monolith reactors is also good. Although the experiments presented in this chapter were limited to a column diameter of 10 cm, the results indicate that scaling from a single channel to a monolith block is feasible and predictable. Further, the distributor used in chapter IV may be modified for a larger column by using several pipes with a contraction to enhance bubble generation in a manner depicted schematically in Fig. 6.11.

With the high mass transfer rates in monoliths, the gas phase may be depleted after a short column length in a catalytic reactor. Although this might be regarded as a drawback of using monoliths, the high mass transfer characteristics imply that only a small column is needed, and a large scale distributor such as the one depicted in Fig. 6.11 may also be used to add gas in between monolith blocks (interstage feeding), because the good distribution characteristics reported in chapter IV were valid for the worst possible feeding conditions.

The good performance at low power input suggests that monoliths should be considered for gas–liquid contacting applications, even if the channels are not coated with a catalyst, *e.g.* in gas–liquid homogeneous (bio-)catalysis. For instance, the large fermentors in biotechnological applications can suffer from gas–liquid mass transfer limitations (for an overview of bioreactors, see *e.g.* van 't Riet & Tramper, 1991). Typically, large bubble columns or air lift reactors are used. The results of this chapter indicate that monoliths can be used to intensify such processes, significantly reducing the volume and energy input for such reactors.

§ VI.8 MONOLITHS FOR THREE-PHASE REACTIONS

For slurry bubble columns and agitated slurry reactors, the overall mass transfer rate in a three–phase system also depends on the liquid–solid mass transfer rate. If the gas–liquid and liquid–solid mass transfer rates may be regarded as resistances in series, then

$$k_{ov}a = \left(\frac{1}{k_{GL}a_{GL}} + \frac{1}{k_{LS}a_{LS}} \right)^{-1} \quad (6.18)$$

This approach is only valid if there is no overlap of the film surrounding the catalyst and the film surrounding the gas bubbles. For catalyst particles that have a tendency to accumulate at the gas–liquid interface, such overlap becomes important. For instance, van der Zon *et al.* (1999) reported for hydrophobic carbon supported catalysts in aqueous media a significant enhancement of the reaction rate compared to γ -Al₂O₃ supported catalysts.

If we ignore the agglomeration of catalysts on the gas–liquid interface, Eq. 6.18 holds. Further, the use of very fine catalyst powder may result in a high value of $k_{LS}a_{LS}$. The maximum overall mass transfer then becomes equal to the gas–liquid mass transfer rate.

$$\max(k_{ov}a) = \lim_{k_{LS}a_{LS} \rightarrow \infty} \left(\frac{1}{k_{GL}a_{GL}} + \frac{1}{k_{LS}a_{LS}} \right)^{-1} = k_{GL}a_{GL} \quad (6.19)$$

For monolith reactors, the situation is somewhat more complex. The numerical analysis in chapter V revealed that the limiting mass transfer step in three-phase reactions is the liquid–solid mass transfer through the film separating the catalyst from the

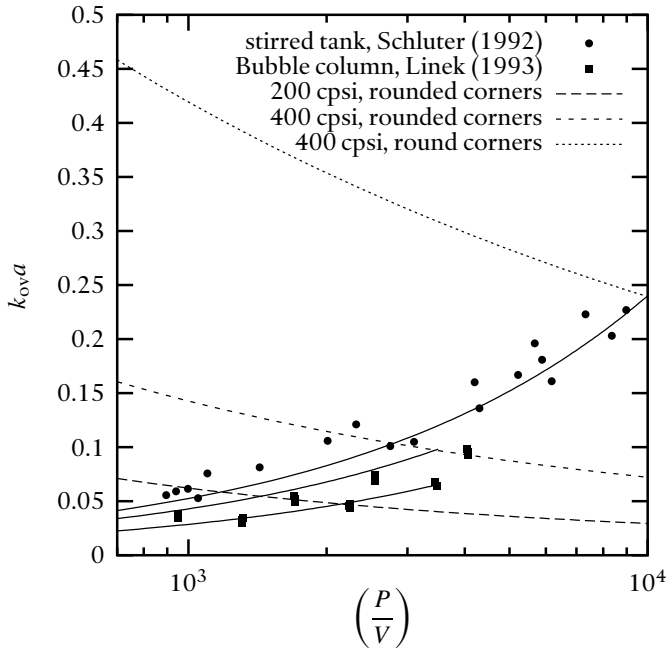


Figure 6.12: The mass transfer group $k_{ov}a$ versus power input per unit volume for several turbulent contactors and for monoliths. In all systems, the properties of oxygen in water are considered.

bubbles and slugs. The thickness of this film depends strongly on the shape of the catalyst, and the use of channels with rounded corners resulted in a film, three times thicker than in round channels.

In Fig. 6.12, a comparison of the overall mass transfer characteristics of slurry bubble columns, agitated slurry reactors and monolith reactors is presented. The data for the slurry bubble column and the agitated slurry reactor are equal to the data for gas-liquid mass transfer. The lines for monoliths were calculated using the model from chapter V and assuming that the power input per unit volume is dominated by the liquid pressure losses in the feed line and the column. For the pressure drop in the column, a friction factor $f=30/Re$ was assumed. For a fair comparison, the data for the monolith were calculated from the model presented in chapter V with the gas and liquid properties of oxygen and water. For a typical hydrogenation reaction in organic liquids, the diffusion coefficient is an order of magnitude larger, and $k_{ov}a$ will increase accordingly.

For a 200 cpsi monolith with rounded corners, the overall mass transfer characteristics are comparable to a bubble column, and a 400 cpsi monoliths with rounded channels are comparable to slurry reactors. The dependence on the power input, however, is reversed for monoliths: the film thickness is reduced by a decrease in power

input (lower velocities), and the mass transfer characteristics of the limiting steps improves. If the washcoating procedure is optimised to produce round channels, then a spectacular increase in the mass transfer of monoliths is obtained: the line for 400 cpsi monoliths with round channels shows that this monolith outperforms all other reactors over the entire range of power consumption.

Since commercial scale stirred tank reactors can usually not be operated at very high power input, the monolith reactor is an excellent alternative for all processes that benefit from good mass transfer characteristics. This includes processes for which the catalysed intrinsic kinetics are very fast, processes where mass transfer limitations lead to a drop in selectivity and processes where the stability of the catalyst deteriorates at low (hydrogen) concentrations inside the catalyst. A skeptical reader could suggest that the distribution issues in monoliths will reduce the performance of monolith reactors, but the work presented in this chapter indicates that the scaling from a single channel to thousands of channels is feasible. An optimistic reader might suggest that 400 cpsi is not the highest feasible cell density for monolith reactors. This is indeed true. For higher cell densities the required power input also increases, but not tremendously: while the frictional pressure drop in the channel scales with the inverse of the diameter, monoliths are typically operated in a range where the frictional pressure drop is roughly balanced by the hydrostatic head in the column.

It is not very realistic to consider the use of monoliths at high power input. At high velocities, the mass transfer characteristics deteriorate and the residence time is low. The only reason for not operating a monolith at low velocities is flow stability. It was shown earlier in this chapter that for a 200 cpsi monolith, the stability criterion is roughly $u_{L,s} > 0.05$ m/s. For higher cell density monoliths, the minimal velocity is lower because the frictional component contributes more to the pressure drop in the column.

§ VI.9 CONCLUSIONS

In this chapter, a strategy was proposed to design large scale monolith reactors based on cold-flow studies. An experimentally obtained residence time distribution curve can be combined with experimental pressure drop data to obtain not only the distribution of gas and liquid superficial velocity, but also the length of the slugs separating the bubbles. This approach becomes inaccurate when the distribution of velocities is very large. If this is the case, then the slug length inside the channels should be determined by different measurements. In this chapter, conductivity measurements were used to validate the approach.

The gas-liquid mass transfer in capillaries is a strong function of the slug length. The gas-liquid mass transfer performance of a 200 cpsi monolith could be predicted by following the strategy based on pressure drop measurements. So, the mass transfer performance can be based on a single channel model. The deviation of the residence time distribution from single channel behaviour caused by maldistribution had already

been shown to be above the limit $Bo=100$ for longer columns. As a result, for many processes a monolith design may be based on a single channel model. This is subject to the use of a good distributor. The cold-flow experiments performed in this work may be performed for a larger column to confidently scale up to larger columns than the ones used in this thesis.

The mass transfer characteristics of a 200 cpsi monolith was determined in a pilot-scale column. The gas-liquid mass transfer rate that was obtained was very high. Monoliths were compared with (agitated) slurry reactors, which also have good mass transfer characteristics. Monoliths were found to be superior when the gas-liquid mass transfer capacity as a function of the power-input per unit reactor volume is used as a criterion. As a rule of thumb, the mass transfer capacity is an order of magnitude higher at similar power input if a 200 cpsi monolith is used. Because the mass transfer characteristics of monoliths are independent of channel size, the use of high cell density monoliths is not recommended. For turbulent gas-liquid contactors, correlations based on this power input are scalable: they are based on physical principles. Note that the monolith correlation was obtained in a single channel with a volume of 5 mL and a monolith column with a volume of 5 L, which demonstrates that the monolith correlation is also scalable.

Finally, the application of monoliths for three-phase reactions was also compared to slurry reactors. In general, a similar conclusion can be drawn: at low power input the monoliths are superior. The performance of monoliths is, however, very sensitive to the shape of the channels and the cell density. For 400 cpsi and higher cell densities, assuming round channels, monoliths are superior to agitated tank reactors, except at extremely high power input.

NOTATION

a	interfacial area, m^{-1}
A	area, m^2
c_1	constant in Eq. 6.6, –
C	concentration, mol/m^3
D	diffusion coefficient, m^2/s
d	diameter, m
g	gravitational constant, m/s^2
H	height, m
k	mass transfer coefficient, m/s
L	length, m
l	eddy size, m
p	pressure, Pa
P	power, W
u	velocity, m/s

u_{TP}	two-phase superficial velocity, m/s
u_{Gs}	superficial gas velocity, m/s
u_{Ls}	superficial liquid velocity, m/s
V	volume, m^3

Greek letters

β_L	dynamic holdup, m^3/m^3
γ	surface tension, N/m
δ	film thickness, m
ϵ_L	liquid holdup, m^3/m^3
ϵ_G	gas holdup, m^3/m^3
μ	viscosity, Pa s
τ	mean residence time from E -curve, s
ϕ	flow rate, m^3/s
ρ	density, kg/m^3

Dimensionless numbers

Ca	Capillary number ($= \mu_L u / \sigma$)
f	friction factor
Re	Reynolds number ($= \rho u d / \mu$)
Sh	Sherwood number ($= kd / D$)
We	Weber number ($= \tau d / \gamma$)
Ψ	aspect ratio, m/m

Subscripts

b	bubble
col	column
dist	distributor
G	gas
GL	gas-liquid
L	liquid
LS	liquid-solid
M	monolith
s	superficial
S	slug
SM	Sauter mean
TP	two-phase

BIBLIOGRAPHY

- BATCHELOR, G. K. 1951 Pressure fluctuations in isotropic turbulence. *Proceedings of the Cambridge Philosophical Society* 47, 359.
- BERČIČ, G. & PINTAR, A. 1997 The role of gas bubbles and liquid slug lengths on mass transport in the Taylor flow through capillaries. *Chemical Engineering Science* 52 (21/22), 3709–3719.
- BERGER, R. J., PEREZ-RAMIREZ, J., KAPTEIJN, F. & MOULIJN, J. A. 2002 Catalyst performance testing: bed dilution revisited. *Chemical Engineering Science* 57 (22), 4921–4932.
- BERGER, R. J., STITT, E. H., MARTIN, G. B., KAPTEIJN, F. & MOULIJN, J. 2001 Eurokin - chemical reaction kinetics in practice. *Cattech* 5 (1), 30–60.
- CALDERBANK, P. H. & MOO-YOUNG, M. B. 1961 The continuous phase heat and mass transfer properties of dispersions. *Chemical Engineering Science* 16, 39–54.
- VAN DER EIJNDEN, M. G. 1999 *Hydrodynamics of Co-Current Two-Phase Flow in Capillaries*. Master Thesis, Section Industrial Catalysis, Delft University of Technology.
- GROLMAN, E., EDVINSSON, R., STANKIEWICZ, A. & MOULIJN, J. 1996 Hydrodynamic instabilities in gas-liquid monolithic reactors. In *Proceedings of the ASME Heat Transfer Division*, vol. 334-3, pp. 171–178.
- HEISZWOLF, J., ENGELVAART, L., VAN DER EIJNDEN, M., KREUTZER, M., KAPTEIJN, F. & MOULIJN, J. 2001a Hydrodynamic aspects of the monolith loop reactor. *Chemical Engineering Science* 56 (3), 805–812.
- HEISZWOLF, J. J., KREUTZER, M. T., VAN DER EIJNDEN, M. G., KAPTEIJN, F. & MOULIJN, J. A. 2001b Gas-liquid mass transfer of aqueous Taylor flow in monoliths. *Catalysis Today* 69 (1-4), 51–55.
- HIGBIE, R. 1935 The rate of absorption of a pure gas into a still liquid during short periods of exposure. *Transactions of the A.I.Ch.E.* 31, 365–389.
- HINZE, J. O. 1955 Fundamentals of the hydrodynamic mechanism of splitting in dispersion processes. *A.I.Ch.E. Journal* 1, 289–295.
- KRISHNA, R. & SIE, S. T. 1994 Strategies for multiphase reactor selection. *Chemical Engineering Science* 49 (24A), 4029–4065.
- LINEK, V., BENEŠ, P., SINKULE, J. & MOUCHA, T. 1990 Pressure and gas density effects on bubble break-up and gas hold-up in bubble columns. *Chemical Engineering Science* 45 (8), 2309–2315.
- MANTLE, M. D., SEDERMAN, A. J. & GLADDEN, L. F. 2002 Dynamic MRI visualization of two-phase flow in a ceramic monolith. *A.I.Ch.E. Journal* 48 (4), 909–912.
- VAN DE RIET, A. C. J. M., KAPTEIJN, F. & MOULIJN, J. A. 1998 Internal recycle monolith reactor for three-phase operation; hydrogenation of benzaldehyde: kinetics. In *Preprints of the second International symposium on catalysis in multiphase reactors (EFCE)*, pp. 153–159. Toulouse (France).
- VAN 'T RIET, K. & TRAMPER, H. 1991 *Basic Bioreactor Design*. Marcel Dekker.
- SATTERFIELD, C. N. & ÖZEL, F. 1977 Some characteristics of two-phase flow in mono-

- lithic catalyst structures. *Industrial and Engineering Chemistry Fundamentals* 16, 61–67.
- SCHLÜTER & DECKWER 1992 Gas/liquid mass transfer in stirred vessels. *Chemical Engineering Science* 47, 2357–2362.
- SHAH, R. K. & LONDON, A. L. 1978 *Laminar flow forced convection in ducts*, *Advances in Heat Transfer*, vol. Supplement 1. New York: Academic Press.
- WEISZ, P. B. & PRATER, D. C. 1954 Interpretation of measurements in experimental catalysis. In *Advances in Catalysis*, , vol. 6, pp. 143–176. New York: Academic Press.
- WHITE, F. M. 1998 *Fluid Mechanics*. New York, McGraw-Hill International Editions, 4th edition.
- WILKINSON, P. M. & VAN DIERENDONCK, L. L. 1990 Pressure and gas density effects on bubble break-up and gas hold-up in bubble columns. *Chemical Engineering Science* 45 (8), 2309–2315.
- VAN DER ZON, M., HAMERSMA, P. J., POELS, E. K. & BLIEK, A. 1999 Gas–solid adhesion and solid–solid agglomeration of carbon supported catalysts in three phase slurry reactors. *Catalysis Today* 48, 131–138.

CHAPTER VII

REACTOR DESIGN: HYDROGENATION OF 2,4-DINITROTOLUENE

§ VII.1 INTRODUCTION

In the previous chapters, monolith reactors have been shown to have good mass transfer characteristics, low pressure drop, and little backmixing. In this chapter, a design for a monolith reactor is presented for the hydrogenation of 2,4-dinitrotoluene (24DNT) to 2,4-toluenediamine (24TDA). This process was selected as a case study for several reasons: (1) there is industrial interest in using monoliths for this process (Machado *et al.*, 1999), (2) it is a fast reaction, which benefits from the good mass transfer characteristics, (3) plug flow behaviour reduces the required reactor volume and (4) the low pressure drop is advantageous, as will be explained later on.

The hydrogenation of 24DNT to 24TDA is highly exothermic ($\Delta H_R = -550$ kJ/mol per nitro group converted), and removal of heat is the primary concern in the design of the process. Typically, stirred tank slurry reactors with internal cooling are used on a commercial scale for the process, and the dinitrotoluene is introduced into this reactor at concentrations of 5–15 mol/m³ along with a solvent. The solvent – generally water, aliphatic alcohols or mixtures thereof – serves two purposes. Without dilution by solvent the high concentration of dinitrotoluene results in too high reaction rates. Further, the temperature rise of the reaction medium may be moderated by evaporation of the solvent. For a modelling study of 24DNT hydrogenation in a stirred reactor with an evaporating solvent, see *e.g.* Janssen *et al.* (1992).

The slurry reactor process has several disadvantages: (1) the solvent has to be removed from the product. This problem can be overcome by using the product 24TDA as the solvent. (2) The fine catalyst powder has to be filtered out of the product. Potential solutions are the use of a filter inside the reactor or the use of a fixed bed reactor. Chimero *et al.* (1965) disclosed a stirred tank reactor employing a filter inside the reactor, such that the catalyst always remained inside the reactor. In this way, the catalyst was always exposed to a high hydrogen pressure, which resulted in an extended catalyst lifetime. In other words, a low hydrogen concentration inside the catalyst leads to deactivation, which can be prevented by designing the catalyst in such a way that the hydro-

gen concentration inside the catalyst is high, and keeping the catalyst under a high hydrogen pressure. (3) The solvent is not completely inert and may lead to unwanted side reactions, although these side reactions can be suppressed by adding carbon monoxide to the gas feed (Bhutani, 1976). (4) Heat removal from the reaction medium and hydrogen supply to the catalyst are coupled in stirred tank reactors. In other words, a temperature excursion cannot be controlled by switching the stirrer off: although the supply of gas components to the catalyst stops, the heat removal also stops. A possible solution to this problem is operating the process in such a way that the heat of reaction can be removed outside of the reactor.

§ VII.2 MONOLITH LOOP REACTOR

Machado *et al.* (1999) have proposed a loop reactor with monolithic catalysts for the DNT hydrogenation. In the proposed reactor, the product 24TDA is used as the solvent, so no solvent separation is necessary. 24TDA has a melting point of 371 K, and if the product is to be used as a liquid solvent, operating temperature must be higher than 371 K. The upper limit for the operating temperature depends on the rate of unwanted side reactions. At temperatures above 430 K, dinitrotoluene starts to decompose, leading to a strong temperature rise which may lead to an explosion. Within the desired temperature limits 375-430 K, the vapour pressure of 24TDA is below 1 kPa, and product evaporation may be ignored. Although this simplifies the reactor modelling, the heat of reaction cannot be moderated by evaporation of toluene diamine. The integral heat balance now simplifies to

$$\phi_L \rho C_p \Delta T = \phi_L (2\Delta H_R \xi_{\text{NO}_2}) c_{\text{DNT},0} \quad (7.1)$$

In Eq. 7.1, ΔT is the temperature rise of the liquid stream (flowrate ϕ_L) in the reactor, ρ and C_p are the liquid density and heat capacity, respectively, ξ_{NO_2} is the fraction of nitro-groups converted, ΔH_R is the heat of reaction per nitro group and $c_{\text{DNT},0}$ is the DNT feed concentration. The left hand side is the amount of heat absorbed by the product stream per unit cross sectional area of the column, and the right hand side is the amount of heat produced by reaction. In the loop reactor concept, the product stream is cooled by an external heat exchanger. Part of the cooled product stream is returned to the reactor after addition of fresh reactant. The rest of the product stream leaves the process. The entire process is depicted schematically in Fig. 7.1

As stated above, in a slurry reactor, the heat transfer characteristics and the mass transfer characteristics are coupled via the intensity of stirring. The use of an external heat exchanger effectively decouples the heat removal from the gas-liquid contacting and leads to more operational flexibility.

The concept of a loop reactor with an external heat exchanger has been proposed before. Zarnack *et al.* (1996) proposed a *venturi loop reactor* with an external heat exchanger for a solvent free DNT hydrogenation process. Apart from avoiding a solvent

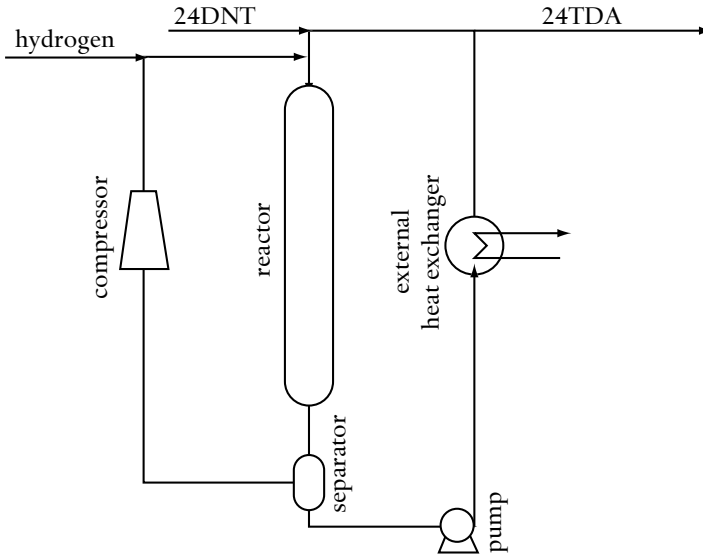


Figure 7.1: Flow sheet of a monolith loop reactor for the hydrogenation of 2,4-dinitrotoluene. Adapted from Machado *et al.* (1999).

separation step, the use of 24TDA as a solvent was motivated by the possibility to operate the process at the highest allowable temperature, so a significant amount of the heat produced can be recovered as high temperature steam. Venturi ejectors are devices that use the kinetic energy of a high velocity liquid jet to suck in and disperse gas. A high amount of energy can be dissipated with a venturi ejector, resulting in high mass transfer in the turbulent bubble dispersion in the draft tube below the venturi (see *e.g.* Cramers *et al.*, 1992; Cramers & Beenackers, 2001). In the process proposed by Zarnack *et al.*, a venturi ejector vigorously mixes the hydrogen and liquid stream, which are allowed to react further in a large vessel that is stirred by the jet leaving the venturi. In short, a venturi loop reactor is a backmixed reactor with good mass transfer characteristics. The catalyst in this reactor is a finely dispersed powder, and this powder still has to be separated from the product stream. For a maximum temperature rise of 10 K at full conversion in the reactor, the ratio of dinitrotoluene mass flow rate to recycle mass flow rate was 1:180. Using Eq. 7.1, the product ρC_p of 24TDA can then be estimated as $3.2 \times 10^3 \text{ kJ/m}^3/\text{K}$.

The advantage of the venturi loop reactor is that no compressor is needed to recycle the gas stream. Of course the gas-liquid contacting is coupled to the liquid flow rate, but a valve in the gas recycle line between the reactor vessel and the venturi allows to shut down the gas-liquid contacting while maintaining liquid flow through the external heat exchanger. A disadvantage of the venturi loop reactor is the high energy requirement.

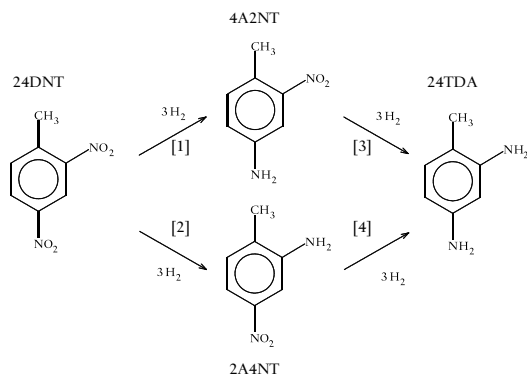


Figure 7.2: Reaction pathway for the hydrogenation of 2,4-dinitrotoluene (24DNT) to the intermediates 2-amino-4-nitrotoluene (2A4NT) and 4-amino-2-nitrotoluene (4A2NT) and subsequently to the product 2,4-toluenediamine. The numbers between brackets are the labels by which the reactions are referred to in the text.

Although in the draft tube of the ejector the mass transfer is high, the energetic cost of forcing the liquid through the nozzle is high. Note that to keep the temperature rise within the 10 K limit, on average each kilogram of produced toluene diamine is forced through this nozzle 180 times before it leaves the loop.

In comparison to the venturi loop reactor, the monolith loop reactor proposed by Machado *et al.* (1999) exploits the plug flow characteristics and low pressure drop of monoliths, while retaining the good mass transfer characteristics. Note that it is possible to operate monoliths at zero pressure drop (see Fig. 6.8 in chapter VI of this thesis), but at zero pressure drop the operating conditions depend on the type of distributor used and the gas flow rate is coupled to the liquid flow rate. With a small compressor and a control valve, the gas flow rate can be set independently of the liquid flow rate. Because of the liquid recycle flow rate, the low pressure drop over the column is a crucial advantage.

§ VII.3 KINETICS

The kinetics of 24DNT hydrogenation has been reported in the open literature (Janssen *et al.*, 1990*a,b*; Molga & Westerterp, 1992; Neri *et al.*, 1995; Malyala *et al.*, 1997, 1998; Malyala & Chaudhari, 1999). The reaction is known to proceed via two intermediates 2-amino-4-nitrotoluene (2A4NT) and 4-amino-2-nitrotoluene (4A2NT) to the final product 24TDA. All agree that the hydrogenation of the nitro group opposite of the methyl group is faster than the hydrogenation of the sterically hindered nitro group next to the methyl group. Janssen *et al.* (1990*a,b*) also observed the intermediate 4-hydroxylamino-2-nitrotoluene in a kinetic study using a pal-

ladium on carbon catalyst, so probably the hydrogenation of each nitro group proceeds through surface reactions to a hydroxylamino group, followed by a surface reaction of the hydroxylamino group with hydrogen to the amine.

The most important difference – apart from the kinetic constants – between the different kinetic models is the description of the absorption of hydrogen. Dissociative hydrogen absorption was reported by Janssen *et al.* (1990b) for Pd/C catalysts and by Malyala & Chaudhari (1999) for Ni/Al₂O₃ catalysts. For Pd/Al₂O₃ catalysts, Malyala *et al.* (1998) reported molecular absorption of hydrogen. All kinetic studies were performed at temperatures, lower than the boiling point of 24TDA in solvents such as ethyl acetate and methanol. As a result, for this work we have to extrapolate the kinetics to higher temperatures using the heat of adsorption of the components and the activation energy for the individual reactions.

In this study, the kinetic constants of Malyala & Chaudhari (1999) at 333 K for a Nickel catalyst were used. All the kinetic parameters are listed in table 7.1. The volumetric rate of the individual reactions follows Langmuir-Hinshelwood kinetics, where the rate limiting step is a reaction of adsorbed dissociated hydrogen with a nitroaromatic compound. Following the kinetics of Malyala & Chaudhari (1999), the adsorption of the sterically hindered nitro group in 2A4NT and the adsorption of the reaction product 24TDA may be ignored in the site balance. Numbering the reactions as shown in Fig. 7.2, the rate expressions are given by

$$r_{V,1} = \frac{k_1 \sqrt{c_H c_A}}{(1 + \sqrt{K_{HC} c_H} + K_{ACA} + K_{BCB})^2} \quad (7.2)$$

$$r_{V,2} = \frac{k_2 \sqrt{c_H c_A}}{(1 + \sqrt{K_{HC} c_H} + K_{ACA} + K_{BCB})^2} \quad (7.3)$$

$$r_{V,3} = \frac{k_3 \sqrt{c_H c_B}}{(1 + \sqrt{K_{HC} c_H} + K_{ACA} + K_{BCB})^2} \quad (7.4)$$

$$r_{V,4} = \frac{k_4 \sqrt{c_H c_C}}{(1 + \sqrt{K_{HC} c_H} + K_{ACA} + K_{BCB})^2} \quad (7.5)$$

$$(7.6)$$

The subscripts H, A, and B represent hydrogen, 24DNT and 4A2NT, respectively. The subscript V indicates that the rate is given per unit catalyst volume. The reaction rates of the individual components may be obtained using the following stoichiometry matrix

$$v = \begin{pmatrix} -3 & -3 & -3 & -3 \\ -1 & -1 & 0 & 0 \\ 1 & 0 & -1 & 0 \\ 0 & 1 & 0 & -1 \\ 0 & 0 & 1 & 1 \\ 2 & 2 & 2 & 2 \end{pmatrix} \quad (7.7)$$

The temperature dependency of the rate constants k_i and the adsorption coefficients K_j are given by the Arrhenius equations

$$k_i(T) = k_i(T_{\text{ref}}) \exp \left[\frac{-E_A}{R} \left(\frac{1}{T} - \frac{1}{T_{\text{ref}}} \right) \right] \quad (7.8)$$

$$K_j(T) = K_j(T_{\text{ref}}) \exp \left[\frac{-\Delta H_j}{R} \left(\frac{1}{T} - \frac{1}{T_{\text{ref}}} \right) \right] \quad (7.9)$$

§ VII.4 REACTOR MODEL

A general model for cocurrent monolith reactor was formulated. The partial differential equations describing the reactor are listed in table 7.3. The assumptions of the model are summarised in table 7.2.

For the liquid phase component balance, the terms on the right hand side are the convective term, the dispersion term and the mass transfer to the catalyst. Maldistribution is taken into account by a dispersion term alone. The two-zone exchange described in chapter IV leads to a contribution to the residence time distribution that is not accurately described by axial dispersion in the slugs. On the other hand, the results of chapter IV also showed that the residence time distribution of monoliths is close to that of plug flow. Further, since the process runs to full conversion and the intermediate compounds 2A4NT and 4A2NT are not the desired products, deviations from plug flow mainly affect the level of conversion to TDA at a given column length and do not negatively affect the maximum attainable selectivity. Since this balance includes a

Table 7.1: Kinetic parameters

i	$k_i(333 \text{ K})$ $\text{m}^3/\text{mol/s}$	$E_{A,i}$ kJ/mol	j	$K_j(333 \text{ K})$ m^3/mol	ΔH_j kJ/mol
1	5.20×10^{-2}	30.7	H	9.36×10^{-4}	-34.07
2	6.88×10^{-3}	33.2	A	1.11×10^{-2}	-14.14
3	8.54×10^{-3}	31.0	B	9.80×10^{-4}	-12.19
4	4.68×10^{-3}	33.8			

second order term, two boundary conditions are needed: the liquid feed concentration, and a no-dispersion boundary condition at the outlet of the reactor. The liquid phase component balance was not solved for hydrogen.

The balance for the gas phase, on the other hand, is only set up for hydrogen. The pressure drop is low with respect to the operating pressure, and the gas-phase concentration p/RT is assumed to be constant in the reactor. The right hand side includes a convective term, a term for mass transfer from a gas bubble directly to the catalyst and a term for mass transfer through the liquid slugs. The left hand side is derived by

$$\frac{\partial \epsilon_G c_{H,g}}{\partial t} = \frac{p}{RT} \frac{u_{Ls}}{(u_{Ls} + u_{Gs})^2} \frac{\partial u_{Gs}}{\partial t} - \epsilon_G \frac{p}{RT^2} \frac{\partial T}{\partial t} \tag{7.10}$$

in which we have used the ideal gas law $c_{H,g} = p/RT$ and $\epsilon_G = u_{Gs}/u_{TP}$. Dispersion is not considered for the gas phase because the concentration is constant. As a result, only one boundary condition is needed: the hydrogen feed velocity. For the right hand side, the following derivation applies:

$$\frac{\partial u_{Gs} c_{H,g}}{\partial z} = -\frac{p}{RT} \frac{\partial u_{Gs}}{\partial z} + \frac{u_{Gs} p}{RT^2} \frac{\partial T}{\partial z} \tag{7.11}$$

The right hand side of the enthalpy balance consists of a convective term, and a reactive term. For the reactive term, we have used the fact that the mass transfer of water from the catalyst equals the reaction rate inside the catalyst, and the fact that per mol nitro group converted two mol of water is formed. The heat of reaction in the enthalpy balance is defined per mol of nitro group converted ($-\Delta H_R = 550 \text{ kJ/mol}$).

Finally, inside the catalyst the mass balance has a diffusive term and a reactive term. For the effective diffusion coefficient inside the catalyst we have assumed $D_{\text{eff}} = 0.1D$. The no-flux boundary condition inside the catalyst may be interpreted as a symmetry boundary condition by realizing that on the opposite side of the wall the same washcoat of catalyst is present. The boundary condition at the washcoat-liquid interface couples

Table 7.2: Model assumptions

Pressure drop over the reactor negligible with respect to reactor pressure
No catalyst deactivation
No internal temperature gradients
No evaporation of liquid phase components
No homogeneous reactions
No side reactions
Maldistribution may be taken into account by axial dispersion in the liquid phase
Gas and liquid temperature in equilibrium

Table 7.3: Differential equations and boundary conditions for the mass and enthalpy balances in the reactor

Liquid phase mass balances for non-volatile components
 ($i=24\text{DNT}, 4\text{A}2\text{NT}, 2\text{A}4\text{NT}, 24\text{TDA}, \text{H}_2\text{O}$)

$$\epsilon_L \frac{\partial c_{L,i}}{\partial t} = -u_{Ls} \frac{\partial c_{L,i}}{\partial z} + D_{ax} \frac{\partial^2 c_{L,i}}{\partial z^2} - k_{LS} a_i (c_{L,i} - c_{S,i})$$

$$\left. \frac{\partial c_{L,i}}{\partial z} \right|_{z=0} = \frac{u_{Ls}}{D_{ax}} (c_{L,i} - c_{L,i,\text{in}}) \quad \left. \frac{\partial c_{L,i}}{\partial z} \right|_{z=L} = 0$$

Gas phase hydrogen mass balance

$$\frac{p}{RT} \frac{u_{Ls}}{u_{TP}^2} \frac{\partial u_{Gs}}{\partial t} - \frac{\epsilon_G p}{RT^2} \frac{\partial T}{\partial t} = -\frac{p}{RT} \frac{\partial u_{Gs}}{\partial z} + \frac{u_{Gs} p}{RT^2} \frac{\partial T}{\partial z} + k_{GLS} a (c^* - c_S) + k_{GSA} (c^* - c_S)$$

$$u_{Gs} \Big|_{z=0} = u_{G,s,\text{in}}$$

Enthalpy balance

$$\epsilon_L \rho C_p \frac{\partial T}{\partial t} = -u_{Ls} \rho C_p \frac{\partial T}{\partial z} - \frac{1}{2} \Delta H_R [k_{LS} a (c_L - c_S)]_{\text{H}_2\text{O}}$$

$$T \Big|_{z=0} = T_{\text{in}}$$

Washcoat mass balance for component i

$$\frac{\partial c_i}{\partial r} = D_{\text{eff}} \frac{\partial^2 c_i}{\partial r^2} + \sum v_{i,j} r v_{j,j}$$

$$D_{\text{eff}} \frac{\partial c_i}{\partial r} \Big|_{r=d_{wc}} = k_{LS} (c_{L,i} - c_{S,i}) \quad \frac{\partial c_i}{\partial r} \Big|_{r=0} = 0 \quad (\text{non-volatile})$$

$$D_{\text{eff}} \frac{\partial c_i}{\partial r} \Big|_{r=d_{wc}} = k_{LS} (c^* - c_S) + k_{GLS} (c^* - c_S) \quad \frac{\partial c_i}{\partial r} \Big|_{r=0} = 0 \quad (\text{H}_2)$$

Table 7.4: Mass Transfer model

$$u_{TP} = u_{Ls} + u_{Gs} \quad \epsilon_L = \frac{u_{Ls}}{u_{TP}} \quad \epsilon_G = \frac{u_{Gs}}{u_{TP}}$$

$$Ca = \frac{\mu u_{TP}}{\gamma}$$

$$\delta = d_{ch} \frac{0.66Ca^{2/3}}{1 + 3.33Ca^{2/3}} \quad (\text{round channels})$$

$$\delta = 3d_{ch} \left(\frac{1}{2} - [0.64 + 0.36 \exp(-3.08Ca^{0.54})] \right) \quad (\text{rounded channels})$$

$$Sh = 90 + 104 \left(\frac{L_{slug}}{d_{ch}} \right)^{-4/3}$$

$$k_{LS} = \epsilon_L \left(\frac{\delta}{D} + \frac{d_{ch}}{ShD} \right)^{-1} \quad k_{LSa} = k_{LS} \frac{4}{d_{ch}}$$

$$k_{GS} = \epsilon_G \frac{D}{\delta} \quad k_{LSa} = k_{GS} \frac{4}{d_{ch}}$$

$$k_{GLS} = \epsilon_L \frac{D}{\delta} \quad k_{GLSa} = k_{GLS} \frac{4}{d_{ch}}$$

$$c_{H,slug} = c_{H,sat} \left(1 + \frac{L_{slug}}{\delta} \sqrt{\frac{D\pi}{8u_{TP}d_{ch}}} \right)^{-1}$$

the liquid and gas axial balances to the internal balances, and reflects that the reaction rate in the catalyst equals the flux to the catalyst.

The mass transfer parameters are given in table 7.4. For the transfer for non-volatile components to the catalyst, the correlation for developed flow from chapter III was used, in series with the resistance in the film. Note that this resistance-in-series model is a lower estimate for this mass transfer step. For the transfer of hydrogen to the catalyst, the hydrogen concentration in the slugs was calculated with the correlation developed in chapter V. This correlation is valid for a fully mass transfer limited reaction. For all simulations, the slug concentration was equal to the saturation concentrations, so even if external hydrogen mass transfer is not fully limiting, the slugs can be assumed to be fully saturated with hydrogen. Two types of channel shapes were considered: round channels and channels with a shape comparable to the catalyst used for chapter V. For round channels, the low inertia correlation of Aussilous & Qu ere (2000) was used to estimate the film thickness, and for rounded channels three times the film thickness predicted by the correlation of Irandoust & Andersson (1989) was used, based on the results obtained in chapter V.

The heat capacity of 24TDA and the solubility of hydrogen in 24TDA are given in Zarnack *et al.* (1996). The viscosity, surface tension and density of 24TDA were taken from Yaws (1999). Because the temperature rise in the column may be significant, the viscosity of 24TDA cannot be assumed to be constant in the column. The viscosity was calculated at each axial position inside the column as a function of temperature. The diffusion coefficients were estimates using the Wilke-Chang correlation (Reid *et al.*, 1987). Since the diffusion coefficients predicted by this correlation are a strong function of viscosity, the diffusion coefficients were also calculated at each axial position. An overview of the physical properties is given in table 7.5.

Table 7.5: Physical properties

Component	Property	Value
Hydrogen	Henry coefficient	0.44 mol/m ³ /bar
	diffusion coefficient (383 K)	2.3 × 10 ⁻⁸ m ² /s
	Diffusion coefficient (433 K)	5.9 × 10 ⁻⁸ m ² /s
Water	diffusion coefficient (383 K)	7.5 × 10 ⁻⁹ m ² /s
	diffusion coefficient (433 K)	1.9 × 10 ⁻⁸ m ² /s
24TDA	density	1020 kg/m ³
	viscosity (383 K)	7.4 × 10 ⁻⁴ Pa s
	viscosity (433 K)	3.2 × 10 ⁻⁴ Pa s
	surface tension	4.2 × 10 ⁻² N/m
24DNT,2A4NT, 4A2NT,TDA	heat capacity	3.1 kJ/kg/K
	diffusion coefficient (383 K)	1.9 × 10 ⁻⁹ m ² /s
	diffusion coefficient (433 K)	4.9 × 10 ⁻⁹ m ² /s

The partial differential equations in table 7.3 were discretised using the finite difference DSS/2 routines (Schiesser, 1991) on a 2D grid of typically 50 points in the axial direction and 15 points in the radial (washcoat) direction. The initial conditions for the simulation was that all variables were equal to the feed conditions.

$$u_{Gs} = u_{G,in} \quad T = T_{in} \quad c_L = c_S = c_{L,in} \quad (7.12)$$

The resulting ODE's were integrated using the LSODES integrator (Hindmarsh, 1983), and the change in the solution was monitored by calculating

$$\Delta sol = \sum_{i=1}^N \frac{(y_i - y_{i-1})^2}{dt} \quad (7.13)$$

in which y_i is the solution of an ODE at time-step i and dt is the time-step. Δsol may be regarded as the sum of squared residuals of the steady state solution, and the simulation was stopped when Δsol was below 10^{-8} .

§ VII.5 RESULTS

As a base case, we have performed the simulations for a column with a volume of 1 m^3 and a height of 5 m. The monoliths channels are assumed to be coated in such a way that channel cross section is round with a diameter of 1.1 mm (400 cpsi), and such that the washcoat thickness is $25 \mu\text{m}$. As we have used the kinetics of Malyala & Chaudhari (1999), the active material is 10 % Ni on zeolite Y. The optimal feed concentration was calculated from the allowable temperature rise. Setting the desired outlet temperature to 433 K and the desired inlet temperature at 383 K (12 K above the melting point of 24TDA), a balance of the heat produced by the hydrogenation and the heat absorbed by the liquid gives

$$c_{DNT,0} = \frac{1000 \text{ kJ/m}^3 \times 3.1 \text{ kJ/kg/K} \times 50 \text{ K}}{2 \times 550 \text{ kJ/mol}} = 140 \text{ mol/m}^3 \quad (7.14)$$

In chapter VI, the hydrodynamic stability criteria for monoliths were discussed. For this process, the friction factor was calculated from

$$f = \frac{16}{Re} \left[1 + 0.17 \frac{1}{\Psi_S} \left(\frac{Re}{Ca} \right)^{0.33} \right] \quad (7.15)$$

at each axial position in the column. Because of the reaction the gas velocity decreases and the temperature dependent fluid properties change, the pressure drop should not be estimated from the inlet conditions. The pressure gradient was integrated over the reactor length to obtain the pressure drop over the column. In Fig. 7.3, the contour

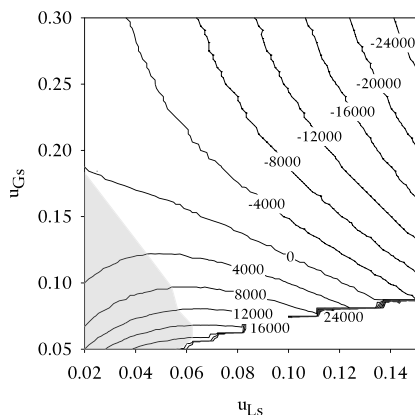


Figure 7.3: Pressure drop contour map for the hydrogenation of 24DNT. Round channels with $d_{\text{ch}} = 1.1$ mm. The numbers for each line give the pressure drop in Pa, where positive numbers indicate that the pressure on top of the column is higher than at the bottom. $L_{\text{col}} = 5\text{m}$, $p_{\text{in}} = 32$ bar, $T_{\text{in}} = 383$ K, 24DNT feed concentration is 140 mol/m^3 .

lines of pressure drop versus $u_{L,S}$ and $u_{G,S}$ are plotted. Using as stability criterion that the pressure drop must increase with an increase of $u_{L,S}$ or $u_{G,S}$, the system is stable above $(u_{L,S} \approx 0.04, u_{G,S} \approx 0.12)$, $(u_{L,S} \approx 0.06, u_{G,S} \approx 0.07)$, and for all liquid velocities if the gas velocity is higher than 0.17.

If the liquid superficial velocity is 0.04 m/s and we set the gas inlet superficial velocity to 0.1 m/s, then the minimum hydrogen pressure needed to completely hydrogenate all DNT is 11 bar. Inside the column, the bubbles shrink due to the hydrogen consumption, and operating the reactor at somewhat higher pressures ensures that the bubbles retain their elongated shape, ensuring Taylor flow over the entire column. Finally, maldistributions were taken into account using a Bodenstein number $Bo = u_{\text{TP}}L/D_{\text{ax}}$ of 500. In chapter IV, the Bodenstein number was close to 30 per meter column length using a non-optimised nozzle. For the static mixer, the Bodenstein number was higher, and increasing the number of blocks per meter length increases the Bodenstein number. For this study we have assumed a Bodenstein number of 100 per meter column and a column length of 5 m, and we have tested the impact of lowering the Bodenstein number to 20 per meter column length.

In Fig. 7.4 the profiles of the liquid phase in the axial direction are shown. The conversion of 24DNT is 100.0% at the exit of the reactor, and the yield of 24TDA 96.4%. Inside the reactor, the intermediates 4A2NT and 2A4NT have a maximum concentration at $z = 1.5$ m. The sterically hindered nitro group next to the methyl group in 24DNT reacts significantly slower. The temperature rise in the reactor is 48 K, which is just low enough to prevent unwanted side reactions.

Table 7.6: DNT conversion, TDA yield and outlet temperature for several simulations.

run	u_{Ls}	u_{Gs}	$c_{DNT,in}$	T_{in}	p	L_{col}	d_{wc}	d_{ch}	shape*	Pe	Conversion	Yield	T_{out}
–	m/s	m/s	mol/m ³	K	bar	m	μ m	mm	–	–	DNT	TDA	K
1	0.04	0.10	140	383	16	5	25	1.1	circ.	500	100.0	96.42	431.7
2	0.04	0.10	70	383	16	5	25	1.1	circ.	500	99.90	87.95	406.2
3	0.04	0.10	70	403	16	5	25	1.1	circ.	500	100.0	97.50	427.5
4	0.04	0.10	140	383	16	5	25	1.1	circ.	100	99.98	94.34	431.2
5	0.04	0.10	140	383	16	5.5	25	1.1	circ.	100	99.99	96.16	431.7
6	0.04	0.10	140	383	32	5	25	1.1	circ.	500	100.0	98.81	432.3
7	0.04	0.05	140	383	32	5	25	1.1	circ.	500	100.0	99.32	432.5
8	0.04	0.10	140	383	16	5	25	0.9	circ.	500	100.0	98.82	432.3
9	0.04	0.10	140	383	16	5	25	1.1	rect.	500	99.80	92.90	430.6
10	0.04	0.10	140	383	32	5	25	1.1	rect.	500	99.86	96.02	431.5
11	0.08	0.20	140	383	16	10	25	1.1	circ.	500	100.0	96.11	431.5
12	0.04	0.10	140	383	16	5	15	1.1	circ.	500	99.98	85.91	428.8

* : rect. = rounded channels; circ. = round channels

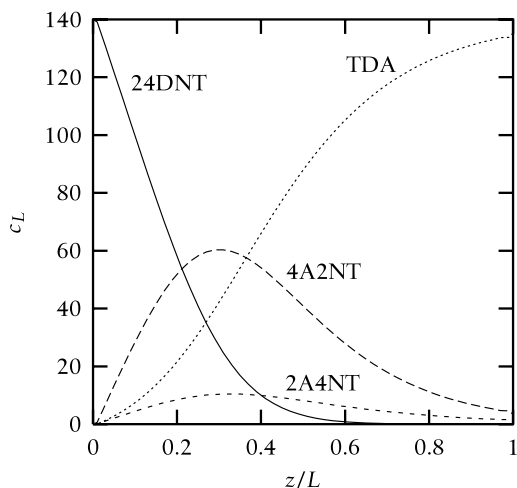


Figure 7.4: Concentration profile of the aromatic components in a 5 m long 400 cpsi monolith reactor with a washcoat of $25 \mu\text{m}$. $u_{Ls} = 4 \text{ cm/s}$ $u_{Gs} = 10 \text{ cm/s}$, $T_{in} = 383 \text{ K}$, 24DNT feed concentration is 140 mol/m^3 .

In Fig. 7.5, the catalyst concentration inside the catalyst, the film and the liquid bulk is plotted. Although three molecules of hydrogen are consumed in the conversion of 24DNT, the impact of reaction on the concentration profiles of 24DNT inside the catalyst and the film is more severe, because the diffusion coefficient of 24DNT is significantly lower than the diffusion coefficient of hydrogen. A high hydrogen concentration inside the catalyst prevents deactivation, so the fact that the reaction is mass transfer limited in aromatic compounds rather than hydrogen is beneficial for the stability of the catalyst. With increasing conversion, the temperature rises and the viscosity of the liquid drops. As a result, the thickness of the film between the bubbles and the slugs is reduced, and the temperature rise decreases the external mass transfer limitations close to full conversion.

In table 7.6, the temperature rise, 24DNT conversion and 24TDA yield are given for several simulations. Run 2 demonstrates the effect of operating the reactor at a lower feed concentration. Although lowering the concentrations of aromatic compounds reduces the driving force for mass transfer to the catalyst, the main reason for the lower yield to 24TDA is that the temperature rise is lower and the high reaction rates associated with high temperatures are not obtained. Run 3 shows the effect of increasing the higher feed temperature at low feed concentrations. Now the feed temperature is high enough to “kick off” the reaction, and the TDA yield is comparable to the process at higher concentration.

Run 4 shows the effect of more severe maldistribution: reducing the Bodenstein number by a factor 5 lowers the yield and even the conversion of 24DNT. For this

REACTOR DESIGN

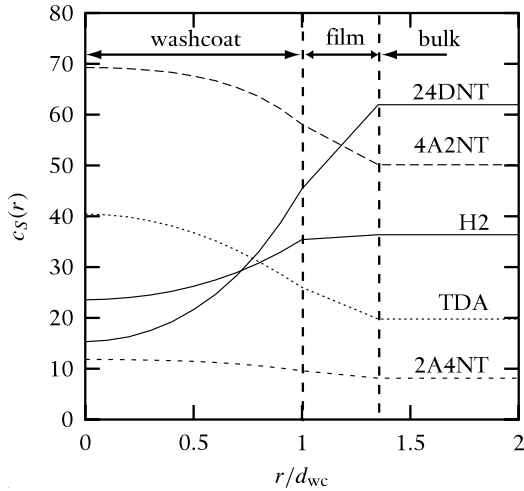


Figure 7.5: Concentration profiles in the catalyst and liquid bulk at $z/L=0.1$ for the same conditions as in Fig. 7.4.

higher extent of maldistribution, a 10 % increase in column length is required to obtain roughly the same yield and conversion, as is shown in run 5. Since the hydrogenation must run to completion, the impact of maldistribution can be overcome by using a longer reactor.

Run 6 shows the effect of increasing the reaction pressure. At higher pressure, the rate of reaction increases, but the residence time of the liquid inside the column is decreased. A lower fraction of the gas is consumed, and as a result, the linear velocity of the bubbles and slugs is not reduced significantly inside the column. As a result, only a slightly higher yield for TDA is found. In run 7, the pressure is increased and the gas superficial velocity is decreased, so the molar feed of hydrogen is equal to the base case run 1. As a result, the yield is substantially higher.

Run 8 and run 9 demonstrate the effect of catalyst geometry: increasing the cell density to 600 cpsi (run 8) improves the yield of 24TDA and using a coating that is not perfectly round (run 9) reduces yield significantly. The effect of using channels that are not perfectly round leads to more severe mass transfer limitations, and can be overcome by increasing the pressure (run 10). The reaction is not severely limited by external mass transfer. Increasing the superficial velocities results in a higher film thickness. In Run 11 increasing the superficial velocities while keeping the residence time constant only results in a very minor decrease in yield.

Finally, run 12 demonstrates the effect of using a thinner washcoat. Since the mass transfer limitations were not severe for a washcoat of $25 \mu\text{m}$ (see Fig. 7.5), reducing the washcoat thickness reduces the yield significantly.

§ VII.6 DISCUSSION

A direct comparison of the simulations presented in this work to the data in the patent of Machado *et al.* (1999) is impossible: the catalyst used by Machado *et al.* (1999) is a 1%Pd/10%Ni/ γ -Al₂O₃ catalyst which is different from the catalyst used to measure the kinetic equations used in this work. However, several of the trends are the same. Machado *et al.* found that increasing the gas–liquid mass transfer had a negligible effect on the conversion and yield, which is consistent with the observation that the slugs are practically saturated with hydrogen. Machado *et al.* also found that the yield increases with pressure, although that result would be obtained using any of the kinetics in the open literature. The temperature of the liquid leaving the monolith is essentially the same as reported by Machado *et al.* for similar feed concentrations, which indicates that the proper value for the heat capacity has been used. Machado *et al.* did not find a decrease in yield for lower feed concentrations, which suggests that their catalyst has a higher activation energy, so the reactor “kicks off” at lower temperatures. Malyala *et al.* (1997) reported activation energies for a palladium–based catalyst that were higher than the activation energies for the nickel–based catalyst used in this work. Also, in this work internal and external temperature gradients were not considered. The heat of reaction may lead to such a gradient, which would also result in a lower “kick-off” temperature.

The simulation for the base case results in a toluene diamine production of 0.13 kg/s or 4 kiloton per year, using a relatively small reactor with a volume of 1 m³. For highly exothermic reactions it is always favourable to minimise the volume in which the reaction takes place. The plug flow characteristics of monoliths lead to the smallest required reactor volume, since the kinetics exhibit a positive reaction order.

The stability criteria that were found in this study are valid for 400 cpsi. If higher cell densities are used, monoliths can be operated at even lower velocities, which would allow a further decrease in reactor size. Note that the mass transfer characteristics improve for higher cell densities and for lower velocities.

No explicit comparison has been made with stirred tank reactors or other fixed bed reactors in this study. However, several remarks can be made in comparison. Stirred tank reactors are backmixed, so a higher reactor volume is required. An interesting observation can be made with respect to operational safety. If in the monolith loop reactor the liquid feed is stopped, and the gas feed is switched from hydrogen to nitrogen, the reaction stops in a time that is equal to the residence time in the reactor. For the base case considered in this study, the residence time is 33 s. If a high velocity nitrogen “blow out” is used, this time can be reduced even further. In other words, monoliths can be emptied quickly in the event of a temperature excursion. In a large stirred tank, the hydrogen gas phase is also backmixed and does not leave the reactor as fast, so such an abrupt stop is not possible.

With respect to trickle bed reactors, that are prone to stagnant zones that lead to hot spots, a similar remark can be made. Further, the attainable mass transfer rates in

trickle beds are much lower. Although the stability problems associated with hydrogen depletion inside the catalyst can be overcome by using egg-shell catalysts, due to mass transfer limitations the required reactor volume for a trickle bed remains very high, especially since a significant pressure drop over the bed must be avoided due to the high recycle ratio of the liquid phase.

The optimal operating conditions are largely determined by the hydrodynamic stability. Reducing the superficial gas and liquid velocities increases the residence time and improves the mass transfer, so the column should be operated at the lowest possible superficial velocities, which can be found from a hydrodynamic stability analysis. Note that this hydrodynamic analysis must be repeated for each different DNT feed concentration and hydrogen pressure, because the change in fluid properties depends on the amount of nitrogroups converted and the decrease in gas velocities depends on the amount of nitro groups converted and the feed pressure.

§ VII.7 CONCLUSIONS

In this chapter, a design for the industrially relevant hydrogenation of 2,4-dinitrotoluene using a monolith loop reactor has been presented. The monolith loop reactor eliminates the disadvantages of other configurations, such as separation of solvent and/or catalyst, deactivation due to catalyst separation outside the reactor and side reactions with solvents. The main advantages of using a monolith for this process are

- Low pressure drop. Since the hydrogenation is carried out at low concentrations, dissolved in the product, large volumes of the product need to be recycled through an external heat exchanger to temper the temperature rise of this very exothermic reaction.
- High mass transfer. The reaction rate is relatively high, the high external mass transfer in monoliths, combined with the limited mass transfer limitations for a thin catalyst washcoat ensures a high hydrogen concentration inside the catalyst, reducing deactivation. Further, since the reaction is carried out at low concentrations of the liquid phase reactants, the good liquid–solid mass transfer characteristics of Taylor flow allow high reaction rates, based on reactor volume.
- Plug flow. Although the reaction runs to completion, the reaction can be carried out in a small reactor because of the limited extent of backmixing in monolith reactors. Although the recycle as a whole is a backmixed system, the reactor section has plug flow characteristics.

The design is based on the results for pressure drop, residence time distribution presented in chapters II–V of this thesis. The design study shows that a reactor of 1 m³ with a dinitrotoluene feed of 1.1 mol/s can run the process to almost complete conversion at an operating pressure of 16 bar. The best results were obtained when operating the monolith at the lowest stable flowrates.

NOTATION

a	interfacial area, m^{-1}
c	concentration, mol/m^3
C_p	specific heat, $\text{kJ}/\text{kg}/\text{K}$
D	diffusion coefficient, m^2/s
D_{ax}	dispersion coefficient, m^2/s
D_{eff}	effective diffusion coefficient inside catalyst, m^2/s
d_{ch}	channel diameter, m
d_{wc}	washcoat thickness, m
E_A	activation energy, kJ/mol
ΔH_R	heat of reaction, kJ/mol
ΔH_j	heat of absorption of component j , kJ/mol
k	mass transfer coefficient, m/s
k	reaction rate constant, $m^{3/2}/\text{mol}^{1/2}/s$
K	absorption constant, m^3/mol
L	length, m
p	pressure, Pa
Δ_{sol}	summed change in solution, various
r	washcoat layer coordinate, m
r_V	reaction rate per unit washcoat volume, $\text{mol}/m^3/s$
R	gas constant, $\text{J}/\text{mol}/\text{K}$, –
t	time, s
T	temperature, K
u	velocity, m/s
u_{TP}	two-phase superficial velocity, m/s
u_{Gs}	superficial gas velocity, m/s
u_{Ls}	superficial liquid velocity, m/s
V	volume, m^3
y	solution of ODE, various
z	axial coordinate, m

Greek letters

γ	surface tension, N/m
δ	film thickness, m
ϵ_L	liquid holdup, m^3/m^3
ϵ_G	gas holdup, m^3/m^3
μ	viscosity, Pa s
ξ	conversion, –
τ	mean residence time from E -curve, s
ϕ	flow rate, m^3/s
ρ	density, kg/m^3

Ψ_S slug aspect ratio ($L_{\text{slug}}/d_{\text{ch}}$), –

Dimensionless numbers

Bo Bodenstein number ($= uL/D_{\text{ax}}$)

Ca capillary number ($= \mu_L u/\gamma$)

Sh Sherwood number ($= kd/D$)

Subscripts

b bubble

col column

G gas

GL gas–liquid

L liquid

LS liquid–solid

s superficial

S slug

SM Sauter mean

TP two–phase

BIBLIOGRAPHY

- AUSILOUS, P. & QUÉRE, D. 2000 Quick deposition of a fluid on the wall of a tube. *Physics of Fluids* 12 (10), 2367–2371.
- BHUTANI, S. K. 1976 Hydrogenation of dinitrotoluene to toluene diamine. *US patent* US 3935264.
- CHIMEROL, J. J., CLARKE, W. M., DENTON, W. I. & HAMMOND, P. D. 1965 Kontiuierliches Verfahren und Vorrichtung zur Hydrierung von aromatischen Polynitroverbindungen. *German patent* DE 1518080.
- CRAMERS, P. H. M. R. & BEENACKERS, A. A. C. M. 2001 Influence of the ejector configuration, scale and the gas density on the mass transfer characteristics of gas–liquid ejectors. *Chemical Engineering Journal* 82, 131–141.
- CRAMERS, P. H. M. R., BEENACKERS, A. A. C. M. & VAN DIERENDONCK, L. L. 1992 Hydrodynamics and mass transfer characteristics of a loop-venturi reactor with a downflow liquid jet ejector. *Chemical Engineering Science* 47 (13/14), 3557–3564.
- HINDMARSH, A. C. 1983 ODEPACK, a systematized collection of ODE solvers. In *Scientific Computing, Applications of Mathematics and Computing to the Physical Sciences* (ed. R. S. Stepleman), *IMACS Transactions on Scientific Computation*, vol. 1, pp. 55–64. Amsterdam: Elsevier Science Ltd.
- IRANDOUST, S. & ANDERSSON, B. 1989 Liquid film in taylor flow through a capillary. *Industrial and Engineering Chemistry Research* 28, 1684.

- JANSSEN, H. J., KRUIHOF, A. J., STEGHUIS, G. J. & WESTERTERP, K. R. 1990a Kinetics of the catalytic hydrogenation of 2,4-dinitrotoluene. 1. experiments, reaction scheme and catalyst activity. *Industrial and Engineering Chemistry Research* 29, 754–766.
- JANSSEN, H. J., KRUIHOF, A. J., STEGHUIS, G. J. & WESTERTERP, K. R. 1990b Kinetics of the catalytic hydrogenation of 2,4-dinitrotoluene. 2. modelling of the reaction rates and catalyst activity. *Industrial and Engineering Chemistry Research* 29, 1822–1829.
- JANSSEN, H. J., VOS, H. J. & WESTERTERP, K. R. 1992 A mathematical model for multiple hydrogenation reactions in a continuously stirred three-phase slurry reactor with an evaporating solvent. *Chemical Engineering Science* 47, 4191–4208.
- MACHADO, R. M., PARRILLO, D. J., BOEHME, R. P. & BROEKHUIS, R. R. 1999 Use of a monolith catalyst for the hydrogenation of dinitrotoluene to toluenediamine. *United States Patent* US 6005143.
- MALYALA, R. V. & CHAUDHARI, R. V. 1999 Hydrogenation of 2,4-dinitrotoluene using a supported Ni catalyst: Reaction kinetics and semibatch slurry reactor modeling. *Industrial and Engineering Chemistry Research* 38, 906–915.
- MALYALA, R. V., JAGANATHAN, R. & CHAUDHARI, R. V. 1998 A trickle bed reactor model for hydrogenation of 2,4 dinitrotoluene: experimental verification. *Chemical Engineering Science* 53 (4), 787–805.
- MALYALA, R. V., NIKALJE, D. D., JAGANATHAN, R. & CHAUDHARI, R. 1997 Hydrogenation of 2,4-dinitrotoluene using a Pd/Al₂O₃ catalyst in a slurry reactor: A molecular level approach to kinetic modeling and nonisothermal effects. *Industrial and Engineering Chemistry Research* 36, 592–604.
- MOLGA, E. J. & WESTERTERP, K. R. 1992 Kinetics of the hydrogenation of 2,4-dinitrotoluene over a palladium on alumina catalyst. *Chemical Engineering Science* 47 (7), 1733–1949.
- NERI, G., MUSOLINO, M. G., MILONE, C. & GALVAGNO, S. 1995 Kinetic modeling of 2,4-dinitrotoluene hydrogenation of Pd/C. *Industrial and Engineering Chemistry Research* 34, 2226–2231.
- REID, R. R., PRAUSNITZ, J. M. & POLING, B. E. 1987 *The properties of gasses and liquids*, 4th edn. New York: McGraw-Hill.
- SCHIESSER, W. E. 1991 *The Numerical Method of Lines – Integration of Partial Differential Equations*. San Diego CA, USA: Academic Press.
- YAWS, C. L. 1999 *Chemical Properties Handbook*. New York, McGraw-Hill.
- ZARNACK, U. J., POHL, F., GRENNER, D., HETZEL, H. & JUDAT, H. 1996 Continuous process for preparing aromatic amines. *U.S. Patent* 5563296.

CHAPTER VIII

CONCLUSIONS AND EPILOGUE

§ VIII.1 INTRODUCTION

In heterogeneous catalysis, it is often advantageous to choose small catalyst particles to ensure their efficient use and high selectivity towards the desired product. On the other hand, pressure drop of packed beds increases with decreasing particle size.

This leads to a classical trade-off in fixed-bed reactor design, and for fast reactions one typically has to resort to stirred tank reactors with vigorous contacting of the gas and liquid phase. For turbulent systems, the coupling of hydrodynamics and mass transfer is described by the well-known Chilton-Colburn analogy. Another example of the coupling of hydrodynamics and mass transfer in multiphase systems is the common correlation of the mass transfer and the power input for stirred tank reactors.

In automotive exhaust gas cleaning, the problem of efficient use of the catalyst at minimal energy requirement was solved by the invention of monoliths: ceramic structures of small parallel straight channels. The open straight channels hardly obstruct flow, while high efficiency is achieved using small channels with thin coatings of active material.

The subject of this thesis was the application of the same monolith structures to three-phase systems, i.e. gas-liquid-solid applications. The first part of the thesis focuses on two-phase flow in a single capillary channel. Correlations for pressure drop, mass transfer and residence time distribution were developed. The second part of the thesis deals with the extension of the single channel work to monoliths on a reactor scale. Even a modest-sized monolith has thousands of parallel channels, and the impact of maldistribution over these channels must be taken into account.

§ VIII.2 SINGLE CHANNEL INVESTIGATIONS

PRESSURE DROP

In chapter II, finite-element computational fluid dynamics was used to calculate the velocity field in the liquid and the shape of the bubbles moving through capillary channels. The results were used to formulate a model for the pressure drop for Taylor flow, based on first principle equations. An important result was that the frictional pressure drop is a strong function of the length of the slugs separating the bubbles. Another key finding was that although the flow is laminar, inertial forces could not be ignored.

In order to validate the model, the pressure drop of Taylor flow was measured in a setup that allowed the bubble and slug length to be varied independently. By using various different liquids, the impact of liquid viscosity, density and surface tension could be investigated experimentally. A significant discrepancy between the numerical work and the experimental work was observed, although the dependencies on the relevant dimensionless groups was comparable. The difference between the numerical work and the experimental data could be explained by Marangoni effects.

LIQUID-TO-SOLID MASS TRANSFER

Although the geometry of segmented gas-liquid flow is simple, the different mass transfer regions are complex and highly interdependent. The lubricating film between the bubble and the wall remains intact as the slug passes by. The thickness of this film is governed by a balance of viscous and interfacial forces, usually described by the dimensionless Capillary number $Ca = \mu u / \gamma$. If the Capillary number is low, the film is so thin that it does not limit the transfer to the wall. Inside the slug, the liquid is circulating, which enhances the mixing in the slug and the transfer of liquid components to the film. Using finite-element modeling of the convection-diffusion equation in the slug, in chapter III a 10-fold increase in mass transfer for developed flow with respect to the single-phase value of $Sh=3.658$ was found for long slugs. For shorter slugs, the enhancement is somewhat larger. A dimensionless correlation was formulated for the developing flow, which is only valid for tubes where the liquid in the slugs has circulated at least once. The data for low Reynolds numbers show good agreement with the modeling work, while at high velocities, the impact of the mass transfer resistance of the film layer becomes significant for long slugs, and the model over-predicts the mass transfer.

GAS-TO-SOLID MASS TRANSFER

While the liquid-to-solid mass transfer is a complex combination of circulating slug flow and film resistance at the wall, for gas-to-solid mass transfer the situation is even more complex. Gas absorbs into the circulating slug at the ends of the bubbles, and

is subsequently transferred from the slug to the film and finally to the catalyst on the wall. Parallel to the route through the slug, gas is also transferred directly from the bubble through the film to the wall. As a result, the observed mass transfer is a complex function of the film thickness, slug length and velocity.

For typical application in square monolith channels with rounded corners, the mass transfer through the film is the most limiting step for both parallel routes if the slugs are short. The most important result here is that the predicted mass transfer is extremely high. Further, lowering the velocity enhances the mass transfer. This last finding is counter-intuitive at first: one usually expects transfer to be enhanced by raising the velocity. Realising that the film thickness in Taylor flow decreases with decreasing velocity explains this behaviour, which has an important implication for reactor design: at low velocity the pressure drop decreases, while the mass transfer increases. This fact shows that the classical trade-off in reactor design can be overcome by the use of monoliths.

§ VIII.3 REACTOR SCALE INVESTIGATIONS

RESIDENCE TIME DISTRIBUTION

Perhaps the most important question in the design of a three-phase monolith reactor is whether a model for a single channel can be used to describe the behaviour of the thousands of channels in parallel. Residence time distribution experiments were found to be the most valuable tool in answering this question.

For single channels, the bubbles separating the liquid slugs effectively prevent axial dispersion of the liquid phase in the channel. A liquid-phase tracer can transfer from a slug to the practically stagnant film, and subsequently transfer from the film to the following slug. The resulting residence time distribution leads to a very asymmetric E -curve. The residence time distribution for a single channel can be described by a model of a stagnant zone and a dynamic zone with mass transfer between them.

If there is a distribution of velocities in the channels, the E -curves will be broader and more symmetric. The effect of the maldistribution can be incorporated mathematically into the PE model by superimposing a false axial dispersion on the channel, resulting in the well-known Piston Dispersion Exchange (PDE) model. The resulting false axial dispersion coefficient is a measure for the extent of maldistribution. The corresponding Peclet number for monoliths was found to increase linearly with increasing column length, which suggests that redistribution of the phases between monolith blocks reduces the observed extent of backmixing. The most important experimental finding of the work in chapter IV was that high Peclet numbers were obtained for downflow monolith columns. This finding is in sharp contrast with experimental data in upflow monolith columns reported in the open literature: in upflow monoliths were found to be almost completely backmixed.

The impact of distributions of gas and liquid superficial velocities in the channels on the residence time depends on the slope of isobars for gas and liquid superficial velocities. With the restriction of constant pressure drop, the increase of the superficial velocity of one phase results in a decrease of the superficial velocity of the other phase for most operating conditions in monoliths. In other words, while the fraction of liquid in the channels may vary substantially, the actual residence time of the phases inside the channels is much less distributed.

SLUG LENGTH

Pressure drop and gas–liquid mass transfer are both functions of the liquid slug length. While in a single channel the length of the slugs can be determined by simple visual observation, in a monolith the slug length is hard to measure. A solution to this problem is found by extracting the slug length from the experimental pressure drop in a monolith. The validity of this approach was verified by comparing the pressure drop predicted by the slug length dependent pressure drop model with direct measurement of the bubble and slug length by mounting electrodes on opposite sides of a channel in a monolith. The passing of a slug could be measured by the decrease in electrical resistance of the liquid.

The slug lengths obtained from the pressure drop allowed the interpretation of experimental gas–liquid mass transfer data. In the absence of reaction on the wall, this mass transfer step is a strong function of the slug length. The slug length obtained from the gas–liquid mass transfer was in good agreement with the slug length obtained from pressure drop.

In the case of fast reaction on the wall, the transfer of gas to the catalyst is not a strong function of the slug length. Nevertheless, knowledge of the slug length in an industrial scale reactor is essential to determine the stable operating conditions for monoliths. The accurate pressure drop model presented in this thesis showed that monoliths can be operated stably at much lower throughput of gas and liquid than reported before. This finding is important, because earlier findings based on less accurate pressure drop models suggested that monoliths can only be operated in a stable manner at such high superficial velocities that the residence time is too short for all but the fastest reactions.

The use of the pressure drop to estimate the slug length in monoliths has its drawbacks: the pressure drop over the distributor must be accounted for and maldistribution reduces the overall pressure drop over the monolith. Nevertheless, the pressure drop method provides a cost–effective method to estimate the slug length. The pressure drop method is especially useful for scale–up purposes since to date more costly alternative methods, such as tomography, cannot (yet) be applied to monoliths at relevant throughputs.

COMPARISON WITH OTHER REACTORS

The work in this thesis demonstrates that monoliths are an attractive alternative to stirred tank reactors for fast three-phase reactions. The single channel modeling provides design equations based on first principles, so their application to a wide variety of process-conditions is feasible. In recent years, so-called process intensification has become an important topic in chemical engineering. An objective of process intensification is an orders-of-magnitude reduction in reactor size. This calls not only for a catalyst that is able to provide the reaction rates needed to reduce reactor volume, but also for a dramatic improvement of the mass transfer characteristics. For typical packed-bed reactors, mass transfer enhancement results in an unacceptable increase in pressure drop. In conventional agitated contactors, bubble break-up is caused by eddies in turbulent flow. The size of the bubble is directly related to the size of these eddies, and turbulence theory provides the fundamental basis for the well-known correlations of mass transfer and power input.

In monolith reactors, small bubbles only have to be generated at the entrance of the reactor. Once inside the channels, the bubbles are separated from the wall by a thin film, and the liquid between bubbles cannot escape the slug that it forms. As a result, bubbles do not coalesce, so no energy is required to maintain the small bubbles, resulting in tremendously improved energy efficiency. The work presented in this thesis demonstrates that in monolith structures, at least an order of magnitude reduction of the power requirement for gas–liquid mass transfer is achieved. This makes monoliths an interesting alternative for gas–liquid contacting without a catalyst on the channel walls.

For gas–liquid–solid mass transfer, equal or better mass transfer characteristics can be obtained in monoliths in comparison with stirred reactors, at a fraction of the energy input. Note that in monoliths these mass transfer rates are obtained in plug flow, while stirred tank reactors are completely backmixed. Together with the demonstrated feasibility of scale-up, this makes monoliths ideal alternatives for fast three-phase reactions and for processes where low energy input is beneficial, such as large scale bioreactors.

As a demonstration of the use of monoliths, a design study was presented for the hydrogenation of 2,4-dinitrotoluene. This process must be carried out at low reactant concentrations. The low pressure drop of monolith reactors allows a large recycle of the product through an external heat exchanger to obtain a loop reactor with plug flow behaviour.

§ VIII.4 OPEN QUESTIONS

The combined findings of the work in this thesis show that the hydrodynamics and transport phenomena in Taylor flow can be used to design compact, efficient and selective reactors on a large scale.

Several questions still remain. With regard to the frictional pressure drop, a numerical study that accounts for both inertial effects and Marangoni effects is still missing. The experimental data presented in chapter II could be valuable in validating such a numerical study.

It would be even more valuable to extend such a numerical investigation of Taylor flow to three dimensional structures. The numerical work in chapter V on circular channels shows that the transfer of gas–phase components to the catalyst depends mainly on the thickness of the lubricating film separating the bubbles and slugs from the catalyst. In the open literature several studies report film thickness in square channels. Although these studies agree on the film thickness in the corners, for the film thickness in the middle of the wall the different sources give very different results. No data, either numerical or experimental, is available for channels with rounded corners, which is in general the relevant three dimensional geometry for coated monoliths.

Apart from improving the understanding of Taylor flow in non-circular channels, an arguably better approach would be to improve the coating procedures to make circular channels. While the choice of circular channels for the numerical studies in this thesis was motivated by the reduced computational cost of 2D studies with respect to 3D studies, the results have shown that circular channels are superior to the channels with rounded corners, especially with respect to mass transfer behaviour. Since bare monolith structures are also mass–produced in enormous quantities with hexagonal channels for automotive applications, it probably makes more sense to use such monoliths: the rounding of the channels in the coating procedure will probably easily result in round channels.

The single channel experiments presented in chapter II should nevertheless be extended to square channels to experimentally study the effect of channel geometry. The same setup can also be used to investigate residence time distribution and gas–liquid mass transfer. The gas–liquid mass transfer correlation from the open literature in this work was not dimensionless, and experiments with different liquids and gasses, *i.e.* for different diffusion coefficients, will be valuable in formulating a dimensionless correlation. It would also be valuable to modify the setup for single channel experiments to allow operation in downflow, especially for RTD studies with square channels. Further, it would be interesting to perform reactive experiments in single channels where the slug and bubble length can be accurately controlled, similar to the literature data presented in chapter III, but then for a gas–liquid–solid reaction.

The wetting characteristics of the channels were not studied in this work. In Taylor flow, the liquid completely wets the channel, and it would be interesting to examine what happens to the flow pattern in for instance a very hydrophobic channel.

With respect to scale-up, the results of chapter IV on residence time distribution cannot be interpreted in terms of the distribution of gas superficial velocity and liquid superficial velocity, because accurate pressure drop data for the setup used for RTD experiments were not obtained. It would be most valuable to measure the residence time distribution simultaneously with pressure drop and slug length by conductivity to validate the scale-up strategy presented in chapter VI. The most intriguing question here is whether the variance of the E -curve can be correlated with the slope of the isobars.

Of course, the amount of pilot-scale data of processes in monoliths is still limited, and further work on demonstration of applications in monoliths would be helpful to eliminate the existing widespread scepticism in industry for all new reactor concepts, to which monoliths are no exception.

Finally, the work in this thesis has been limited to gas-liquid two phase flow in the monolith channels. Extending the work to liquid-liquid flow would be interesting. In a liquid-liquid Taylor flow, the enhancement of liquid-solid mass transfer caused by the circulating pattern and the reduction of the residence time distribution compared with single phase flow would probably still apply, which suggests that energy-efficient reaction and extraction processes with two immiscible liquid phases could benefit from the characteristics of Taylor flow described in this thesis.

SAMENVATTING

INLEIDING

Een *chemische reactor* is een apparaat waarin reactanten (zeg A en B) worden omgezet in produkten (zeg C en D). Chemische reacties vinden plaats omdat moleculen op elkaar botsen. Een fractie van deze botsingen is krachtig genoeg om de reactanten om te zetten in produkten. Een katalysator is een stof die noch gevormd noch verbruikt wordt in een reactie maar er wel bij betrokken is. Het Japanse woord voor katalysator betekent letterlijk huwelijksmakelaar en dat geeft veelal aardig de werking van een katalysator weer: de reactanten binden aan de katalysator waarbij ze zodanig met elkaar in contact worden gebracht, dat ze sneller met elkaar reageren.

In de industriële praktijk wordt veelal gebruik gemaakt van *heterogene* katalysatoren. Het woord heteroëen duidt erop dat de katalysator zich in een andere fase bevindt dan de reactanten en produkten. In het meest voorkomende geval is de katalysator de vaste stof en bevinden de reactanten en produkten zich in de gas- of vloeistoffase. Het belangrijkste voordeel van de vaste katalysator is dat deze redelijk makkelijk is te scheiden van de produkten. Hoewel een goede katalysator een reactie versnelt, introduceert het gebruik van meer dan één fase in een reactor een nieuw probleem: de reactanten moeten worden overgebracht naar de vaste katalysator om te reageren en de produkten moeten de vaste katalysator weer verlaten. Het proces waarin een component van de ene naar de andere fase wordt overgebracht noemt men *stofoverdracht*. Indien de reactie snel is of de stofoverdracht langzaam, kunnen zulke overdrachtstappen het gedrag van de reactor beïnvloeden: een proces is zo snel als de langzaamste stap. Behalve de snelheid van het proces leiden *stofoverdrachtlimiteringen* vaak ook tot lagere opbrengst van het gewenste product en tot een snellere veroudering van de katalysator.

Het onderzoek dat in dit proefschrift wordt beschreven, heeft betrekking op drie-fase reactoren, waarin zich een gasfase, vloeistoffase en een vaste fase bevinden. Hoewel drie-fase reactoren complex zijn door de vele overdrachtstappen, komen ze in de industriële praktijk veel voor. Hierbij kan men bijvoorbeeld denken aan de reactie van plantaardige oliën met waterstofgas in de productie van margarine; het ontzwallen van aardolie met waterstofgas bij olieraffinage en de productie van synthetische diesel uit synthese-gas.

Men onderscheidt over het algemeen twee typen drie-fase reactoren: *vast-bed* reactoren en *slurry* reactoren. In een vast-bed reactor is de vaste fase stationair en wor-

den de gassen en vloeistoffen er over heen geleid. Denk aan een grote bak met hagelslag met een douchekop er boven. Bij een slurry reactor bestaat de vaste fase uit een zeer fijn poeder dat meestroomt met de vloeistoffase. Slurry reactoren kunnen worden geroerd door opstijgende gasbellen alleen, in welk geval men spreekt van een bellenkolom, of ook nog door een roerder in de reactor, in welk geval men spreekt van een geroerde slurry reactor. Grofweg kan men zeggen, dat vast-bed reactoren ideaal zijn voor langzamere reacties: ze zitten propvol met katalystor, maar het kalme sijpelen van de vloeistof over de katalysator resulteert in een matige stofoverdracht. Aan de andere kant zijn slurry reactoren ideaal voor snelle reacties. Het intensieve contact van de fasen en het grote specifiek oppervlak* van het fijne poeder geeft een goede stofoverdracht. Een nadeel van slurry reactoren is dat het fijne poeder afgefilterd moet worden. Een nadeel van vast-bed reactoren is dat de katalysator deeltjes niet kleiner kunnen zijn dan grofweg 1 mm: kleinere deeltjes met hoger specifiek oppervlak zouden de stofoverdracht weliswaar verbeteren, maar de drukval over een bed met fijn poeder is te hoog.

MONOLIETEN

Uit de bovenstaande zeer korte introductie in de meerfase-reactorkunde blijkt, dat het wenselijk is een vast-bed reactor te ontwikkelen met goede stofoverdracht eigenschappen. Voor gas-vast reactoren bestaan die al lang: onder iedere auto zit tegenwoordig een katalysator, die schadelijke componenten van uitlaatgas omzet in minder schadelijke stoffen. Dit is een snelle reactie. Aanvankelijk werd voor dit proces een vast-bed reactor ingezet, maar de drukval over het katalysator-bed in de uitlaat was onacceptabel hoog. Bovendien leiden trillingen in de auto tot slijtage van de katalysatordeeltjes.

Dit probleem werd opgelost door de ontwikkeling van *monolieten*. Monolieten zijn keramische structuren die bestaan uit duizenden parallele rechte kanalen, zie Figuur 1.1 op pagina 2. Bij monolieten kan men de wanddikte onafhankelijk van de kanaaldiameter kiezen. Door dunne wandjes te gebruiken en relatief grote kanalen met een diameter van een millimeter, krijgt men een katalysator-*dragermateriaal* dat de voordelen van kleine katalysatordeeltjes combineert met een lage drukval. Monolieten zijn een voorbeeld van *gestructureerde* reactoren, waarbij de katalysatordrager een regelmatige repeterende structuur heeft met specifieke voordelen voor het katalytisch proces.

Het onderzoek dat is beschreven in dit proefschrift betreft de toepassing van monoliet reactoren in gas-vloeistof-vast systemen. De aanwezigheid van de extra fase in vergelijking met de autokatalysator introduceert een aantal nieuwe aspecten die bij het ontwerp van driefase monoliet reactoren moeten worden beschreven.

Ten eerste is er het *stromingspatroon*: er stroomt nu zowel gas als vloeistof door de kanalen: de manier waarop ze door de kanalen stromen is van cruciaal belang. In grote kanalen zijn er vele manieren waarop een gas en een vloeistof door een buis kun-

*Specifiek oppervlak is het oppervlak per eenheid volume. Hoe kleiner een katalysatordeeltje, hoe groter het specifiek oppervlak

nen bewegen: kleine belletjes, grote bellen, een schuimachtige laag, enz. In capillaire kanalen (buisjes kleiner dan 2–3 mm) ontstaat bij niet al te hoge snelheden maar één patroon: Taylor–stroming. De buisjes zijn zo klein dat bellen er eigenlijk niet meer in passen: de bellen worden uitgerekt. Door oppervlaktespanningen probeert een bel zo rond mogelijk te zijn. In capillairen leiden die oppervlaktespanningen ertoe dat de bel de vloeistof tussen de bel en de wand probeert weg te duwen: er blijft een dunne vloeistoffilm tussen de wand en de bel over. Tussen de bellen bevinden zich propjes (eng: *slugs*) vloeistof. Een foto van Taylorstroming staat op pagina 4 in Figuur 1.3. Verder is Figuur 1.4 op pagina 5 illustratief. Dit is een berekening van de vorm van een bel tussen twee vloeistof propjes. De lijntjes in de propjes zijn stroomlijnen, die aangeven hoe de vloeistof in de propjes stroomt. Het is duidelijk te zien dat de vloeistof circuleert in de propjes.

In de rest van deze samenvatting worden de belangrijkste conclusies uit de individuele hoofdstukken weergegeven.

DRUKVAL

In Hoofdstuk II wordt de drukval, dat wil zeggen het drukverlies van de inlaat tot de uitlaat, beschreven. De drukval in de propjes komt redelijk overeen met de drukval van vloeistofstroming in een buis zonder belletjes. De drukval over het cilindrische deel van de uitgerekte belletjes is nagenoeg nul: gas heeft een zo lage viscositeit (stroperigheid) en dichtheid ten opzichte van de vloeistof dat de wrijving die door het gas wordt veroorzaakt verwaarloosd mag worden.

Over de gehele bel is de drukval echter niet nul: aan de uiteinden leiden de krachten die de vloeistof wegdrücken tot een extra drukterm. Dit drukverlies is afhankelijk van een aantal krachten. In de chemische technologie wordt vaak gebruik gemaakt van dimensieloze verhoudingen, zgn. kentallen. Voor de extra drukval van de belletjes is het *Reynolds* (ken-)getal, de verhouding van traagheidskrachten en visceuze krachten, en het *Capillair* getal, de verhouding van visceuze krachten en oppervlakte krachten, van belang.

De drukval in Taylorstroming is op twee manieren onderzocht. Ten eerste is op de computer het gedrag van Taylor stroming gesimuleerd. Bij de bestudering van stroming op de computer, de numerieke stromingsleer (eng: *computational fluid dynamics*, CFD), wordt het te bestuderen gebied opgedeeld in een groot aantal vakjes. In het zo onstane fijnmazige net (grid) worden de stromingsvergelijkingen opgelost. Figuur 2.3 op pagina 19 laat zo een grid zien voor Taylor flow. De bovenste helft is het grid aan het begin van de simulatie, en de onderste helft is het grid aan het einde van de simulatie. Gedurende de simulatie vervormt het grid dus, en de vorm van de bel is onderdeel van de oplossing. Door de simulaties voor veel combinaties van het Reynoldsgetal, Capillairgetal, bellengte en sluglengte uit te voeren, werd inzicht verkregen in de extra drukval die door de belletjes wordt veroorzaakt.

Ten tweede is de drukval in Taylorstroming ook experimenteel bepaald in een capillair. Een speciaal voor dit onderzoek ontworpen inlaatsectie (zie Figuur 2.13(b) op pagina 29) maakte het mogelijk de bellengte en de prop lengte onafhankelijk van elkaar in te stellen. Door gebruik te maken van verschillende vloeistoffen konden het Reynoldsgetal en het Capillairgetal ook onafhankelijk van elkaar worden gevarieerd.

De resultaten van de numerieke studie en de experimentele studie kwamen niet exact met elkaar overeen. In een simulatie heeft men geen last van verontreinigingen in de vloeistof. Zulke verontreinigingen hebben wel een grote invloed op de experimenteel bepaalde drukval. Door op basis van literatuurgegevens te corrigeren voor zulke verontreinigingen, konden de numerieke en experimentele data met elkaar in overeenstemming worden gebracht.

Het belangrijkste resultaat is dat de extra drukval die door de belletjes veroorzaakt wordt significant is. Daardoor is het van belang te weten hoeveel belletjes er zijn per meter capillair. Indien dat bekend is, kan met de in hoofdstuk II ontwikkelde vergelijking 2.22 op pagina 34 de drukval nauwkeurig voorspeld worden. Andersom kan ook: door de drukval te meten kan het aantal belletjes per meter capillair worden uitgerekend.

STOFOVERDRACHT

In de hoofdstukken III en V is de stofoverdracht van respectievelijk vloeistofcomponenten en gascomponenten beschreven. Hierbij is het van belang te weten hoe het patroon in Taylorstroming er precies uitziet.

Voor de overdracht van vloeistofcomponenten is de circulatie in de propjes het belangrijkste. Zonder belletjes stromen alle vloeistofelementjes parallel aan de wand. De enige manier waarop componenten naar de wand kunnen worden overgebracht is dan door diffusie. Diffusie is het stoftransport-equivalent van warmtegeleiding. Door de circulatie in de propjes worden componenten echter ook door stroming naar de wand gebracht; deze bijdrage noemt men *convectief*. Convectief transport gaat over het algemeen sneller dan diffusie transport: denk maar aan het roeren met een theezakje in water om de thee sneller op sterkte te brengen.

De overdracht van vloeistofcomponenten is numeriek bestudeerd. De resultaten werden vergeleken met experimentele data uit de literatuur. De numerieke studie voorspelde de experimentele data goed, mits de circulatie de dominante bijdrage aan het stoftransport was. Indien de snelheden in Taylorstroming hoog zijn, is de film tussen de bel en de wand dik. Dit komt omdat bij hogere snelheden visceuze krachten beter in staat zijn het wegdrücken van vloeistof door de bel tegen te gaan. Deze film blijft bestaan tussen de propjes en de wand: de circulerende stroming bereikt de wand dus nooit helemaal. Hoe dikker die film is, hoe groter de weerstand van die film tegen stofoverdracht.

Voor de overdracht van gas componenten naar de katalysatorwand is die film zelfs de dominante weerstand tegen stofoverdracht. Het is dus van belang de dikte van die

film nauwkeurig te weten. Voor ronde kanalen is de filmdikte theoretisch goed te voorspellen. De berekening aan drukval in hoofdstuk II bevestigden zulke theoretische voorspellingen ook. In monolieten zijn de kanalen echter in het algemeen aanvankelijk vierkant. Tijdens het aanbrengen van de katalysator worden de kanalen rond. Figuur 1.2 op pagina 3 laat een opname met een elektronenmicroscop zien van een gecoat monoliet kanaal. Voor de kanalen met afgeronde hoeken zijn geen filmdikte correlaties bekend.

Experimenteel werd de stofoverdracht van gas componenten bestudeerd met een zeer snelle reactie, de hydrogenering van α -methylstyreen, in een proeffabriek met monolieten. Als de reactie heel snel is ten opzichte van de stofoverdracht, wordt de waargenomen snelheid van de reactie geheel door de snelheid van stofoverdracht bepaald. Uit de waargenomen reactiesnelheid (dat wil zeggen: stofoverdrachtsnelheid) werd vervolgens de filmdikte uitgerekend. De resultaten lieten zien dat de film in kanalen met afgeronde hoeken ongeveer drie keer zo dik is als in ronde kanalen. Door die kennis toe te passen in het stofoverdrachtsmodel, kan worden uitrekend dat in ronde kanalen de stofoverdracht drie maal sneller is dan in kanalen met afgeronde hoeken.

Een gunstig aspect van Taylorstroming is dat bij lagere snelheid de vloeistof-film dunner wordt. Bij lagere snelheden is de drukval ook lager. Het plezierige van Taylorstroming is dus dat bij *lagere* drukval de stofoverdracht *beter* wordt. Dit is op het eerste gezicht contra-intuïtief: bij een hogere drukval wordt meer energie gedissipeerd in de tweefase stroming, en in de meeste reactoren betekent dat een heftiger contact tussen de fasen. In Taylorstroming kan een bel bij lagere snelheden beter de vloeistof tussen de wand en de bel wegdrukken, en een betere stofoverdracht is dan het gevolg.

Alleen als de reactie met α -methylstyreen bij zeer hoge temperaturen werd uitgevoerd, was de stofoverdracht geheel limiterend. Hoewel dit de interpretatie van de metingen in termen van overdrachtsnelheden bemoeilijkte, geeft het wel aan dat de stofoverdracht in monolieten zeer snel is. Voor de meeste vast-bed reactoren is deze hydrogenering al iets boven kamertemperatuur volledig gelimiteerd door stofoverdracht. Door de veel betere stofoverdracht werd dat punt in monolieten pas bereikt boven de honderd graden Celsius – men moet zich realiseren dat de reactiesnelheid van de hydrogenering van α -methylstyreen verdubbelt ongeveer bij iedere 10 graden Celsius temperatuursverhoging. Tenslotte werd de verbetering van stofoverdracht door het verlagen van de snelheid experimenteel aangetoond.

VERBLIJFTIJDSPREIDING

In hoofdstuk IV wordt de verblijftijdspreiding in monolieten behandeld. Het woord verblijftijdspreiding geeft de betekenis al goed weer: het geeft niet alleen aan hoelang het gas en de vloeistof in de kanalen verblijven, maar geeft ook aan wat de spreiding van die verblijftijd is.

Voor veel processen is een smalle verblijftijdspreiding gewenst. Een voorbeeld is het doorreageren van een gewenst reactieproduct: je wilt in dat geval dat de reactanten

precies lang genoeg in de reactor verblijven om tot het gewenste product te worden omgezet. Bij een kortere verblijftijd is de omzetting naar het gewenste product niet compleet en bij een langere verblijftijd is de door-reactie te groot. Verblijftijdspreiding zegt iets over menging op reactorschaal. Indien de reactor goed gemengd is, is de verblijftijdspreiding breed. Als alle vloeistofpakketjes echter zonder met andere vloeistofpakketjes te mengen met dezelfde snelheid door de reactor stromen, dan is de verblijftijd voor ieder pakketje hetzelfde en spreken we van *propstroomgedrag*. In Taylorstroming mengen achtereenvolgende propjes nauwelijks met elkaar omdat ze van elkaar gescheiden worden door bellen die bijna de hele doorsnede van het kanaal opvullen. Dit suggereert dat een scherpe verblijftijdspreiding mogelijk is. Een monoliet bestaat echter uit duizenden kanalen. In al die kanalen hoeft de snelheid niet het zelfde te zijn.

In monolieten zijn er twee bijdragen aan de verblijftijdspreiding. De eerste bijdrage beschrijft de uitwisseling tussen achtereenvolgende propjes in een kanaal. De tweede bijdrage hangt samen met snelheidsfluctuaties. Experimenten in een monoliet-kolom hebben aangetoond dat de tweede bijdrage steeds minder wordt als de kolom langer wordt. De experimenten konden worden beschreven met een model dat beide bijdragen meeneemt.

De mate waarin snelheidsfluctuaties optreden, is afhankelijk van hoe gelijkmatig het gas en de vloeistof over de kanalen wordt verdeeld. In hoofdstuk IV is een verdelers ontwikkeld die gelijkmatiger verdeelt dan sproeiers. Bij het stapelen van monolietblokken in een kolom treedt herverdeling op tussen de blokken. Het effect van snelheidsfluctuaties neemt af naar mate er meer van zulke herverdelingen tussen blokken optreden.

OPSCHALEN

Een van de lastigste aspecten van het ontwerpen van grote chemische fabrieken is opschalen, dat wil zeggen het voorspellen van het gedrag van de grote reactor op basis van kleinschalige proeven. Indien de snelheidsfluctuaties in monolieten verwaarloosbaar zijn, kan men een model voor een enkel kanaal met het aantal kanalen vermenigvuldigen om het gedrag van de grote reactor te beschrijven. In dat geval zijn monolieten zeer makkelijk schaalbaar.

Indien er behoorlijke snelheidsfluctuaties optreden, dan is het meten van de verblijftijdspreiding niet genoeg: ook de drukval moet bekend zijn. In hoofdstuk VI worden een aantal experimenten beschreven waaruit blijkt dat het drukval-model gebruikt kan worden om het aantal belletjes per meter kanaal uit te rekenen.

Uit de bestudering van stofoverdracht bleek dat het wenselijk is monolieten bij zo laag mogelijke snelheden te bedienen. Maar als de snelheid erg laag is, dan wordt een monoliet onstabiel en kunnen er grote snelheidsfluctuaties optreden. Dit is al langer bekend, en in de open literatuur is met simpele drukval-modellen uitgerekend dat de snelheden in monolieten enkele tientallen centimeters per seconde zouden moeten be-

dragen om stabiel te zijn. Nu kwam het nauwkeurige drukvalmodel goed van pas: monolieten blijken bij veel lagere snelheden nog stabiel te zijn.

VERGELIJKING MET ANDERE REACTOREN

Met behulp van de beschrijvingen van drukval en stofoverdracht in monolieten kon een vergelijking met “klassieke” reactoren worden gemaakt. Kort gezegd zijn monolieten vastbed reactoren met stofoverdracht-karakteristieken die vergelijkbaar zijn met slurry reactoren bij een veel lager energie-gebruik. Omdat ook is aangetoond dat monolieten goed schaalbaar zijn, kan worden vastgesteld dat Taylorstroming in capillairen inderdaad de mogelijkheid opent om de voordelen van vastbed reactoren en slurry reactoren te combineren.

Voor processen zonder een vaste katalysator is aangetoond dat de verbeteringen nog spectaculairder zijn: voor het door elkaar klutsen van een gas en een vloeistof kan een monoliet worden gebruikt die minstens tien keer kleiner is dan een geroerde reactor.

PROCES-VOORBEELD

Om de toepassing van monolieten te illustreren voor een industrieel proces is de hydrogenering (reactie met waterstof) van 2,4-dinitrotolueen gekozen. Dit is een reactie waarbij zoveel warmte vrijkomt, dat het gevaar van een explosie reëel is. Traditioneel wordt dit proces uitgevoerd met een sterk verdunde oplossing van de reaktant in bijvoorbeeld ethanol in een geroerde slurry reactor. Door een monoliet in een kringloop met een warmtewisselaar te zetten kan het oplosmiddel vervangen worden door het product, zodat het oplosmiddel niet meer afgedampt hoeft te worden. Dit idee is overgenomen uit een patent voor het toepassen van monolieten voor dit proces. Verder hoeven katalysatordeeltjes ook niet meer afgefilterd te worden, omdat een monoliet een vastbed reactor is. In het kringloop systeem worden grote hoeveelheden vloeistof verpompt, zodat de lage drukval over monolieten een voordeel is. Omdat de heftige reactie snel is, heeft een monoliet het voordeel dat de stofoverdracht de reactie kan bijhouden. Dit alles resulteert in een compacte reactor, en voor reacties die uit de hand kunnen lopen is dat een groot voordeel.

SAMENVATTING

PUBLICATIONS AND PRESENTATIONS

PUBLICATIONS

HEISZWOLF, J. J., ENGELVAART, L., VAN DER EIJNDEN, M., KREUTZER, M. T., KAPTEIJN, F. & MOULIJN, J. A. 2001*a* Hydrodynamic aspects of the monolith loop reactor. *Chemical Engineering Science* 56 (3), 805–812.

NIJHUIS, T. A., KREUTZER, M. T., ROMIJN, A. C. J., KAPTEIJN, F. & MOULIJN, J. A. 2001*a* Monolith catalysts as more efficient three-phase reactors. *Catalysis Today* 66 (2–4), 51–55.

NIJHUIS, T. A., KREUTZER, M. T., ROMIJN, A. C. J., KAPTEIJN, F. & MOULIJN, J. A. 2001*b* Monolith catalysts as efficient three-phase reactors. *Chemical Engineering Science* 56 (3), 823–829.

KREUTZER, M. T., DU, P., HEISZWOLF, J. J., KAPTEIJN, F. & MOULIJN, J. A. 2001 Mass transfer characteristics of three phase monolith reactors. *Chemical Engineering Science* 56 (22), 6015–6023.

HEISZWOLF, J. J., KREUTZER, M. T., VAN DER EIJNDEN, M., KAPTEIJN, F. & MOULIJN, J. A. 2001*b* Gas-liquid mass transfer of aqueous Taylor flow in monoliths. *Catalysis Today* 69 (1-4), 51–55.

DE DEUGD, R.M., CHOUGULE, R., KREUTZER, M.T., MEEUWSE, M., GRIEVINK, J., KAPTEIJN, F. & MOULIJN, J. A. 2003 Is a monolith loop reactor a viable option for fisher tropsch synthesis?, *Chemical Engineering Science* 58, 583–591.

MOULIJN, J. A., PEREZ-RAMIREZ, J., VAN DIEPEN, A. E., KREUTZER, M. T., KAPTEIJN, F. 2003 Catalysis Engineering of Three Levels, *International Journal of Chemical Reactor Engineering*, accepted.

IN PREPARATION

KREUTZER, M. T., J. J. W. BAKKER, KAPTEIJN, F. & MOULIJN, J. A. Liquid phase residence time distribution in three-phase monolith reactors.

KREUTZER, M. T., J. J. HEISZWOLF, KAPTEIJN, F. & MOULIJN, J. A. A strategy for monolith reactor scale-up by accurate pressure drop modelling.

KREUTZER, M. T., KRITZINGER, H. P., KLEIJN, C. R., KAPTEIJN, F. & MOULIJN, J. A. Pressure drop in segmented two-phase flow in capillaries.

LECTURE NOTES

KAPTEIJN, F., MOULIJN, J. A., KREUTZER, M.T. AND VAN DIEPEN, A. E. 2001, Catalysis Engineering

ORAL PRESENTATIONS

KREUTZER, M.T., DU, P., HEISZWOLF, J.J., KAPTEIJN, F. & MOULIJN, J.A. 2001 Mass transfer characteristics of three-phase monolith reactors. Presented at the fifth international conference on Gas-Liquid-Solid Reactors, Melbourne, Australia.

KREUTZER, M.T., HEISZWOLF, J.J., KAPTEIJN, F. & MOULIJN, J.A. 2001 Mass transfer in monolith reactors. Invited Lecture at Air Products and Chemicals, USA

KREUTZER, M.T., WEI, W., HEISZWOLF, J.J., KAPTEIJN, F. & MOULIJN, J.A. 2003 Pressure drop of Taylor flow in capillaries: impact of slug length. Proceedings of the first international conference on microchannels and minichannels (Rochester NY, USA), ASME.

KREUTZER, M.T., KAPTEIJN, F. & MOULIJN, J.A. 2003 Hydrodynamics of Taylor flow in Three Phase Monolith Reactors, Invited Lecture at Air Products and Chemicals, Inc. and Corning, Inc., USA.

MOULIJN, J. A., KAPTEIJN, F., KREUTZER, M. T & STANKIEWICZ, A. 2003 Structured Catalysis and Reactors: a contribution to sustainable technology. Presented at the university of Porto, Portugal, 2003

MOULIJN, J. A., KAPTEIJN, F., KREUTZER, M. T & STANKIEWICZ, A. 2003 Chemistry and Chemical Technology for a Sustainable Society. Presented at the Gramata Workshop, Utrecht, the Netherlands, 2003

MOULIJN, J. A., NIJHUIS, X. A., KREUTZER, M. T., STANKIEWICZ, A. & KAPTEIJN, F. 2003 Potential of Monolith Reactors in Multiphase Heterogeneous Catalysis, Presented in the framework of the DOW M.M. Sharma Professorship, Mumbai, India, 2003

POSTER PRESENTATIONS

KREUTZER, M. T., HEISZWOLF, J. J., NIJHUIS, T. A., KAPTEIJN, F. & MOULIJN, J. A. 1999 Hydrodynamics and mass transfer in three-phase monolith reactors. Presented at the OSPT symposium, Lunteren 1999.

HEISZWOLF, J. J., KREUTZER, M. T., HEIBEL, A. K., KAPTEIJN, F. & MOULIJN, J. A. 2003 The monolithic support for biotechnological applications. Presented at the NBC conference, Wageningen 2000.

BAKKER, J. J. W., WEI, W., KREUTZER, M. T., KAPTEIJN, F. & MOULIJN, J. A. 2002 Hydrodynamics of monoliths in three-phase systems. Presented at the meeting Mastering Molecules in Motion, Delft, 2002.

KREUTZER, M. T., KAPTEIJN, F. KAPTEIJN & MOULIJN, J. A. 2003 Hydrodynamics of monoliths in three-phase systems. Presented at the Rhodia conference "Chemical Engineering for sustainable chemistry", Lyon 2003.

KREUTZER, M. T., J. J. W. BAKKER, KAPTEIJN, F. & MOULIJN, J. A. 2003 Three phase monolith reactors: plug-flow of maldistributed? Presented at the ISMR3, Bath 2003.

KREUTZER, M. T., KAPTEIJN, F., MOULIJN, J. A., KRITZINGER, H. P., KLEIJN, C. R. & VAN DEN AKKER, H. E. A. 2003 Finite element modeling of inertial effects on Taylor flow, Presented at the FOM meeting, Veldhoven 2003.

EBRAHIMI, S., PICIOREANU, C., KLEEREBEZEM, R., KREUTZER, M. T. HEIJNEN, J. J. AND M.C.M. VAN LOOSDRECHT, M. C. M. 2003 The monolith reactor - A Novel Reactor Concept for Biological Gas Purification, Presented at the A.I.Ch.E. Annual Meeting, 2003

DANKWOORD

Volgens de gangbare definitie doe je gedurende je promotie vier jaar lang zelfstandig onderzoek. Ik heb dat niet zo ervaren: voor het doen van wetenschappelijk onderzoek is de wisselwerking met je collega's van essentieel belang. Aan de totstandkoming van dit proefschrift hebben dan ook verschillende mensen een belangrijke bijdrage geleverd.

Allereerst wil ik mijn promotoren Jacob Moulijn en Freek Kapteijn bedanken. Toen ik aan dit onderzoek begon, was het onderwerp nog niet in detail vastgelegd. Op mijn vraag de eerste ochtend in Delft welke kant ik als eerste op moest gaan was jullie antwoord: "Naar boven, naar de bieb!" Lichtelijk perplex ben ik daar dan maar heen gegaan. Achteraf gezien was die eerste dag tekenend voor de jaren van plezierige samenwerking die volgden. De vrijheid die jullie me hebben gegeven om het onderzoek zelf richting te geven, getuigt van een vertrouwen dat jullie in me hadden. De discussies aan het einde van het traject hebt ik als zeer waardevol ervaren. Daarbij wil ik jullie verder bedanken voor de gelegenheid die jullie me hebben geboden om betrokken te zijn bij het geven van onderwijs. Toen ik begon in Delft had ik nagenoeg geen kennis van katalyse, en aan jullie suggestie om dat hiaat te vullen door katalyse te onderwijzen heb ik veel te danken.

Johan Heiszwolf, Paul Lebens en Achim Heibel wil ik in het bijzonder bedanken voor de vele discussies over hydrodynamica in monolieten. Johan, jij hebt me de eerste jaren van het onderzoek zeer kundig van dag tot dag begeleid. Na je vertrek naar de Verenigde Staten heb ik nog vele nachtelijke discussies over de telefoon met je mogen voeren, die zeer stimulerend waren. Bovendien verheug ik me dat we goede vrienden zijn gebleven. Achim, you have been a stimulating colleague, a pleasant roommate and a good friend. With joy I look back on the long evenings soldering away on the data acquisition boxes and discussing our work. The first International Symposium on Hydrodynamics in Monoliths (ISHM1) in the beautiful scenery of the French Languedoc is exemplary for the good atmosphere I have had the pleasure to work in. Johan and Achim, thanks!

Ik beschouw het als een privilege dat ik vele studenten heb mogen begeleiden tijdens hun afstudeeronderzoek. Peng Du, Martijn Zieverink, Raoul Chougule, Sachin Singare, Wei Wei, Pablo Poveda Martinez, Dario Puertas Otones and Jasper Bakker: I want to thank you all for the pleasure of working with you. A lot of the hard work that you have done significantly contributed to this thesis.

Peter Verheijen wil ik bedanken voor de waardevolle discussies. Chris Kleijn en H.P. Kritzinger wil ik bedanken voor de samenwerking bij het modelleren van drukval en gebruik van de rekencapaciteit op het Kramerslab. I want to thank Tracy Gardner and Mertijn Zieverink for their valuable comments in the final stages of preparing the manuscript.

Alle technici van de vakgroep en de werkplaats wil ik graag bedanken voor alle hulp bij het sleutelen aan de opstellingen. In het bijzonder wil ik de glasblazerij bedanken. De hulp van Peter Hiddinga van Avantès BV bij het ontwikkelen van de meetmethode voor hoofdstuk IV wordt zeer gewaardeerd.

Alle (ex)-collega's van de vakgroep bedank ik voor de plezierige werksfeer.

Bij voorbaat wil ik mijn paranimphen Erik Rammeloo en Adriaan Waiboer bedanken voor de hulp bij de promotie-plechtigheid zelf.

Papa, je hebt ons altijd plagend voorgehouden dat men pas klaar is met studeren na het voltooien van een proefschrift. Ik heb dat vrij letterlijk genomen, en ik heb steeds genoten van de warme belangstelling waarmee je je op de hoogte hield van mijn vooruitgang. Tot mijn aangename verbazing heb je ook nog eens kunnen bijdragen aan het onderzoek door me te wijzen op een aantal studies in jouw vakliteratuur.

Papa en Ietje, ik wil jullie bedanken voor de steun die ik gedurende het hele promotietraject heb mogen genieten. Het was altijd fijn om thuis te komen.

Lieve Merel, jouw mentale steun bij het voltooien van dit boek was voor mij van onschatbare waarde. Steeds kon je inschatten of je me moest verleiden tot een pauze of dat je me moest aansporen om door te zetten. Met name aan de pauzes heb ik dierbare herinneringen.

Tenslotte is er iemand die ik hier graag had willen bedanken, en dat degene die mijn plezier in de wetenschap heeft aangewakkerd: prof. Laurent van Dierendonck. Tijdens mijn afstuderen en de maanden daarna heb ik met zeer veel plezier met hem gewerkt, en hij is degene geweest die mij heeft geadviseerd om bij Jacob en Freek te gaan promoveren, een suggestie waar ik nog altijd dankbaar voor ben. Ik kan mij als de dag van gisteren herinneren dat Jacob mij het droeve nieuws bracht dat hij op weg naar een bespreking met ons veel te vroeg is overleden. Af en toe kom ik een artikel van hem tegen, dat ik dan steeds lees, en waarbij ik mij meestal realiseer hoeveel ik veel van hem heb geleerd.

CURRICULUM VITAE

Michiel Kreutzer werd geboren op 19 april 1971 te Haarlem. Na het behalen van het Gymnasium β diploma aan het Lingecollege in Tiel begon hij in september 1990 met de studie Scheikundige Technologie aan de Rijksuniversiteit Groningen. In augustus 1998 studeerde hij af onder leiding van prof. dr. ir. L.L. van Dierendonck. In september 1998 begon hij als promovendus met zijn promotieonderzoek aan de Technische Universiteit Delft. De resultaten van dat onderzoek zijn beschreven in dit proefschrift. Op dit moment is hij werkzaam als tenure-track postdoc bij de TU Delft in de vakgroep Reactor and Catalysis Engineering.